UNIVERSITA' DI PADOVA FACOLTA' DI INGEGNERIA

Dipartimento di Ingegneria dell'Informazione

Scuola di Dottorato di Ricerca in Ingegneria dell'Informazione
Indirizzo: Bioingegneria

CICLO XXIII

BIOMEDICAL APPLICATIONS OF ELECTROMAGNETIC FIELDS: HUMAN EXPOSURE, HYPERTHERMIA AND CELLULAR STIMULATION

Direttore della Scuola: Ch.mo Prof. Matteo Bertocco

Supervisore: Ch.mo Prof. Fabrizio Dughiero

Dottoranda: Elisabetta Sieni

Special thanks

Part of this work has been developed in Inova Lab srl a Spin Off of the Padova University.

A special thanks to Telwin S.p.A., in the person of Ing. Andrea Cortiana, and Telea, in the person of Ing. Giannantonio Pozzato, for the permission to use some of the materials and results derived by some projects developed in collaboration with Inova Lab srl. Telwin for the study of the emission of magnetic field due to welding equipments (arc and resistance) and Telea for the study of the electric stimulation of human and rat cells of the brain by means of an electric field. In particular these projects allowed me to develop the human body and rat head models for FEM simulations. In particular, I want to thanks the Laboratory of Magnetic Resonance Imaging of the Verona University for the magnetic resonance images of the rat head.

The experimental part with rat models and the implementation of the measurement set-up has been developed in collaboration with the Physiology Department of the Padova University in the laboratory of prof. Stefano Vassanelli, with the collaboration of Dott. Stefano Girardi, who has lent the instrumentation for the experiments with rats. Part of the experiments with the rat has been developed by Azzurra Carlon undergraduate student (supervisor prof. Alfredo Ruggeri of the Department of Information Engineering of the Padova University) during her thesis for the bachelor degree.

Part of the work about the human exposure due to welding equipments has been implemented by Francesco Menestrina (supervisor prof. Fabrizio Dughiero of the Department of Electrical Engineering of the Padova University) during his thesis for the Master degree. The optimization part has been supervised by prof. Paolo Di Barba of the Pavia University. Morover, I want to thank the Prof. Dughiero and Ing. Forzan that give me the possibility to develop the present work and teach me about electromagnetic fields. I must to remember, also, the Ing. Bullo that helps me in some practical aspects and all people of the LEP (Laboratory of Electroheat) at the Padova University that work in electromagnetic problems and biomedical applications of electromagnetic fields (Alessandro, Aristide, Dario, …).

Abstract

Electromagnetic fields are present in some environments of everybody life. Some of the most common sources of electromagnetic field that everybody experiments are the sun radiation, the electric current that supplies household (lights, television set, refrigerator, *etc*) and antennas for telecommunications. In industrial environments the magnetic and electric fields are exploited to the metal treatments and fusion, some magnetic fields are generated by means of electric welding applications or devices that use high intensity electric currents. In residential environment the diffusion of the induction cooktop increases the possibility of domestic exposure to magnetic fields. Nevertheless, electromagnetic fields can also be used with medical purpose.

This thesis evaluates the effects due to the interaction between electromagnetic fields and biological tissues. It is to be noted that the interaction of the magnetic field with a conductor material produces induced currents density that circulating in the media might heat it by means of the Joule effect. The most important application of this phenomenon is the treatment and melting of metals that have a large electrical conductivity (in the order of the millions of S/m) and high relative magnetic permeability. Nevertheless, in spite of the tissues of the human body are bad electrical conductors (conductivity in the order of the unity or lower and a unitary relative magnetic permeability), the induced current density might cause muscle contraction. The intensity of these currents depends on the intensity of the magnetic field that generates them and the effect is perceived if overcomes a given threshold. In this case adverse effect, like nerve or muscle stimulation might be induced. Then, every equipment that uses a high intensity electric current produces a magnetic field that might generate an induced current in the biological tissues. Some standards regulate the maximum of the electromagnetic field at which every person can be exposed. Among equipments that generate high magnetic field this work analyzed arc and resistance welding equipments and induction cooktops. In order to evaluate human exposure to magnetic field below 100 kHz, the magnetic flux density and induced current density have been computed using the Finite Element Method. Some simplified models of the human body have been implemented. The computation results obtained in these simplified volumes by means of numerical methods have been compared with these ones obtained using models that describe accurately the tissues of the human body.

Electric and magnetic fields can be exploited in some medical applications. For instance, the magnetic and electric fields are used in malignant tumor therapies. For instance, examples are the thermal ablation or the tissues heating in localized areas (laser, radiofrequency antennas, thermoseed, *etc*). A technique of new application is the Magnetic Fluid Hyperthermia (MFH), which the original idea is of 1950, but the first prototype device is of the end ninety. This technique uses magnetic nanoparticles inserted in the treatment areas. Nanoparticles are heated by means of an external time-varying magnetic field of suitable frequency and intensity and act as an internal source of heat. In this case the aim is reached a temperature close to a therapeutic value (42-43°C for the mild hyperthermia or overcome 60 °C for the thermal ablation).

Electric fields can also be used in order to stimulate different areas of the brain. An initial

study shows some simulation results obtained in both human and rat brains. Moreover, in this case an experimental set up for measurements *in vivo* in a rat's head has been developed.

All the computations of thermal and electromagnetic fields have been solved using Finite Element Analysis. Some of the algorithms for the solution of coupled magnetic and thermal problems and the code for the optimization procedure have been implemented inside a commercial software tool. In particular, the optimization algorithm included in the Finite Element Analysis tool is an Evolution Strategy code.

In order to calculate magnetic field, magnetic flux density, induced current density and electric field for the solution of the Maxwell equations, different formulations have been used, whereas the thermal problem has been solved using the heat transfer equation, including the Pennes term that describes the effect of the blood perfusion.

Optimization codes have been used in order to design a Magnetic Fluid Hyperthermia device. At first, optimization the uniformity of the magnetic field has been optimized, under the hypothesis that magnetic nanoparticles are uniformly distributed in tissues. This step has allowed the generation of a first design of the magnetic field source. In a second step, the optimization code has been used to search the temperature uniformity in the treated areas; then, the coupling of a magnetic with a thermal problem has been developed. In this case, the transition from the magnetic problem to the thermal one has required the computation of the power density generated by means of magnetic nanoparticles, from the value of the intensity of the magnetic field, using an analytical relation that depend also on instantaneous temperature and physical characteristics and the concentration of magnetic nanoparticles.

The optimization of the temperature uniformity in the treated area, also in term of temperature rate, can be also seen from the point of view of the design of the magnetic field source that is the magnetic fluid design (dimensions and concentration of nanoparticles). Both these aspects have been investigated. Finally, the problem of the real distribution of nanoparticles in tumor tissues has been investigated in term of temperature disuniformity, due to the different nanoparticles concentration. An algorithm for the optimization of the points of injection of nanoparticles *in situ* has been developed, in order to limit the temperature disuniformity related to nanoparticles local concentration.

Some computations of the electric field have been performed in order to evaluate the feasibility to reach internal structures of the brain with electric fields, applying a voltage to suitable points of the external skull. The frequency of the applied voltage is 4 MHz, an unusual frequency for the instrumentation normally used to measure electric potentials *in vivo* in laboratory animals. The experimental part has been developed in order to compare the voltage computed with the Finite Element models with the voltage measured inside the brain tissue using glass micropipettes. It is to be noted that at 4 MHz the micropipette has a different impedance from the one it has in the normal use of instruments (below 1 kHz). A measurement set up has been designed in order to convert the signal measured by means of a micropipette and an oscilloscope, considering the real impedance of the micropipette. The potential at the micropipette point is derived by means of calibration curves evaluated through specific experiments. Measurements have been used to validate the Finite Element simulations of electric fields.

The main results of this thesis are models of living organisms implemented for biomedical applications in order to evaluate the effect of electromagnetic fields in biological tissues. Moreover, different formulations have been used to solve electromagnetic problems, and the solution of magnetic and thermal coupled problems has been proposed. Optimization algorithms have been used for the design of magnetic devices and treatment planning (*e.g.* position of the magnetic field source as a function of the patient and treatment area) or in the magneto fluid drug composition (size of nanoparticles and concentration).

Sommario

I campi elettromagnetici sono diffusi in molti ambienti industriali e residenziali. Alcune delle più comuni sorgenti di campo elettromagnetico sono le radiazioni solari, la corrente elettrica che alimenta gli elettrodomestici (luci, televisore, frigorifero, ecc.) e le antenne per le telecomunicazioni. Negli ambienti industriali i campi elettrici e magnetici sono utilizzati per la fusione e il trattamento dei metalli, in particolare alcuni dispositivi per la saldatura possono generare campi elettromagnetici di intensità elevata. In ambiente residenziale la diffusione del piano di cottura a induzione ha aumentato la possibilità di esposizione della popolazione a campi magnetici che potrebbero essere intensi. Inoltre i campi elettromagnetici possono essere utilizzati a scopo medico in alcune terapie.

Questa tesi analizza l'interazione tra campi elettromagnetici e tessuti biologici. È da notare che l'interazione del campo magnetico con un materiale conduttore produce correnti indotte che circolano nel materiale e producono calore per effetto Joule. L'applicazione più importante di questo fenomeno è il trattamento e la fusione dei metalli che hanno una elevata conducibilità elettrica (dell'ordine dei milioni di Sm^{-1}) ed alta permeabilità magnetica relativa. Nonostante i tessuti del corpo umano siano cattivi conduttori elettrici (conducibilità dell'ordine l'unità o più bassa e una permeabilità magnetica relativa unitaria), la densità di corrente indotta può causare la contrazione muscolare. L'intensità di queste correnti indotte dipende dall'intensità del campo magnetico che le genera e il loro effetto è percepibile se superano la soglia di stimolazione dei nervi o dei muscoli. Quindi, ogni apparecchiatura che utilizza una corrente elettrica produce un campo magnetico che può generare correnti indotte nei tessuti biologici. Alcune norme regolano il massimo valore del campo elettromagnetico a cui ogni persona può essere esposta. Tra le apparecchiature che generano campi magnetici questo lavoro analizza le saldatrici ad arco e a resistenza e i piani di cottura a induzione. Al fine di valutare l'esposizione umana al campo magnetico sotto i 100 kHz, si valuta l'induzione magnetica e la corrente indotta in opportuni volumi che simulano il corpo umano mediante il metodo degli Elementi Finiti. La corrente indotta calcolata con i modelli semplificati del corpo umano è stata confrontata con quella calcolata utilizzando modelli che descrivono con precisione i tessuti del corpo umano.

Campi elettrici e magnetici possono inoltre essere utilizzati in alcune applicazioni mediche. Ad esempio, il campo magnetico ed elettrico possono trovare impiego nella terapia dei tumori. Esempi sono l'ablazione termica dei tessuti o il riscaldamento di zone localizzate (laser, antenne a radiofrequenza, thermoseed, ecc.). Una tecnica di nuova generazione è l'ipertermia magneto fluida, la cui idea originaria risale agli anni '50, ma il primo prototipo è della fine degli anni novanta. Questa tecnica utilizza nanoparticelle magnetiche inserite nelle aree da trattare. Le nanoparticelle sono riscaldate per mezzo di un campo magnetico tempo variante esterno di frequenza e di intensità adeguate e agiscono come una fonte interna di calore. In questo caso la temperatura raggiunta dai tessuti deve raggiungere la soglia terapeutica (42-43°C per l'ipertermia o superare i 60 °C per l'ablazione termica).

Il campo elettrico può essere utilizzato anche per stimolare diverse aree del cervello. Un primo studio mostra alcuni risultati di simulazione ottenuti sia in un cervello umano sia di

ratto. Inoltre, per questo esempio è stato sviluppato un set up sperimentale per misure *in vivo* nei tessuti della testa di un ratto.

Il calcolo del campo termico ed elettromagnetico è stato risolto utilizzando il Metodo degli Elementi Finiti. Inoltre sono stati implementati alcuni algoritmi per la soluzione di problemi di accoppiamento magnetico e termico e un codice per la procedura di ottimizzazione. Il codice di ottimizzazione, di tipo Evolution Strategy, è stato implementato all'interno di un software commerciale per risolvere problemi elettromagnetici e termici mediante il metodo degli Elementi Finiti.

Per la soluzione delle equazioni di Maxwell per il calcolo del campo magnetico, l'induzione magnetica, la densità di corrente indotta e il campo elettrico sono state utilizzate diverse formulazioni, mentre il problema termico è stato risolto utilizzando l'equazione di trasferimento del calore, includendo il termine Pennes che descrive l'effetto della perfusione sanguigna.

I codici di ottimizzazione sono stati utilizzati principalmente per la progettazione di un dispositivo per l'ipertermia magneto fluida. Per un primo disegno della sorgente di campo magnetico si è ottimizzata l'uniformità del campo magnetico, sotto l'ipotesi che le nanoparticelle magnetiche fossero distribuite uniformemente nei tessuti. In seguito il codice di ottimizzazione è stato utilizzato per cercare l'uniformità della temperatura nelle zone da trattare, e quindi è si è risolto un problema magnetico-termico accoppiato. In questo caso il passaggio dal problema magnetico a quello termico ha richiesto il calcolo della densità di potenza generata dalle nanoparticelle magnetiche a partire dall'intensità del campo magnetico. In questo caso si è utilizzata una relazione analitica che valuta la potenza a partire dalla temperatura istantanea dei tessuti, le caratteristiche fisiche delle nanoparticelle magnetiche e l'intensità e la frequenza del campo magnetico.

L'ottimizzazione dell'uniformità della temperatura nella zona trattata, anche in termini di rateo di temperatura, può essere vista come progettazione sia della sorgente del campo magnetico sia del magnetofluido (dimensioni e concentrazione delle nanoparticelle) . Entrambi questi aspetti sono stati indagati. Infine è stato valutato l'effetto della reale distribuzione delle nanoparticelle nei tessuti tumorali sulla disuniformità di temperatura legata alla disuniformità della concentrazione delle nanoparticelle. In questo caso, per limitare la disuniformità di temperatura correlata alla concentrazione delle nanoparticelle, si è sviluppato un algoritmo per l'ottimizzazione dei punti di iniezione *in situ* delle nanoparticelle.

Infine è stata studiata la distribuzione del campo elettrico creato da una differenza di potenziale applicata alla scatola cranica per valutare la fattibilità di raggiungere le strutture interne del cervello. Il segnale di tensione utilizzato è a 4 MHz, una frequenza non usuale per la strumentazione normalmente utilizzata per misurare i potenziali elettrici *in vivo* su animali. Per confrontare la tensione calcolata con i codici numerici con quella misurata all'interno del tessuto cerebrale usando micropipette di vetro, è stato studiato un set up di misura. La micropipetta alla frequenza di 4 MHz ha impedenza differente rispetto quella che si ha nel normale uso dello strumento (frequenze inferiori a 1 kHz). Mediante l'esperimento progettato si sono ottenute delle curve di taratura per convertire il segnale misurato con la micropipetta e l'oscilloscopio. Tali curve tengono conto della reale impedenza della micropipetta. Queste misurazioni sono state utilizzate per validare le simulazioni numeriche del campo elettrico.

I principali risultati di questa tesi sono i modelli di organismi viventi implementati per valutare le interazione dei campi elettromagnetici con i tessuti biologici. In particolare, per risolvere i problemi elettromagnetici e di accoppiamento magnetico e termico sono state utilizzate diverse formulazioni. Inoltre, per la progettazione dei dispositivi magnetici, la pianificazione del trattamento (posizionamento della sorgente di campo magnetico in funzione paziente) e la composizione del magneto fluido (dimensioni e concentrazione delle nanoparticelle) sono stati utilizzati algoritmi di ottimizzazione.

Table of Contents

Summary

Electromagnetic fields are spread in the environment because a lot of the modern devices are supplied by means of an electric current and others equipments use electromagnetic waves. It is well known that electromagnetic fields can interact with metal structures, then with electrical conductor material, inducing a temperature increasing by means of Joule effect or energy deposition.

Since electromagnetic fields can interact with electrical conductors, they might induce also the same effects on the human body structures. In fact, with the same mechanisms the electromagnetic fields can induce current density or heat in the human body. These interactions can be studied in order to prevent adverse effects, but also to use them in medical treatments. For instance, the human body tissue heating can be used for the reduction of some cancer mass and, then, they might have a therapeutic effect, whereas in some case they might induce muscles contractions or nerve stimulation.

Finite Element Analysis has been used to solve electromagnetic and thermal problems in structure with electric and thermal characteristics like the human body tissue, whereas optimizations techniques have been used to design a medical device.

Example on the electromagnetic field exposure, Magnetic Fluid Hyperthermia cancer treatments and electric field distribution in the brain when a voltage difference is applied to the skull bone have been presented and solved by means of the above mentioned techniques.

Chapter 1

1 Introduction

Finite Element Analysis is applied to bioelectromagnetic problems in order to study different aspects of the electromagnetic field interaction with human body tissues. Maxwell equations for low frequency electric and magnetic fields in a quasi-static formulation and heat transfer equation for thermal heat transfer problems have been solved in order to evaluate in models simulating the human body electric and thermal characteristics:

- Induced current density;
- Electric field;
- Power density;
- Magnetic field;
- Tissue temperature.

Since the interaction between electromagnetic fields and biological structures might induce current density or heat deposition and these interaction modes might induce both adverse and therapeutic effects it is important to evaluate the entity of the interaction.

For electromagnetic analysis the human body is an electrical conductor and a dielectric medium depending on the frequency range and the evaluated quantity (*e.g.* induced current density or electric field distribution) whereas for the thermal analysis is a thermal conductor media. It is to be noted that the biological tissues are not good electrical conductors because they have a lower conductivity, then a high resistivity with respect of a metal (few ten of Ωm versus 10^{-8} Ωm), but it is well known that the intensity of the induced current can interact with the biological matter causing some adverse effects like muscle and nerves stimulation or heat induction. The interaction of the electromagnetic field and the human body can be also exploited for therapeutic purposes like hyperthermia treatment or electric field cell stimulation. For instance, if a heat source is posed inside an organ, a heat transfer phenomenon, with a temperature increasing effect, might arrive. Then, the analysis of the induced current and energy deposition on biological tissues is important in order to avoid some possible dangerous situations or quantifies a possible therapeutic effect.

Since the human body in terms of electric and thermal characteristics is a heterogeneous volume the biological effects of electromagnetic field can be evaluated by means of numerical computation techniques. In general, the most important elements for the numerical resolution of the electromagnetic and thermal problems in biological field are:

- The model in which the electric and thermal characteristics of the biological tissue are considered;
- The source of electric or magnetic field that may induce the biological effect;

- The computation method for the resolution of the numerical problem (*e.g.* Finite Element Method) and the optimization methods.

Given the electromagnetic or thermal problem and electric and thermal characteristics of the biological tissues, some models of human body organism, simplified or realistic ones, have been developed in order to evaluate:

- Adverse effects deriving from the human body low frequency magnetic field exposure;
- Therapeutic effects due to:
    - heat deposition on the tissue for the cancer therapy by means of hyperthermia treatments;
    - electric field induced in tissues for the cells stimulation.

Given the different aspects of the electromagnetic field interaction with biological structures, adverse or therapeutic ones, the practical problems analyzed involve:

- Welding equipments exposure in industrial environment;
- Hyperthermia mediated by means of magnetic nanoparticles (Magnetic Fluid Hyperthermia);
- Hippocampus cells stimulation.

In particular the proposed examples have some common aspects that involve the method to solve the problem and the used models like:

- The analysis of the effects deriving by the interaction of the electromagnetic fields and the biological tissues;
- The application of the numerical analysis for the solution of the electric, magnetic or thermal problem (Finite Element Analysis);
- The type of the electromagnetic field formulations used to solve the electromagnetic problem;
- The use of an human body model (realistic or simplified) with electric and thermal characteristics of biological tissues;
- The use of optimization methods to design electric and thermal devices.

Chapter 2

2 About the interaction of electromagnetic fields with biological tissues: adverse and therapeutic aspects

The conductive and dielectric nature of the biological structures implies that might occur a possible interaction with electromagnetic field. The interactions between the biological tissues and the electromagnetic fields are of two types: the former includes all the effects deriving by the induction of magnetic flux density and electric field or the voltage difference appliance like the circulation of induced currents or electric field distribution, the latter includes all the interactions between the electromagnetic waves and the tissues like the energy absorption. Then, the most important effects deriving from the interaction between the electromagnetic field and the biological tissues are the induction of electric currents, electric fields or heat. Some of these effects can be harmful like current induction, and others can be used in therapeutic application, like heat in hyperthermia application. In order to protect the people from the electromagnetic field exposure some guidelines and standards have been emitted [1-3], whereas some research groups have studied effects of the electromagnetic field in order to apply them in medical therapies (*e.g.* hyperthermia, cell stimulation).

2.1 Exposure protection guidelines

The European Community has recently emitted the Directive 2004/40/CE [4], which acknowledges the limits suggested on the ICNIRP[1] guidelines [1-3], in order to regulate the exposure to electromagnetic fields of workers. In the industrial environment the sources of magnetic field are so much spread (*e.g.* induction heating devices, power transformer, welding equipment, melting plants, arc furnaces, *etc*.), that the intensity of the magnetic field in the environment might be so high that some effects can be detected. Some of these effects that might cause some biological consequences on human body are:

- Induction of electric current density and some correlated effects;
- Induction of the electric fields;
- Heating of the tissues.

2.1.1. Adverse effects of the electromagnetic fields: human exposure

The exposure of human body to magnetic fields gives rise induced electric fields and electric currents. The coupling of the fields with body depends on the electrical characteristics of the tissue, the morphology of the structures involved in the field exposure and the characteristics of the field. The fact that the human body isn't an electrically homogeneous system means that the localization and intensity of the induced current depends on the resistivity of the particular tissue (*e.g.* liver, muscle, *see* the chapter 3).

[1] International Committee Non Ionizing Radiation Protection

The study of effects of the human exposure to electromagnetic field is important because time-varying electromagnetic fields at frequencies below 100 kHz sufficiently intense might cause some macroscopic effects (in absence of direct contact) as:

- Cardiac fibrillation;
- Vision of phosphenes;
- Nerve and muscle stimulation.

The basic restrictions and related limits introduced by the ICNIRP are determined in order to prevent the occurrence of such effects. Moreover, time-varying electromagnetic field can also interfere with implanted medical device like pacemaker [5], [6], whereas static magnetic field can interact with orthopedic prosthesis like metal bars or screws in bones (*e.g.* like can occur in the medical Magnetic Resonance Imaging devices).

a. Mechanisms of nerve stimulation

It is well known that magnetic fields sufficiently intense or magnetic field gradients can cause stimulation of the peripheral nerves and muscle tissue. The excitation of nerves depends on the duration and intensity of electromagnetic field [7]. In particular, in case of long duration pulses, the excitement of the nerves arrives if the stimulus intensity on the surface of the nervous beam is above a minimum threshold. Since the excitation of a nervous cell arrives if the variation of the voltage difference between the two sides of the cell membrane is upper to a prescribed threshold, a minimum on the induced current density is needed. The main characteristics related to the propagation of nerve pulses and muscle stimulation are:

- the intensity required to cause nerve stimulation rises reducing the pulse duration;
- after the passage of a stimulus the nerve remains in a refractory state for a few milliseconds and is unable to receive any other stimulus;
- nerve cells adapt themselves to the stimulus, then a constant current is effective at the beginning of its application, but lose the effectiveness in the following instants;
- a sinusoidal time-varying current at low frequency is ineffective because the rate of change of current is too low;
- a very high frequency alternating current is ineffective because the cycles are too short to move the membrane potential.

Given the excitation mechanisms of the nerve and muscles of the human body and mechanisms of the field coupling with the body, the limitation of the exposure to constant and low frequency time-varying electromagnetic field wants to prevent the possible occurrence of phenomena of nerve and muscle stimulation that may appear consequently to the electromagnetic fields exposure. It is to be noted that the appearance of more or less intense effects depends not only on the intensity, but also on the signal frequency.

b. Induced currents

A time-varying magnetic field at low frequency in a conductive medium induces electric field and electric current density. Since the biological tissues are conductive, even if it has a resistivity eight orders greater than the metals, some electric currents can be induced on human body [1].

c. Electric field

A time-varying electric field generates a flux of electric charge and the formation and

orientation of electric dipoles. External electric fields induce a surface charge distribution that generates an induced electric current density [1].

d. Energy absorption

Exposure of a body to an electromagnetic field at a frequency above 100 kHz might induce temperature rise if the field is sufficiently intense. This phenomenon is due to deposition of the energy transported by means of the electromagnetic wave [1].

e. Direct heating of biological tissues by means of electromagnetic fields

It is well know that electromagnetic fields cause a rise on body temperature because the electromagnetic radiation transports energy. The first observations about some heating effects due to electromagnetic field exposure of human body have been made since the Thirties and during the Second World War in the operations of maintaining the radar devices. Consequently of these observations the first standards have been emitted by the USA government [8]. Actually, some devices that use electromagnetic fields are diffused both on industrial environment and in household appliances [9],[10]. For instance the electromagnetic fields at radio frequency are used to cook some foods both in home and industrial ovens and to dry textile products[2].

2.1.2. Scientific data about possible electromagnetic fields interaction and toxicity

In order to understand the entity of the biological tissues heating induced by electromagnetic fields a lot of studies have been conducted for observing the possible effects of power lines, microwaves or mobile phone radiation. A lot of studies, epidemiologic and *in vitro*, have been conducted in order to estimate the toxicity of the electromagnetic field for living organism [1],[11],[12]. Few results and sometime inconsistent or contradictory have been reported [13]. For instance in [14] after exposure to electromagnetic field of cell cultures any DNA damages are evident and cells seem to adapt themselves to electromagnetic stress. From the results obtained in scientific studies the WHO[3] has classified the electromagnetic field as "possible human carcinogen" [15] using the IARC[4] classification [16], [17]. A scientific certainty only for acute effects has been demonstrated [1].

a. The case of the low frequency

In the past a great effort has been made to study the possible biological effects and health risks of the low frequency electromagnetic field, especially at 50 Hz for the fear of the power lines and electric appliances [13],[18],[19], [20] but any evidence on cancer occurrence or other disease has been confirmed for people living under power lines. A lot of studies have been conducted in order to evaluate the incidence of the childhood leukemia in relation with the exposure to low frequency electromagnetic field [21-24], but without any certainty of correlation. Other studies have been conducted in order to verify a correlation between low frequency electromagnetic field and the cancer and neurodegenerative diseases in residential and working environments, but any evidence and contrasting results have been found [25-28]. Then, any long term effect hypothesized has been confirmed by the research conducted. The evident effects of the low frequency electromagnetic field are the acute ones that are linked with the electric coupling of the electromagnetic field with the tissues like nerve and muscle stimulation [1], [29-35].

[2] http://www.stalam.it/homepage_eng.html (last access January 2011)
[3] World Health Organization, http://www.who.int/en/ (last access January 2011)
[4] International Agency for Research on Cancer, http://www.iarc.fr/ (last access January 2011)

b. The case of the Intermediate Frequency

With the term “Intermediate Frequency” (IF) is named the frequency range between 300 Hz and 10 MHz. The effects of the electromagnetic field in this range are not largely studied [35], but appliances that generate IF electromagnetic fields exist and are widespread. Some examples are induction cooktop (20-90 kHz), melting furnaces, induction industrial devices (few kHz) [36] or medical equipments like electromagnetic nerve or bone stimulator or electrosurgical units [37]. Since induction cooktop are popular devices, especially in Asiatic countries for the rice cooking or in North-Europe regions due to the low cost of the electric energy and the high efficiency (>90%) related to the cooking technique [38-40], a bit of efforts to study the IF effects related to this technology have been made.

In the IF range both the induced current (non-thermal) and thermal effects subsist. In literature, there are few studies about the biological toxicity of IF magnetic field and cancer promotion [35],[37],[41]. For instance, in [42] the genotoxicity *in vitro* has been tested, but any cell modifications (grow, mutagenicity, DNA damage, *etc.*) have been shown a clear evidence. Fujita [43] has developed an apparatus in order to study the electromagnetic field exposure of cells *in vitro*, whereas Kim [44] and Lee [41] have exposed mice to a sawtooth magnetic field at 20 kHz (the frequency of the PC and TV monitors), but any abnormalities of teratological or cancer promotion effects have been detected [13].

c. The case of the radio frequency

The first observations on Radio Frequency (RF) electromagnetic health effects have been observed on heating tissues. Some research groups have searched a correlation between cancer and the exposure to electromagnetic fields generated by mobile phones, antennas, microwave ovens and other sources [1], [45-49], but, in the case of an exposition to a continuous electromagnetic field, the only evident effects are the tissues heating and cataract induction both in humans and animals [50-52]. In the case of an exposure to a pulsed RF electromagnetic field some experimental data have shown that, if the field is able to induces a significant temperature rise, it can be teratogenic [13], [53].

2.1.3. Electromagnetic field protection in practice

The literature about the possible health effects of electromagnetic field suggests practical indications resumed in some operative standards. For instance for household electric appliances some methods for electromagnetic field evaluation and measurements are reported on the standard EN 50366 [54], while for welding equipments computations on human model are also allowed in order to evaluate the induced current density [55], [56]. Other standards give some indications about the measurement techniques or the estimation of the electromagnetic field generated by power lines, power transformers, *etc*.[57-59].

a. Welding equipments

In case of welding equipments human exposure can be evaluated as described in the standard EN 505055 [56] for resistance and EN 50444 [55] for arc equipments. In the case of arc equipments the welding current is continuous and the following evaluation techniques are allowed:

- Measurement of the magnetic flux density;
- Computation of induced current density in human body models;
- Computation of induced current density in simplified models like disc or cylinder.

Whereas in the case of resistance equipments measurements are not simple to perform for the pulse nature of the welding current and the exposure can be evaluated by means of:

- Computation of induced current density in simplified models like disc or cylinder;
- Computation of induced current density in human body models.

Then, given the shape of the source and the frequency and intensity of the current, simplified models and human body model allow the evaluation of both magnetic flux density and induced current density in the considered volume.

b. Induction cooktop equipments

In the case of cooktop equipments the evaluation of the human exposure can be made as described in the standard EN 50366 [54] that reports the magnetic flux density measurement techniques for household appliances.

In this work the electromagnetic field exposure is evaluated by means of a computation strategy with suitable simplified models of the human body like the ones used in the welding equipments exposure assessment.

2.2 Some medical use of the electromagnetic fields

Electromagnetic fields can be used in medical treatments for some diseases or in diagnostic investigations. Some of these therapeutic or diagnostic applications, more or less widespread, are, for instance:

- Magnetic resonance imaging used in diagnostic. In this case is used a static magnetic field (a few Tesla) with a radio frequency signal superimposed [60];
- Hyperthermia uses electromagnetic fields for the treatment of cancer by means of tissue heating;
- Electric stimulation: the stimulation of the hippocampus by means of electric field can be used in some brain therapy like Parkinson or neurological diseases (*e.g.* transcranial electric stimulation [61]).
- Pulsed electromagnetic fields can affect the osteoblaste proliferation for bone reparation and favorite the wound healing [62-64].

2.3 Therapeutic effect of the power deposition: hyperthermia in the cancer therapy

The term hyperthermia identifies some therapeutic techniques that use the heat to damage the cancer cells [65-70]. In fact, it is well known that tumor tissues are more sensitive to heat than healthy tissues. This fact is due to some changes that occur both in vascular architecture and environmental characteristics [65], [71], [72]. The chaotic vascularization of tumor mass, due to a not controlled blood vessel grown, might cause a reduction on the efficiency of the blood cooling effect [65], [73], [74]. In fact, the thermal homeostasis of tissues is regulated by the blood flow that removes the heat produced by metabolism of the tissues and transports it toward the skin surface, through which it is transferred to the surrounding environment [75]. The vascular network in the tumor tissue is made both by the vessel of the original tissues and the ones growing in the tumor mass. So, it results that tumor tissue is vascularized chaotically: some of the vessels are those of the original tissue in which the tumor is established and maintain their physiological characteristics, unless they are incorporated in the tumor mass during its growth, whereas the other vessels are created by an abnormal angiogenesis and

have an architecture that alters their functionality [73]. In this way, the blood flow in the tumor mass is changed [74] and might lose the capacity to maintain the homeostasis. Moreover, it is known that tumor tissue has a low pH and the acidic environment increases the cells sensitive to the heat. Then, since the tumor cells might be more sensitive to the heat they might lose their capacity to survive in some stress conditions [65], [76].

Depending on the rate of the temperature increasing on the tumor mass, the apoptosis of the cells or their necrosis can be induced [77-79]. The apoptosis, or programmed death, is the natural mechanism by which damaged cells are eliminated. This metabolic pathway may be induced by the increasing on the tissue temperature few degrees above 42 °C. In [68], [77], [80] it is observed that the temperature increase of one degree reduces the percentage of the cell survival. Nevertheless the increasing on the temperatures above 50-60 °C leads to the cell necrosis, coagulation and charring of tissue [66],[69],[81],[82]. The former condition is named “mild Hyperthermia”, whereas the second one “thermal ablation”.

2.3.1. Hyperthermia techniques

In biological applications the term hyperthermia identifies all external or internal treatments that can induce a temperature increase over the basal value (for the human body 37°C). Among hyperthermia treatments are included both total body applications and localized ones. In the former the temperature rise is induced throughout the whole body and examples are thermostatic bathrooms or exposure to some energetic radiation sources like microwaves or electromagnetic fields [72], [80], [83],[84]. In the second type of therapy the heating source is focused on a target area. Examples are the laser, directional antennas or suitable electromagnetic applicators. Other possible devices for the hyperthermia treatments use radio frequency, magnetic field at industrial frequency, electric field or infrared radiation as external sources of heat [77]. Alternatively, the temperature rise can be induced by means of some internal heat sources such as the thermoseeds or electrodes [83],[85-87] used to treat some types of cancer (*e.g.*: prostate, neurological, melanoma) or the magnetic nanoparticles suspended in a suitable fluid. The techniques for the localized hyperthermia might allow the reduction of the damage occurred to the healthy tissues in the surrounding area of the tumor mass that is the limitation of the use of the total body hyperthermia techniques.

a. Direct heating of biological tissues by means of electromagnetic fields

Some medical therapies use electromagnetic field in order to heat therapeutically the tissues in local or whole body treatments. The heating effect might be due to the absorption of the energy transported by means of electromagnetic waves that interact with the body.

b. Indirect heating of biological tissues by means of electromagnetic fields

The indirect heating of biological tissues might be performed by means of the interaction of some implanted devices with electromagnetic field. The device is inserted in the targeting areas of one or more organs and an external electromagnetic field induces its heating. Some examples of these devices are the thermoseeds [85] or the magnetic fluid. The former devices are seeds of magnetic material. A time-varying magnetic field generates an induced current in the magnetic material that produces a temperature increasing due to the Joule effect. In this way the device heats the area in which it is inserted by heat transfer. Whereas the second one, which is formed by spheres of magnetic material with nanometric sizes suspended in a fluid [69],[88],[89], generates heat if a time-varying magnetic field is applied. The electromagnetic field interacts with the magnetic moment of the magnetic nanoparticles that can rotate in the fluid or flip their magnetic moment. Then, relaxation phenomena, that cause the generation of heat, are induced. In this last case the power density generated by means of the magnetic field

is a non linear function of the field intensity and frequency and depends, also, on the physical characteristics of nanoparticles, their concentration and dimension (*see* chapter 8).

2.4 Magnetic fluid hyperthermia: principle

The hyperthermia with magnetic nanoparticles is also called Magnetic Fluid Hyperthermia from the drug with which the nanospheres are injected in the tumor tissues. The magnetic nanoparticles are spheres of a magnetic material in the size of nanometers, suitably coated with molecules to increase their biocompatibility, and dipped in a fluid that facilitates their injection *in situ* or in the systemic circulation [66], [86], [89].

2.4.1. **Magnetic nanoparticles**

Magnetic nanoparticles can be formed by means of a magnetic nucleus of single or multidomain type (Figure 2.1) [90], [91]:

- **Multidomain**: the magnetic material is formed by some magnetic domains that are areas in the magnetic medium characterized by a magnetic moment with a direction that is different by the one of the neighboring domains (Figure 2.1 (a)) [92].
- **Single domain**: in this case, a single magnetic domain occurs when the size of the magnetic material is under a characteristic threshold that depends on the magnetic composite (Figure 2.1 (b)). The formation of domain walls is unfavorable, thermal fluctuations prevent a stable magnetization and a single magnetization occurs. In this case the coercive field, characteristic of the magnetization curve, tends to be null. In this case the nanoparticles are in condition of "superparamagnetism". The magnetic moment of a superparamagnetic material is much larger than the one of a paramagnetic material, but with the same behavior in terms of the magnetic moment orientation in a magnetic field [92]. Then, the superparamagnetic behavior dominates, that is the coercive field tends to zero (there is no hysteresis) and the magnetization curve is independent of the temperature [91],[93-95]. At the end a superparamagnetic state transition depends also on the temperature of the medium (*see* chapter 4).

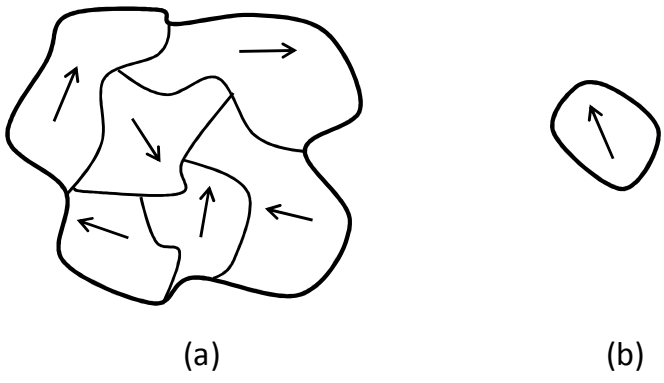

Figure 2.1: Magnetic domains: (a) multidomains and (b) single domain.

In the practice multidomain nanoparticles are not used because it is well known that superparamagnetic nanoparticles generate a power greater than the one deriving from multidomain nanoparticles [70]. Then, in hyperthermia treatment single-core elements are the most used as heat sources. The superparamagnetic nanoparticles used in biomedical application can be single core or multi-core [96], covered with different materials in order to make them hydrophobic or hydrophilic. The former, the single core ones, are formed by a

magnetic nucleus covered by means of a surfactant layer, like dextran, a molecule similar to glucose, which makes them more biocompatible [66], [97-99] or siloxane, or other compounds [100] like polyethylene glycol, oleic acid, proteins, amilosilan *etc.*, [101] to improve the biocompatibility [66], [100]. The multi-core nanoparticles, named magnetic probes [102], [103], are formed by means of a biocompatible matrix, *e.g*. dextran, in which magnetic elements are dipped, *e.g.* iron oxides (see Figure 2.2) [91].

a. Magnetic nanoparticles heating phenomena

The magnetic nanoparticles for medical use are usually small particles of a magnetic material like magnetite (Fe_3O_4), maghemite (Fe_2O_3) and sometimes CobaltoFerrite [91], [96], [100], [104],[105], which, subjected to a suitable time-varying magnetic field, can produce heat [66], [106], [107]. The heating mechanisms of magnetic nanoparticles are due to the interaction of the time-varying magnetic field with the nanoparticle magnetic core [69], [70], [90], [106]. The heating of magnetic nanoparticles can be due to:

- **Magnetic relaxation effects**, developed if the magnetic nanoparticles are of single magnetic domain type and that are due to the magnetic properties of the material. These effects are:
    - **Brown relaxation**: torque of the magnetic nanoparticles in a fluid and heating generation by friction with the viscous media. This mechanism interests the whole nanoparticle, its core and covering layer, and can be suppressed if the nanoparticles are dipped in a high viscosity media.
    - **Néel relaxation**: in this case the torque force interests the magnetic moment of the internal magnetic core. In this case it is the magnetic moment that flips and not the whole nanoparticle.
- **Ohmic losses phenomena**: due to the induced currents that flows in the magnetic material and generated by means of a time-varying magnetic field. In this case the heating is due to Joule effect caused by the induced current density.
- **Hysteresis**: due to irreversibility of the magnetic material magnetization.

In the case of single domain superparamagnetic nanoparticles the heating by magnetic relaxation phenomena is dominant with respect to the ohmic and hysteresis ones, whereas in the multidomain nanoparticles the heat is generated by hysteretic losses [86].

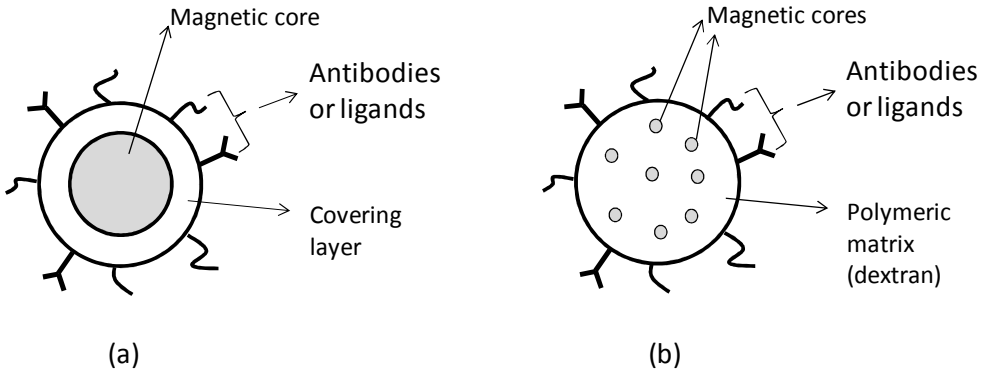

Figure 2.2: Magnetic nanoparticles: (a) single core (b) multi-core.

In the case of a single magnetic core both the relaxation phenomena, Néel and Brown, can interact in the heating generation, whereas in the multi-core iron oxide nanoparticles the Néel relaxation phenomenon is dominating because nanoparticle are immobilized in the matrix and are not able to rotate [108].

In any case the therapeutic effect of the magnetic material is due to the application of a magnetic field that generates the heat in order to increase the temperature locally. Then, the hyperthermia is an adjuvant therapy because might induce the damage of plasma membrane, cytoskeleton and nucleus leading to cell death and might activate some proteins that might induce cellular apoptosis, like some proteins in the family of the Heat Shock Proteins (HSP) [109]. Generally, these proteins act like a protector in case of a rapid increasing in the cell temperature reducing the heat damages [69]. But it should be noted that the HSP may, in some cases, trigger the mechanisms of a thermo-tolerance [66] and, thus, reduce the effects of the hyperthermia treatment [80] [110]. For example in [66] it is suggested a rapid initial heating in order to improve the effects of thermal therapy, although having care that the temperature distribution is as smooth as possible.

b. Magnetic nanoparticles deposition in biological tissues

The positioning of the nanoparticles in the treating tissues is not easy. In the hyperthermia with magnetic nanoparticles the magnetic fluid is generally administered by direct injection into the target tissue [67]. Alternatively, some authors have studied the possibility to inject the drug intravenously or in arteries [86], [111]. The problems related to these techniques are due to the action of the immune system which operates if the injected substances are recognized as foreign. These substances are quickly captured by macrophages and eliminated, unless they are not properly covered in order to trick the immune system [112]. Nevertheless, nanoparticles coated with dextran or aminosilan or other surfactant can be incorporated into the cells by endocytosis as described in [86], [100], [113], [114] and used as internal source of heat.

Moreover, other difficults in magnetic fluid injection are due to the morphology of blood vessels in various organs. For instance, the endothelial cells of blood vessels of the nervous system have joints, the blood-brain barrier, difficult to penetrate, the windowing capillaries of the gastrointestinal and renal system eliminate particles down to 50 nm, and the sinusoidal capillaries of the liver and spleen eliminate particles above 200 nm. It is known that in tumor tissues the capillaries are more permeable than the ones with a continuous wall, and then, because the lymphatic drainage is insufficient, the nanoparticles may be easier deposited [66], [115]. In some case nanoparticles extravasation might occur [116].

Since cancer cells have specific binding sites different from the ones of the healthy tissue, the nanoparticles can be functionalized appropriately and directed to the target site. For example, in [97] the outer surface of the nanoparticles was functionalized with molecules that bind with antigens and receptors expressed by target cells, while in [98] are incorporated in liposomes and functionalized with antibodies, whereas in [102], [103] nanoparticles dipped in the matrix of dextran that are functionalized on the surface with specific antibodies.

Limitations of the techniques of Magnetic Fluid Hyperthermia with the injection of the nanoparticle drug directly in the vascular system are due to the effective concentration of the nanoparticle in tissues [89], [111]. Jones and Winter [117] reported some experimental results carried out on rabbits linked to the administration of nanospheres containing nanoparticles of ferromagnetic iron oxide (γ-Fe_2O_3) through the renal artery and applying a suitable magnetic field (H = 40 kA/m at 53 kHz). The therapeutic temperature achieved is directly related to the actual concentration of nanoparticles.

Injection into an artery of the magnetic nanoparticles fluid, known as arterial embolization, might form clusters of particles as it is shown in [86], [114] for liver cancer. It should be noted that the perfusion of the healthy liver parenchyma is coming mainly from branches of the portal vein, while the vascular network of the tumor is generated by the hepatic arterial system [118]. In [86] the Magnetic Resonance Image is used to study how the nanoparticles are distributed on the healthy and tumor tissue after the injection into the hepatic artery. The

study was performed on rabbit liver *in vivo*. In this case the ferromagnetic iron oxide (γ-Fe_2O_3) nanoparticles with a diameter of 150 nm suspended on lipidol (100mg/2ml) have been used. The magnetic field used to produce the thermal effect has amplitude of 45 kA/m at a frequency of 53 kHz, and the treatment is 5 min long. The analysis of the tissues showed that the distribution of nanoparticles in tumor tissue is heterogeneous, and depends mainly on the vascular system; a much vascularized region contains a higher concentration of nanoparticles. Moreover, the variability of the nanoparticle concentration might depend, also, on the chaotic nature of the tumor vasculature [73], [119], [120]. For instance Baisha and Jain have suggested a fractal structure of the vascular network of the cancer [121].

Then, the nanoparticle concentration affects the temperature rise in a hyperthermia treatment; the real concentration of nanoparticles has been studied by means of mathematical models. The real concentration can be considered a variable during the evaluation of the power generated by means of nanoparticles [122-127].

c. Magnetic nanoparticles kinetic

Magnetic nanoparticles can be administered by different ways in order to better achieve the target organs. Like other drugs the release of the therapeutic agents, the effective quantity that reaches the target organ, depends on absorption, metabolism, distribution and elimination. The nanoparticles kinetic can be described by mathematical equation in order to determine the quantity that arrives to target site as a function of the administered quantity [96], [128].

In general releases model for drug dissolution can be described by Fickian kinetics. Other models can introduce also diffusion phenomena. For the Fick's second law the local drug concentration, c, at a time t, at a distance r from the particle center, can be described by the following differential equation:

$$\frac{\partial c}{\partial t} = D\left(\frac{\partial^2 c}{\partial r^2} + \frac{2}{r}\frac{\partial c}{\partial r}\right) \tag{2.1}$$

that describes the release of a drug from a polymeric matrix. In this equation D is the diffusion coefficient.

2.4.2. Hyperthermia and other conventional therapies for cancer treatments

Hyperthermia treatment can be used with some other conventional cancer therapies like the radio-therapy or chemio-therapies and improves their effects [80], [90]. For instance, in the case of the radiotherapy, the hyperthermia treatment increases the blood circulation in response to the temperature rise. In this way the presence of oxygen-bearing in tissues is increased [84]. This is important because the radiotherapy destroys the cancer cells thought the oxygen radicals that attack the cell DNA. It is to be noted that the tissues with a low blood flow are less sensible to the ionizing radiation, but more sensible to the heat therapy and *viceversa*. Then, hyperthermia might improve radiotherapy effects [76].

Let consider the chemotherapy drugs. Since the hyperthermia enhances blood flow in tumor, the drug uptake in cancer cells can be increased. Moreover, recently, hyperthermia therapy has been, also, coupled with dendritic cells therapy [110].

2.4.3. Some results and experimental data about heat generation

Magnetic Fluid Hyperthermia has attracted some researchers for its selectivity in tumor treating. First applications are studied between the fifties and sixties [88]. In the years different types of magnetic core have been tried and coupled with various coating layers and

functionalizing molecules with antibodies, antigens, ligands, receptors, *etc.* [66], [91], [97], [98], [129] or hormones like the Luteinizing Hormone Releasing Hormone[5] (LHRH) [130].

The most diffuses core materials are Iron-oxides. Sometimes other materials used in the magnetic nanoparticles for medical uses are some composites of Iron and Cobalt. In literature some results about the therapy efficiency using different materials are reported. Some treatment input data are:

- Material of the nanoparticle core;
- Magnetic field intensity;
- Frequency of the magnetic field.

In order to study the efficacy of the therapy the evaluated parameters are:

- The power given to the treating mass (measured by means of a temperature) expressed as a Specific Loss Power (SLP);
- The rate of the survival cell;
- The decreasing on the tumor mass (until its suppression).

In Table 2.1 a summary of some nanoparticles characteristics used in [131] is reported, whereas some data about the intensity and frequency of the magnetic field used in Magnetic Fluid Hyperthermia experimental treatments in animals are reported in Table 2.2.

In [131] Fortin uses colloidal maghemite, an iron-oxide (γ-Fe_2O_3), or the Cobalt Ferrite ($CoFe_2O_4$) dispersed in water or in a glycerol-water mixture [131]. In this case the magnetic field intensity is 24.8 kA/m at 700 kHz and the nanoparticles diameter is between 5.3 and 16.5 nm. It is shown that for the maghemite particles the SLP (Specific Loss Power) increases if the particle diameter increases. While for Cobalt-Ferrite nanoparticles the SLP decreases if the viscosity increases (in this case Néel relaxation contribution is predominant with respect the Brownian one). For the maghemite nanoparticle the SLP varies between 4 and 1650 W/g, while for the Cobalt-Ferrite ones is between 40 and 420 W/g.

Table 2.1: Some characteristics of nanoparticles used by [131].

material	γ-Fe_2O_3				$CoFe_2O_4$		γ-Fe_2O_3		$CoFe_2O_4$	
Size [nm]	5.3	8	10.2	16.5	3.9	9.1	7.1	7.1	9.7	9.7
Carrier	water				water		Water + glycerol		Water + glycerol	
Density[Pl]$\cdot 10^{-3}$	0.7				0.7		0.75	5.8	0.75	5.8
SLP [W/g]	4	37	275	1650	40	360	135	125	420	145

In [132] iron oxide superparamagnetic nanoparticles coated with carboxidextran[6] have been used. In this paper the temperature rate is correlated with the nanoparticles concentration. *In vitro* experiment shows that a concentration of 28 $mgml^{-1}$ increases the solution temperature up to 59.5°C, while a concentration of 56 $mgml^{-1}$ up to 71.3°C.

Actually magnetic nanoparticles have been applied in some experiments in order to study the effect on tumor tissues. Animal *in vivo* experiments have shown appreciable results. For

[5] In this case nanoparticles are accumulated in primary in the breast cancer cells and in metastases in lungs by endocytosys mediated by receptors. Nanoparticles aggregated in cells and can be used to transport drugs in cells and in the nucleus because they can pass nuclear membrane.

[6] this drug is named Resovist

instance in [133] tumor regression has been observed in mouse treated with Magnetic Fluid Hyperthermia. Other positive results are reported in [114], [86], [96], [132], [134].

Table 2.2: Some characteristics of nanoparticles and magnetic field used by different research groups.

Material	Core diameter [nm]	External diameter [nm]	coating	H field	Frequency [kHz]	Fluid	Ref.
Maghemite and Cobalt-Ferrite	5.3 -16.5	--	any	24.8 kA/m	700	glycerol	[131]
Iron oxide	9	62	carboxide xtran	P=2.4kW	62.1		[132]
Maghemite	11-13			3.2 kA/m	0.6	isoparaffin	[134]
Maghemite	14.5		dextran	11.2 kA/m	410		[135]
Magnetite Fe3O4	19-32		dextran	200Oe	55		[136]
Maghemite			carboxide xtran	11 kA/m	410		[99]

Some data about the capacity to heat tissues by means of the magnetic nanoparticles are reported in [70] where some advantages and drawbacks of nanoparticles thermotherapy are described. In this paper thermal properties of multidomain and single domain nanoparticles have been examined. The magnetic field source used to heat nanoparticles is a generator between 300 kHz and 80 MHz that produces a magnetic field between 200 and 1400 Am^{-1}. A first equipment for human solid tumor hyperthermia has been designed by MagForce and is in the Berlin Charity Hospital [137], [138]. The equipment generates a time-varying magnetic field at 100 kHz with magnetic field amplitude adjustable until 15 kA/m. The applicator is a ferrite-core applicator. Treated tumors are malignant gliomas, breast cancer, prostate carcinoma, hepatic and superficial tumors. Other information are reported in the web site[7] of MagForce.

2.5 Therapeutic effect of the electric field: cells stimulation

Some of cells, like neurons or muscular cells, have a natural electric activity [139], [75], [140]. The interest of some research groups is in the stimulation of brain cells by means of, for instance, the transcranial electric stimulation has produced some studies in this field [61], [141].

In some experimental studies the neurons in the hippocampus region or cortex have been stimulated with electric field in order to treat nervous system disorders [142-144]. For instance, the electric field in the order of 20-30 mV/mm (20-30 V/m) might affect the initiation of the action potentials [145]. Moreover electric field seems might interact with the cell membrane [146] and transport enzymes [147].

[7] http://www.magforce.de/english/home1.html (last access January 2011)

Chapter 3

3 Methods and models for the electromagnetic and thermal analysis

The electromagnetic fields effect on living organisms can be evaluated solving Maxwell equations by means of some numerical techniques like Finite Elements, Finite Difference Time Domains or other methods [148] in suitable models. The same computation methods and models can be used to solve also thermal problems.

3.1 Numerical techniques for the analysis of the electromagnetic field effects

The effects of the electromagnetic fields on the biological tissues can be estimated by means of analytical or numerical techniques. Analytical computation methods can be used to estimate the magnetic flux density in the space around the magnetic field source, whereas the induced current in a volume immersed in a not-uniform magnetic field can be estimated using some numerical techniques.

Given the shape of the magnetic or electric field source (*e.g.* the frequency and amplitude of the current, a voltage difference) or source of heat (*e.g.* power density), numerical techniques, in order to evaluate the electromagnetic field to assess the human exposure or some therapeutic effects like tissues heating or cells stimulation, allow the evaluation of the following quantities:

- magnetic flux density [T];
- induced current density [Am^{-2}];
- magnetic field [Am^{-1}];
- electric field [Vm^{-1}];
- power density in tissues [Wm^{-3}];
- thermal field in tissues [K];
- temperature increasing in tissues [K].

In order to evaluate the effects of electromagnetic fields and temperature on the tissues of the human body, electromagnetic and thermal problems can be solved in some simplified models, like cylinders, as proposed in some documents [55], [56], [149] or a real human body models.

3.2 Solve a problem using numerical analysis

In order to solve an electromagnetic or thermal problem by means of numerical analysis the main elements of the problem are:

- The numerical computation method;
- The computation domain that includes the model describing the volume in with the electromagnetic or thermal problem must be solved and other volumes required for the computation;
- The field source.

3.2.1. Numerical analysis: computation methods

The computation methods used to evaluate numerically the electric and magnetic field or the thermal field in order to assess the exposure of people or their therapeutic effects are different and the choice of the method depends on the problem to be solved. A review of numerical methods used in biological structures to solve bioelectromagnetic problems can be found in [149-151]. For instance, the calculation methods more commonly used in numerical analysis are:

- **Finite Element Method (FEM or FEA, FE Analysis)**: used in [152] for the computation of the induced currents density in the human body produced by low frequency magnetic fields. This method was also used in [49];
- **Finite Difference Time Domain (FDTD)**: introduced by Yee [153] for the evaluation of the SAR[8] in human body models [154], [155]. This method is generally used in Radio Frequency range; nevertheless it was also extended to the quasi-static case (*e.g.* eddy currents produced by power lines [156] or in proximity of melting crucibles [157]);
- **Impedance Method:** used, for instance, to evaluate the energy deposition in hyperthermia treatments for cancer therapy [158], the human exposure to a time-varying electromagnetic field [159-165] or to calculate the SAR [161], [165];
- **Finite Integration Technique (FIT):** used by [166] for the evaluation of the SAR in an accurate model of human body;
- **Scalar Potential Finite-Differences (SPFD):** was used in [31], [167] and [168] for evaluation of the electric field and induced currents density in some models of the human body;
- **Method of Moments:** used, for example, in [169] together with an integral equation for the computation of the surface charge density to assess the interaction between the ELF[9] electromagnetic fields and the human body;
- **Boundary Element Method (BEM):** used in [170-172] for the computation of the induced current density in a conductive regions;
- **Cell-Method (CM):** introduced by Tonti [173] and used to solve problems that involve biological structures [174],[175].

It worth noted that the choice of the computation method depends on the type of the problem to be solved. In fact, some of them are better suited to study the effects of the high-frequency electromagnetic fields, whereas the others are more suitable for the low frequency fields. In the following examples for the computation of the induced currents in a conductive medium, the solution of thermal problems the Finite Element Analysis has been used [176].

[8] Specific Absorption Rate
[9] Extremely Low Frequency

3.2.2. Description of the computation domain for a numerical problem

In an electromagnetic problem for the evaluation of the electromagnetic field exposure or electromagnetic field therapeutic effects the main elements of the computation domain are (*see* Figure 3.1):

- The source of the electromagnetic field, *e.g.* an electric current, a charge distribution, a voltage difference, *etc*;
- The conductive volumes;
- The surrounding air volumes.

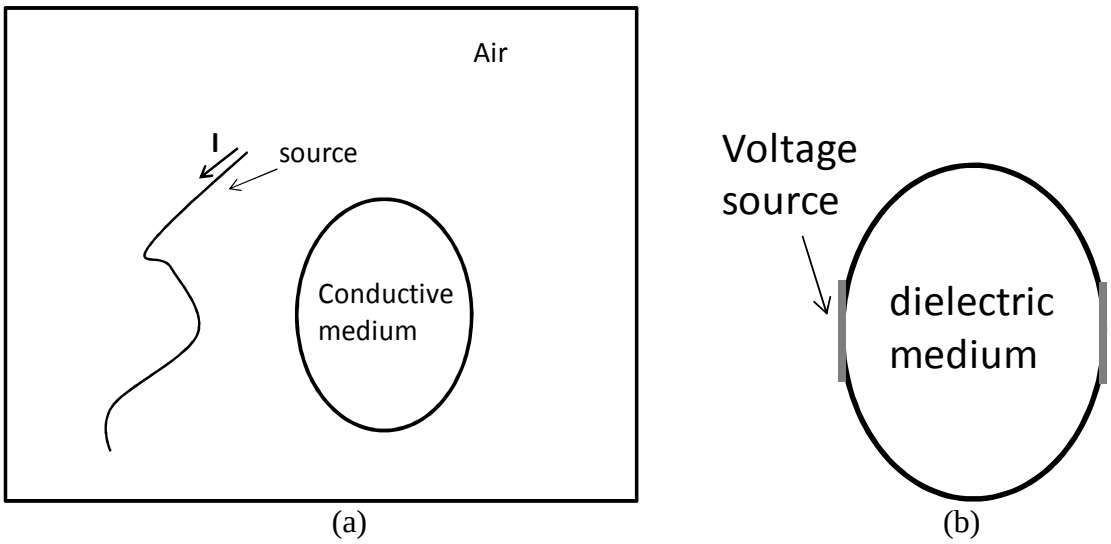

Figure 3.1 :Elements of an electromagnetic problem in some biological models (a) magnetic field evaluation and (b) electric field evaluation.

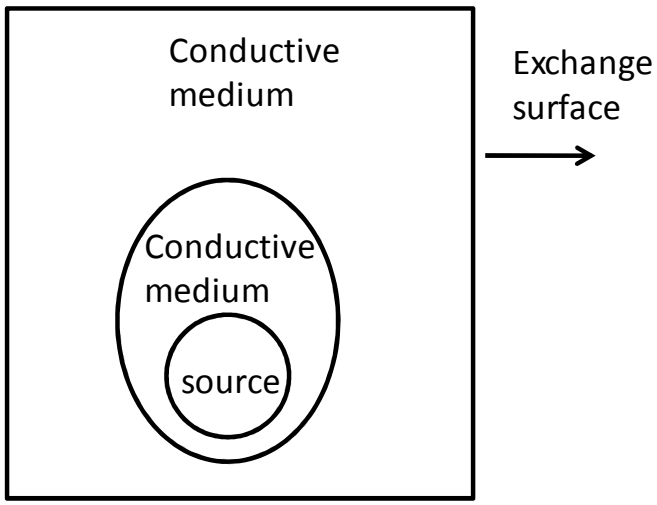

Figure 3.2 :Elements of a thermal problem.

Whereas in a thermal problem the main elements of the models are (*see* Figure 3.2):

- The heat source, *e.g.* power density;
- The conductive volumes;
- Thermal exchange surfaces.

3.3 Existing models for living organisms

Conductive medium of the computation domain can be modeled by suitable models. Some research groups have proposed several human body models, simplified or more accurate ones, that can be used in the numerical evaluation for the evaluation of the human exposure to electromagnetic field [56], [166], [177], [178].

The most spread models for the human body, used to analyze the fields intensity and induced currents, divide the volume into a set of cubic volumes (voxels), whose side is in the order of several millimeters. Other models use tetrahedral elements [179]. In each of these voxel the electrical and thermal characteristics of tissues can be considered constant and the value of the conductivity corresponding to the dominant tissue is associated. For example, in [168], some voxel with the side of 3.6 mm have been considered. The realistic human body models are sufficiently accurate to describe the most important organs of living organisms. Once given an accurate description of the dis-homogeneity of electrical and thermal characteristics of the body, given the intensity of the external electromagnetic fields source or the thermal source intensity, it is possible to evaluate the entity of the fields, induced current density and temperature inside each volume.

Among the models of living organisms developed by different research groups, Hugo is the more known and is meshed by means of cubic elements [166], [176]. The human body is a so much complicated model because is composed by different organs each with different electrical characteristics and dimensions. In the practice some simplified models have been proposed in order to reduce the computation complexity. The most used models are the homogeneous disc and cylinder with a constant resistivity that simulates the one of an average tissue like proposed in some standards (*e.g.* cylinder). Some other models use humanoid shape, in order to identify the head and thorax zones, with uniform electrical characteristics [157],[169],[180],[181]. Table 4.1 shows a schematic overview of the model and corresponding computation methods, some of assumptions and frequency range used.

Stuchly *et Al*, in [150], shows the main biological mechanisms that can affect the interaction of low frequency electromagnetic fields with the human body. This paper summarizes some of the main numerical methods used in the literature for the evaluation of the induced currents in the tissues of the human body from electric and magnetic fields. It refers to the Method of Impedances (IM), the method of Scalar Potential Finite Difference (SPFD), the method of Finite Differences in Time Domain (FDTD) and Finite Element Method (FEM).

Dawson [168] evaluates the electric field and induced currents density in some organs of the human body using the method of Scalar Potential Finite Difference (SPFD). The model of the human body had a resolution of 3.6 mm and was constructed from Magnetic Resonance Images (MRI) data of the Yale Medical School[10] [177] integrated with those obtained by means of Computer Tomography (CT) images of the "Visible Human Project[11]". The effects of non-homogeneity of the tissue conductivity and the magnetic field source orientation are analyzed. The method SPFD is also used by Dimbylow [182], [183] in order to compute the current density induced in the different tissues of the human body by external electric and magnetic fields. In this case Dimbylow uses NAOMI (aNAtOMIcal model) [183] and NORMAN (NORmalised MAN) [182-184] that are built from MRI[12] data. These models have a resolution of 2 mm (side of the voxel). Dimbylow [184] uses the NORMAN model also with the Impedance Method.

[10] http://www.med.yale.edu/ysm/research/ (last access January 2011)
[11] National Library of Medicine, Bethesda, MD, http://www.nlm.nih.gov/research/visible/visible_human.html (last access January 2011)
[12] Magnetic Resonance Images

Table 3.1: Some papers in which the human model is used for electromagnetic computation.

First author	Year	Method	Freq.	Hypothesis	Model	Resolution	Remarks	Ref.
Gandhi	1984	IM	HF	--	--	--	SAR	[158]
DeFord	1985	IM	LF and HF	--	--	--	SAR	[161]
Sullivan	1988	FDTD	HF	--	Human model	2.62 or 1.31 cm	SAR	[155]
Mouchawar	1993	FEM	--	--	--	--	Field generated by MRI device	[185]
Xi	1994	IM	60 Hz	Quasi static approximation	Human model	1.31 cm	Sphere model with two layer	[162]
Wang	1994	FEM	LF	Quasi static approximation	--	--	sheet	[186]
Gandhi	1995	IM+ FDTD	LF+HF	--	--	1.31 cm - 3x1.875 mm	--	[151]
Dawson	1998	SPFD	60 Hz	Quasi static approximation, conduction currents dominate the displacement ones	university of Victoria (Yale medical school)	--	--	[178]
Dimbylow	1998	IM+ SPFD	LF	Quasi static approximation, the magnetic field due to the induced current is neglected	NORMAN	~2x2x2 mm	--	[184]
Gustrau	1999	FDTD scaled in freq.	0.25-10kHz (sim. at 5MHz)	--	--	1 cm	Ellipsoid	[157]
Stuchly	2000	FDTD, IM, FEM, SPFD	60 Hz	Quasi static approximation, induced current greater than the displacement ones, linear properties of tissues	University of Utah, university of Victoria	--	Rewiew	[150]

(Continued….)

(….continued)

First author	Year	Method	Freq.	Hypothesis	Model	Risoluzione	Remarks	Ref.
Dimbylow	2000	Quasi-static FD	LF	--	NORMAN	~2x2x2 mm	--	[182]
Gandhi	2001	IM	LF	Quasi static approximation	Univesity of Utah	1.875 mm	--	[187]
Gjonaj	2002	FIT		--	Hugo	2x2x2 mm	SAR	[166]
Matsumoto	2003	analytic	60 Hz	Quasi static approximation	--	--	Ellipsoid	[180]
Scorretti	2004	Quasi static A-ϕ	LF	Quasi static approximation	amira model	--	Amira and Flux, sphera	[152]
Nadeem	2004	IM	50 Hz	Approximation of electric characteristics of the tissues	Brooks Air Force Laboratory, USA	--	Welding equipments	[160]
Scorretti	2005	Quasi-static A-ϕ	LF	Quasi static approximation	amira model	--	Amira and Flux, cylindric model	[179]
Dimbylow	2005	SPFD - FDTD	LF	--	NAOMI	~2x2x2 mm	Computetion of the electric field contribution	[183]
Barchnski	2007	Ex-SPFDF	LF	Approximated vector potential	Human model	1.5 mm	--	[188]
Bullo	2006	CM	450 kHz		Human model	--	3D model	[175]
D'Ambrosio	2007	FEM	RF		Human model		3D model	[189]

*LF = low frequency, HF = high frequency, IM= impedance method, MRI = Magnetic Resonance Imaging, FD = Finite difference, FEM = Finite Element Method, SPFD = Scalar Potential Finite Difference, FIT = Finite Integration Technique, FDTD = Finite Differences in Time Domain, CM= Cell method.

The Extended Scalar Potential Finite Difference (Ex-SPFD) is used by Barchanski in a recent paper [188] for the computation of induced currents in biological tissues by low-frequency magnetic field. The field produced by electric blankets and TMS (Transcranial Magnetic Stimulation) treatments have been analyzed. Furse in [190] uses a body model developed by the University of Utah[13] from Magnetic Resonance Images in order to assess the current density induced in different tissues from an external electric field. In this study the method of Finite Differences in Time Domain (FDTD) has been used. Simulations were carried out at a frequency of 10 MHz and the results were scaled to 60 Hz. Whereas Gustrau [157], evaluates the induced currents density in a human model with a resolution of a 1 mm, based on data of the "Visible Human Project[11]", by means of the method of FDTD, suitably scaled at the correct frequency. The results obtained by means of the numerical method are compared with the ones obtained using an analytical method. In this case an ellipsoid with homogeneous electrical characteristics immersed in a uniform magnetic field is considered.

Gjonaj [166] uses the human model Hugo in the CST software tool[14] for evaluation of the electromagnetic fields induced in the human body by high-frequency radiation (mobile phones). Let note that in this case the SAR (Specific Absorption Rate), which is directly correlated with the tissue heating, is evaluated. The electromagnetic field is computed by means of the Finite Integration Technique (FIT). Whereas Gandhi [187] and Xi [162] use the Impedance Method (IM) to assess the current density induced by a time-varying magnetic field in the tissues of the human body. Cell Method (CM) has been used in [174] and [175] in order to solve coupled magnetic and thermal problems in biological models.

The Finite Element Method (FEM) was used in [179] in order to evaluate of the induced currents density in biological tissues using real models of the human body, whereas [189], [191-193] use the FEM in realistic human body models in order to evaluate the efficacy of the radio frequency therapy in tumor treatment.

In this work the Finite Element Analysis (FEA) has been used in the evaluation of the human exposure to magnetic field. The magnetic flux density and current density inside a conductor in a relatively low frequency range (up 100 kHz) are computed. Moreover, using the Finite Element Method it is possible to solve both the Maxwell equations for the magnetic problem and the heat transfer equation in order to evaluate the thermal diffusion in a complex domain where an analytical solution is not applicable.

3.4 Human body models used for numerical analysis in some practical cases

Different models have been used in order to solve electromagnetic and thermal problems by means of the Finite Element Analysis. The chosen model for the solution of the electromagnetic and thermal problem in order to evaluate the electromagnetic field effects depends on the type of the problem to be solved. For instance, in some practical cases the following models have been used:

- Human exposure to electromagnetic field due to welding equipment:
    - Simplified model like cylinders with homogeneous electrical characteristics as suggested by standards [55],[56];
    - Realistic human body models with the description of the electrical characteristics of the different tissues [55],[56];
- Human exposure to electromagnetic field due to induction cooktop:

[13] http://www.utah.edu/portal/site/uuhome/ (last access January 2011)
[14] www.cst.de (last access January 2011)

- Cylindrical model with homogeneous electrical characteristics;

- Magnetic Fluid Hyperthermia treatments:
  - Simplified model with different volumes in order to simulate different tissue (*e.g.* tumor and healthy tissue) with thermal and electrical characteristics of real tissues;

- Electric field cell stimulation:
  - Realistic models that simulate the human and rat head built from medical images. Volumes are described with electrical characteristics of real tissues.

3.4.1. Simplified models

Figure 3.3 shows some examples of simplified models used in the evaluation of the effects of the electromagnetic fields on the biological tissues. The most simple is the discus that is a 2D model, whereas the cylinder and ellipsoid are 3D models that simulate better the volume of the human body. In those models the electrical characteristics are homogeneous.

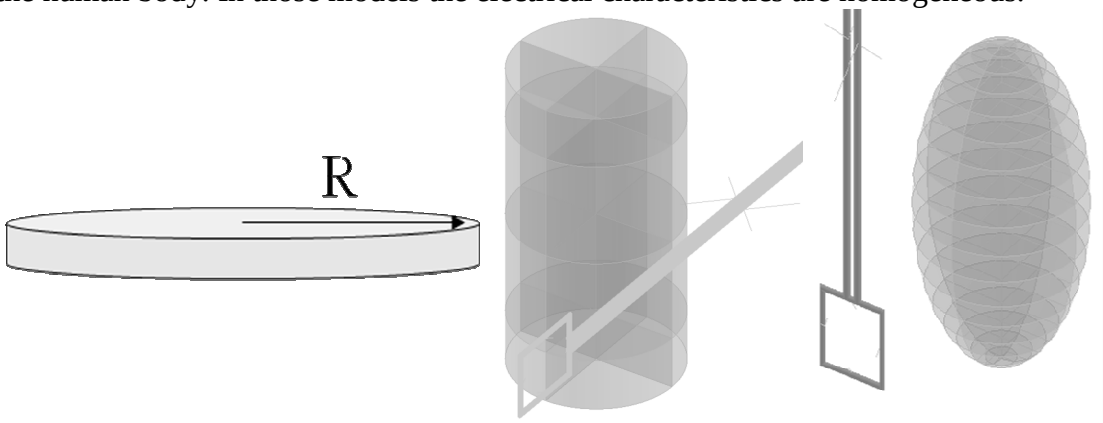

Figure 3.3: Simplified models.

In Table 3.2 the sizes of the simplified models in Figure 3.3 used in numerical simulations and the distance between the model and the electromagnetic field source in the case the electromagnetic field analyzed is generated by welding equipments are reported.

Table 3.2: Size of the simplified models for the analysis of exposure in the case of welding equipments.

R Disc	200 mm
H Disc height	10 mm
R Cylinder – Ellipsoid	150 mm
H Cylinder – Ellipsoid height	600 mm
d – model- conductor distance – Source arc welding	200 mm
d – model- conductor distance – Source resistance welding	30 mm

3.4.2. Building complex models of living organisms

A model of biological organisms like human or animal can be built from a set of the Magnetic Resonance Images (MRI) or Computer Tomography (CT) medical images by means

of some suitable programs[15]. Each image of the set is a slice that represents a section of the human body with corresponding organs. The segmentation operation identifies the organ tissues on each slice. The organs identified in each slice concurrent on the reconstruction of the volume of each organ in the whole model. The meshing tool of the software package used for the segmentation is quite versatile and powerful. The mesh controls are very useful and permit to refine properly the zones where the values of current density are expected large or in the interfaces between two different tissues. In this case the edges of the mesh elements have been forced to be no longer than 1.5 cm. It is to be pointed out that the single organs can be meshed separately, so the mesh of a single organ can be opportunely refined. Finally the meshed volumes have been imported in a Finite Element package[16] for the electromagnetic or thermal simulation as UNV-IDEAS data format, and inserted in a volume which represents a simplified human body surface. The final geometric and meshed human body model is the result of the merging of models of organs, each with its properly mesh.

Figure 3.4 sketches the step to build a human body model from medical images data. At first the medical images are loaded in the software for the segmentation. The segmentation step allows the identification of organs and tissues to built volumes. The volumes recognized can be meshed with tetrahedral elements and then imported in a Finite Element (FEM) computation tool to solve the electromagnetic or thermal problem by means of numeric techniques.

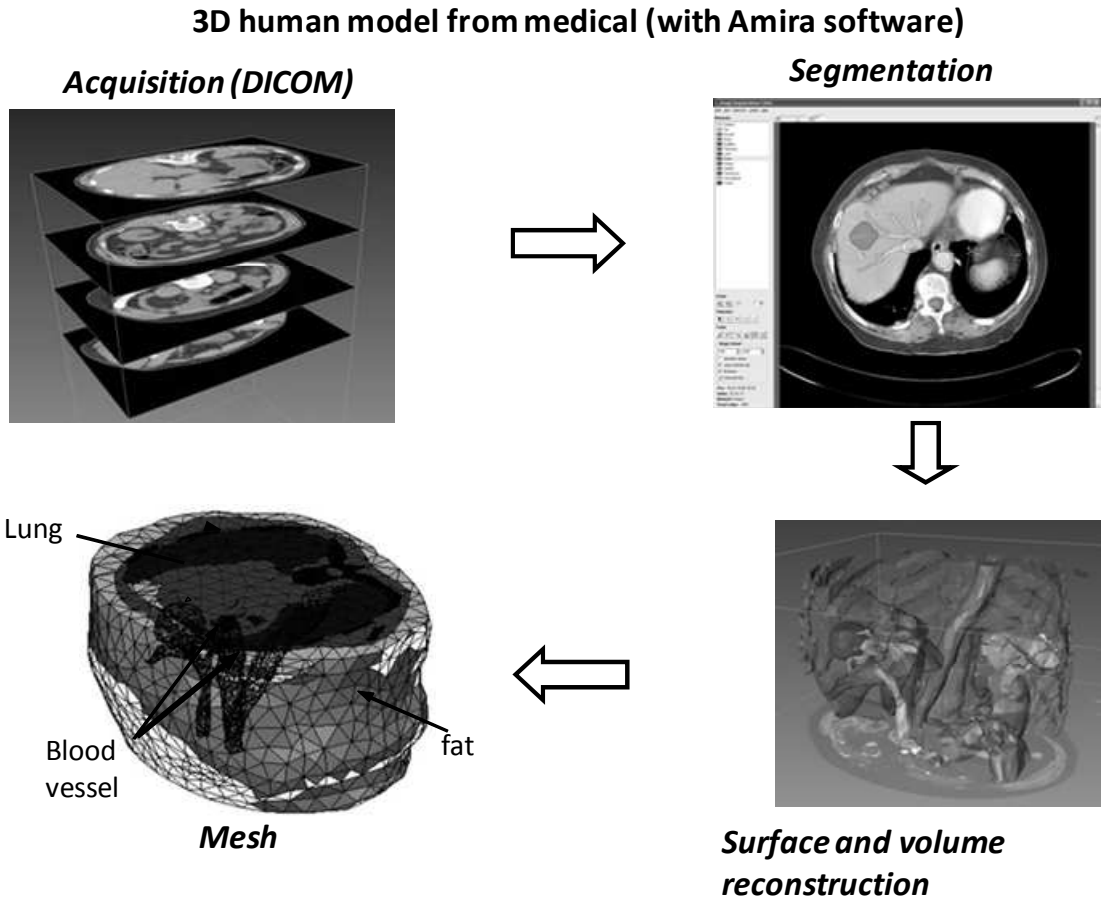

Figure 3.4: Steps for the generation of a model for FEM simulation tools from medical images.

Resuming, the steps for the model reconstruction from medical images are:

1. Images acquisition;

[15] For instance Amira, or Avizo, manufactured by VSG, http://www.vsg3d.com/ (last access December 2010)
[16] For instance Flux 3D manufactured by Cedrat, http://www.cedrat.com/ (last access December 2010)

2. Images load in the treating software;
3. Segmentation;
4. Volumes reconstruction;
5. Mesh preparation (small volumes – tetrahedral elements);
6. Model importation in the FEM software.

a. Some examples of models

A description of the characteristics of the human and animal model used in the simulations is proposed in Table 3.3; the number of nodes and volume elements generated in order to solve the electromagnetic or thermal problem, the origin of data, MRI or CT, the problem in which the model has been used are resumed[17].

Table 3.3: Chracteristics of the living organism models.

Model	Nodes	Volume elements	Images origin	Use	Mesh order
Human body	239,516	1,430,096	TAC	Welding exposure	first
Human body	222,884	1,334,611	TAC	Human model test	first
Cylinder	157,000	1,130,000	--	Cooktop exposure	second
Human head	560,699	395,170	MRI	Electric field evaluation	second
Rat head	199,876	1,137,654	MRI	Electric field evaluation	first
Tumor model	688,700	515,100	--	Magnetic field design in MFH – magnetic problem	second
Tumor model	500,000	--	--	Magnetic field design in MFH – thermal problem	second
Tumor model	515,095	382,246	--	MFH magnetic fluid design – magnetic problem	second
Tumor model	268,000	--	--	MFH magnetic fluid design – thermal problem	second

b. Human body model thorax and abdomen

In Figure 3.5 some human models used for the simulation of the induced current density generated by welding equipments are reported. The abdomen, head and thorax organs are included. The tetrahedral model has been inserted in a “box” of conductive material that simulated the shape of the human body. The model of the Figure 3.5 (c) has been built inserting the single organs in the human-shape “box”.

[17] Numerical evaluations have run with a 64 bit workstation and up to 15 GB of RAM.

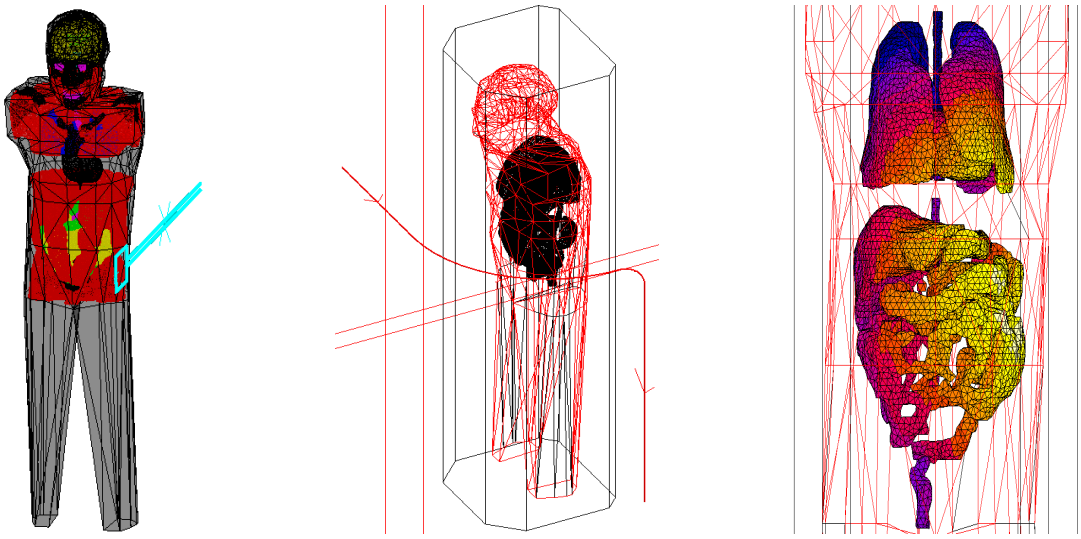

(a) (b) (c)

Figure 3.5: Human boby models.

c. Human head

In Figure 3.6 the model of an human head built from MRI images is reported. Some of the tissue regions simulated in this model are reported in the planar section in Figure 3.7.

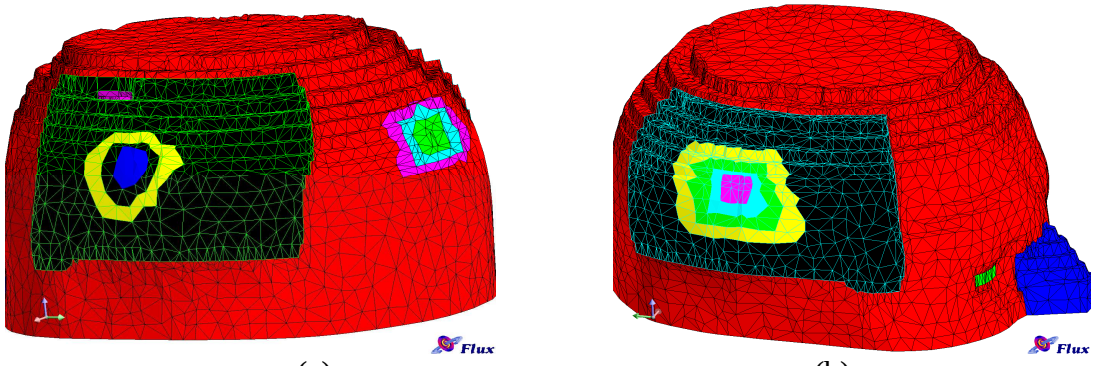

(a) (b)

Figure 3.6: Human head model where the skull bone is shown.

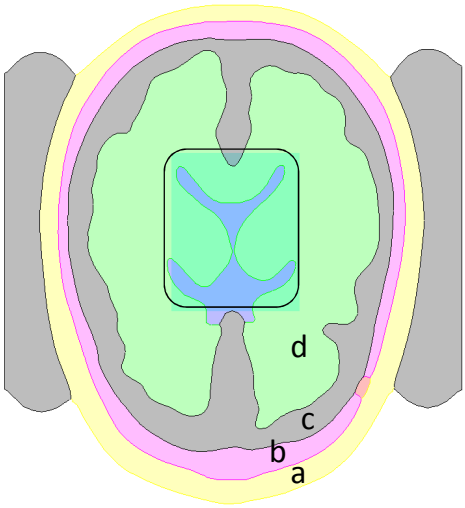

Figure 3.7: Regions in the human head model. Section of the head: (a) bone, (b) dura madre, (c) white matter (d) gray matter.

d. Rat head

In Figure 3.8 the model of a realistic rat head built from MRI images[18] is reported. Figure 3.8 (a) represents the whole head, whereas Figure 3.8 (b) and (c) show the muscle mass and the bone of the skull. Figure 3.9 represents a rat head slice in which some of the tissues considered in the simulation are identified.

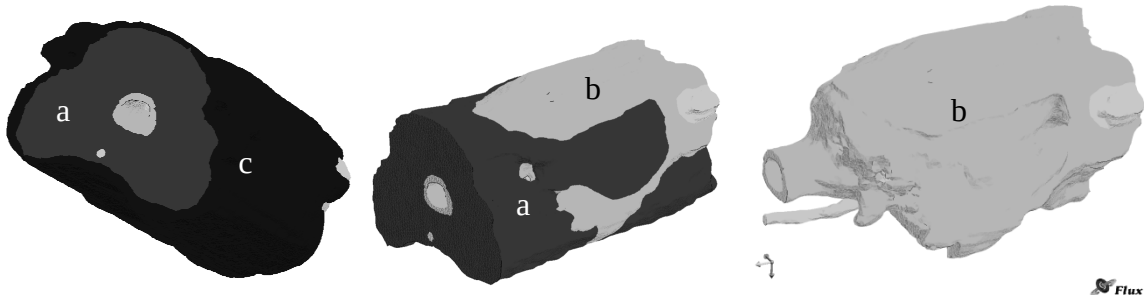

(a) (b) (c)

Figure 3.8: Rat head where (a) muscle, (b) bone, (c) skin are shown.

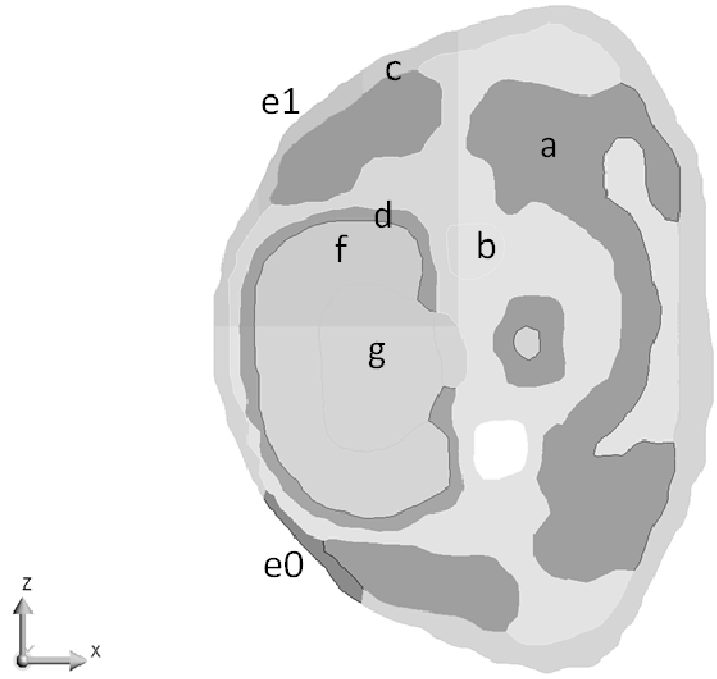

Figure 3.9: Rat head tissues (a) muscle, (b) bone, (c) skin, (d) dura, (e1) and (e0) electrodes, (f) cortex and (g) white matter.

e. Liver model used in Hyperthermia devices design

In Figure 3.10 a simplified model of human body used in the design of Magnetic Fluid Hyperthermia devices is reported. In this simplified model the human body is represented by a elongated box where a sphere representing the liver is dipped. An internal sphere in the liver volume represents the tumor mass.

[18] The MRI data of the rat head have been provided by the Laboratory of Magnetic Resonance of the Verona University, Italy.

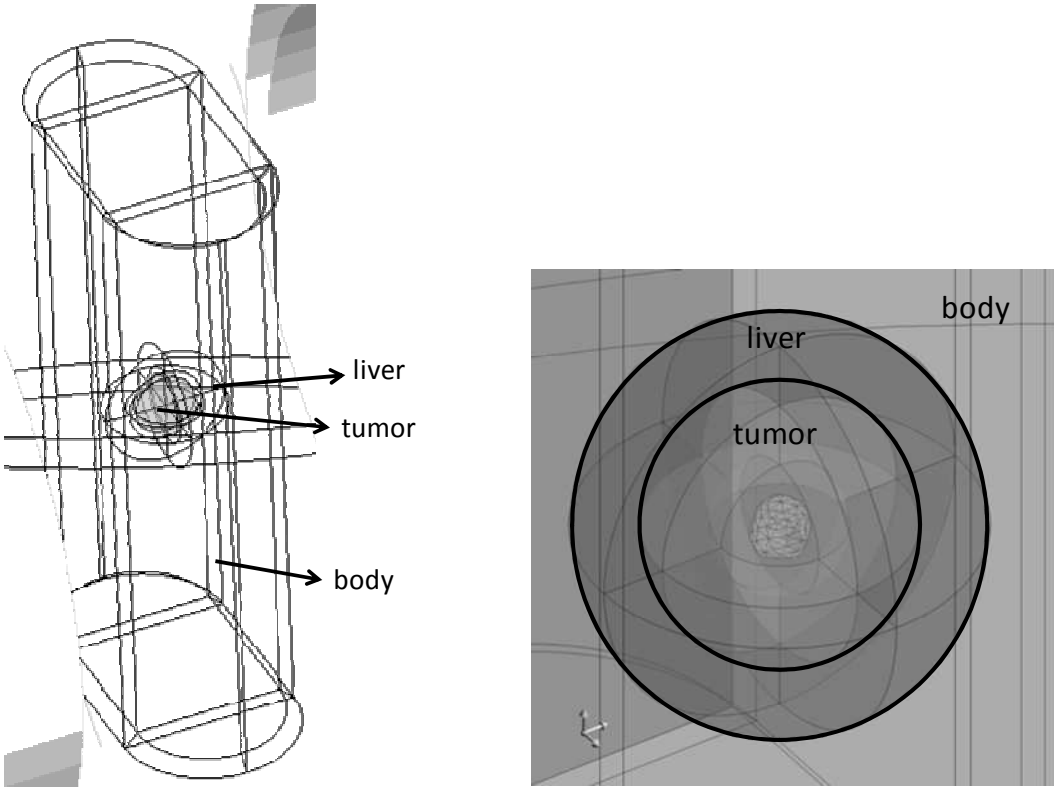

(a) (b)

Figure 3.10: Human body model for the design of Magnetic Fluid Hyperthermia devices.

3.5 Description of the specific problems

Given the previous models that describe in a realistic or simplified way the human body, the elements of the numerical problems (Finite Element Analysis) in order to solve some specific electromagnetic or thermal problems include:

- Evaluation of the human exposure (electromagnetic problem) in a model like the one in Figure 3.11 (a):
  - Human body model (realistic or simplified);
  - Magnetic field source (*e.g.* electric current or induction cooktop element);
  - Air volume that include magnetic field source and human model.
- Design of Magnetic Fluid Hyperthermia devices (electromagnetic and thermal problem) in a model like the one in Figure 3.11 (b)
  - Simplified human body model (with realistic tissue characteristics);
  - Magnetic field source (*e.g.* inductors);
  - Air volume that include magnetic field source and human model.
- Evaluation of the electric field in therapies for the electric stimulation of cells (for instance Figure 3.12 reports the electrodes configuration on a slice of the human and rat model):
  - Realistic human body model;
  - Electric field source (*e.g.* voltage difference).

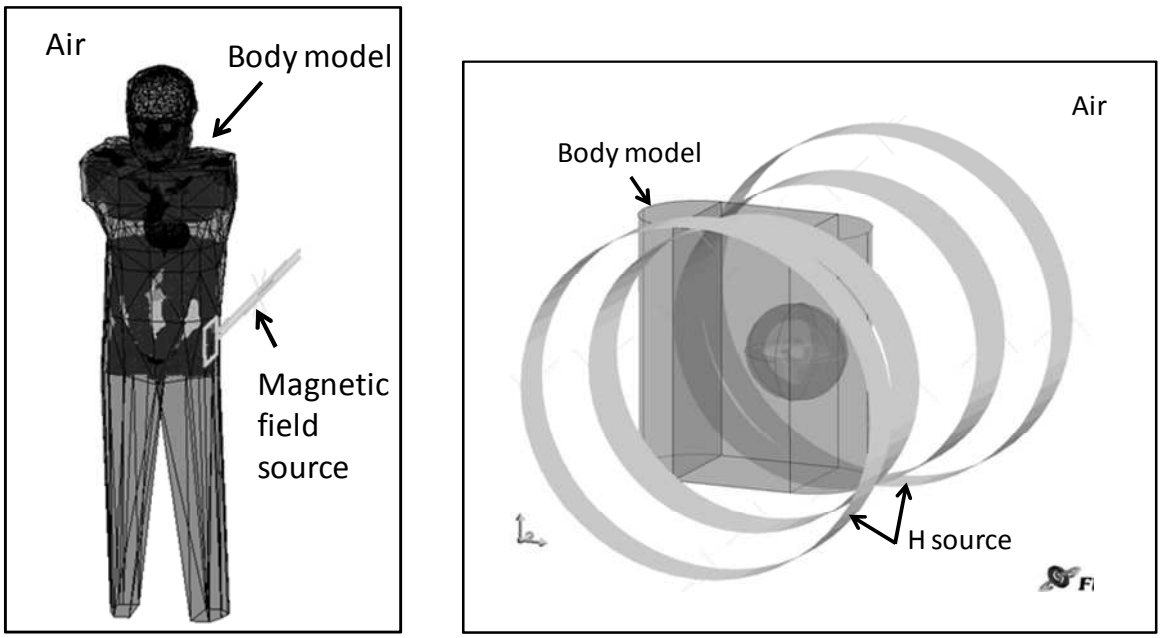

Figure 3.11: Human body model for the (a) evaluation of the human exposure to electromagnetic field and (b) design of Magnetic Fluid Hyperthermia devices.

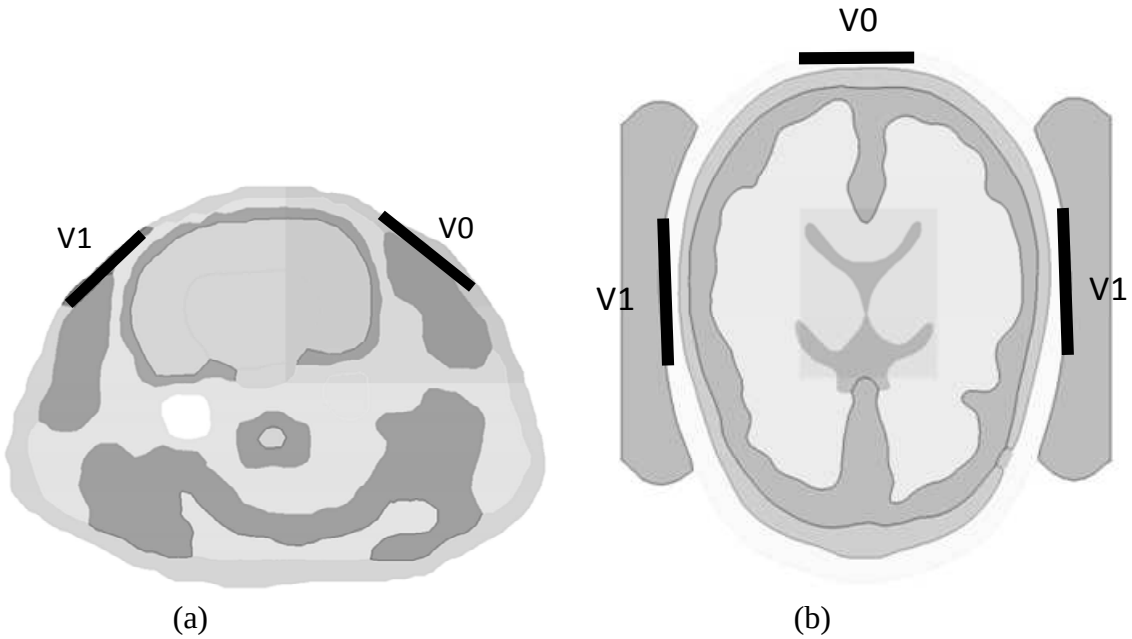

Figure 3.12: (a) Rat and (b) human head model with the electrode configuration for electric field generation.

3.6 Electrical and thermal characteristics of biological tissues

The biological tissues have different electric (resistivity and dielectric permeability) and thermal properties (thermal conductivity and specific heat). The electrical properties are a function of the frequency.

a. Electrical properties

All the proposed models of living organisms use the electrical properties of the biological tissues. Some research groups had worked in order to measure these properties that are published in various papers of the literature including[19] [177], [178], [194-197]. The most complete work is the one of Gabriel that provides a model of the conductivity and the dielectric permittivity as a function of the frequency. In Table 3.4 is reported an example of tissues resistivity at 50 and 200 Hz: at different frequencies the tissues can have a different resistivity. The resistivity values in Table 3.4 have been used in the evaluation of the human exposure to the magnetic field at low frequency in order to evaluate the induced current density in biological tissues. The tissue "homogeneous" is the resistivity value corresponding to the average tissue used in the homogenous, simplified models like discs and cylinders [55], [179], [180].

Table 3.4: Resistivity of biological tissues at 50 and 200 Hz[19].

	50Hz	**200Hz**		**50Hz**	**200Hz**
Tissue	**ρ [Ωm]**	**ρ [Ωm]**	**Tissue**	**ρ [Ωm]**	**ρ [Ωm]**
gall	0.71	0.71	Spleen	11.67	10.1
liver	27.26	25.6	Marrow	36.50	35.4
Heart	12.09	10.22	cartilage	5.83	5.79
intestine	1.92	1.9	Tongue	3.68	3.67
Colon	18.34	5.3	Eye	0.67	0.67
Bone	49.85	49.83	CerebellarFluid	0.50	0.5
pancreas	1.92	1.9	BrainStem	13.29	10.66
Kidney	11.21	9.3	cerebellum	10.50	8.79
Bladder	4.87	4.86	Brain	18.77	16.64
Stomach	1.92	1.9	trachea	3.33	3.33
Lung	14.62	13.4	Fat	51.15	46.95
Muscle	4.29	3.44	Homogeneous	5.00	5.00

In Table 3.5 the resistivity and relative electric permeability values are reported for some tissues. In this case the values are evaluated at 4 MHz and 450 kHz. Both the quantities are a function of the frequency. These values have been used in the electric field computation in the head model (resistivity and relative dielectric permittivity values at 4 MHz) and in the abdominal hyperthermia cancer treatment (resistivity value at 450 kHz).

Table 3.5: Resistivity and relative electric permittivity of biological tissues at 450 kHz and 4 MHz[19].

	450 kHz		**4 MHz**	
	ρ [Ωm]	**ε_r**	**ρ [Ωm]**	**ε_r**
BoneCortical	45.54	178.3	29.04	68.73
BrainGreyMatter	6.65	1254	4.72	504.6
BrainWhiteMatter	10.68	759.6	7.97	253.8
Cartilage	5.06	2006	3.11	420.3
Eye	0.67	92.23	0.66	72.26
Muscle	2.29	3972	1.72	384.9
Fat	40.328	36.15	37.84	19.43
Liver	7.02	3008	3.79	452.4

[19] computed using the IFAC software at *http://niremf.ifac.cnr.it/tissprop,* (last access December 2010)

b. Magnetic properties

The biological tissues have a unitary relative magnetic permeability.

c. Thermal properties

Biological tissues are thermal conducting materials and have properties like thermal conductivity and specific heat. In addition the mass flow rate is the term that describes the contribution, in term of subtracted heat, of the blood perfusion in the tissues.

The chaotic nature of the tumor vasculature made that the tumor tissues have a mass flow rate that has a different behavior, as a function of the temperature, than the healthy tissues [198], [199]. In particular in the tumor tissue the mass flow rate decreases if the temperature increases up to 41-42°C [74]. In Table 3.6 are reported some values for mass flow rate and thermal properties for some healthy and tumor tissues.

Table 3.6: Thermal characteristics (thermal conductivity, specific heat and mass flow rate) of some biological tissues. Temperature [°C].

Tissue	**λ [W/m/K]**	**c_p [J/kg/K]**	**γ [kg/m^3]**	**w_b [kg s^{-1} m^{-3}]**
Tumor	0.57	3500	1000	$\begin{cases} 0.833 - 0.833(-\frac{(T-37)^5}{5400}) & 37 < T \le 42 \\ 0{,}416 & T > 42 \end{cases}$
Liver	0.512	3816	1000	16.67
Fat	0.21	2973	920	$\begin{cases} 0.36 + 0.36\exp(-\frac{(T-45)^2}{12}) & T \le 45 \\ 0.72 & T > 45 \end{cases}$

Chapter 4

4 Methods for the solution of Maxwell equations and thermal problems using Finite Element Analysis

The interaction of the electric and magnetic fields with the human body, can be described in terms of induced current density, power density deposition, or temperature increasing over a basal value and it can be studied solving the Maxwell equations and Fourier equation by means of the Finite Element Analysis (FEA) [200],[201].

Given a magnetic field source Maxwell equations can be solved in close domains imposing suitable boundary conditions [202]. The temperature field can be studied solving a thermal heat transfer problem imposing a thermal source. The intensity of the power density source can be derived from the power density deposed by means of the electric and magnetic fields or, like in the case of the magnetic nanoparticles, can be computed by means of the magnetic material characteristics of the nanoparticles injected on the tissues.

In this chapter a brief description of the formulations applied in this work is presented.

4.1 Maxwell equations

The electric field, $\boldsymbol{E}$, can be divided into two components, $\boldsymbol{E_c}$, due to the presence of electric charges with opposite sign in the space, and $\boldsymbol{E_i}$, due to a time-varying magnetic flux density:

$$\mathbf{E} = \mathbf{E_c} + \mathbf{E_i} \tag{4.1}$$

In a dielectric medium with a relative dielectric permeability, ε_r, the electric flux density vector, $\boldsymbol{D}$, can be defined as:

$$\boldsymbol{D} = \varepsilon \boldsymbol{E} = \varepsilon_r \varepsilon_0 \boldsymbol{E} \tag{4.2}$$

where ε and ε_0 are, respectively, the absolute dielectric constant of the medium and the one of the vacuum, such that $\varepsilon = \varepsilon_r \varepsilon_0$.

The magnetic field, $\boldsymbol{H}$, is generated by means of an electric current as described by means of the Ampère law with l_c a close path and $\boldsymbol{i}$ the total current inside the considered path:

$$\oint_{l_c} \boldsymbol{H} \cdot \boldsymbol{t}\, \boldsymbol{dl} = \boldsymbol{i} \tag{4.3}$$

The four Maxwell equations, under quasi-static hypothesis, can be written with the following equations in terms of the divergence of the magnetic flux density, $\boldsymbol{B}$, and electric flux density, $\boldsymbol{D}$, and of the curl of the electric, $\boldsymbol{E}$, and magnetic field, $\boldsymbol{H}$:

$$\text{(I)} \quad \nabla \cdot \boldsymbol{D} = \rho \tag{4.4}$$

(II) $\nabla \cdot \boldsymbol{B} = 0$ (4.5)

(III) $\nabla \times \boldsymbol{E} = -\frac{\partial \boldsymbol{B}}{\partial t}$ (4.6)

(IV) $\nabla \times \boldsymbol{H} = \boldsymbol{J} + \frac{\partial \boldsymbol{D}}{\partial t}$ (4.7)

with ρ is the volume charge density, μ the magnetic permeability of the medium, like that $\mu = \mu_r \mu_0$, where μ_r and μ_0 are, respectively, the relative magnetic permeability of the medium and the one of vacuum and $\boldsymbol{J}$ is the vector of the current density source. If there are not free charges the divergence of the electric flux density vector $\boldsymbol{D}$ is null e and the (4.4) can be written as:

(I)' $\nabla \cdot \boldsymbol{D} = 0$ (4.8)

The electric flux density vector, $\boldsymbol{D}$, and magnetic flux density, $\boldsymbol{B}$, are correlated, respectively, to the magnetic and electric field through the following material constitutive properties:

$\boldsymbol{D} = \varepsilon \boldsymbol{E}$ (4.2)

$\boldsymbol{B} = \mu \boldsymbol{H}$ (4.9)

$\boldsymbol{J} = \sigma \boldsymbol{E}$ (4.10)

For the quasi-static approximation the (IV) Maxwell equation is:

(IV)' $\nabla \times \boldsymbol{H} = \boldsymbol{J}$ (4.7)

4.1.1. Magnetic vector potential and scalar electric potential

From equation (4.5) it derives that $\boldsymbol{B}$ is solenoidal, that is it is conservative on the flux, so it can be written as a curl of a vectorial field. This is the magnetic vector potential, $\boldsymbol{A}$, related to $\boldsymbol{B}$ in the following way [200],[203]:

$\boldsymbol{B} = \nabla \times \boldsymbol{A}$ (4.11)

Substituting (4.11) in the (4.6) is:

$$\nabla \times \boldsymbol{E} = -\frac{\partial \boldsymbol{B}}{\partial t} = -\frac{\partial (\nabla \times \boldsymbol{A})}{\partial t} \quad \rightarrow \quad -\nabla \times \left(\boldsymbol{E} + \frac{\partial \boldsymbol{A}}{\partial t} \right) = 0 \tag{4.12}$$

and considering the condition of irrotational field, a scalar electric potential V exists such that the rotor of the gradient is null:

$$-\nabla V = \boldsymbol{E} + \frac{\partial \boldsymbol{A}}{\partial t} \tag{4.13}$$

Then, from the (4.13) the electric field, $\boldsymbol{E}$, can be computed using the time derivative of the magnetic vector potential, $\boldsymbol{A}$, adding the gradient of a scalar electric potential, V:

$$\boldsymbol{E} = -\left(\frac{\partial \boldsymbol{A}}{\partial t} + \nabla V\right) \tag{4.14}$$

4.1.2. Electric vector potential and scalar magnetic potential

From the (4.2), (4.8) and (4.10) the vector $\boldsymbol{J}$ is solenoidal, $\nabla \cdot \boldsymbol{J} = (\sigma/\boldsymbol{\varepsilon})\, \nabla \cdot (\boldsymbol{D}) = 0$, such that the current density vector, $\boldsymbol{J}$, can be expressed like the curl of the electric vector potential, $\boldsymbol{T}$ [204-207]:

$$\boldsymbol{J} = \nabla \times \boldsymbol{T} \tag{4.15}$$

In analogy with the electric field a magnetic scalar potential Φ, can be defined. From (4.7) and (4.15) and quasi-static approximation for which the displacement current, $\partial \boldsymbol{D}/\partial t$, is negligible, the following relations can be written:

$$\nabla \times \boldsymbol{H} = \boldsymbol{J} = \nabla \times \boldsymbol{T} \qquad \rightarrow \quad \nabla \times (\boldsymbol{H} - \boldsymbol{T}) = 0 \tag{4.16}$$

such that the gradient of the scalar magnetic potential can be defined as:

$$-\nabla \Phi = \boldsymbol{H} - \boldsymbol{T} \tag{4.17}$$

then $\boldsymbol{H}$ can be written as the difference between the electric vector potential $\boldsymbol{T}$ and the gradient of the scalar magnetic potential Φ:

$$\boldsymbol{H} = \boldsymbol{T} - \nabla \Phi \tag{4.18}$$

4.1.3. Reduced scalar magnetic potential

In a non conductive region (σ=0), like an air region, where a current source, $\boldsymbol{J}_S$, generates a magnetic field $\boldsymbol{H}_S$ it is $\nabla \times \boldsymbol{H}_{\boldsymbol{S}} = \boldsymbol{J}_S$. Since the total magnetic field is due to the magnetic field sources, $\boldsymbol{H}_s$, and to the gradient of the reduced scalar potential, $\boldsymbol{H} = \boldsymbol{H}_{\boldsymbol{S}} - \nabla \phi_{\mathrm{RED}}$, for the (4.5) the equation solved in order to compute the reduced scalar potential, ϕ_{RED}, [208],[209] is:

$$\nabla \cdot \mu \nabla \phi_{\mathrm{RED}} = \nabla \cdot \mu H_S \tag{4.19}$$

in which ϕ_{RED} is the reduced magnetic scalar potential.

4.2 Formulations for the solution of Maxwell equations in different materials

In order to find the relations that describe the magnetic fields in different regions, conductive media or air regions with or without electric current sources, the Maxwell equations can be solved in terms of the magnetic vector potential, $\boldsymbol{A}$, or the electric vector potential, $\boldsymbol{T}$, imposing suitable boundary conditions and gauges. In the following Figure 4.1 the considered regions are sketched:

Ω_C: is a conductive region with a non null conductivity, σ, and a relative magnetic permeability μ;

J_S: is a current density source region;

Ω_H: is an air region that contains the current density source J_S;

Ω_A: is an air region without any current density source;

Ω_I: is an infinity region in which suitable conditions on the field value are imposed.

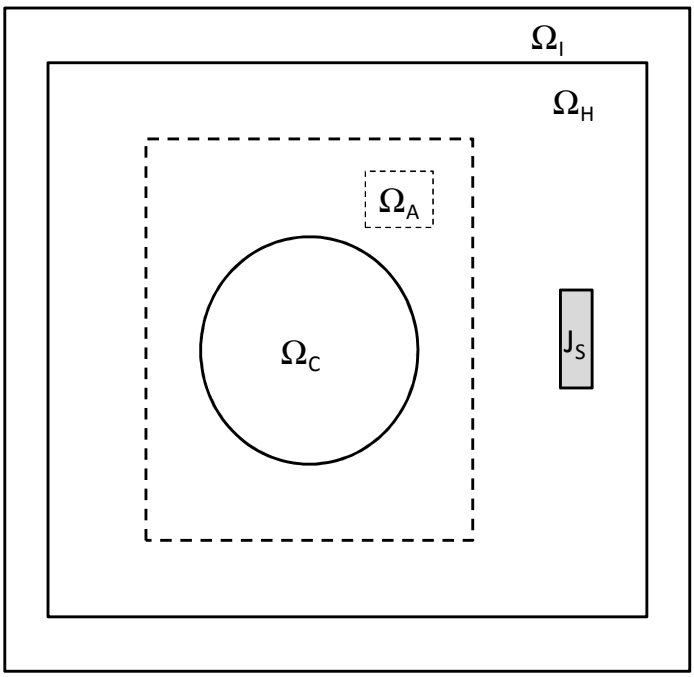

Figure 4.1: Regions considered in the electromagnetic problem.

4.2.1. Boundary conditions

The boundary conditions define some relations that describe the behavior of the electric and magnetic field in surface regions between two different volumes or at the computation boundary regions. On the surface regions between two different volumes some conditions on the continuity of the field values must be imposed, whereas at the computation boundaries conditions on the solution value must be defined.

For the electric and magnetic flux density some continuity conditions are valid at interface. The continuity of the tangential component of the electric and normal component of the magnetic flux density is valid and expressed by means of the following relations:

$$E_{1,t} = E_{2,t} \tag{4.20}$$

$$B_{1,n} = B_{2,n} \tag{4.21}$$

At the computation boundary the Dirichlet and Neumann conditions can be imposed to a given field value, Σ, and in the time harmonic case are, respectively:

- **Dirichlet**: fixes the value of the considered field value at the boundary region, *e.g.* the definition of an electric potential on a face:

$$\Sigma = 0 \text{ or constant} \tag{4.22}$$

- **Neumann**: imposes the value to the derivative of the field value. In this case a vanish condition on the derivative of the field value is imposed:

$$\partial\Sigma/\partial n = 0 \tag{4.23}$$

4.2.2. Condition on the divergence

Since the Maxwell equations have not a unique solution in terms of the field potential, some specification on the divergence, gauge, of the magnetic vector potential value can be imposed. The most common gauges, in the time harmonic case, are the following [203],[210],[211]:

- **Coulomb gauge**: in which the divergence of the magnetic vector potential, $\boldsymbol{A}$, is null:

$$\nabla \cdot \boldsymbol{A} = 0 \tag{4.24}$$

- **Lorentz gauge**: in which the divergence of the magnetic vector potential, $\boldsymbol{A}$, has a defined value and is proportional, for example, to the electric scalar potential, V:

$$\nabla \cdot \boldsymbol{A} = \mu\sigma V \tag{4.25}$$

4.2.3. Solution of an induced current problem in a conductive media

Considering a region Ω_C inside a region, Ω_H, like the one represented in Figure 4.1, where the magnetic field, $\boldsymbol{H_S}$, is generated by means of a current density distribution, $\boldsymbol{J_S}$. In the Ω_C region the induced current must be computed solving Maxwell equations. The current density $\boldsymbol{J_S}$ is related to the magnetic field, $\boldsymbol{H}$, by means of the (IV)' Maxwell equation, the (4.7). Imposing outside the conductive region, in Ω_H, the value of the curl of the magnetic vector potential using (4.11), the magnetic vector inside this region, Ω_C, is computed in the following way. Since for the (III) Maxwell equation, (4.6), $\boldsymbol{B}$ is solenoidal, in the Ω_C region a vector potential can be defined and from the (4.11) the following equation can be written [204],[205]:

$$\nabla \times \nabla \times \boldsymbol{A} = \nabla(\nabla \cdot \boldsymbol{A}) - \nabla^2 \boldsymbol{A} \tag{4.26}$$

Imposing the Coulomb gauge (4.24) on the magnetic vector potential, $\boldsymbol{A}$:

$$\nabla \cdot \boldsymbol{A} = 0 \tag{4.27}$$

like in [212],[203],[205]:

$$\boldsymbol{J} + \boldsymbol{J_S} = \sigma \boldsymbol{E} \tag{4.28}$$

Rearranging the equations (4.26) and (4.27), imposing $\boldsymbol{J_S}$ null because in this region there is any current source and considering only the induced current density component, the following equation can be written:

$$-\nabla^2 \boldsymbol{A} = \nabla \times \nabla \times \boldsymbol{A} = \mu\,(\boldsymbol{J} + \boldsymbol{J_S}) = \mu\sigma \boldsymbol{E} \tag{4.29}$$

then, from (4.7) rearranged like in (4.29) using (4.10), (4.11), (4.14) and the Coulomb Gauge the following equation in the magnetic vector potential $\boldsymbol{A}$ and in the electric scalar potential V can be written:

$$\nabla \times \frac{1}{\mu} \nabla \times \boldsymbol{A} = \frac{1}{\mu} \nabla \times \nabla \times \boldsymbol{A} = -\frac{1}{\mu} \nabla^2 \boldsymbol{A} = \boldsymbol{J} = \sigma \boldsymbol{E} = -\sigma \left(\frac{\partial \boldsymbol{A}}{\partial t} + \nabla V \right) \tag{4.30}$$

that is a Helmholtz equation. In the sinusoidal case the (4.30) can be written in terms of phasors as:

$$\nabla^2 \boldsymbol{A} = \sigma \mu (\mathrm{j}\omega \boldsymbol{A} + \nabla V) \tag{4.31}$$

that is:

$$\nabla^2 \boldsymbol{A} - \mathrm{j}\omega \sigma \mu \boldsymbol{A} = \sigma \mu \nabla V \tag{4.32}$$

Solving the electromagnetic problem by means of the magnetic vector potential, the induced current problem is solved directly from the solution in terms of the magnetic vector potential, ***A***, and the scalar electric potential, *V*. In this case the magnetic flux density, ***B***, can be derived using equation (4.11) computing the curl of the vector potential, ***A***.

4.2.4. Solution of a magnetic field problem in conductive media

The magnetic field value is computed in the same regions like in the previous case by means of the (III)' Maxwell equation (4.6). In a same way that in the previous case, imposing outside the conductive region, in Ω_H, the value of curl of the electric vector potential using (4.10) and (4.15) the electric vector potential inside this region, in Ω_C, is computed in the following way. Since the current density vector, ***J***, is solenoidal such that an electric vector potential, ***T***, exists, writing the (4.26) for the vector ***T***, the following relation is obtained [204],[205]:

$$\nabla \times \nabla \times \boldsymbol{T} = \nabla (\nabla \cdot \boldsymbol{T}) - \nabla^2 \boldsymbol{T} \tag{4.33}$$

Applying (4.5) to (4.18) the following equation is obtained:

$$\nabla \cdot \mu \boldsymbol{H} = \nabla \cdot \mu (\boldsymbol{T} - \nabla \Phi) = 0 \tag{4.34}$$

and the divergence of the electric scalar potential can be posed equal to:

$$\nabla \cdot \boldsymbol{T} = \nabla \cdot \nabla \Phi \tag{4.35}$$

then, rearranging (4.33) imposing (4.35) and using (4.6), (4.9) and (4.18), the following equation in the electric vector potential ***T*** and in the scalar magnetic potential Φ can be written:

$$\begin{aligned} \nabla \times \frac{1}{\sigma} \nabla \times \boldsymbol{T} = \frac{1}{\sigma} \nabla \times \nabla \times \boldsymbol{T} = \frac{1}{\sigma} (\nabla (\nabla \cdot \boldsymbol{T}) - \nabla^2 \boldsymbol{T}) = -\frac{\partial \boldsymbol{B}}{\partial t} = -\mu \frac{\partial \boldsymbol{H}}{\partial t} \\ = -\mu \frac{\partial}{\partial t} (\boldsymbol{T} - \nabla \Phi) \end{aligned} \tag{4.36}$$

Posing $\nabla \cdot \boldsymbol{T} = \nabla \cdot \boldsymbol{H} = 0$ in the equation (4.5), the (4.36) is a Helmholtz equation. In fact in the sinusoidal case the (4.36) can be written in terms of phasors as:

$$\nabla^2 \boldsymbol{T} = \sigma \mu (\mathrm{j}\omega \boldsymbol{T} - \nabla \Phi) + \nabla (\nabla \cdot \boldsymbol{T}) \tag{4.37}$$

that is:

$$\nabla^2 \boldsymbol{T} - \mathrm{j}\omega\sigma\mu\boldsymbol{T} = -\mathrm{j}\omega\sigma\mu\nabla\Phi \tag{4.38}$$

Solving the Maxwell equations in the electric vector potential the magnetic field vector, $\boldsymbol{H}$, can be derived from the value of electric vector potential and scalar magnetic potential using the relation (4.18), whereas the induced current can be derived computing the curl of the electric vector potential, $\boldsymbol{T}$ vector using (4.15).

4.2.5. Some comments

It can be pointed out that the formulations (4.30) and (4.36) can be used to solve, respectively, an induced current density and a magnetic field problem. The former estimates directly the induced current density and derives the value of the magnetic field by means of a curl operation, whereas the second estimates directly the magnetic field and derives the value of the induced current density by means of another curl operation.

4.2.6. Solution of magnetic field problem in a non conductive media with magnetic field sources

The magnetic field, $\boldsymbol{H}_S$, generated in a vacuum region by means of an electric current density, $\boldsymbol{J}_S$, (the source) can be described using the Biot-Savart relation [200]:

$$\boldsymbol{H}_S = \frac{1}{4\pi}\int_{\Omega} J \times \nabla\left(\frac{1}{R}\right) d\Omega \tag{4.39}$$

where R is the distance between the source and the computation point and Ω the infinitesimal current element. In the region that contains the source the magnetic field $\boldsymbol{H}$ can be computed by means of the (4.18) and (4.39). When the magnetic field generated by means of the current source is computed using (4.18) a reduced scalar potential formulation can be used in order to solve the magnetic field problem [208]:

$$\boldsymbol{H} = \boldsymbol{H}_{\boldsymbol{s}} - \nabla\phi_{RED} \tag{4.40}$$

In which ϕ_{RED} is the reduced magnetic scalar potential that fulfils the Poisson equation:

$$\nabla \cdot \mu_0 \nabla\phi_{RED} = \nabla \cdot \mu \boldsymbol{H}_S \tag{4.41}$$

In the first case, in which the magnetic vector potential is evaluated, the first term of the (4.11) is computed solving a reduced scalar potential problem from the value of the current density that flows in the source, whereas in the second case the value of the current source is imposed directly in the first term of the (4.15).

Considering the (IV)' Maxwell equation (4.7) the (4.29) is:

$$\nabla \times \nabla \times \boldsymbol{A} = \nabla(\nabla \cdot \boldsymbol{A}) - \nabla^2 \boldsymbol{A} = \mu(\boldsymbol{J} + \boldsymbol{J}_{\boldsymbol{S}}) \tag{4.42}$$

$$\nabla^2 \boldsymbol{A} = \nabla(\nabla \cdot \boldsymbol{A}) - \mu \boldsymbol{J}_{\boldsymbol{S}} \tag{4.43}$$

imposing the Lorentz gauge (4.25) and considering that the conductivity of the medium is null the (4.43), in terms of phasors, is:

$$\nabla^2 \boldsymbol{A} = \nabla(\mu\sigma V) - \mu \boldsymbol{J_S} = -\mu \boldsymbol{J_S} \tag{4.44}$$

that has the form of an Helmholtz equation:

$$\nabla^2 \boldsymbol{A} + \mathrm{k}^2 \boldsymbol{A} = -\mu \boldsymbol{J_S} \tag{4.45}$$

with $\mathrm{k}^2 = -\mathrm{j}\omega\sigma\mu$. Since in the air region the conductivity of the medium is null, so that the $\mathrm{k}^2 = 0$, and in the considered region the current source, $\boldsymbol{J_S}$, is non null, the (4.45) is a Poisson equation:

$$\nabla^2 \boldsymbol{A} = -\mu \boldsymbol{J_S} \tag{4.46}$$

4.2.7. Solution of magnetic field problem in a non conductive media

Considering the region Ω_A dotted in Figure 4.1. This region is an air region without any magnetic field source inside the Ω_H air region considered in the previous paragraph that surrounds the conductive region Ω_C. In this case the (IV)' Maxwell equation (4.7) is null because there is not any current source:

$$\nabla \times \boldsymbol{H} = 0 \tag{4.47}$$

then, a scalar potential exists such that the magnetic field $\boldsymbol{H}$ can be written as a gradient of a magnetic scalar potential Φ:

$$\boldsymbol{H} = -\nabla\Phi \tag{4.48}$$

In this case, since in the air the conductivity is null, so that the second term of the Helmholtz equation (4.45) has the coefficient k^2 equal to 0, $\mathrm{k}^2 = 0$, and in the considered region there is not any current source, $\boldsymbol{J_S}$, the (4.45) is reduced to a Laplace equation:

$$\nabla^2 \boldsymbol{A} = 0 \tag{4.49}$$

4.2.8. Coupling of formulations

In order to couple different formulations some interface boundary conditions must be verified [204],[205],[209]. For instance, considering the interface region between Ω_C and Ω_H in Figure 4.1[20]:

$$B_{\boldsymbol{n},\Omega_C} = B_{\boldsymbol{n},\Omega_H} \tag{4.50}$$

$$H_{\boldsymbol{t},\Omega_C} = H_{\boldsymbol{t},\Omega_H} \tag{4.51}$$

[20] In this case the region Ω_A is not considered.

a. Magnetic vector potential in the conductive region

The Maxwell equations in the conductive region can be solved by means of the magnetic vector potential, whereas in an air region they are solved by means of the reduced magnetic scalar potential [213]. Considering the regions Ω_C and Ω_H in the Figure 4.1 and the previous interface conditions, the electric and magnetic field are, respectively:

$$\Omega_C: \boldsymbol{B} = \nabla \times \boldsymbol{A} \text{ and } \boldsymbol{E} = -\left(\frac{\partial \boldsymbol{A}}{\partial t} + \nabla V\right)$$

$$\Omega_H: \boldsymbol{H} = \boldsymbol{H_s} - \nabla\phi_{\boldsymbol{RED}} \quad \text{and} \quad \boldsymbol{E} = \boldsymbol{J}/\sigma$$

It can be pointed out that is better avoid the direct coupling of a reduced scalar potential and a magnetic vector potential formulation [213]. That is the case at the boundary region between the two volumes where the two previous problems (reduced scalar potential and magnetic vector potential problem) must be solved; the following conditions in the magnetic flux density and magnetic field are verified at the interface between Ω_C and Ω_H:

- continuity of the normal component of the magnetic flux density $\boldsymbol{B}$:

$$\boldsymbol{n}_{\Omega_C} \cdot \nabla \times \boldsymbol{A}_{\Omega_C} + \boldsymbol{n}_{\Omega_H} \cdot \mu_0 \boldsymbol{H}_{\Omega_H} = 0$$

- continuity of the tangential component of the magnetic field $\boldsymbol{H}$:

$$\frac{1}{\mu}\nabla \times \boldsymbol{A}_{\Omega_C} \times \boldsymbol{n}_{\Omega_C} + \boldsymbol{H}_{\Omega_H} \times \boldsymbol{n}_{\Omega_H} = 0$$

Then, in this case a coupling region must be interposed between the region where the induced current are computed and the one that contains the source, because it allows a better interface condition. This is the region, Ω_A, dotted in Figure 4.1. In this case the coupling conditions at the interface between Ω_C and Ω_A are:

- continuity of the normal component of the magnetic flux density $\boldsymbol{B}$:

$$\boldsymbol{n}_{\Omega_C} \cdot \nabla \times \boldsymbol{A}_{\Omega_C} + \boldsymbol{n}_{\Omega_H} \cdot \nabla \times \boldsymbol{A}_{\Omega_H} = 0$$

- continuity of the tangential component of the magnetic field $\boldsymbol{H}$

$$\frac{1}{\mu}\nabla \times \boldsymbol{A}_{\Omega_C} \times \boldsymbol{n}_{\Omega_C} + \frac{1}{\mu_0}\nabla \times \boldsymbol{A}_{\Omega_H} \times \boldsymbol{n}_{\Omega_H} = 0$$

In this case the interface condition is imposed only on the magnetic vector potential, $\boldsymbol{A}$.

b. Electric vector potential in the conductive region

The Maxwell equations in the conductive region are solved in the total electric vector potential, whereas in an air region they are solved in the reduced magnetic scalar potential. Let consider the regions Ω_C and Ω_H in the Figure 4.1 the previous interface conditions are derived from the magnetic flux density and electric field continuity:

$$\Omega_C : \boldsymbol{H} = \boldsymbol{T} - \nabla\Phi \quad \text{and} \quad \boldsymbol{E} = \boldsymbol{J}/\sigma$$

$$\Omega_H : \boldsymbol{H} = \boldsymbol{H_s} - \nabla\phi_{\boldsymbol{RED}} \quad \text{and} \quad \boldsymbol{E} = \boldsymbol{J}/\sigma$$

In this case any coupling region between Ω_C and Ω_H is needed and the continuity conditions on the magnetic flux density and magnetic field at the region interface are:

- continuity of the normal component of the magnetic flux density ***B***:

$$n_{\Omega_C} \cdot \mu H_{\Omega_C} + n_{\Omega_H} \cdot \mu_0 H_{\Omega_H} = 0$$

- continuity of the tangential component of the magnetic field ***H***

$$H_{\Omega_C} \times n_{\Omega_C} + H_{\Omega_H} \times n_{\Omega_H} = 0$$

that are expressed in the magnetic field value.

4.2.9. Electric field problem

In a dielectric medium a steady state time-varying electric field problem can be solved in order to compute the electric field in volumes in which the electric permittivity is not homogeneous [189], [191-193]. In this case the electric field source is a voltage difference applied by means of two electrodes. An example of the solution domain is sketched in Figure 4.2. The regions Ω_1 and Ω_2 are dielectric and conductive media with different values of the conductibility and relative electric permeability, whereas V_1 and V_0 are two voltage values applied on the boundary of the domain.

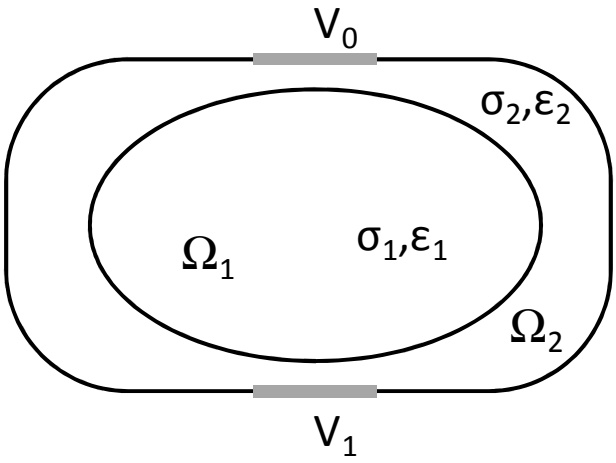

Figure 4.2: Regions for the electric field problem.

In this case the electric field in the domain, regions Ω_1 and Ω_2, is generated by means of a voltage difference, then the component due to the induced current is null and only the Columbian component exists and the curl of electric field in equation (4.6) is null:

$$\nabla \times \boldsymbol{E} = 0 \tag{4.52}$$

then, since the gradient of a scalar exists such that the curl of the electric field vector is null, given the electric scalar potential, *V*:

$$\boldsymbol{E} = -\nabla V \tag{4.53}$$

For equation (4.5) and vectorial identities the divergence of the second member of the equation (4.7) is null:

$$\nabla \cdot \left(\boldsymbol{J} + \frac{\partial \boldsymbol{D}}{\partial t} \right) = 0 \tag{4.54}$$

substituting in (4.54) the equation (4.2), (4.10) and (4.53) the following relations can be written for dielectric media where some surface potentials are defined and the following equation can be written:

$$\nabla \cdot (-([\sigma] + j\omega[\varepsilon_r]\varepsilon_0)\nabla V) = 0 \tag{4.55}$$

in which ε_r is the relative dielectric permeability of the medium.

4.3 Fourier equation: solution of the heat transfer thermal problem

Let consider the regions Ω_T, Ω_L and Ω_F in Figure 4.3. All the regions Ω_T, Ω_L and Ω_F are thermal conducting regions. In particular the Ω_F region exchanges heat with the external environment at temperature T_e (*e.g.* 25°C), whereas the region Ω_T contains the heat source.

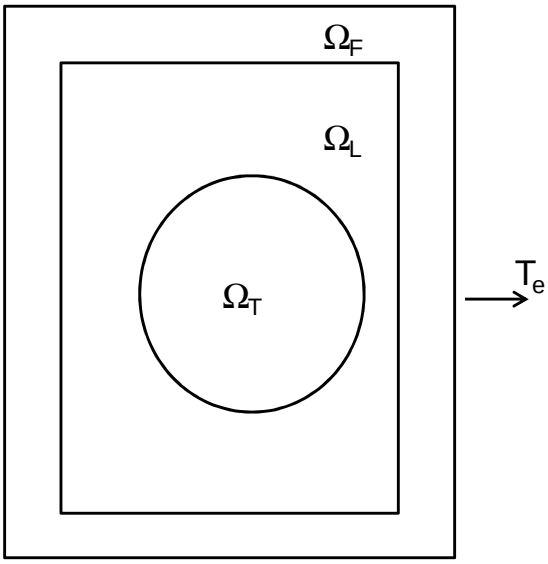

Figure 4.3: Regions of the thermal domain for FEM computation.

Given the power density and the exchange conditions with the external environments the temperature increasing as a function of the time in Ω_T, Ω_L and Ω_F regions can be evaluated solving a time dependent conductive problem using the thermal transfer Fourier equation [201]:

$$c_p \gamma \frac{\partial T(t)}{\partial t} = \lambda \nabla^2 T(t) + P \tag{4.56}$$

where λ is the thermal conductivity [$Wm^{-1}K^{-1}$], c_p the specific heat [$Jkg^{-1}K^{-1}$], γ the density of the tissue [kgm^{-3}] and P the power density inside the regions Ω_T, Ω_L and Ω_F, the source of heat, in [Wm^{-3}]. At the boundary of the thermal domain an exchange condition with the ambient environment at 25°C is imposed, whereas transmission conditions hold at the boundary of different regions, *i.e.* biological tissues in the considered problems.

4.3.1. Perfusion term in the Fourier equation

In biological tissues the blood vessels subtract heat to maintain the temperature in a physiological value (37°C) [75]. Then, this contribute can be represented as a “negative” thermal source that is subtracted to the power density P in the equation (4.56).

This term is the Pennes blood perfusion contribution [214] and the equation (4.56) can be written as:

$$c_p \gamma \frac{\partial T}{\partial t} = \lambda \nabla^2 T - c_b w_b (T - T_a) + P \tag{4.57}$$

where T_a is the basal body temperature (at 37°C), w_b is the mass flow rate [kg/m^3/s] which depends on tissue and temperature, and c_b is the blood specific heat (3.5 kJ/kg/K). In the implementation of the thermal equation, the cooling effect due to big vessels as well as the phase change of the blood has not been considered. The thermal properties and the mass flow rate of the tissues are reported in Table 3.6 [13], [17], [18]. For instance, the mass flow rate w_b is non-linear with respect to the temperature in the hyperthermia treatment temperature range (>42°C).

4.3.2. The heat source

The heat source, *P*, in the equation (4.56) and (4.57) can be the power density produced by means of the Joule effect due to an electric current circulating in biological tissue induced by means of a magnetic field or the one produced by means of suitable devices implanted on tissues like thermoseeds or magnetic nanoparticles.

a. The heat generated by means of the induced current

In a conductive media the power density, P_J, in [W/m^3] generated by means of an electric current density can be computed from the following equation:

$$P_J = \rho J^2 \tag{4.58}$$

in which ρ is the medium resistivity [Ωm] and *J* is the current density.

b. The heat generated by means of the magnetic nanoparticles

As discussed in paragraph 2.4.1 the mechanisms that allow the heating of magnetic nanoparticles are due to two effects related to relaxation phenomena induced by a time-varying magnetic field. The time-varying magnetic field, if the nanoparticles are free to move in a fluid, allows the rotation of nanoparticles (relaxation of Brown) and then the heat is generated by means of a friction effect. This phenomenon is superimposed on the effect of rotation of the magnetic nanoparticle moment that is the Néel relaxation [107].

Chapter 5

5 Automated design of electromagnetic devices by means of optimization techniques

Mathematical tools can be used in order to design electromagnetic field sources or heating sources. Optimization techniques are versatile tools that can be used to design different aspects of a single device [215] or process by means of the same computation code.

5.1 Introduction

An optimization problem is an inverse problem because the output of the optimal design generally can be known, for instance searching a minimum of a function, a target value for a quantity, *etc.*, and inputs are generally known [215], [216]. The unknown is the way according to reach, for instance, the shape of the electromagnetic device that gives a prescribed field or the electromagnetic source that generates the electromagnetic field.

5.2 Formulation of a design problem in terms of an optimization problem

The elements of an optimization problem are [215]:

- The design variables that are the quantities that act in the optimal design and vary in a prescribed range modifying the output value;
- The input values: are the values of the optimization variables used to compute the value of the actual solution of the objective function. These values are inside the range of allowed values, the input domain;
- The objective function: is the relation between the optimization variables. Given a set of values for optimization variables, the computation of the solution of the objective function is a direct problem. The objective function can be an analytical expression of the design variables, but, in generally, it can be derived by a solution of a numerical problem (*e.g.* FEA) or a combination of analytical expressions;
- Solution: is the actual value of the objective function. The set of the objective function value forms the solution domain.

The optimization objective is to find the set of the design variables (inputs), $x \in \Omega$, that match the design criterion. Given the space of design variables, $\Omega \subseteq R^N$, and a vector of values in the space of design variables, x, the most popular design criterions are minimizing a function, $f(x)$, or finding a prescribed behavior $a(x)$ for the function $f(x)$, *e.g.* a constant value c, for the function $f(x)$. The latter can be expressed in term of searching the minimum of the difference between the actual value of a function $f(x)$ and the prescribed value:

$$find \min_{x} f(x), \quad x \in \Omega \subseteq R^N \tag{5.1}$$

or

$$find \min_{x} |f(x) - a(x)|, \quad x \in \Omega \subseteq R^N \tag{5.2}$$

The optimization can be with or without constraints, in an optimization problem with constraints some limitations can be introduced on:

- Possible values of the design variables, such that inferior and superior limits of the design variable space (*e.g.* geometrical constraints, *etc.*)
- Possible values of the objective function (*e.g.* not allowed values)

5.3 Algorithms for the optimization

In literature some optimization strategies exist. For instance Genetic Algorithms [217],[218], Evolutionary algorithms [219-221], Tabu search algorithms [222], simulated annealing [223], Evolutionary Migration Algorithms [224],[225].

The Evolutionary Algorithm and Genetic Algorithms have been introduced since the 1950 [217],[218]. This class of algorithms has been successful because they are gradient free and therefore are global minimum oriented. They are based on the natural evolution, reproduction and selection of a population. A parent generates one or more children that have characteristics derived from these of the parent by means of mutations ad crossover. The Genetic algorithms belong to the Evolutionary Algorithms class and simulate the "evolutionary behavior" of a species like it has been described by Darwin.

5.3.1. Evolution Strategy algorithm

In the class of the Evolution Strategy algorithms the Evolution Strategy of the first order (ESTRA) is an algorithm in which a parent, *m*, generate a child, *x*, by means of a mutation event [215]. The optimization algorithm is built with the following elements:

- **Objective function:** given a parent, *m*, the corresponding value of the objective function is computed;
- **Evaluation of constraints**: this functionality evaluates if a new child, *x*, is a "possible child" given the space of the optimization variables, **Ω**;
- **Mutation**: is the algorithm for the generation of a child, *x*, from the parent *m*. Given a Gaussian distribution with null average and dispersion *d*, *N(0,d)*, a child is *x=m+N(0,d)*, the dispersion *d* is the radius of the searching region which is a sub set of the optimization variables space, **Ω**;
- **Annealing**: is the updating process of the dispersion *d* of the searching region radius. This value can be increased or decreased as a function of the actual value of the objective function. If a better point is found the search radius is increased in order to evaluate if a better point exists, otherwise it is decreased.

The most important steps in an ESTRA optimization algorithm for the minimization of the objective function are:

1. Given the initial parent $m_0 \in \Omega$, the value of the objective function $f(m_0)$ is computed;

2. The first child x_0 is evaluated by means of the mutation code;
3. The constraints are verified and if the chosen child, x_0, satisfies the constraints is the new parent, m_i, for the following generation, otherwise a new child is generated;
4. The value of the objective function $f(m_i)$ is computed and compared with the previous value, $f(m_0)$ in order to evaluate if the new solution is better than the previous;
5. The search radius, d, is updated by means of the annealing process;
6. The new parent m_i generates a new child x_i by means of the mutation function until one child that satisfied constraints is found. The new child is the parent for the next generation;
7. Points from 4 to 6 are repeated until a minimum of the objective function is found.

If only an objective function is considered the process is a single objective optimization, whereas if it has more objective functions is a multiobjective optimization.

a. Multi-objective optimization

In the multobjective optimization [215] a vector of objective functions $F(x) \subseteq R^M$, $F(x)=(f_1(x),f_2(x),\ldots)$, that has values in the objective space $Y \subseteq R^M$, is considered and then the (5.1) is:

$$find \min_x F(x), \quad x \in \Omega \subseteq R^N \tag{5.3}$$

A solution x_i is named dominate if it is better than another solution with respect to one objective, without worsening all the other objectives. Whereas two solutions are indifferent to each other if the first is optimal for some objectives while the second is better than the first in all the other objectives. The following definitions for dominate and indifferent solutions are given [215]:

Def: Let $\Omega \subseteq R^N$ be a design space and let $F(x) \subseteq R^M$ be a vector of M objectives, where each $f_j(x)$, $j=1, M$ is to be minimized with respect to x. Given two vectors $x_1 \in \Omega$ and $x_2 \in \Omega$ with $x_1 \neq x_2$, the following relationships hold:

- x_1 is said to dominate x_2 if

$\exists i$ such that $f_i(x_1) < f_j(x_2)$ and $f_j(x_1) \leq f_j(x_2)$ $\forall j = 1, M, j \neq i$;

- x_1 is said to be indifferent x_2 if

$\exists i$ such that $f_i(x_1) < f_j(x_2)$

and

$\exists q$ such that $f_q(x_2) < f_j(x_1)$ $\forall j = 1, M, j \neq i, j \neq q$;

For the sake of completeness, the definition of strong dominance follows:

- x_1 is said to strongly dominate x_2 if

$\exists$i such that $f_i(x_1) < f_j(x_2)$ and $f_j(x_1) < f_j(x_2)$ $\forall j = 1$, M, $j \neq i$.

The goal of a multiobjective optimization is to find all the non-dominated solutions called also non-inferior or efficient solutions. So, the definition of optimality is [215]:

Def: Let $Y \subseteq R^M$ be an objective space. Then, a point $y \in Y$ is said to be Pareto optimal if any point $\tilde{y} \in Y$ exists such that $F^{-1}(\tilde{y})$ dominates $F^{-1}(y)$.

The locus of non-dominate solutions is named Pareto front. In Figure 5.1 (a) a classical Pareto front whereas in Figure 5.1 (b) a weakly front are shown. In this case M=2.

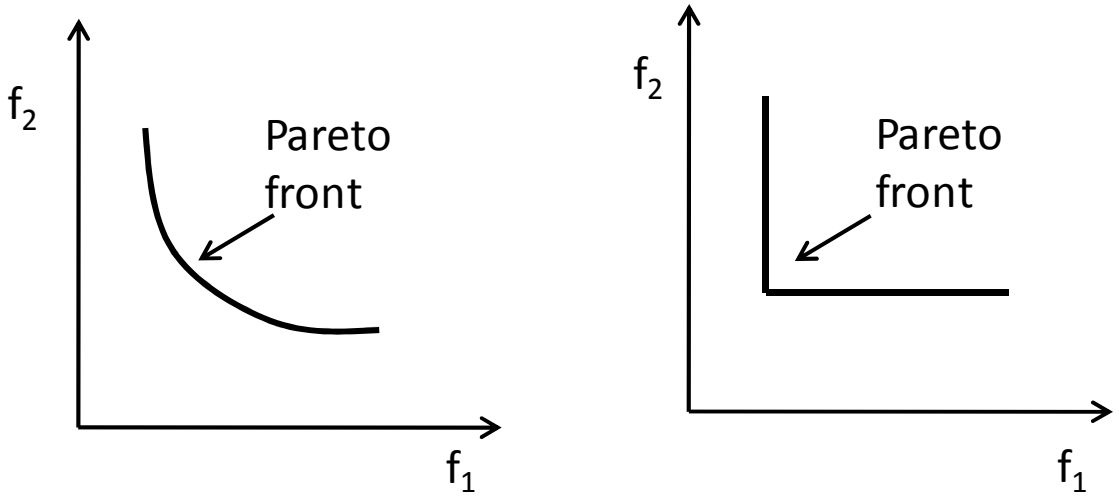

(a) (b)

Figure 5.1: (a) Classic Pareto front and (b) weakly Pareto front.

Given a Pareto front, ϕ, *i.e.* the set of optimal values in the objective space, the Nadir and Utopia points can be identified as in the two following definitions [215]:

Def: Let (F, Ω, Y) with $\Omega \subseteq R^N$ and $Y \subseteq R^M$ represents a two-objective problem, *i.e. M=2*. Then, the point $R=(R_1, R_2)$ such that:

$$R_j = \sup_{\phi} y_i, \quad j = 1,2 \tag{5.4}$$

is called Nadir point.

Whereas the definition of the Utopia point is [215]:

Def: Given *M* objectives, they are said to be in conflict if $\exists \tilde{x}_i \in \Omega$ such that:

$$f_i(\tilde{x}_i) = \inf_{x} f_i(x) \tag{5.5}$$

with $\tilde{x}_i \neq \tilde{x}_j,\ i \neq j, i, j = 1, M.$

In practice the extreme points of a Pareto front can be built using single objective optimization in two optimization steps. Given two objective functions, $f_1(x)$ and $f_2(x)$, in the first step the function $f_1(x)$ is used as the objective function and a minimum is searched, whereas the value of the second function, $f_2(x)$, is recorded. In the second step the minimized function is $f_2(x)$ whereas the value of the function $f_1(x)$ is recorded.

b. Sampling optimization process

The objectives space can be, also, investigated by means of a sampling procedure without any automated optimization procedure. This process is intuitive and can be used if the

objective functions can be expressed by means of analytical functions on the optimization variables and the number of the design variables is low enough. In this case the computation cost is, hypothetically, limited. This process is time expensive if a FEA analysis must be used to compute the value of the objective function.

The sampling method can be resumed with three steps:

- Sampling of the design variable space, $\Omega \subseteq R^N$, with a large enough number of sampling points, P, (*e.g.* P>1000). The points might be chosen using a random process with uniform distribution on the range of the variability of each design variable;
- Computation of the objective function values for each point;
- Representation of the objective function values in a chart like, for instance, the one in Figure 5.2 where each point represents the value assumed by the two objective functions (another example is in the first example of the paragraph 8.2). In this case the combinations of design variables that optimize both the objective functions can be found.

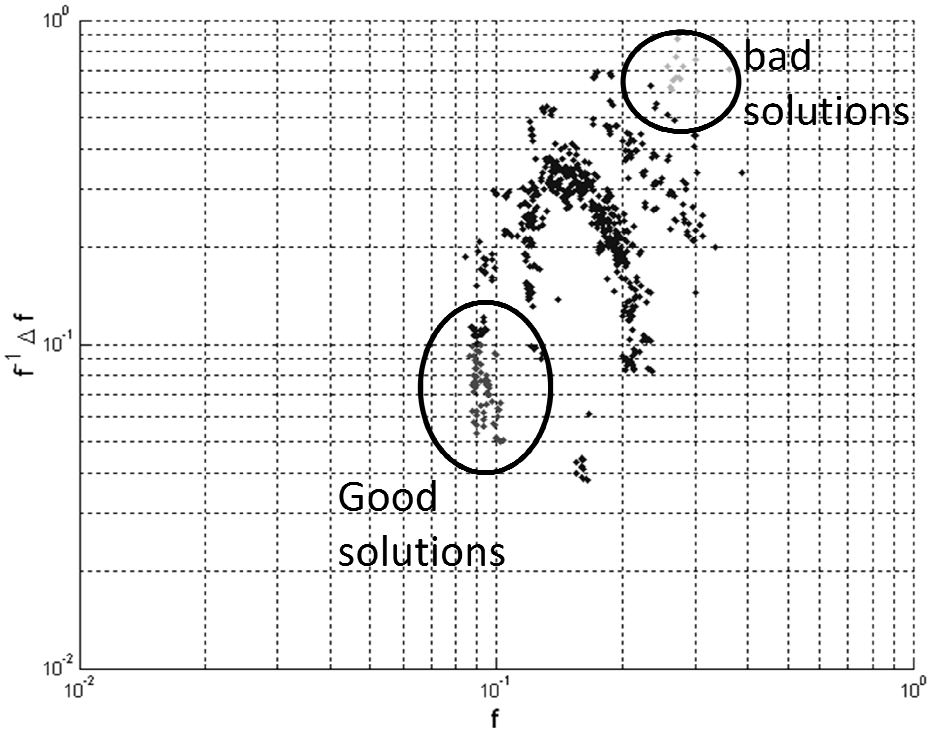

Figure 5.2: Representation of the values assumed by two objective functions, to be minimized, in a sampling optimization process.

Using the sampling optimization process the optimized solutions and the Pareto front are a consequence of the analysis of the generated data.

5.4 Optimization process

The design of electromagnetic devices by means of optimization process involves the use of almost two different computation codes that must be suitable coupled:

- A software tool that allows the analysis of the electromagnetic field (*e.g.* an analytical code or a FEA tool);
- An optimization algorithm.

Starting from a set of values of the design variables the first code computes the solution of the electromagnetic or thermal problem used in the second one in order to compute a new set of values of the design variables until an optimal point is found.

Chapter 6

6 Method for the evaluation of the human exposure to the electromagnetic fields

The exposure of human body to electromagnetic field can be evaluated by means of some rules suggested by the ICNIRP and adopted by prevention national and international committees.

6.1 Introduction

The electromagnetic field might cause harmful effects to the human health. National and international committees have studied some methods to evaluate the potential damage of the electromagnetic fields. The electromagnetic field as regard the effects evaluation can be divided into:

- Static fields;
- Single frequency sinusoidal fields;
- Multi-frequency and periodical fields;
- Pulsed fields.

In order to protect the public from risks related to electromagnetic field exposure, the ICNIRP has issued some documents in which it describes the methods to estimate the compliance of exposure to sinusoidal, pulsed, non-sinusoidal and static electromagnetic fields [1-3]. These limits refer to the fact that the electromagnetic fields might cause some adverse effects on the tissues of the human body. Until 10 MHz the most important effect is due to electric current induction, whereas an exposure to field up to 100 kHz can lead energy absorption. Therefore, effects at lower frequency can be instantaneously felt, whereas for the ones at higher frequency an average effect[21] is evaluated. In particular, some restrictions are derived by the effects of the electromagnetic field on the stimulation of nerves and muscle on tissues heating. Before 10 MHz the induced current density and above 100 kHz energy absorption are evaluated. Whereas between 100 kHz and 10 MHz both the two effects must be considered in order to evaluate the electromagnetic field exposure.

6.2 Basic on the exposure limits to electromagnetic field

The possibility of acute effects deriving from exposure to high levels of electromagnetic fields has highlighted the need to protect the public. It is worth noting that the exposure limits are different for general population and workers exposition. Particularly the general public

[21] In this last case, for instance, the effects of electromagnetic fields are evaluated computing the average on a 6 min interval.

limits, evaluated in residential and public environment, are lower than those provided for occupational exposure in working environments. In fact, the workers can be considered a population that is aware about the possible hazards deriving from the exposure to intense electromagnetic fields, while a generic population includes individuals of different ages and healthy status which are usually not informed about the possible risks related to the electromagnetic field exposure.

The exposure of electromagnetic field is evaluated in terms of some dosimetric quantities in function of the frequency at which the exposure is evaluated:

- Magnetic flux density, B [T]
- Induced current density, J [Am^{-2}]
- Magnetic field, H [Am^{-1}]
- Electric field, E [Vm^{-1}]
- Specific Absorption Rate (SAR) [Wkg^{-1}]
- Power density, S [Wm^{-2}]

The levels based on the previous quantities recommended in the ICNIRP guidelines for the limitation of the electromagnetic field exposure are given in terms of [1]:

- **Basic restrictions**: the values of some physical quantities related to electric, magnetic and electromagnetic fields based on some established health effects. The values of the threshold of the effect depend on the physical quantity that is evaluated and on the frequency of the field. Basic restriction quantities are induced current density, ***J***, and **SAR**. Generally, these quantities cannot be directly measured in a living organism in a non-invasive way.
- **Reference levels**: the levels that are provided for a practical assessment of the field exposure and that are directly correlated to the basic restrictions that generally cannot be directly measured outside the living organism. In particular, reference levels are derived from basic restrictions by the application of numerical models or by measurements. These quantities are electric and magnetic field, magnetic flux density and power density and the corresponding threshold values depend on the field frequency.

Table 6.1 reports the dosimetric quantities related to basic restrictions and reference limits and their frequency range [1].

The threshold value of the basic restrictions is derived from the appearance of certain phenomena and feelings that have been documented in literature. Appearance of some effects follows to the exposure to electromagnetic field particularly intense. For example, for Extremely Low Frequency (ELF) fields the exposure limit is given in terms of the maximum on induced current density. For instance, in this last case the threshold of excitability of the human nervous system is 100 mA/m^2 in the 4 Hz - 1 kHz frequency range. The corresponding basic restrictions allowed for general public and occupational environments can be derived dividing this limit for a suitable safety coefficient (10 for occupational and 50 for general public exposure).

In order to simplify the evaluation of the exposure level to electromagnetic fields using measurable quantities (is difficult to measure the induced current density in human body tissues directly in a non invasive way) the reference limits are derived from the basic restriction. In fact, reference limits are expressed as more practical measurable quantities. These limits are derived using suitable mathematical models [1], [3]. For instance, in a disc,

with radius R and uniform conductivity, σ, the intensity of the induced current density, J, due to a spatial uniform time-varying magnetic flux density, $\boldsymbol{B}$, normal to the disc surface, is:

$$J = \pi f R \sigma B \tag{6.1}$$

Table 6.1: Dosimetric quantities for the evaluation of the electromagnetic field exposure.

Quantity	Measurement unity	f minimum	f maximum	Limit	Remarks
B	T			Reference limits	
H	A/m			Reference limits	
E	V/m			Reference limits	
J	mA/m^2	1 Hz	10 MHz	Basic restriction	100 mA/m^2 (between 4 Hz – 1 kHz)
SAR	W/kg	100 kHz	10 GHz	Basic restriction	4 W/kg (30 min – temperature increasing 1°C)
S	W/m^2	10 GHz	300 GHz	Reference limits	10 W/m^2 residential, 50 W/m^2 occupational exposure

Moreover, in order to study the induced current density in different tissues of the human body characterized by different conductivity values, accurate models of the body and numerical methods can be used for determining the real induced currents in volumes that are characterized by different values of conductivity. It should be noted that the compliance with reference levels generally ensures the basic restrictions' respect [3] [226]; however, from the overcoming of reference levels it does not follow the overcoming of basic restrictions. In fact, the reference levels are measured from the basic restrictions given the maximum coupling of the field with the body exposed to the electromagnetic field.

The limits recommended by the ICNIRP have been adopted by the European Community in a Directive issue on 2004 [4] about the protection of workers from risks related to an intense electromagnetic fields exposure.

6.2.1. Sinusoidal field

For sinusoidal single frequency magnetic fields up to 1 MHz the ICNIRP suggests basic restrictions and reference levels as has been reported in Table 6.2 [1]. The limits values in terms of magnetic fields and magnetic flux density and basic restriction in terms of induced current density are a function of the frequency [1] [2].

6.2.2. Non-sinusoidal and pulsed electromagnetic fields

Electromagnetic fields periodic and non-sinusoidal or pulsed field have more frequency components and sometimes a continuous component superimposed. The ICNIRP guidelines provide exposure limits as a function of the frequency of the field. If the spectrum of the electromagnetic field contains more than one frequency component and each frequency component has a different value of the limit, in order to evaluate if a field complies with the limits of the exposure level the whole spectrum of the analyzed signal must be taken into account. In the case of non-sinusoidal or pulsed behavior the electromagnetic field exposure should be assessed for:

- the AC component (the limits for time-varying fields)
- the DC component (the limits for static fields)

Let consider electric equipments. The magnetic field emitted is proportional to the current that supplies the equipment. In order to evaluate the field emitted by a periodic current, the knowledge of the waveforms of the output current is needed. In this way the period, intensity, harmonics and, in the case of a pulse, the timing of rise up and drop down can be evaluated.

Table 6.2: Basic restriction and limits until 1 MHz.

frequency	**J [mA/m^2]**	**H [A/m]**	**B [μT]**
Static	--	--	$2 \cdot 10^5$
Until 1 Hz	40	$1.63 \cdot 10^5$	$2 \cdot 10^5$
1-4 Hz	$40/f$	$1.63 \cdot 10^5/f^2$	$2 \cdot 10^5/f^2$
4-8 Hz	10	$1.63 \cdot 10^5/f^2$	$2 \cdot 10^5/f^2$
8-25 Hz	10	$2 \cdot 10^4/f$	$2.5 \cdot 10^4/f$
0.025-0.82 kHz	10	$20/f$	$25/f$
0.82 - 1kHz	10	$20/f$	$25/f$
1-65 kHz	$f/100$	24.4	30.7
0.065-1 MHz	$f/100$	$1.6/f$	$2.0/f$

The effects of tissue stimulation due to induced currents (frequency up to 1 MHz) should be studied separately from the ones due to the tissues heating, typical of fields at frequencies above 100 kHz. In the standards and guidelines of ICNIRP some rules and procedures for the sum of various effects of the fields above and before 100 kHz are proposed. For instance, in the case of multi-frequency waveforms the amplitude of each frequency component is evaluated and each effect is summed like in [1].

In the case of pulsed fields the exposure can be assessed by means of some considerations on the amplitude of the peak. The corresponding limits for the induced current density in the case of a pulsed field are derived from that for the sinusoidal case by multiplying the value of the reference limits for $\sqrt{2}$. Alternatively, in the case of a rectangular pulse of the current source, an equivalent frequency of a sinusoidal signal can be evaluated and, then, the single frequency limit and basic restriction can be applied. Given a pulse with duration t_r, the equivalent frequency, f_{eq} is equal to the inverse of the twice time the pulse duration:

$$f_{eq} = \frac{1}{2t_r} \tag{6.2}$$

Regarding the compliance of the exposure to non-sinusoidal and pulsed fields the ICNIRP guidelines of 2003 [3] provide also some weight functions dependent on the limit value and its frequency. For instance, the electromagnetic field exposure can be assessed by means of the value of dB/dt that considers the biological nature of the field interactions with the tissues of the human body. The value of the time derivative of the magnetic flux density dB/dt is multiplied by an appropriate weight function. The current density is, then, tied to dB/dt using the following equation:

$$J = K_B \frac{dB}{dt} \tag{6.3}$$

where K_B = 0.064 Am^2sT^{-1} according to ICNIRP model used to compute the reference levels from the basic restrictions [3]. In particular, the reference levels for the quantity dB/dt are constant for the frequency values below 820 Hz (cut-off frequency). Below this cut-off frequency of the limit value is, respectively, 0.22 Ts^{-1} for exposure in the workplace and 0.44 Ts^{-1} in the public environments.

Then, in the case of the exposure to pulsed fields or broad-band fields (with multiple frequency components) the compliance with the limits can be evaluated using the following equation:

$$\sum_i (WF)_i \, A_i \leq 1 \tag{6.4}$$

where A_i is the amplitude of the *i-th* component for the quantity B or dB/dt and $(WF)_i$ the value of the weight function whose value is the inverse of the corresponding limit at $\{i\}$*-th* frequency. In (6.4) all the frequency components are considered and summed as in phase. This is a worst-case evaluation. However, in reality, the field components at different frequencies are not in phase, and then the restrictions provided by the (6.4) are too restrictive. The (6.4) can be modified to take into account the phase of each component:

$$\left| \sum_i (WF)_i \, A_i \cos\left(2\pi f_i t + \theta_i + \varphi_i\right) \right| \leq 1 \tag{6.5}$$

where θ_i is the phase of the *i-th* component of the A_i quantity and φ_i the phase of the weight function. The weight function phase for the dB/dt and J quantities are:

$$\begin{cases} \varphi(f) = 0 & f < f_c \\ \varphi(f) = -\dfrac{\pi}{2} & f > f_c \end{cases} \tag{6.6}$$

whereas for the magnetic flux density $\boldsymbol{B}$ are:

$$\begin{cases} \varphi(f) = \dfrac{\pi}{2} & f < f_c \\ \varphi(f) = 0 & f > f_c \end{cases} \tag{6.7}$$

6.2.3. Static fields

The ICNIRP document of the 1994 [2] provides some guidelines for limiting human exposure to static magnetic fields. This paper examines the mechanisms by which the static field interacts with the biological matter of the living organisms. In particular the three main mechanisms by which the static magnetic fields interact with tissues of living systems are:

- Magnetic induction:
    - electrodynamic interactions with moving electrolytes: static field exerts a Lorentz force on moving ionic charges and may cause the induction of electric fields and currents;
    - Faraday currents: time-varying magnetic fields induce electric currents in biological tissues. In the case of static fields the same phenomenon can be generated by the movement of the person in the area where the static magnetic field acts;
- Magnetomechanical effects:

- Magnetic orientation: in a uniform magnetic field diamagnetic or paramagnetic molecules are affected by a force that orients them in order to minimize the free energy;
- Magneto-mechanical translation: the static magnetic fields produces a force that causes a translation movement on the paramagnetic or ferromagnetic materials;

- Electronic interactions:
  - Affects the state of the electron spins.

In the case of the static magnetic field exposure limits specified in the ICNIRP guidelines are:

- 200 mT (peak value of 2T for the whole body, 5 T if the exposure is limited to the arts) for the occupational exposure;
- 40 mT in the case of general public exposure (*e.g*. residential fields).

6.3 Welding equipment example

The resistance and arc welding devices use high intensity current density in order to melt the metal pieces to be joined. Then, these equipments during the welding process might generate high intensity electromagnetic fields. In order to protect workers from risks arising from exposure to these fields, EN50505 standard for the resistance welders, and EN50444, for the arc ones, provide methods for the assessment of possible effects that could be harmful to human body [55], [56].

Let consider welding equipment, the electromagnetic field must be evaluated:

- Near the welding cable, in which the welding current flows (Figure 6.1 (a));
- Around the equipment box in which can be the transformer or the power supply devices (Figure 6.1 (b)).

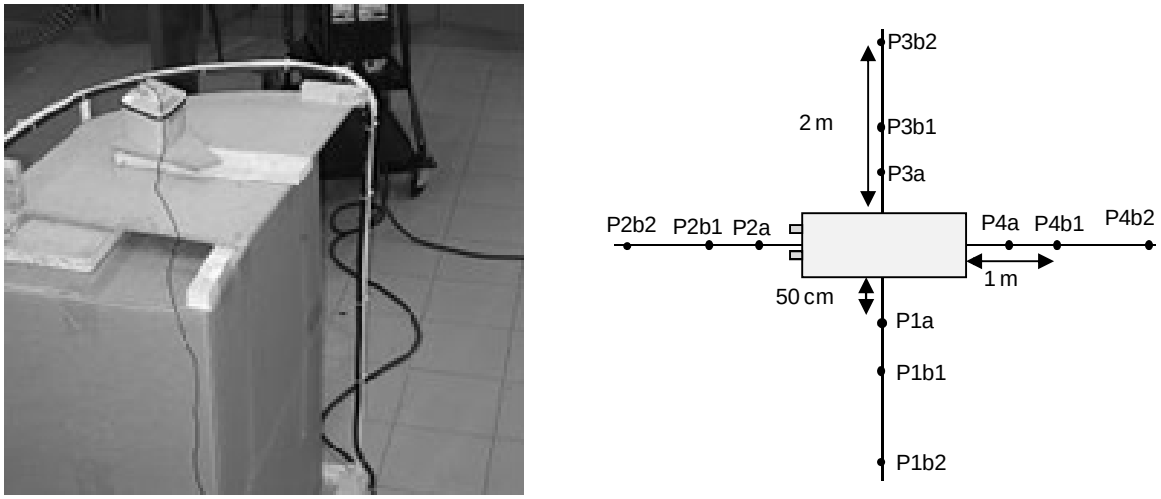

(a) (b)

Figure 6.1: Measurent set-up: (a) near the welding cable and (b) around the welding box.

The assessment of the exposure to the electromagnetic fields generated by electric devices can be evaluated by means of some computation strategies, analytical or numerical, or by means of direct measurements [36]. In the first case the two evaluation strategies,

computation and measurement, can be used because the shape of the source is known, whereas around the equipment only measurement can be used because the exact position and shape of the power transformer is not known. It should be noted that:

- the electromagnetic field around the device (cable and box equipment) is not homogeneous;
- the magnetic field is generated only if an electric current flows in the device.

In the case of welding equipments the magnetic field generated by means of the welding and supply currents may be sinusoidal or non-sinusoidal (pulsed, with more frequency components or with DC component) depending on the waveform of the welding current. In the case of non-sinusoidal waveform the harmonic content of the signal is evaluated by means of the Fourier analysis and the values of each component is compared with the corresponding single-frequency limit in Table 6.2. The considered components have the amplitude higher than 3% of the fundamental one. The frequency range in which the field components are searched is defined by the equipment generating stage (inverter, transformer, etc). Whereas in the case of non-sinusoidal magnetic fields with more than only one spectral component the relative effect on the exposure evaluated using the intensity of the magnetic flux density, *B*, magnetic field *H*, or tissues induced current, *J*, can be evaluated using the following expressions on the reference limits A_t and basic restriction J_t [1]:

$$A_t = \sum_{i=1Hz}^{f_o} \frac{A_i}{A_{L,i}} + \sum_{f_o}^{10\,MHz} \frac{A_i}{b} \tag{6.8}$$

$$J_t = \sum_{i=1Hz}^{10\,MHz} \frac{J_i}{J_{L,i}} \tag{6.9}$$

where A_i and $A_{L;i}$ are, respectively, the intensity of the magnetic field *H* or the magnetic flux density *B* and theirs limits, and J_i and $J_{L;i}$ are, respectively, the current induced in tissues by the field component and the corresponding limit evaluated for the *i-th* component. The (6.8) and (6.9) are a worst case evaluation because the phase of each component is not considered and all frequency components are added as were in phase. Let consider the phase of each component the following equation can be considered [1]:

$$A_t = \left| \sum_{i=1Hz}^{10\,MHz} \frac{A_i}{A_{L,i}} \cos\left(2\pi f_i t + \theta_i + \varphi_i\right) \right| \tag{6.10}$$

where A_i can be the intensity of the magnetic field *H*, magnetic flux density, *B*, or induced current, *J*. Previous quantity is evaluated at different time instants in a signal period (pulsed or sinusoidal). Similarly the SAR can be estimated [1]:

$$SAR_t = \sum_{i=100\,kHz}^{10\,GHz} \frac{SAR_i}{SAR_{L,i}} \tag{6.11}$$

6.4 Summary of assessment methods for time-varying fields

To assess the compliance of the electromagnetic fields generated by welding equipments with the reference limits or basic restriction the following evaluation can be made:

- Single frequency:
  - comparison of the *rms* value of the corresponding evaluated quantity with the given threshold in Table 6.2. The cases in Table 6.3 can be found;
- non-sinusoidal case:
  - computation of the frequency spectrum;
  - evaluation of the magnetic field density and induced current density in a human body model given the shape of the source and the distance between the model and the source (*e.g.* numerical computation);
  - evaluation of the conformity of each components with the corresponding limits;
  - evaluation of the exposure using equations (6.8) - (6.11). In particular the cases in Table 6.3 can be found.

Table 6.3: Rules for the exposure evaluation.

Reference values	**Basic restrictions**	**Result**
$\sum_i \frac{A_i}{A_{L,i}} < 1$	$\sum_i \frac{J_i}{J_{L,i}} < 1$	Exposure complies the limits
$\sum_i \frac{A_i}{A_{L,i}} > 1$	$\sum_i \frac{J_i}{J_{L,i}} < 1$	Exposure complies the limits
$\sum_i \frac{A_i}{A_{L,i}} > 1$	$\sum_i \frac{J_i}{J_{L,i}} > 1$	Exposure doesn’t comply the limits

Chapter 7

7 Human exposure to magnetic fields

The models introduced in the chapter 3 and computation methods in chapter 4 and 6 have been used in order to compute the induced current density in the human body tissues generated by means of a magnetic field at frequency under 100 kHz. Some examples of evaluation of the magnetic field effects rising from welding equipments and induction cooktop are reported.

Some methods can be used in order to evaluate the human exposure to magnetic field: both computation and measurements can be exploited. Some models and numerical computation methods have been proposed in order to solve some practical cases. A human body model discretized by tetrahedral elements has been developed as reported in chapter 3 in order to use the Finite Element Analysis to solve the electromagnetic problem. The numerical computation of induced current density is important in cases where the magnetic flux density overcomes prescribed limits. In fact it can arrive that the corresponding induced current density might respect them. Then, both magnetic flux density and induced current density must be evaluated. The magnetic flux density can be estimated by means of measurements or analytical methods, whereas the induced current density can be only computed by means of numerical ones. Since in some practical cases the current that supplies the device can be so high that the magnetic flux density overcomes limits, the induced current density must be evaluated in order to decide if equipment satisfies field limits suggested by standards.

The induced current density has been evaluated in a cylindrical model or in a realistic human body model. An example of those models is in chapter 3 and in Figure 7.1 and Figure 7.4. The human model has been built from real CT data, as in chapter 3, segmenting each slice in order to distinguish the different organs and tissues of the body and discretizing them with a tetrahedral mesh. Each volume has the electrical characteristics of the corresponding organ. Simplified models as disc or cylinders with uniform electrical characteristics have been used in order to evaluate the induced current density in a simplified way. In practice, given the source and its position with respect the human body model the human exposure to electromagnetic field can be analyzed.

In some cases for simplified models, like cylindrical ones, some coefficients can be evaluated in order to evaluate the exposure from the value of the current intensity and its frequency. In this case a practical solution for the exposure evaluation is proposed.

7.1 Welding equipments

A welding equipment is a device that, during the welding process, generates high intensity current in order to melt and join two metal pieces between themselves or by means of a soldering wire.

Welding equipments can be divided, on the basis of the welding wave current, into:

- Arc device: the current waveform is continuous. A DC component can be superimposed (DC welding device) or not (AC devices);
- Resistance device: the welding current is formed by means of pulses of a time-varying waveform;
- Spot device: device with a single spot event with high intensity peak.

A welding device is composed by the welding cable that carries the welding current, the welding head (a single electrode device or a clamp) and a transformer in order to drop down the voltage and increasing the current flowing in the welding section.

In the welding cable the welding current can have high intensity and generate not negligible magnetic fields, whereas the transformer is the device supplied by the power line, then, a 50 Hz magnetic field component is always present.

7.1.1. Models for welding equipments

As the maximum frequency is lower than 100 kHz, the magnetic flux density and the induced current density have been computed solving the electromagnetic (EM) problem in quasi-static condition [200],[208],[227],[228]. The models of the conductive media, where the induced current density is evaluated, are sketched in Figure 7.1: a human body model with heterogeneous electrical conductivity and a homogeneous cylinder are used with a current source suitably positioned.

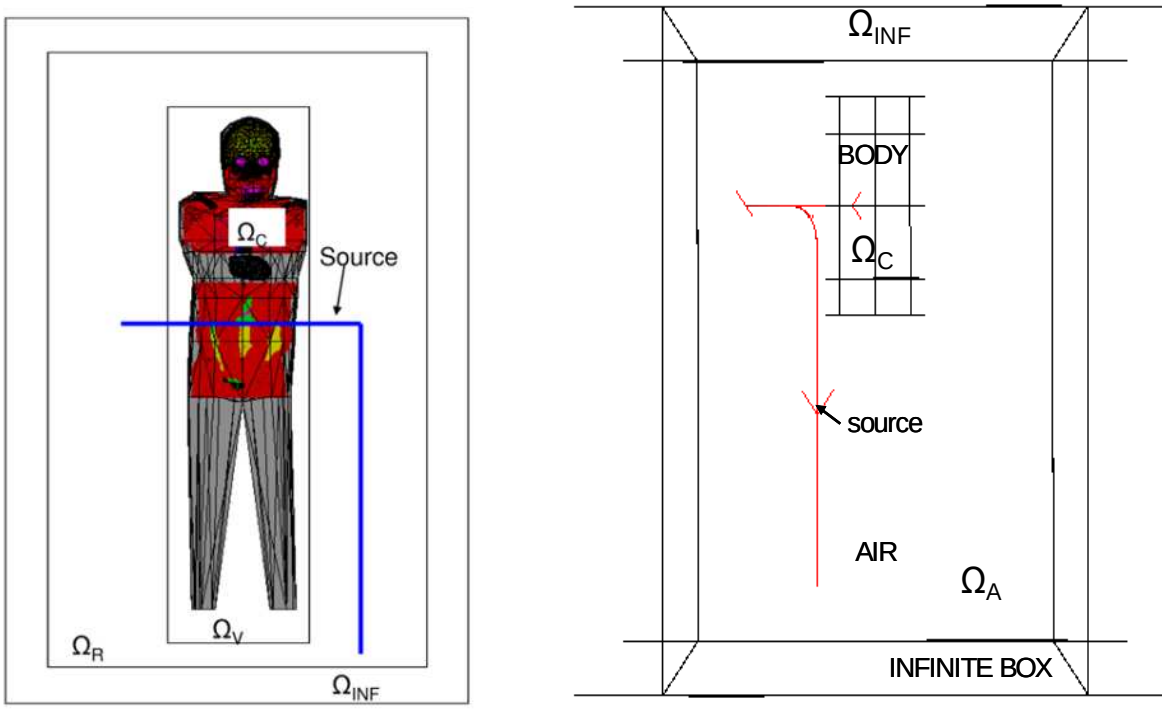

(a) (b)

Figure 7.1: (a) Human body and (b) cylindrical model model used in the evaluation of the exposure to electromagnetic field generated by welding equipments.

7.1.2. Formulation for FEM models: magnetic vector potential

Let consider the human body model in Figure 7.1 (a) and an eddy current problem. The magnetic field source is a wire in which a current density flows. As the maximum frequency is lower than 100 kHz, the magnetic flux density and the induced current density can be computed solving an electromagnetic (EM) problem in quasi-static condition. The simulated domain is sketched in Figure 7.1 (a) and it includes a conductive region (Ω_C), two vacuum

regions (Ω_V and Ω_R) one of them containing the magnetic field source (Ω_R) and an infinite region, Ω_{INF}.

In the conductive region, Ω_C, the electric field $\boldsymbol{E}$ is computed in terms of time-harmonic magnetic vector potential, $\boldsymbol{A}$, and scalar electric potential, V, components solving the equation (4.31) and using (4.14) in terms of phasors:

$$\boldsymbol{E} = -(j\omega\boldsymbol{A} + \nabla V) \tag{7.1}$$

then, the eddy currents in the electric conductive region, Ω_C, are derived substituting (7.1) on the (4.10):

$$\boldsymbol{J} = \sigma\boldsymbol{E} = -\sigma(j\omega\boldsymbol{A} + \nabla V) \tag{7.2}$$

where $\boldsymbol{E}$ is the phasor of the electric field, $\boldsymbol{A}$ the phasor of vector potential, V the phasor of the scalar electric potential and ω the angular frequency.

The source of the magnetic field is a wire supplied by an electric current. The evaluation of the magnetic field in the vacuum volume, Ω_R, the one that contains the source, is solved in the reduced scalar potential, ϕ_{RED} using the (4.39) and (4.40):

$$\boldsymbol{H} = \boldsymbol{H_S} - \nabla\phi_{RED} \tag{7.3}$$

where $\boldsymbol{H}$ is the term due to the current source, $\boldsymbol{J}$, computed by means of Biot-Savart formula, (4.39). Between Ω_C and Ω_R a region Ω_V has been interposed. In this region the EM problem is solved only in terms of the magnetic vector potential $\boldsymbol{A}$. This part of the domain has been modeled to surround the conductive region where the EM problem is solved in terms of $\boldsymbol{A}$ and V potentials in order to properly describe interface conditions between conducting and not-conducting regions. At the boundary between Ω_V and Ω_R proper interface conditions have been posed. In the conductive medium and vacuum region the Helmholtz equation can be solved:

$$\nabla^2\boldsymbol{A} + \mathrm{k}^2\boldsymbol{A} = -\mu\boldsymbol{J_S}, \quad k^2 = -j\omega\mu\sigma \tag{7.4}$$

where μ and σ are respectively the magnetic permeability and the conductivity of the medium and the Lorentz gauge has been imposed. In particular in the Ω_V region the value of $\boldsymbol{J_s}$ and k^2 in (7.4) are null because the region is not conductive, whereas in the Ω_C region $\boldsymbol{J_s} = \sigma\boldsymbol{E_c}$, $\boldsymbol{E_c}$ conservative component of the electric field $\boldsymbol{E}$. At last, at the boundary of the simulation domain, in the region Ω_{INF}, infinite boundary conditions have been posed in order to let the magnetic field vanishing at infinite distance.

a. Formulation for FEM models: total magnetic scalar potential

The volumes of the cylindrical model, Figure 7.1 (b), have been simulated solving Maxwell equations under suitable boundary conditions. In the conductive volume, Ω_C, the electromagnetic (EM) problem has been solved in terms of the electric vector potential, $\boldsymbol{T}$, and the total magnetic scalar potential, Φ, by means of:

$$\boldsymbol{H} = \boldsymbol{T} - \nabla\Phi \tag{7.5}$$

In this volume region the induced current density $\boldsymbol{J}$ is derived from (7.5) by means of:

$$\boldsymbol{J} = \nabla \times \boldsymbol{H} = \nabla \times \boldsymbol{T} \tag{7.6}$$

The magnetic field source has been modeled as an electric current using analytical Biot-Savart law and in the air volume, Ω_A region in Figure 7.1 (b), the electromagnetic problem has been solved in terms of the reduced scalar potential formulation, ϕ_{RED}, by means of:

$$\boldsymbol{H} = \boldsymbol{H_S} - \nabla\phi_{RED} \tag{7.7}$$

where $\boldsymbol{H_s}$ is the term due to the current source, $\boldsymbol{J_s}$, computed by means of Biot-Savart formula (4.39) and in which the reduced scalar potential, ϕ_{RED}, fulfils the Poisson equation:

$$\nabla \cdot \mu_0 \nabla \phi_{RED} = \nabla \cdot \mu H_S \tag{7.8}$$

At the boundary of the simulation domain, Ω_{INF}, infinite boundary conditions have been posed in order to let the magnetic field vanishing at infinite distance.

7.2 Induction cooktop

The induction cooktop is an electric household that allows cooking the food by electromagnetic field. The most important elements of this device are (Figure 7.2):

- The inductor with a planar shape;
- The pot in which the heat is produced by means of the induction of a current density inside the metal;
- The generator.

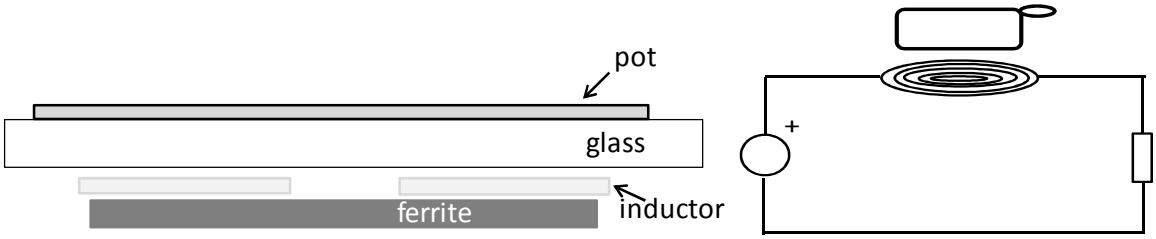

Figure 7.2: (a) Model of the inductor and (b) simplified supply circuit.

7.2.1. Models for induction cooktop equipments

The electromagnetic field exposure evaluation is developed considering the actual cooking appliance sketched in Figure 7.3 [229]. The magnetic field source is composed by means of the inductor winding, where an electric current is imposed, the pot (modelled only with its ferromagnetic layer) and the ferrite layer under the inductor. The geometry of the model, which simulates an average human body, used in the electromagnetic field exposure analysis is a homogeneous cylinder with a radius of 150 mm and a height of 600 mm positioned at a distance *D* from the inductor, with *D* equals to 300 mm, 100 mm and 50 mm. The electrical characteristics of the materials considered in the computations are in Table 7.1, where the equivalent average resistivity of the phantom is assumed equal to 5 Ωm according to [230]. The electromagnetic problem, involving the computation of the magnetic flux density and the corresponding induced current density in the cylinder, is solved using Finite Element method [227].

In the FEM approach the domain is divided in different regions (*see* Figure 7.4): Ω_C is the cylindrical phantom, where the magnetic flux density and induced current density are computed, Ω_S is the current source that generates the magnetic field, Ω_P is the pot region where the eddy currents are induced to heat the pot bottom, Ω_F is the ferrite layer. The regions Ω_P, Ω_F, Ω_S are surrounded by an air box region, Ω_B, used to couple different field formulations, which in turn is inserted in the Ω_A and Ω_{INF}, air box and infinite, regions.

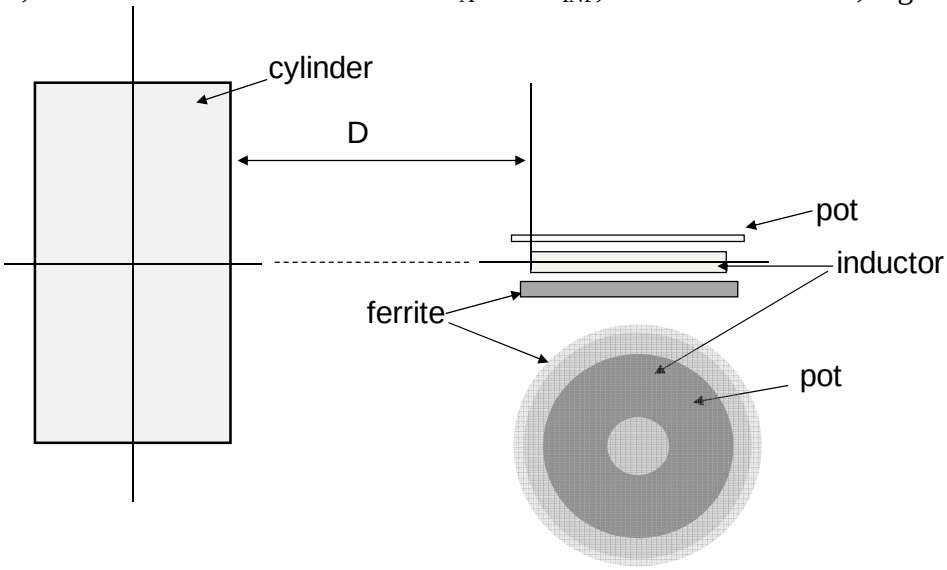

Figure 7.3: Induction cooktop system geometry.

Table 7.1: Electrical characteristics of the materials.

Material	Resistivity [Ωm]	Initial relative magnetic permeability	Flux density saturation [T]
Pot	$60 \cdot 10^{-8}$	1100	1.8
Cylinder	5 (f < 100kHz)	1	--
Ferrite	--	2500	--

The magnetic field source is modelled by means of analytical Biot-Savart formula (4.39), which derives the magnetic field $\boldsymbol{H_S}$ from the source current density $\boldsymbol{J_S}$ in the Ω_S region. The pot region, Ω_P, is handled by means of impedance surface conditions [231] and the induced currents are derived. In the ferrite region, Ω_F, the total scalar potential Φ is computed by means of:

$$\nabla \cdot \nabla \Phi = 0 \tag{7.9}$$

where μ is the magnetic permeability of the medium. The magnetic field $\boldsymbol{H}$ is derived by means of the total scalar potential, Φ, as:

$$\boldsymbol{H} = -\nabla \Phi \tag{7.10}$$

In the air region, Ω_B, that surrounds pot, ferrite and source regions, the Poisson equation is solved in order to compute the reduced scalar potential, ϕ_{RED}:

$$\nabla \cdot \mu \nabla \phi_{\mathrm{RED}} = \nabla \cdot \mu \boldsymbol{H_S} \tag{7.11}$$

so that the contribution of the magnetic field source is derived by means of the reduced scalar potential, ϕ_{RED} by means of the (7.7).

In the cylindrical phantom Ω_C the electromagnetic problem is solved in terms of the magnetic vector potential $\boldsymbol{A}$ and an electric scalar potential, V. In the conductive medium, Ω_C, the magnetic vector potential $\boldsymbol{A}$ is obtained solving the non-homogeneous Helmholtz equation in terms of phasors:

$$\nabla^2 \boldsymbol{A} + \mathrm{k}^2 \boldsymbol{A} = -\mu \boldsymbol{J_S}, \quad k^2 = -j\omega\mu\sigma \tag{7.12}$$

where σ is the conductivity of the medium. The electric scalar potential, V, is derived imposing the Lorentz gauge on the divergence of the magnetic vector potential $\boldsymbol{A}$ [203]. From the magnetic vector potential $\boldsymbol{A}$ and the electric scalar potential V the electric field $\boldsymbol{E}$ is computed and the induced current density $\boldsymbol{J}$ is obtained using (7.8) [209].

In the air volume (Ω_A) the Helmholtz equation (7.12) is solved assuming k^2 and $\boldsymbol{J_S}$ null, whereas in the Ω_{INF} region around the air volume (Ω_A), vanishing conditions are imposed.

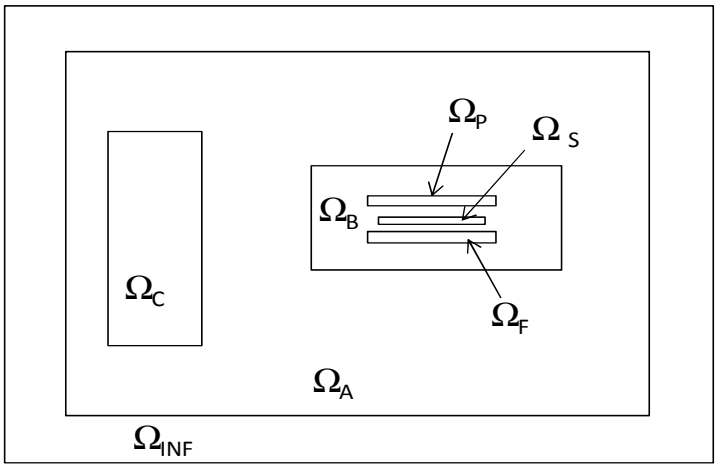

Figure 7.4: Regions of the domain for the FEM analysis. Induction cooktop.

7.3 Analysis of the results for welding equipments

The magnetic flux density and induced current density have been computed in suitable human body models with homogeneous and not–homogeneous electrical conductivity in order to verify the exposure level to low frequency magnetic field. Examples for arc and resistance welding equipments have been analyzed. For arc equipments measurements of the magnetic flux density have been compared with computation results.

7.3.1. Arc welding equipment

The magnetic field emitted by welding equipments is characterized by a time variable waveform. Consequently its frequency spectrum is characterized by the presence of a lot of harmonics superimposed to the fundamental. The magnetic field spectrum can be determined from the one of the welding current. All the tests follow a procedure suggested by standards [55] and for each test the current waveform has been measured using an oscilloscope Tektronix 3032B[22] and a suitable current probe, PAC 11 Chauvin Arnoux[23]. The frequency content has been derived from the current waveform using the Fast Fourier Transform (FFT) mathematical tool of the oscilloscope because the considered media in which the magnetic field is induced are linear with relative magnetic permeability equal to 1.

For instance the examined arc welding equipment has periodical time-varying with a DC

[22] http://www.tek.com/ (last access January 2011)
[23] http://www.chauvin-arnoux.com/ (last access January 2011)

component current waveform that contains eight harmonics as shown in Figure 7.5.

Simulations of the magnetic flux density and induced current density have been performed using the software Flux3D, a commercial Finite Element Method tool for electromagnetic problems[24]. The magnetic flux density has been measured using suitable probes[25] [232-234].

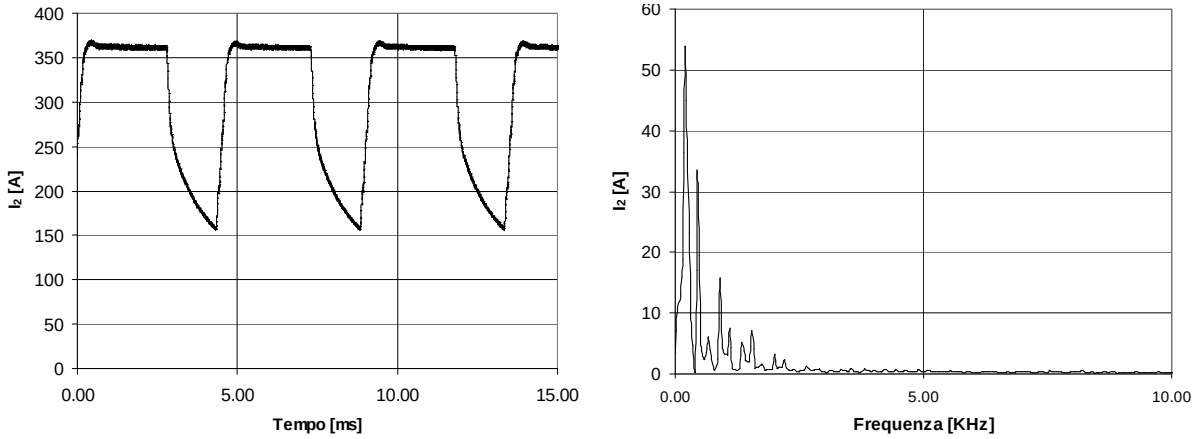

(a) (b)

Figure 7.5: (a) Periodical current waveform as a function of the time and (b) corresponding Fast Fourier spectrum for an arc welding equipment.

Table 7.2: Magnetic flux density and induced current density for different frequencies.

f [Hz]	I [Arms]	B [μT]	B_L [μT]	B/B_L	J [mA/m^2]	J_L [mA/m^2]	J/J_L
DC	335	418.7	2.00E+05	2.09E-03			
200	53.7	66.61	125.00	0.53	1.06	10.00	0.11
450	33.5	41.55	55.56	0.75	1.49	10.00	0.15
650	6.0	7.48	38.46	0.19	0.39	10.00	0.04
900	15.8	19.64	30.70	0.64	1.41	10.00	0.14
1100	7.6	9.41	30.70	0.31	0.82	11.00	0.07
1350	5.2	6.47	30.70	0.21	0.70	13.50	0.05
1550	7.2	8.90	30.70	0.29	1.10	15.50	0.07
2000	1.6	4.07	30.70	0.13	0.65	20.00	0.03
2200	3.3	2.94	30.70	0.10	0.51	22.00	0.02
Σ				3.15			0.69

In Table 7.2, frequency values and current amplitude of each harmonic and simulation results for all frequencies of the spectrum of the welding current waveform of the tested arc welding equipment have been reported. The last row reports the value of the formulae (6.8) and (6.9) evaluated for the magnetic flux density and the induced current density. In this case the magnetic flux density shows that the magnetic field limits are overcome whereas the ones for the induced current density are respected [228]. Then the equipment is compliant with the prescribed ICNIRP limits (*see* Table 6.3).

In Figure 7.6 the maximum of the magnetic flux density and the induced current density (bars) computed in the cylindrical model are reported for each frequency and compared with their limit values (solid line). Simulation results obtained with the cylindrical and human body

[24] http://www.cedrat.com/ (last access January 2011)
[25] http://www.pmm.it/narda/default_en.asp (last access January 2011)

model have been compared in Table 7.3. In this table data of magnetic flux density and the corresponding induced current density evaluated at the fundamental frequency, 200 Hz, have been reported for some tissues of the human body model. The electrical characteristics of biological tissues at 200 Hz are in Table 3.4.

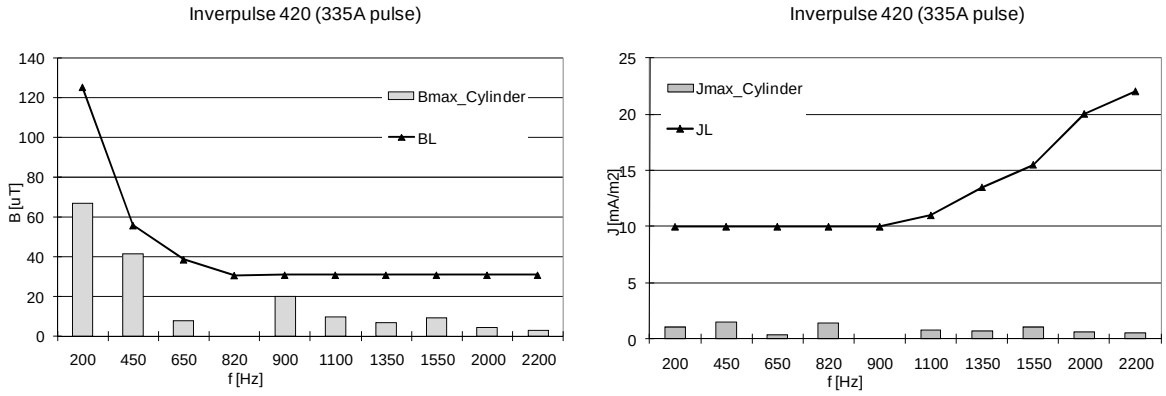

(a) (b)

Figure 7.6: Comparison between FEM computed magnetic flux density and induced current density at each frequency spectrum with the corresponding limit.

Table 7.3:Magnetic flux density and induced current density at fundamental frequency for some tissues and cylinder model. *f*, frequency, *B* and B_L magnetic flux density and its limit, *J* and J_L current density and its limit.

Tissue	**f [Hz]**	**B [μT]**	**B_L [μT]**	**B/B_L**	**J [mA/m^2]**	**J_L [mA/m^2]**	**J/J_L**
liver	200	47.52	125	0.38	0.33	10	0.033
heart	200	37.9	125.0	0.30	0.4	10	0.04
intestine	200	62.4	125.0	0.50	3.88	10	0.39
colon	200	55.0	125.0	0.44	1.43	10	0.14
bone	200	50.3	125.0	0.40	0.4	10	0.04
pancreas	200	44.2	125.0	0.35	0.9	10	0.09
kidney	200	42.6	125.0	0.34	0.2	10	0.02
stomach	200	45.9	125.0	0.37	1.4	10	0.14
lung	200	43.7	125.0	0.35	0.3	10	0.03
muscle	200	64.0	125.0	0.51	3.0	10	0.30
spleen	200	46.7	125.0	0.37	0.4	10	0.04
cerebellum	200	12.39	125.0	0.10	0.19	10	0.02
brain	200	11.61	125.0	0.09	0.08	10	0.01
cylinder	**200**	**66.61**	**125.0**	**0.53**	**1.06**	**10**	**0.11**

For some tissues the induced current, *J*, is lower than the one evaluated by means of the cylindrical model, whereas for some other *J* is higher. These results are coherent with the ones obtained by other research groups [226], [235]. Then the simplified cylindrical model can be a good compromise to reduce the computation time in order to analyze the magnetic field emission of welding equipment.

Measurements (average values) of the magnetic flux density, with both the set-up shown in Figure 7.7, $B_{mean,A}$ and $B_{mean,B}$, at the fundamental frequency for a set of welding machines are reported on Table 7.4 and compared with limits. For the set-up B the maximum of the simulated magnetic flux density, $B_{sim,B}$, in the cylindrical model has been also reported. In Table 7.4 the limit, B_L, the amplitude and frequency of the fundamental of the current, *Idc* and *f*, are reported. The measurement result for the set-up B, $B_{mean,B}$, is lower than the one for the set-up A, $B_{mean,A}$, because in the former case the probe is more distant from the cable. Data in Table 7.4 show that the magnetic flux density measured can overcome the ICNIRP limits [1],

whereas the maximum of the simulated value is lower than the limit. As it is pointed out in ICNIRP guidelines the induced current density in human tissues can satisfy limits even if the magnetic flux density exceeds them.

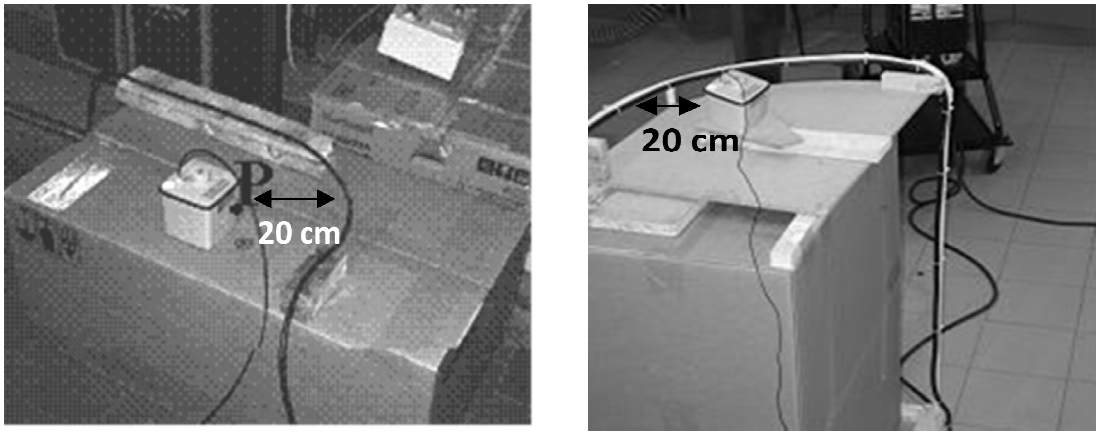

(a) (b)

Figure 7.7: Measurements set-up: (a) suggested by standards and (b) the one used to compare measurements and computation results.

Table 7.4: Measurement and simulation results. *f*, frequency, Idc, amplitude of the DC component of the current, If, amplitude of the AC fundamental component of the current, B_L magnetic flux density limit, $B_{mean,A}$ and $B_{mean,B}$ magnetic flux density measured in the geometry A and B, $B_{sim,B}$ magnetic flux density simulated for the geometry B.

Equipment	**Idc [A]**	**f [Hz]**	**If [A]**	**$B_{mean,A}$ [μT]**	**$B_{mean,B}$ [μT]**	**$B_{sim,B}$ [μT]**	**B_L[μT]**
Weld 2 - A	550	300	8.23	10.5	7.9		83.3
Weld 3 – A	350	150	37.8	50	44.85	46.9	167
Weld 3 - C	225	200	53.7	187.5	166	106.4	125

7.3.2. Resistance welding equipment

In order to evaluate the current density induced by means of a magnetic field produced by a resistance welding equipment both simplified cylindrical and human body model have been simulated.

In the human body model simulations using two magnetic field sources, GA and GB as shown in Figure 7.8, have been performed, whereas for the simulations with the cylindrical model only the GA source position has been considered. In both simplified and human body models a current of 6938 Arms at 50 Hz flows in the source.

For each organs of human body the maximum values of the magnetic flux density and the induced current density have been derived from simulation results. These maximum values have been compared with corresponding magnetic flux density and induced current density limits at 50 Hz. At this frequency the corresponding limits are 500 μT and 10 mA/m^2, respectively. Figure 7.9 reports the colored map of induced current density in the human body tissues for the geometry GA.

In Table 7.5 the value of the equations (6.8) and (6.9), named ratio α, has been reported for some human organs for both the geometries GA and GB. The ratio α has been computed for magnetic flux density, $\alpha(B)$, and for the induced current density, $\alpha(J)$, values.

Obtained results with human body model and geometry GA have been compared with the ones of the cylindrical model (last bottom row in Table 7.5). It is pointed out that the cylindrical model is proposed by Standards [56] for the evaluation of the exposure to

magnetic field generated by welding equipments. From data in Table 7.5 it can be pointed out that the more accurate model might show a worse exposure in term of induced current density than the one of the cylindrical model. This fact is reasonable because the resistivity of some tissues is lower than the one used in the cylinder [235]. For instance in [226] a comparison between homogeneous and heterogeneous models has been performed. The homogeneous models might give lower induced current densities than heterogeneous ones.

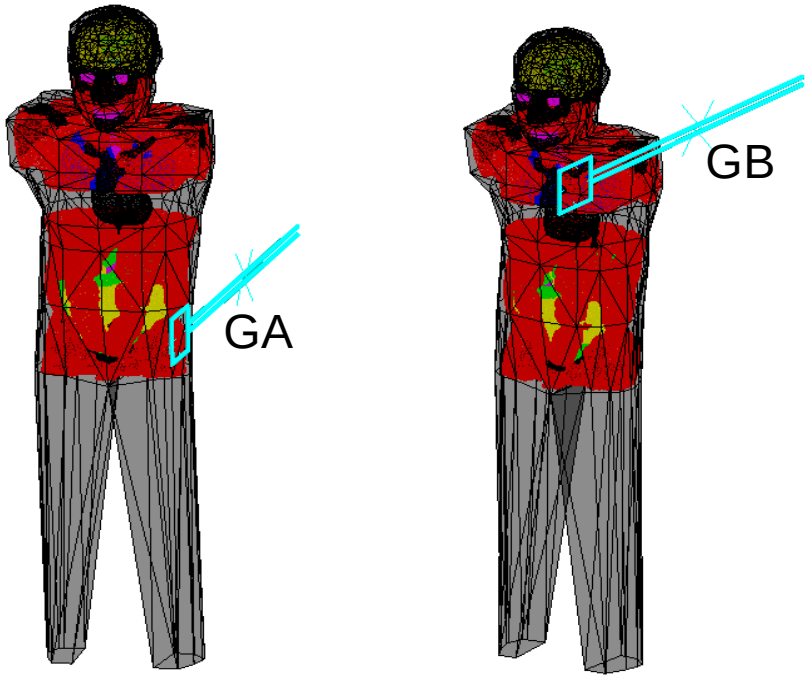

(a) (b)

Figure 7.8: Human model geometry. GA and GB are the sources of the magnetic field that have the geometry of the source in the cylindrical model.

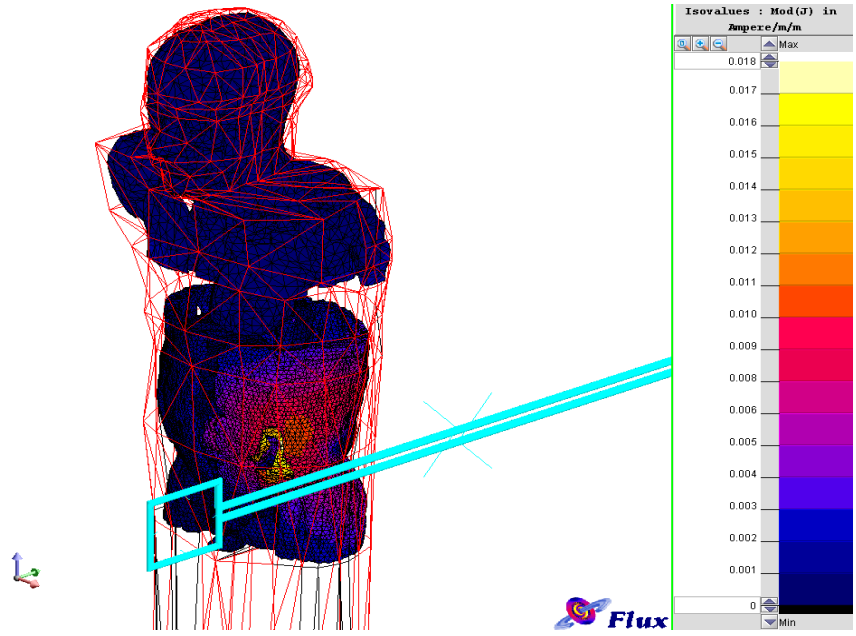

Figure 7.9: Induced current density in human body model.

In Table 7.5 the exposure level has been evaluated using (6.8) and (6.9) for the magnetic flux density, $\alpha(B)$, and compared with the one evaluated from induced current density, $\alpha(J)$.

The evaluation of the exposure on the basis of the magnetic flux density can be worst with respect to the one evaluated from the induced current density.

Considering data in Table 7.5 the two numerical simulation strategies with the human body model (GA and GB) lead to different results in terms of satisfaction of exposure limits because the source is placed in different positions and consequently organs and tissues near the source are different.

With the source in the position GA, induced current density in each tissue computed with the human model is lower than the ones computed using the homogeneous cylindrical model, whereas using the cable configuration GB, the human model provides in some tissues (*e.g.* muscle) a higher induced current density than the homogeneous cylindrical model.

The more complex model gives more accurate information than the simplified homogeneous one. A lower induced current density in some tissues with respect to the one computed in the simplified model is due to their relative position from the source, their real dimension and their own resistivity.

Table 7.5: Simulation results for human body and cylinder models.

	GA		**GB**	
Tissue	**α (B)**	**α (J)**	**α (B)**	**α (B)**
Gall	0.44	0.18	0.14	0.18
Liver	0.78	0.03	0.26	0.02
Heart	0.64	0.06	0.66	0.03
Intestine	5.3	1.22	0.2	0.09
Colon	3.37	0.13	0.26	0.02
Bone	2.68	0.05	33.38	0.18
Pancreas	1.37	0.34	0.25	0.07
Kidney	2.2	0.1	0.24	0.03
Bladder	0.58	0.09	0.08	0.02
Stomach	1.32	0.45	0.3	0.09
Lung	0.48	0.04	2.09	0.09
Muscle	7.29	0.73	27.75	1.8
Spleen	3.37	0.2	0.33	0.04
Marrow	0.87	0.03	1.11	0.03
Cartilage	0.05	0.02	1.31	0.12
Tongue	0.09	0.04	1.45	0.32
Eye	0.04	0.05	1.01	0.56
CerebellarFluid	0.06	0.07	0.63	0.56
BrainStem	0.09	0.01	1.02	0.1
Cerebellum	0.08	0.02	1.19	0.19
Brain	0.07	0.01	1.17	0.08
Trachea	0.28	0.04	1.05	0.21
Fat	9.37	0.87	95.85	2.51
Cylinder	49.3	1.97	47.4	1.5

7.3.3. Arc welding: coefficients for the model extension

In the analysis of the electromagnetic field generated by an arc welding equipment the magnetic field source is a cable with a normalized form and position like the one shown in Figure 7.1 (b) for all welding equipments analyzed. The magnetic flux density and current density are evaluated in a homogeneous cylindrical model. Since the relative magnetic

permeability is unitary the problem is linear and a proportionality coefficient can be found between magnetic flux density and the current flowing in the magnetic field source. Given the intensity of the current in the source, *I*, the intensity of the magnetic flux density in the homogeneous cylinder is done by means of a function, f_I, multiplied by the current intensity:

$$B(x,y,z) = f_I(x,y,z) \cdot I \tag{7.13}$$

The current density in equation (6.1) depends on the frequency and the spatial value of the magnetic flux density *B(x,y,z)*:

$$J(x,y,z) = \pi f R \sigma B(x,y,z) \tag{7.14}$$

and introducing the (7.13) the induced current density depends on the frequency and the current in the magnetic field source by means of two new coefficients f_2 and f_2'

$$J(x,y,z) = \pi f R \sigma f_I(x,y,z) \cdot I = f_2(x,y,z) \cdot f \cdot I = f_2'(x,y,z) \cdot f \cdot \sigma \cdot I \tag{7.15}$$

Since the problem is linear and the magnetic flux density in the considered volume is not homogeneous the (7.13) and (7.14) can be written for their maximum value in the cylindrical model.

Given the coefficients, f_I, f_2 the current source frequency, *f*, and its intensity *I*, the maximum value of the magnetic flux density and current density in the cylindrical model can be computed using the (7.13) and (7.15). In some case also the variability with the frequency of the tissues conductivity can be introduced on the (7.15). Then, given the maximum values of the magnetic flux density *B* and induced current density *J* in the cylinder model the coefficients f_I, f_2 and f_2' can be derived from the following relations:

$$f_I = \frac{B_{max}}{I} \tag{7.16}$$

$$f_2 = \pi f R \sigma = \frac{J_{max}}{I \cdot f} \tag{7.17}$$

$$f_2' = \pi f R = \frac{J_{max}}{\sigma I \cdot f} \tag{7.18}$$

The coefficients f_I, f_2 and f_2'computed in the cylindrical model for different welding equipment models are reported in Table 7.6. In the last raw of the table the variability, computed on all the coefficient values, is reported. The f_I coefficient in the DC case has been also evaluated.

Table 7.6: Coefficient for the cylindrical model extension on the evaluation of the magnetic field by means of an homogeneous cylinder.

		f_I	f_2	f_2'
	DC	1.29	--	--
Model A	**AC**	1.24	9.88E-05	4.94E-04
Model B	**AC**	1.24	9.87E-05	4.94E-04
Model C	**AC**	1.24	9.87E-05	4.94E-04
Model D	**AC**	1.24	9.86E-05	4.93E-04
	variability	4.55E-03	1.40E-06	6.98E-06

Similarly coefficients can be computed for disc and ellipsoid models[26]. Using the previous coefficients, given the frequency and amplitude of the current component of the welding current, and eventually the tissue conductivity[27], the corresponding magnetic flux density and induced current density can be computed without using a new FEM model.

7.4 Analysis of the results for induction cooktop devices

The magnetic flux density and induced current density due to the magnetic field generated by an induction cooktop device can be evaluated in the cylindrical model that simulates the human body characteristics by means of numerical techniques. The starting point of the analysis is the measurement of the time evolution of the electric current flowing in the coil. For instance, the frequency spectrum in Figure 7.10, given by a Fourier Transform[28], shows that the highest components, for which the simulations have been performed, are found for the frequencies 26.6 kHz and 79.6 kHz (*rms* value: 24.7 A_{rms} and 2.1 A_{rms} respectively).

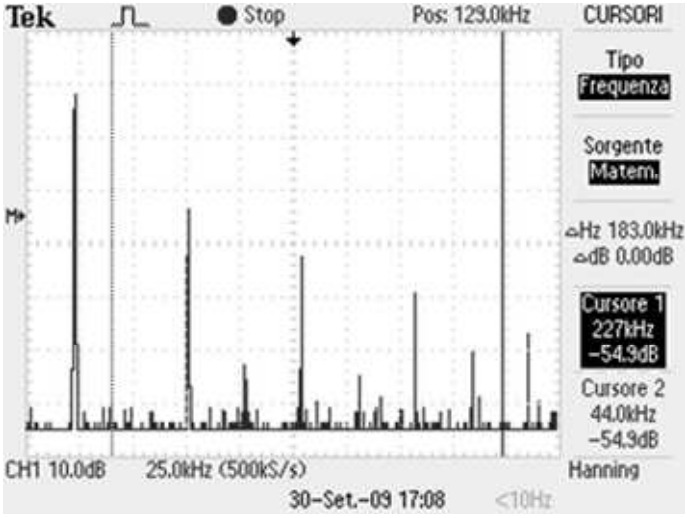

Figure 7.10: Frequency spectrum of the current flowing in the inductor (peaks amplitude in logaritmic scale).

At the considered frequencies, for the exposure of the general public, ICNIRP provides a reference level equal to 6.25 μT, while the basic restrictions are 53.2 mA/m^2 and 159.2 mA/m^2 respectively.

The computations have been carried out for the following configurations:

- Without the pot and without the ferrite layer
- Without the pot but with the ferrite layer
- With the pot and the ferrite layer

The positions of the paths along which the magnetic flux density is sampled are sketched in Figure 7.11 (a) and (b); obviously, the current density is evaluated only for the line shown in Figure 7.11 (b). The sampling line in Figure 7.11 (b) corresponds to the diameter of the cylinder located at middle height and directed towards the cook-top. In this position both the flux density and the induced current density are expected to reach the highest values.

[26] For a disc in DC case f_1,=1.25 and in AC case f_1,=1.23, f_2 = 1,09E-04 and f_2'= 5.45E-04, for an ellipsoid in AC case f_1,=1.24, f_2 = 9.74E-05 and f_2'= 4.87E-04.

[27] In the homogeneous cylinder the tissue conductivity varies for frequency above 100 kHz.

[28] Measured by means of an oscilloscope Tektronix TDS 2024B.

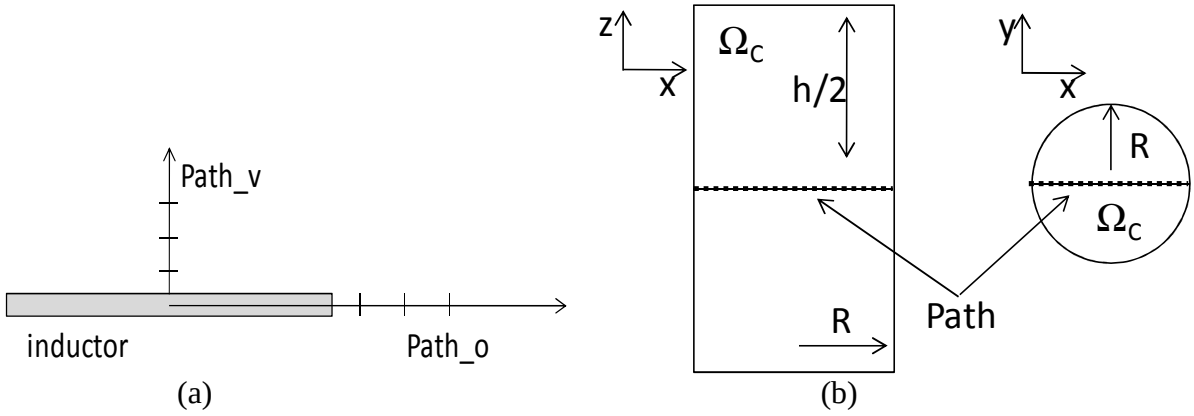

(a) (b)

Figure 7.11: Computational paths: (a) near the inductor; (b) in the cylinder.

Table 7.7 reports the magnetic flux density computed in presence of the only inductor. The considered points, at a distance *d* from the inductor centre, are along Path_v and Path_o (*see* Figure 7.11 (a)) respectively.

Table 7.7: Magnetic flux density generated by the inductor at a distance *d* along the paths indicated in Figure 7.11 (a) (I = 24.7 A, f = 26.6 kHz).

Path_v		**Path_o**	
***d* [mm]**	**B_{FEM} [mT]**	***d* [mm]**	**B_{FEM} [μT]**
40	2.97	303	22.2
50	2.25	404	9.01
100	0.67	505	4.56

The magnetic flux density and induced current density in the cylinder has been evaluated for two different configurations, with and without the pot, for three different distances between the cylinder and the inductor (distance *D* in Figure 7.3). Figure 7.12 shows the magnetic flux density (*rms* value) along the path reported in Figure 7.11 (b) for configurations 2 and 3, respectively without and with the pot, having considered a distance D = 300 mm. Figure 7.13 shows the current density induced in the cylinder under the same conditions. It must be noted that, in both the figures, the points at 300 mm correspond to the side of the cylinder nearest the inductor, whereas points at 0 m to the opposite.

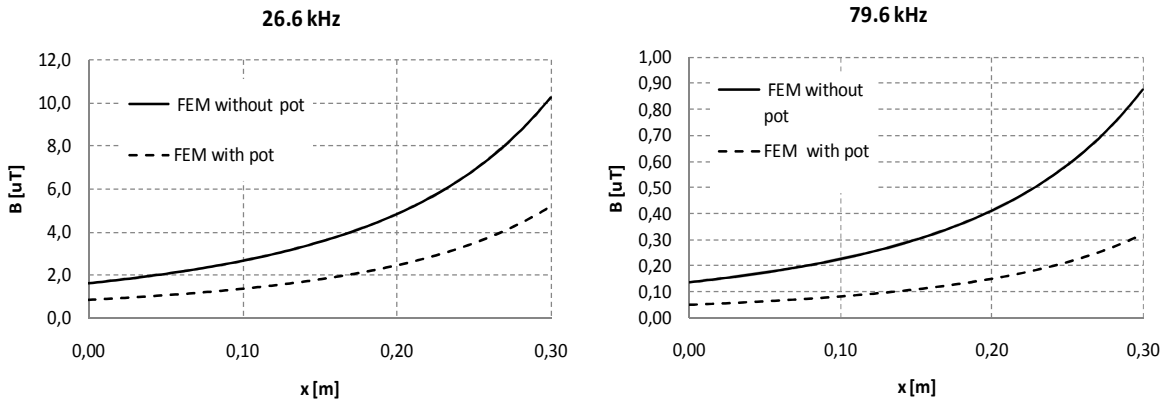

(a) (b)

Figure 7.12: Magnetic flux density for D = 300 mm: (a) 26.6 kHz; (b) 79.6 kHz. Limit 6.25 μT.

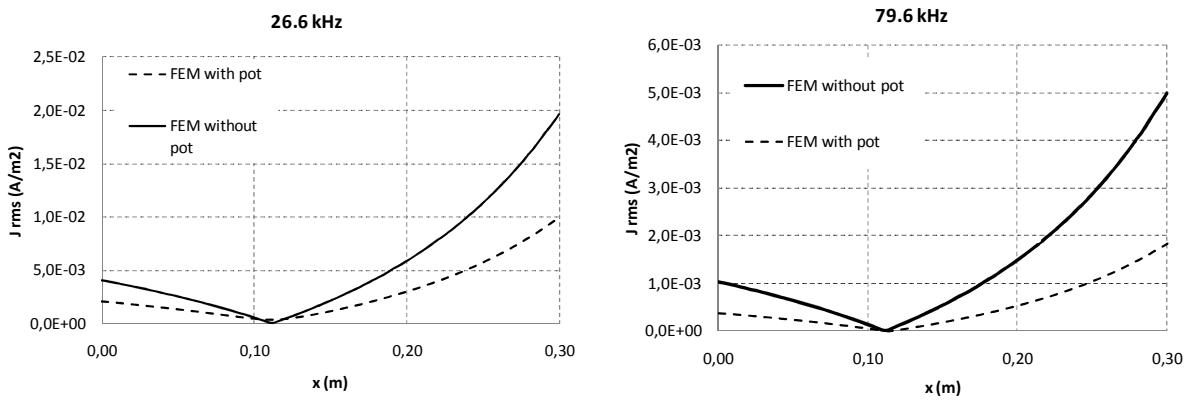

(a) (b)

Figure 7.13: Induced current density for D = 300 mm: (a) 26.6 kHz, limit ; (b) 79.6 kHz. Basic restrictions are respectively 53.2 mA/m^2 at 26.6 kHz and 159.2 mA/m^2 at 79.6 kHz.

As indicated by Figure 7.12 and Figure 7.13, when D = 300 mm, the computed current density values respect the ICNIRP basic restrictions with a quite wide margin, even if at 26.6 kHz the magnetic flux density could overcome the reference level (this happens because the reference levels are deduced from the basic restrictions by applying suitable safety factors).

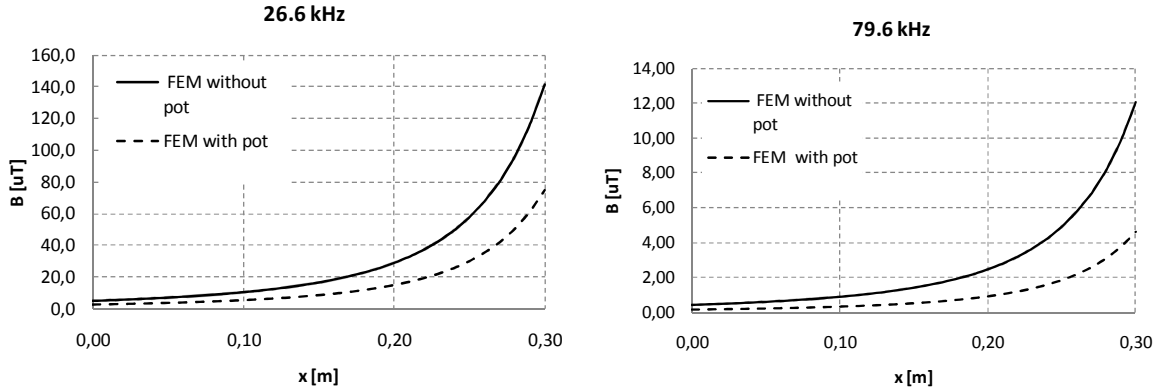

(a) (b)

Figure 7.14: Magnetic flux density for D = 100 mm: (a) 26.6kHz, (b) 79.6 kHz. Limit 6.25μT.

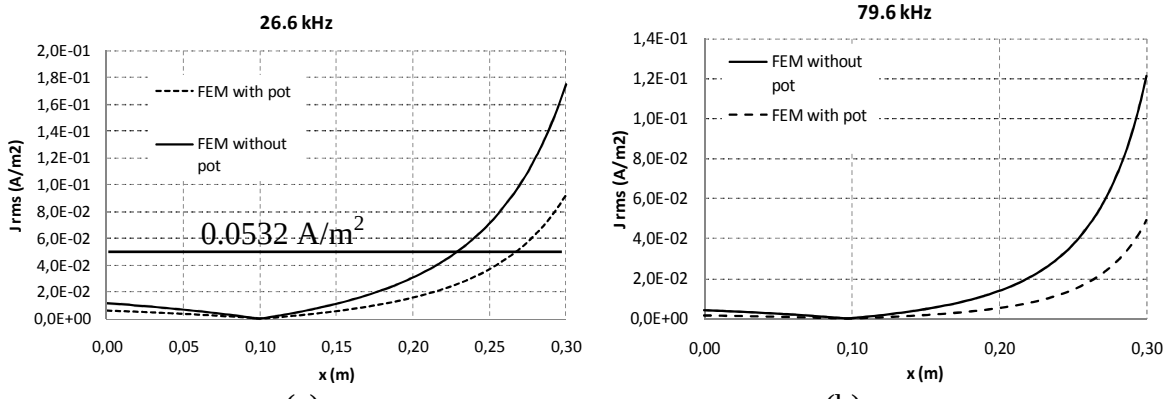

(a) (b)

Figure 7.15: Induced current density for D = 100 mm: (a) 26.6 kHz; (b) 79.6 kHz. Basic restrictions are, respectively, 53.2 mA/m^2 at 26.6 kHz and 159.2 mA/m^2 at 79.6 kHz.

In order to assess the compliance with the exposure limits in close proximity to the cooktop, the distance D has been firstly reduced to 100 mm and then to 50 mm. For what concerns the case D = 100 mm, the results (shown in Figure 7.14 and Figure 7.15) put in

evidence how the reference level and the basic restriction are not satisfied at 26.6 kHz either for configuration 2 (without the pot), nor for configuration 3 (with the pot). At 79.6 kHz the basic restriction is always respected, even if the magnetic flux density could not respect the corresponding reference level.

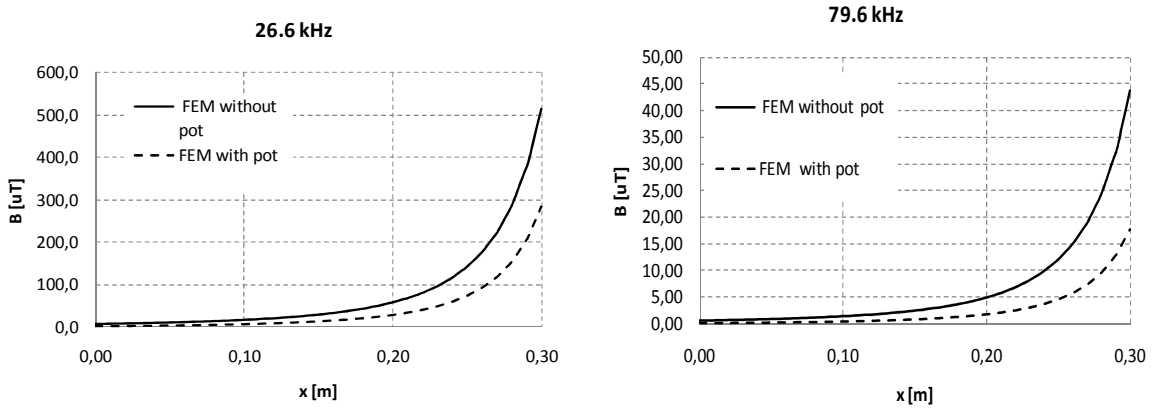

(a) (b)

Figure 7.16: Magnetic flux density for D = 50 mm: (a) 26.6 kHz; (b) 79.6 kHz. Limit 6.25 μT.

Finally, Figure 7.16 and Figure 7.17 show the results obtained when the distance D is further reduced to 50 mm. As expected, there is no compliance with the ICNIRP limits for the harmonic component at 26.6 kHz. On the contrary, at 79.6 kHz the magnetic flux density is surely higher than the reference level, but anyway the basic restriction is satisfied. In this case the permissible level for the induced current density is 159.2 mA/m^2, and the computed one is not higher than 120 mA/m^2.

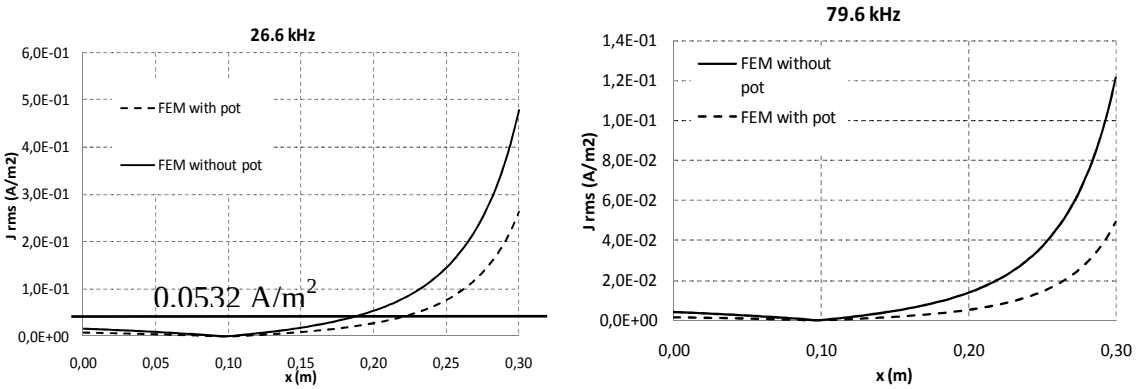

(a) (b)

Figure 7.17: Induced current density for D = 50 mm: (a) 26.6 kHz; (b) 79.6 kHz. Basic restrictions are, respectively, 53.2 mA/m^2 at 26.6 kHz and 159.2 mA/m^2 at 79.6 kHz.

It is interesting to note that, owing to the gradient in the magnetic field components, the minimum of the induced current density moves away from the cooktop when the distance D decreases. Moreover, at lower distances than the one suggested by standards the prescribed limits can be overcome both for the magnetic flux density and for the induced current density.

7.5 Limitations of the homogeneous human model

The non homogeneous model of the human body provides a more careful description of the electrical characteristics of the different tissues than the homogeneous model. It should be noted that the complication of the model can lead to different results in terms of estimation of

induced current density [226]. For instance, in [226] is noted that in tissues with conductivity higher than the one used in the homogeneous model the induced current density evaluated can be locally higher than those computed using a homogeneous model.

In order to evaluate the effect of the organ resistivity two different levels of complexity of human body have been taken into consideration [236]. The simplified model considers a restricted set of organs in the abdomen and thorax regions, while the complete model contains additional information about the head tissues, muscle and a more extensive set of thorax and abdomen organs. In addition, a homogeneous model describing the human body with constant resistivity value has been considered (*see* Figure 3.5 (c)). In Figure 7.18 an example of the current density induced in a human body model with, respectively, homogeneous and specific organ electrical characteristics is shown. In the non-homogeneous model the induced current density can be very different from the one of the homogeneous one. Examples of the evaluation of the induced current in homogeneous and non-homogeneous human model are reported in [228],[236-238]. In those evaluations a human model with some organs in a box with human-shape has been used. The volume around organ is a homogeneous tissue, named "body", with suitable resistivity. In Table 7.8 have been reported some results: M_1 is a human body model with a homogeneous resistivity for all the organs, M_2, M_3 and M_4 are the same models than M_1 with the organ resistivity reported in Table 3.4. The M_2 and M_3 models have, respectively, a "body" resistivity of 5 and 46.9 Ωm. The former is the average value that takes into account the muscle resistivity (is the one used in the homogeneous model, 5 Ωm) and the second is the fat resistivity (at 200 Hz). In the M_4 model the muscle is modeled with a suitable volume and the "body" resistivity is set to the fat one, at 46.9 Ωm.

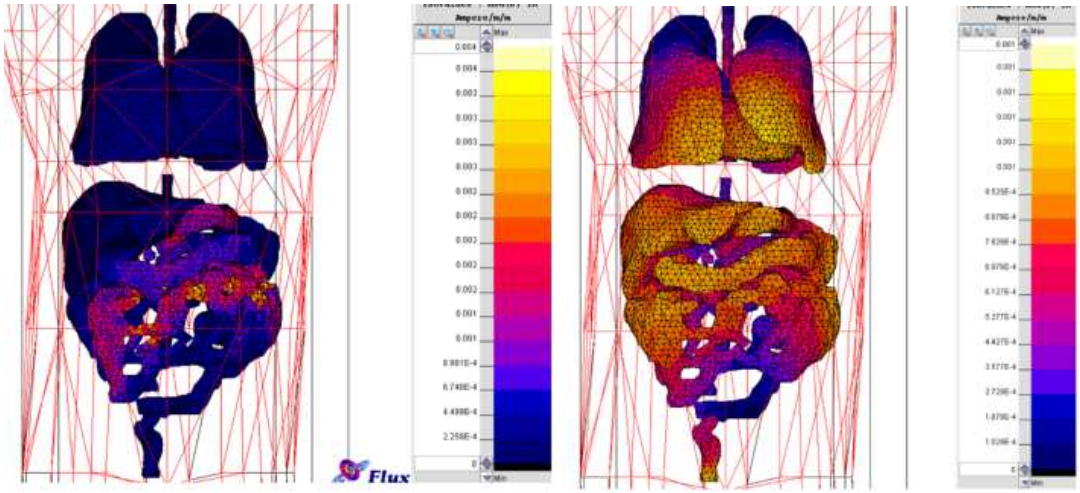

(a) (b)

Figure 7.18: Induced current density inside organs of the human body for (a) M1, homogeneous model, (b) M3, body resistivity 46.9 Ωm.

The magnetic field source is a cable suitably positioned with electric current amplitude of 170 A_{rms} at 200 Hz. An example of the induced current in the organs of the model M_1- M_4 is reported in Table 7.8, whereas Figure 7.19 compares the induced current density in each organ of the models M_1-M_4. The induced current in the homogeneous model is sometimes higher (*e.g.* liver, ρ=25.6 Ωm, spleen, ρ=10.1 Ωm, kidney, ρ=9.3 Ωm) and sometimes lower (*e.g.* intestine and stomach ρ=1.9 Ωm) that the one found using the heterogeneous model with suitable tissue resistivity. Then the homogeneous model can under- or over-estimates the organ induced current density.

Table 7.8: Induced current density in human body tissue and corresponding magnetic flux density. Current source intensity 170 A_{rms} at 200Hz.

tissue	B[μT]		M_1 [mA/m^2]		M_2 [mA/m^2]		M_3 [mA/m^2]		M_4 [mA/m^2]	
	B	**R_L**	**J**	**R_L**	**J**	**R_L**	**J**	**R_L**	**J**	**R_L**
body	158	1.27	5.95	0.60	6.01	0.60	1.74	0.17	2.12	0.21
colon	139	1.11	3.01	0.30	2.88	0.29	2.41	0.24	3.89	0.39
liver	123	0.99	2.31	0.23	0.60	0.06	1.39	0.14	1.01	0.10
intestine	142	1.14	2.53	0.25	5.92	0.59	7.12	0.71	9.50	0.95
pancreas	117	0.94	1.14	0.11	2.91	0.29	2.53	0.25	2.66	0.27
kidney	111	0.89	1.84	0.18	1.11	0.11	0.73	0.07	0.70	0.07
stomach	133	1.06	2.25	0.22	4.62	0.46	4.12	0.41	4.56	0.46
spleen	133	1.06	2.37	0.24	1.27	0.13	0.98	0.10	1.04	0.10
midolla	92	0.73	1.36	0.14	0.28	0.03	0.25	0.03	0.28	0.03

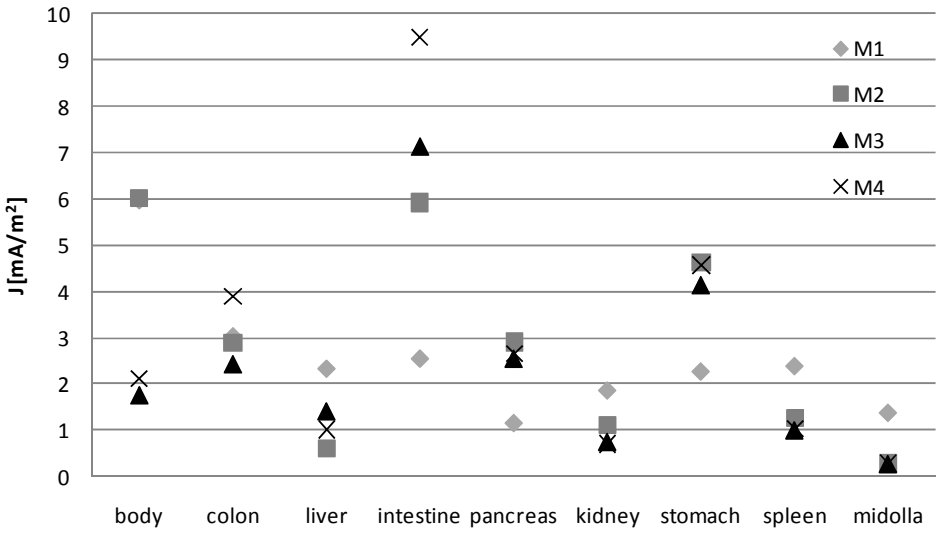

Figure 7.19: Comparison of the organ current density.

7.5.1. Limitations of the human body model

The human model has some limitations due to its complexity. The size of organs in human body depends on the morphological sizes of the person (*e.g.* thin, fat, tall, *etc.*). In the following analysis variations in the size of organs (*e.g.* liver) have been considered.

a. Variation of the organs size

The geometry of the human body model is the one in Figure 3.5 (c). The shape of the magnetic field source is the one in Figure 3.5 (b). The size of the liver is modified in order to study the effect of the organ dimension in the evaluation of the induced current density. In this case the volume of the whole body and the source position is fixed and the reference system of the liver is the same in both two models. “Mod_B” refers to a human body model with the liver volume smaller than the one in “Mod_A” (-14%).

In Table 7.9 the maximum of the current density evaluated in anatomical models with different organ sizes is reported. The difference in the maximum value of the induced current density is close to 60 % and might be due to the difference in the organ size and in the magnetic flux density. The volume of the liver in the “Mod_B” is 14 % smaller than the one

in “Mod_A” and the maximum in the magnetic flux density is lower than 3.8 %. This last result is coherent with the fact that the liver surface is more distant from the magnetic field source. It can be noted that both the organ size and position with respect the magnetic field source can affect the induced current value.

Table 7.9: Induced current density in human liver with different volume.

	Mod_A	**Mod_B**	**Δ%**
Volume [cm^3]	1623	1391	-14.3
B [μT]	125.1	120.3	-3.8
J [mA/m^2]	1.396	0.562	-59.7

7.6 Conclusions

Numerical models have been developed in order to evaluate the exposure to electromagnetic fields. In particular, the exposure to electromagnetic field rising from welding equipments and induction cooktop has been examined. Simple and more realistic human body models have been used in order to evaluate the induced current density in biological tissues. Results of the induced current density obtained by means of the human body model are more accurate with respect to those ones computed using the homogeneous cylinder. Nevertheless the advantages derived by a more detailed model are not so higher than the effort that needs to prepare the model.

A procedure to evaluate the exposure to electromagnetic field by means of numerical model has been implemented and used in order to analyze the effects on biological tissues of electromagnetic fields generated by welding equipments and induction cooktop devices.

Nevertheless, numerical evaluation of the exposure requires a great effort to generate the models, run simulations and analyze data especially if the supply current has a large number of harmonics. For some configurations of simplified human body model and some source positions, a set of coefficient have been developed in order to analyze the exposure to the field generated by some welding equipments. Given the current and frequency of the welding current the corresponding level of the magnetic flux density can be evaluated by the intensity of the current, its frequency and the computed coefficients. In this way the computation effort can be reduced.

As regard the induction cooktop devices homogeneous cylinder models have been used to evaluate the electromagnetic field exposure. The distance between the source and the human body model suggested by standard has been tested but also lower distances have been examined. It appears that at the distance prescribed by standard the device easily satisfies the limits as regard of both the magnetic flux density and the induced current density. This fact didn’t appear evident if the source is closer to the human body model. For lower distances the magnetic flux density or both the magnetic flux density and induced current density can overcome limits. It is to be noted that the distances examined, also lower than the one prescribed by standards, are plausible for a user.

Using the same numerical procedures and models, the human exposure in terms of induced current density can be examined for other types of sources especially if the evaluations by means of measurements or analytical computations of magnetic flux density show the overcoming of limits suggested by standards.

Chapter 8

8 Electromagnetic fields in medical applications: Magnetic Fluid Hyperthermia as tumor therapy

The magnetic nanoparticles are used as an internal heating source in Magnetic Fluid Hyperthermia (MFH). Both the magnetic fluid drug and the magnetic field source must be opportunely designed. Optimization techniques discussed in chapter 5 are used in order to shape the magnetic field source and for the choice of the magnetic fluid parameters.

The Magnetic Fluid Hyperthermia provides the heating of cancer lesions up to a temperature that can damage tumor tissues. In this therapy the nanoparticles, injected in the human tissues, are heated by means of a time-varying magnetic field which should be as much as possible uniform in the treatment area [91]. In the design of the magnetic field source the magnetic field uniformity at first and the resulting temperature uniformity are the most important objective functions. Moreover, since the power density generated by nanoparticles depends on their local concentration, diameter, as well as the local intensity of magnetic field and temperature, the design of the magnetic fluid characteristics can be performed in order to obtain the desired increasing on the local temperature. Then, in the design of the magnetic fluid characteristics, in addition to the temperature uniformity, the temperature rate in a predefined time interval that allows a temperature rise up to the therapeutic value (*e.g.* 42°C in mild hyperthermia or 60°C in the thermal ablation) can be another plausible objective function.

Furthermore, since nanoparticles are generally injected in tumor mass by means of a finite number of injections and the distribution in tissues depends on their diffusion, a uniform concentration is difficult to be reached. Then, another objective can be the design of the heat source with reference to the position of the nanoparticles injections in the tumor mass in order to obtain a concentration that induces, as far as it is possible, uniformity on the temperature in the target region. The temperature might be close to the therapeutic value and the uniformity temperature at the tumor surface might be a prerequisite in order to reach almost a minimum therapeutic temperature value in the treating volume.

The proposed and solved problems for a Magnetic Fluid Hyperthermia treatment devices and therapy design are:

- Design of the electromagnetic source based on considerations in the magnetic field uniformity
- Design of the electromagnetic source based on considerations in the thermal field uniformity; the solution of a coupled electromagnetic and thermal problem is proposed;
- Design of the heating source focusing some aspects of a therapeutic treatment;
- Design of the nanoparticles injection sites focusing the thermal and the therapy design problems.

8.1 Magnetic fluid: physical properties and heating characteristic

Magnetic fluids have interest in biological application because they combine normal liquid behavior with the possibility to control their flow and properties with a magnetic field [239].

A magnetic fluid is a suspension of some particles with nanometric sizes. The most used material for magnetic nanoparticles is the magnetite (Fe_3O_4), but also other magnetic materials have been used. For example in 1993 Jordan uses ferrite particles [70], and Fortin colloidal maghemite (γ-Fe_2O_3) and cobalt ferrite ($CoFe_2O_4$) dispersed in water or a glycerol-water mixture [131]. A stable suspension is achieved if nanoparticles are protected against agglomeration due to Van Der Waals interactions [91], [239]. The coating with organic molecules originating a repulsive force can aid to prevent agglomeration. The stability of the colloids depends on the balance between attractive (Van Der Waals and dipole-dipole) and repulsive (steric and electrostatic) forces [91].

The influence of the magnetic field on the magnetic nanoparticles is due to the fact that the nanoparticles can be considered a set of thermally agitated single domain particles that carry a magnetic moment [239]. Since the magnetic nanoparticles can be treated like some dipoles, the magnetization of the fluid can be described, like a paramagnetic system, by the Langevin equation [92]. In [239] it is observed that the normal paramagnetic systems have a initial susceptibility of the order of 10^{-4}, while the one of ferrofluids is of the order of 1.

An analysis of the magnetic nanoparticles heating properties is in the paper of Rosensweig [106]. In this paper an analytical formulation of the power density generated by a magnetic ferrofluid is reported. The discovery of the behavior of magnetic nanoparticles in a fluid medium subjected to a time-varying magnetic field has been described by Rosensweig in 1969 [239], [240].

In the model of the heating phenomena the magnetic nanoparticles are considered not to interact each other and each of them has its fixed magnetic moment. It is a shear flow that generates a rotation of the particles and their magnetic moment. When a magnetic field is applied to the system, the magnetic moment of the particle will align to the field direction. If the magnetic moment of the nanoparticles is fixed the shear flow causes a misalignment that, consequently, generates a magnetic torque that counteracts the mechanic torque.

Then, each particle can aligns itself with the magnetic field direction by means of a rotation of the whole particle, that is the Brownian relaxation mechanism, or changing the direction of the magnetic moment inside, that is the Néel relaxation mechanism (*see* chapter 2). Both these two relaxation mechanisms contribute to the heat generation due to a time-varying magnetic field. For each of them mechanisms the relaxation time is, respectively, τ_B, for the Brownian and τ_N, for the Néel one [106]:

$$\tau_B = \frac{3\eta V_H}{k_B T} \tag{8.1}$$

$$\tau_N = f_0^{-1} exp\left(\frac{\Delta E}{kT}\right) = f_0^{-1} exp\left(\frac{K_a V_m}{kT}\right) \tag{8.2}$$

where V_m is the nanoparticle core volume ($V_m = 4\pi r^3/3$, with r is the nanoparticle radius), V_H is the nanoparticle volume including the surfactant layer ($V_H = (1 + \delta/r)^3 V_m$ with δ the thickness of surfactant layer), and η the fluid viscosity, K_a is the anisotropy constant of the nanoparticle material, f_0 is the Larmour frequency of the magnetic moment, T the temperature in Kelvin and k the Boltzman constant. In [90] f_0^{-1} is assumed between 10^{-8}s and 10^{-12}s, whereas in [99], [135] is 10^{-9}s. Given the previous relaxation times, (8.1) and (8.2), the effective relaxation time is:

$$\tau = \left(\frac{1}{\tau_B} + \frac{1}{\tau_N}\right)^{-1} \tag{8.3}$$

It is be pointed out that for small nanoparticles the Néel relaxation term dominates, while for large nanoparticles it is the Brownian one that dominates on the resultant relaxation time (8.3) [107].

Both the Brownian and Néel relaxation times are a function of the nanoparticle diameter (the hydrodynamic one, D_h, in the first case and the magnetic one, D_c, in the second case). The magnetic diameter is the one of magnetic nanoparticle core, whereas the hydrodynamic one includes the surfactant layer as sketched in Figure 8.1. Since the two relaxation mechanisms have a different behavior as a function of the particle diameter (Figure 8.2), the one that is the lowest dominates the relaxation mechanism.

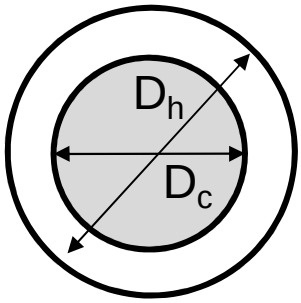

Figure 8.1: Magnetic and hydrodinamic diameter of a nanoparticle core with its surfactant layer.

The transition between Néel and Brownian mechanisms arrived for a particular particle diameter that is the one for which is $\tau_N = \tau_B = \tau$.

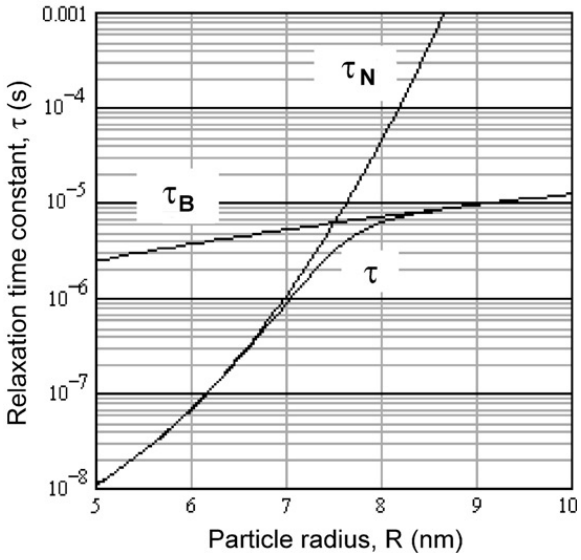

Figure 8.2: Relaxation time as a function of the frequency for Fe3O4 nanoperticles. From [106].

It is to be noted that in some case, in biological applications the magnetic interaction between the particles can be neglected [90] since biological ligand coating, used to functionalize the nanoparticles, helps to separate them. Moreover, the relaxation time can be influenced by the magnetic interactions between near nanoparticles that can cause the formation of straight chains or agglomerates that modify the final heating effects [96], [107],

[113], [136]. The importance of interaction is assessed by the ratio between the interaction energy and thermal energy, $\lambda = E_{int}/kT$, where the internal energy, E_{int}, depends on the magnetization and the interparticles distance.

The nanoparticle magnetization is also due to the magnetic anisotropy of the material that creates an energy barrier between different orientations of the magnetic moments. If the anisotropy is uniaxial the energy barrier is $\Delta E = K_a V$ [93], [136]. This value appears on the exponential term of the Néel relaxation time constant (8.2). Since the single domain magnetic materials can fluctuate in a time-varying magnetic field the magnetization is time variant, then for magnetic fluid in a time-varying magnetic field the magnetization derivative is [106], [239]:

$$\frac{\partial M(t)}{\partial t} = \frac{1}{\tau}(M_0(t) - M(t)) \tag{8.4}$$

where M_0 is the equilibrium magnetization equal to $M_0 = \chi_0 H_0 \cos \omega t = Re(\chi_0 H_0 e^{j\omega t})$ in which, χ_0 is the static susceptibility, τ is the characteristic relaxation time that has the form in (8.3) and the magnetization is:

$$M(t) = Re\left(H_0 e^{j\omega t}\right) = H_0(\chi' cos\omega t + \chi'' \sin \omega t) \tag{8.5}$$

with χ' and χ'' are the real and imaginary part of the magnetic susceptibility χ [94]. From previous relations the magnetic susceptibility is:

$$\chi = \frac{\chi_0}{1 + j\omega\tau} \tag{8.6}$$

In order to determine the effect of the relaxation mechanisms the frequency dependence of the susceptibility in the previous relations can be written as a complex quantity [241], [242]:

$$\chi(\omega) = \frac{\chi_0}{1 + (j\omega\tau)^2} - j\frac{\chi_0 \omega\tau}{1 + (j\omega\tau)^2} \tag{8.7}$$

with χ_0 is the static susceptibility and ω the frequency pulsation. Figure 8.3 shows typical shapes of real, $\chi'(\omega)$, and imaginary, $\chi''(\omega)$, part of the magnetic susceptibility as a function of the frequency for nanoparticles suspended in a water solution or in a gel media [66], [135], [243]. It is been pointed out that the susceptibility depends also on the fluid temperature since the relaxation time is a function of the temperature (*see* (8.1) and (8.2)), [106], [134]. In order to avoid Néel phenomena the nanoparticles must over to a minimum size threshold (if they are too small the Néel relaxation time is predominant).

It is been pointed out that a magnetic fluid can be composed by nanoparticles that not have all the same dimensions, but it is a dispersion of nanoparticles with different diameter. This fluid with nanoparticles with different diameter is named a polydispersion with the nanoparticles diameter distribution that follows a log-normal distribution [106]:

$$g(r) = \frac{1}{\sigma\sqrt{2\pi}} exp\left(-\frac{\ln r - \ln \bar{r}}{2\sigma^2}\right) \tag{8.8}$$

where r is the particle radius, $\bar{r}$ is the average radius, σ is the logarithm of the standard deviation. This expression can be introduced in the one of the susceptibility in order to better approximate the magnetic fluid characteristics [66], [99], [106], [135]. The dispersion of nanoparticles diameter affects the power density given to the tissue [243].

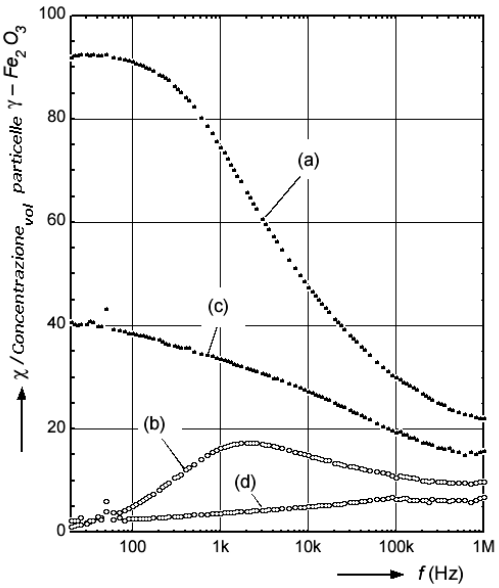

Figure 8.3: Magnetic susceptibility as a function of the frequency for maghemite suspension. (a) real and (b) imaginary part for nanoparticles in water, (c) real and (d) imaginary part of nanoparticles in gel. From [135].

8.1.1. Derivation of heating generated by a nanoparticles suspension

From the magnetic susceptivity and relaxation time characteristics the heat generated by means of the nanoparticles can be assessed [106]. For the first law of thermodynamic the internal energy in a unitary volume is:

(8.9)

where Q is the heat that is given to the process and W is the work applied to the system. If $Q=0$ the process is adiabatic and the heating is only due to the work given by the magnetic field, H [A/m], that is:

(8.10)

where the magnetic flux density $\boldsymbol{B}$ is a function of the magnetic properties of the system. So, in this case the system energy (8.9) is:

(8.11)

where with M is the material magnetization [Am^{-1}] and μ_0 the magnetic permeability of the free space. Using previous relations the time variation of the internal energy due to the application of a time-varying magnetic field is:

(8.12)

Magnetization can be alternatively expressed in terms of the complex susceptibility, χ, that is, (*see* (8.7)):

(8.13)

Let consider a cosinusoidal magnetic field, , the magnetization depends on the magnetic susceptibility and is:

$$M(t) = Re\left(H_0 e^{j\omega t}\right) = H_0(\chi' cos\omega t + \chi'' \sin \omega t) \tag{8.14}$$

From the previous expression the internal energy (8.12) is:

$$\Delta U = 2\mu_0 H_0^2 \chi'' \int_0^{2\pi/\omega} sin^2 \omega t dt \tag{8.15}$$

that depends only on the imaginary part of the magnetic susceptibility, χ''. Integrating the internal energy the volume power density is:

$$P = f\Delta U = f\pi\mu_0 H_0^2 \chi'' \tag{8.16}$$

where $f = \omega/2\pi$ is the frequency of the magnetic field. Using the expression of the magnetic susceptibility the (8.16) can be written as:

$$P = f\pi\mu_0 H_0^2 \frac{\chi_0 \omega\tau}{1 + (j\omega\tau)^2} \tag{8.17}$$

In this expression χ_0 is a constant. Nevertheless this parameter depends on the magnetic field intensity. Given the Langevin equation:

$$L(\xi) = \frac{M}{M_s} = coth\xi - \frac{1}{\xi} \tag{8.18}$$

where

$$\xi = \frac{\mu_0 M_d H V_m}{kT} \tag{8.19}$$

is the Langevin parameter in which M_s is the saturation magnetization of the ferrofluid, that is $M_s = \phi M_d$ with M_d the domain magnetization of the suspended nanoparticles and ϕ the nanoparticles concentration, the static susceptibility, χ_0 is:

$$\chi_0 = \chi_i \frac{3}{\xi}\left(coth\xi - \frac{1}{\xi}\right) \tag{8.20}$$

with χ_i is the initial susceptibility that is:

$$\chi_i = \left(\frac{\partial M}{\partial H}\right)_i = \frac{\mu_0 \phi M_d^2 V_m}{3kT} \tag{8.21}$$

From previous relations some quantities in order to evaluate the heat deposed by means of a nanoparticles fluid can be derived. For instance, in Fortin [131] the Specific Loss Power (SLP) for a monodisperse particles solution is defined as:

$$SLP = \frac{P}{\rho\phi} = \frac{1}{\rho\phi}\pi\mu_0 f H_0^2 \frac{\chi_0 \omega\tau}{1 + (j\omega\tau)^2} \tag{8.22}$$

where ρ is the mass per unit volume of iron oxide; the previous quantity is independent of the nanoparticles concentration. Given the power density generated by means of the nanoparticles, for a monodisperse fluid (all nanoparticles have the same diameter), the temperature rise, ΔT, is:

$$\Delta T = P\frac{\Delta t}{c} \tag{8.23}$$

where c is the specific heat of the ferrofluid and Δt is the heating time interval. Whereas for a polydisperse nanoparticles solution (nanoparticles with different diameters) the dissipated power is:

$$\Delta T = \bar{P} = \int_0^\infty P g(r) dr \tag{8.24}$$

and the corresponding temperature rate is:

$$\Delta T = \bar{P}\frac{\Delta t}{c} \tag{8.25}$$

The temperature distribution around a spherical source is described in [244]. In this paper a thermal model has been developed using the heat transfer equation. Nevertheless, it must be noted that the temperature increasing in a tissue induced by means of a power density source depends also on the blood perfusion that has a cooling effect.

8.1.2. Model for the computation of the power density generated by means of the magnetic nanoparticles

Both electromagnetic and thermal problems are solved using Finite Elements Analysis (FEA). The power density is computed as in the (8.17) in order to compute the thermal source that is the input of the thermal problem in (4.57).

In magnetic nanoparticle therapy the heat is generated by means of a time-varying magnetic field $\boldsymbol{H}$ that produces the rotation of nanoparticles and their magnetic moments in the biological fluid. From the results of the previous paragraph the power density depends on the local value of the:

- intensity of the magnetic field [Am^{-1}];
- frequency of the magnetic field [Hz];
- tissue temperature [K];
- concentration of nanoparticles [%];
- diameter of nanoparticles [nm];

Then, according to [106], the power generated by means of the nanoparticle motion can be evaluated using the following equation where the local dependence on spatial variables is highlined:

$$P(x,y,z,T,H,\phi,D) = \pi\mu_0\chi''(x,y,z,T,H,\phi,D) f H^2(x,y,z) \tag{8.26}$$

where μ_0 is the magnetic permeability of the vacuum, f the magnetic field frequency, χ'' the magnetic susceptibility of the nanoparticles. The dependence on temperature, concentration and diameter of nanoparticles is inside the magnetic susceptivity term, whereas the dependence on the intensity of the magnetic field is both inside and outside the magnetic susceptivity term.

In a first example the power density can be computed locally using local value of the temperature and the magnetic field intensity by means of a FEA coupled problem. The

magnetic susceptibility is a function of the magnetic field intensity H and the Langevin parameter, ξ [106]:

$$\chi''(\phi, H, D) = \frac{\chi_0(\phi, H, D)\ \omega\ \tau(D)}{1 + (j\omega\tau(D))^2} \tag{8.27}$$

where ω is the angular frequency of the field $\boldsymbol{H}$, τ the relaxation time of the nanoparticles due to Néel, τ_N, and Brown, τ_B, relaxation time constants such that (8.3), $\tau^{-1} = \tau_N^{-1} + \tau_B^{-1}$ [106]. It can be noted that the Brown relaxation time depends on temperature and diameter nanoparticles as in (8.1):

$$\tau_B = \frac{3\eta V_H(D)}{k_B T} \tag{8.28}$$

where V_H is the hydrodynamic volume of a nanoparticle with diameter D and magnetic volume V_m, ($V_H = (1 + \delta/r)^3 V_m, V_m = 4\pi(D/2)^3/3$). Whereas the Néel relaxation time depends only on the tissue temperature (*see* (8.2)).

In previous relations δ is the thickness of the layer that covers the magnetic part of the nanoparticle, k_B the Boltzman constant, T the temperature. The following relationships are incorporated in (8.27):

$$\chi_0(\phi, H, D, T) = \chi_i(\phi, D, T)\frac{3}{\xi(H, D, T)}\left(coth\xi(H, D, T) - \frac{1}{\xi(H, D, T)}\right) \tag{8.29}$$

with ξ the Langevin parameter in the (8.19) that depends on the magnetic field intensity as well as the temperature and nanoparticles diameter:

$$\xi = \frac{\mu_0 M_d H V_m(D)}{kT} \tag{8.30}$$

whereas the initial magnetic susceptibility depends on the temperature, T, and nanoparticles diameter, D, and concentration, ϕ, as in the (8.21):

$$\chi_i = \frac{\mu_0 \phi M_d^2 V_m(D)}{3kT} \tag{8.31}$$

Previous relations put in evidence the dependence of the power density P in (8.23) on some characteristics of the nanoparticles as their concentration and diameter and the fluid temperature as well as the magnetic field intensity.

8.1.3. Hyperthermia and electromagnetic field exposure

Even in the case of tissues heating by means of magnetic nanoparticles it must be considered that a magnetic field is generated and, therefore, the possible occurrence of systemic effects, like tissues heating or stimulation, might be assessed. For this evaluation there are some empirical models that allow an assessment of the possible limits on the intensity of the field [66], [77]. For example, in [85] the magnetic field limit given for a diameter of 30 cm is [243]:

$$H\ f < 4.85\ \cdot 10^8 \tag{8.32}$$

where H is the intensity of the magnetic field and f the frequency. The (8.32) has been evaluated at a specific radius R of the region exposed to the magnetic field.

8.2 Finite Element models for Magnetic Fluid Hyperthermia equipments

In Figure 8.4 the computation domain and the volumes used to solve electromagnetic and thermal problem by means of Finite Element tools are reported. The geometry for the solution of the electromagnetic problem is characterized by two conductive regions, namely Ω_T, the tumor, and Ω_L and Ω_H, the healthy tissues regions; they are embedded in an air region, Ω_A, that includes the sources J_c and J_m of the magnetic field *H* (Figure 8.4). Between the two conductive regions and Ω_A, an air box Ω_B is laid in order to adapt the mesh. In turn, the thermal domain includes the tumor, Ω_T, and the healthy tissue, Ω_H, regions only. Suitable heat exchange conditions are imposed on the external surface of the thermal domain. In particular, the healthy tissue considered in the Ω_H region is fat, whereas the healthy tissue that surrounds the tumor region, Ω_L, is the liver tissue. The electrical characteristics of the tissues are in Table 3.5.

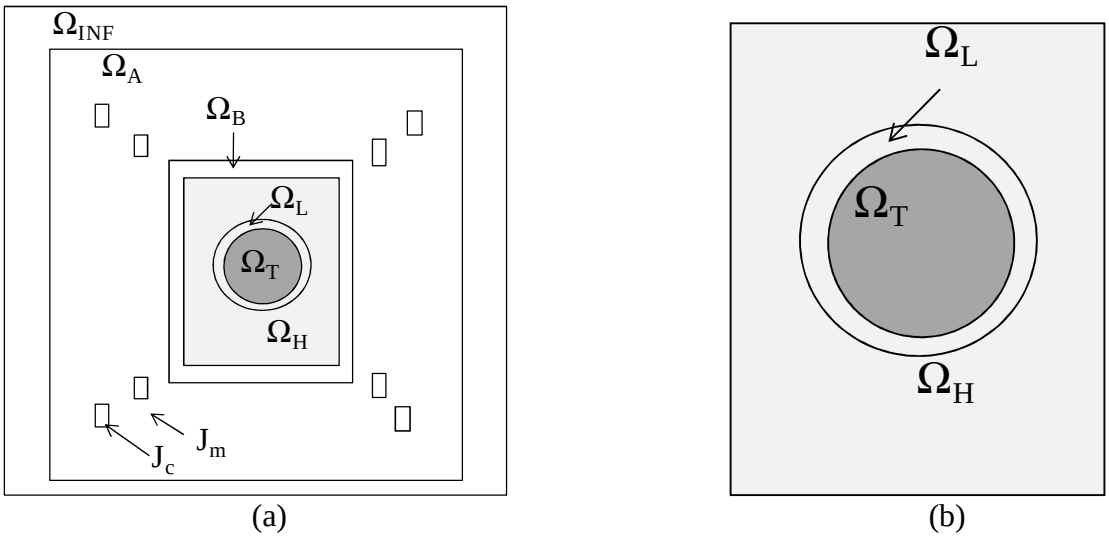

Figure 8.4: FEM geometry (b) domains of the magnetic and the thermal problems with Ω_T=tumor, Ω_L=liver, Ω_F = fat, Ω_A and Ω_B = air, and Ω_{INF}= truncated external region.

The electromagnetic problem is solved in terms of total electric scalar potential, Φ, because this formulation solves in a better way the magnetic field problem. The solved equations in the conductive media Ω_T, Ω_L and Ω_H are the (7.5)-(7.6), whereas in the air region the Biot-Savart formula is used to compute the magnetic field generated by means of the inductors and the (7.7) is used in order to solve the magnetic problem. In the air region the equations on the reduced scalar potential (4.40) and (4.41) are used to solve the magnetic field problem.

Given the thermal source in terms of the power density *P* in the Fourier equation with the Pennes term (4.57) is solved in the thermal domain of the Figure 8.4 (b).

8.2.1. Magnetic field source design

A clinical device for Magnetic Fluid Hyperthermia (MFH) is installed *e.g.* at the Charité hospital in Berlin [138]. In this equipment the time-varying magnetic field source is a coil with a ferrite yoke which is able to guarantee, in a cylinder with diameter of 20 cm a magnetic field strength with a uniformity of 90 % [138]. In this paragraph, the synthesis of an iron-free magnetic field source, inspired by Loney solenoid system [245] is proposed. The proposed design is a completely new solution with respect to existing devices, with the possibility of adaptation of shape and currents based on patient size and region to be treated. The aim is to synthesize a uniform field in the treatment region, insensitive to small variations of coil system parameters [251].

Actually, in various applications of bioengineering, the generation of uniform magnetic fields is required. For instance, in magnetic resonance imaging (MRI) [245], as well as in magnetic induction tomography (MIT) [246], the field synthesis problem is characterized by a small size of the controlled region and a high degree of uniformity (in the order of *ppm*). Instead, in MFH the controlled region size is one order bigger than in MRI and MIT systems, because the anthropometric dimensions should be taken into account; this, in turn, has a consequence in terms of the degree of field uniformity achievable in practice.

Scope of the automated optimal-design procedure of inductors for MFH for clinical treatment of cancer lesions is providing a control in the uniformity of magnetic field and hence a uniform therapeutic temperature in wide body regions. In particular, an air-cored solenoid system, which offers a possible advantage in terms of reduced size due to the lack of ferromagnetic material, is considered. The design problem is formulated in terms of a multiobjective problem [247].

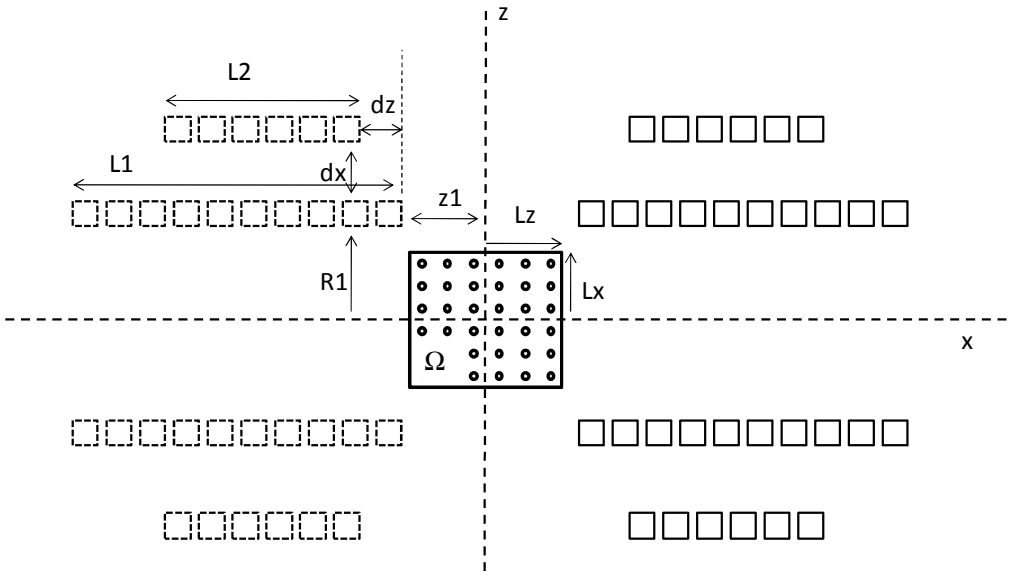

Figure 8.5: Geometry of the magnetic field source.

The geometry of the magnetic field source is represented in Figure 8.5. It is composed by a set of two couples of coils (the system of inductors) with the same axis. The main coil is the internal one, and the external is the secondary coil. The latest it is the correcting coil used to uniform the field distribution generated by the main coil. The system is symmetric both along the *z* and *x* axis. The inductors at left of the *z* axis are supplied by the same current values, in amplitude and phase, that the ones in the right part.

The uniformity of the magnetic field or thermal field is evaluated in a volume at the center of the space between the two inductors system. Since the axial symmetry subsists the magnetic field has been evaluated in a 2D layer. In Figure 8.5 the evaluation area, the Ω region, has been represented as a square with points. This area has dimensions *2Lz* and *2Lx*.

Table 8.1: Range of the geometry and current data used in the optimization.

	R_1[m]	dx[m]	Z_1[m]	dz[m]	L_1[m]	L_2[m]	I_1[A]	I_2[A]
Min	0.25	0.05	0.15	-0.05	0.2	0.15	1000	500
Max	0.5	--	0.4	0.45	--	--	--	--

The section of the axis symmetric device in Figure 8.5 shows some possible design variables. L_1 and L_2 are the lengths of main and correcting coils, respectively, R_1 is the radius

of main coil, *dx* the gap between main and correcting coil, z_1 the distance of the main coil from the *z* axis, *dz* is the shift of the correcting coil with respect the main one. Table 8.1 the variation ranges of the chosen design variables $x = (R_1, z_1, dz)$ used in the optimization process and the fixed values of the inductor geometry parameters are reported. The square at the system centre, Ω region, with side $L_x=L_z$ of 20 cm, is the area where the field uniformity is to be controlled.

8.2.2. Design of the magnetic field: objective functions and some results

The design of the time-varying magnetic field source requires the studying of the sizing and the position of the inductors in order to generate a magnetic field as more as uniform under some geometrical constraints like the size of the treating person and the volume and position of the cancer lesion. In the first analysis, the sizing of the source, the magnetic field has been computed using a semi-analytical model, *i.e.* superimposing the field generated by each turn composing a coil. To this end, a classical analytical formula [248] that involves the evaluation of elliptic integrals has been used. This method has been chosen for its computational speed in repeated field analyses, and with reference of an optimization procedure. In the first design of the magnetic field source the uniformity of the magnetic field, in terms of inhomogeneity, is analyzed and the sensitivity of the solution is evaluated. Then the magnetic field source design is configured as a two objectives optimization problem.

Given the magnetic field intensity the inhomogeneity function, *f*, the first objective function considered, is defined as follows:

$$f = \frac{H_{max} - H_{min}}{H_{mean}} \tag{8.33}$$

where H_{max} , H_{min}, and H_{mean} are the maximum, minimum and average value of the magnetic field in the controlled region Ω , respectively; numerically, inhomogeneity has been computed in a set of *N=231* points, located in the Ω region.

An inexpensive evaluation of sensitivity is possible when a set of $n_p>>1$ points discretizing the search space is available. Each point of the set is considered as the centroid of a hypercube ω, composed of all the other points whose distance from the given one is less than a threshold [239]. Then, sensitivity *s*, the second objective function, is approximated as:

$$s \equiv [f(\tilde{g})]^{-1}[\sup_{g} f(g) - \inf_{g} f(g)],\ g \in \omega \tag{8.34}$$

where *sup* and *inf* are computed within the hypercube ω, and $f(\tilde{g})$ is the inhomogeneity function value at the hypercube centroid $\tilde{g}$.

a. Some results of the random shape optimization

In Figure 8.6, the sensitivity *s* is plotted as a function of inhomogeneity *f*. The cloud of points has been obtained after sampling the three-dimensional search region formed by the variables R_1, z_1 and *dz*. In particular, z_1 and *dz* have a practical significance because they have to be adjusted during the set-up phase of therapy equipment, and their setting depends on the patient size. The sampling is based on a random search governed by a uniform probability density function, and is composed of 1,000 points.

The final aim of the magnetic system is to generate a field uniform enough in the controlled region Ω. For this reason a real shape design of the system has been performed using a multiobjective formulation. Ensuring the maximum homogeneity of the magnetic field in a prescribed volume was the main target of the design. In fact, a uniform magnetic field is a preliminary condition for a uniform power density and then for almost uniform heating of

human body tissues. On the other hand, since the opening of the system has to be adjusted depending on the anthropometric sizes of the patient, the sensitivity of configurations minimizing the field inhomogeneity should be evaluated. Among all feasible solutions, the ones exhibiting both low inhomogeneity and sensitivity will be selected. Therefore, the design problem has been cast as a two-objective optimization problem: find the set of feasible solutions *x* such that both *f(x)* and *s(x)* are minimum, according to Pareto optimality [247].

In Figure 8.7 (a) and (b) two feasible geometries are shown: the former is an example of good solution, the latter of bad solution. The first one represents an optimal case and the second one a sub-optimal case.

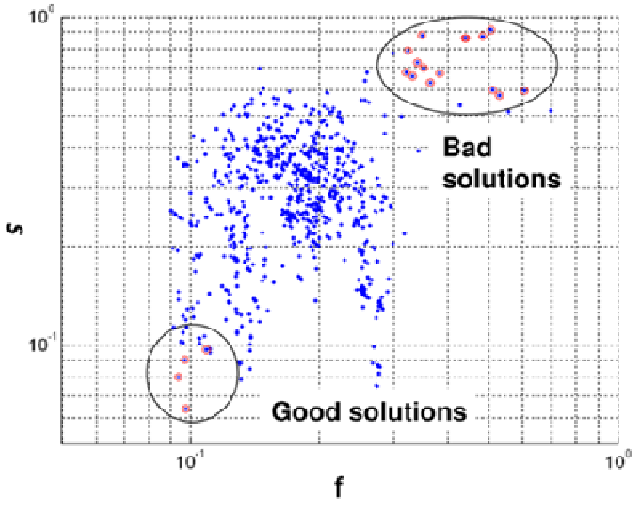

Figure 8.6: Sensitivity versus inhomogeneity function. Points in the lower left and upper right corner are good and bad solutions, respectively.

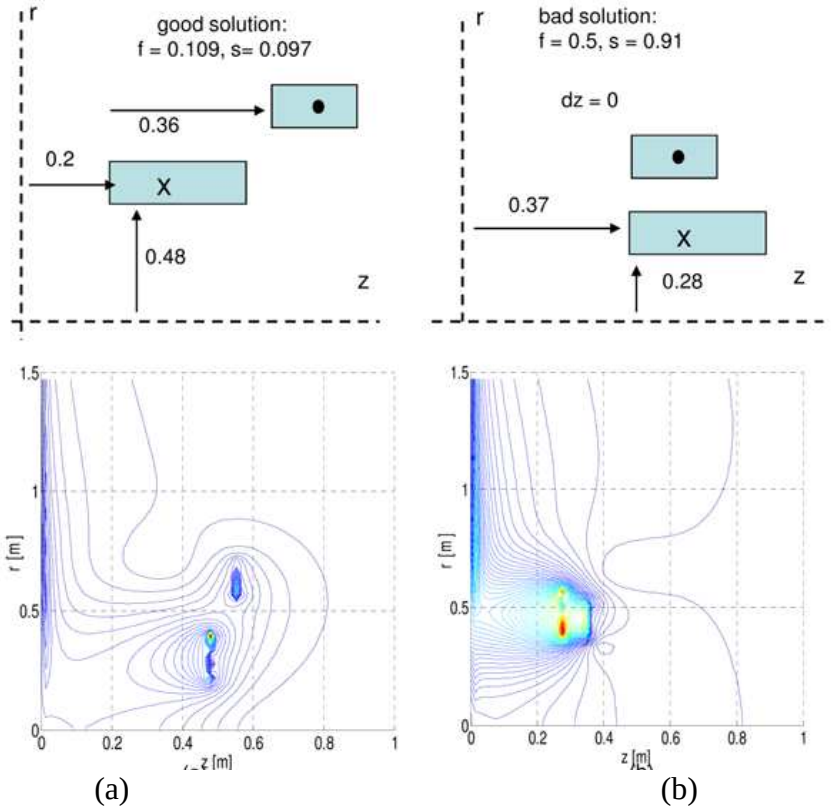

(a) (b)

Figure 8.7: Geometry and H field contour lines for a (a) good and a (b) bad solution.

In Figure 8.8 (b) the percentage variation of the *H* field intensity is shown; the maximum of the magnetic field *H* in the controlled region Ω is close to 15,000 A/m in the case of the good solution and to 3,200 A/m in the case of the bad solution, respectively. The maximum has been evaluated as the global one along three directions (d_1,d_2,d_3), defined inside the controlled region (Figure 8.8 (a)). It can be noted that the field uniformity is higher than 95% between 2 cm and 20 cm from the axis system.

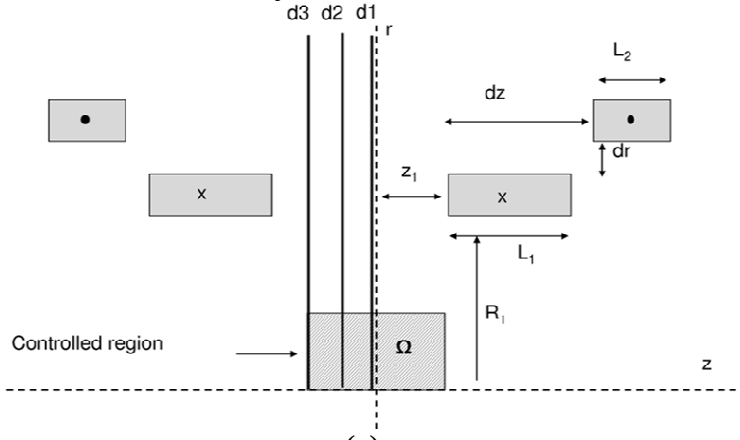

(a)

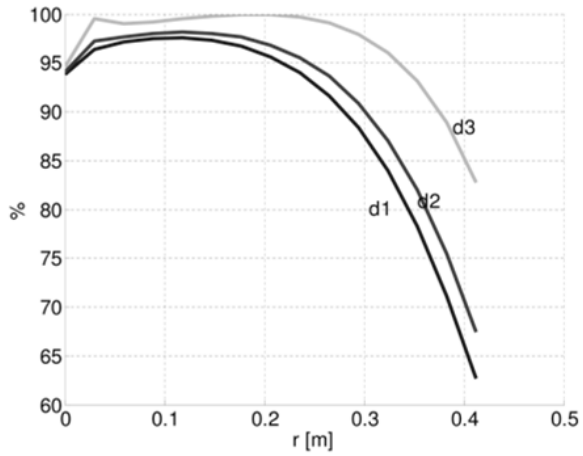

(b)

Figure 8.8: (a) Geometry of the system and (b) percentage variation of H field.

b. Some results of the automated shape optimization

Starting from a tentative solution and using an Evolution Strategy algorithm for the shape optimization of the inductor system geometry, an improved solution can be found in an automated way [247]. For the bad solution in Figure 8.7 two possible improved solutions, found with the evolution strategy algorithm, are reported in Table 8.1.

Table 8.2: Automated shape optimization results using evolution strategy approach

z [m]	dz [m]	x [m]	*f*	*s*
Start point				
0.37	0	0.28	0.2527	$1.92 \cdot 10^{-06}$
Stop Points				
0.1964	0.5781	0.5	0.0396	$1.36 \cdot 10^{-07}$
0.1961	0.5969	0.5	0.0396	$6.4 \cdot 10^{-09}$

It can be noted that the ratio between the sensitivity of a bad solution to the sensitivity of a good solution is conservative and it is equal almost to 10.

c. FEA Validation and coupled field simulation

In Figure 8.9 the geometry implemented in Flux3D, a Finite Element Analysis (FEA) commercial code for electromagnetic simulation is sketched. The tumor, *i.e.* the region where the magnetic field must be synthesized, is modeled by a sphere inserted in a spherical volume that represents the liver. In turn, the liver is embedded in a cylinder with elliptical cross-section, representing the human body. In this case a typical FEM mesh for the electromagnetic (EM) problem is composed of 683,758 tetrahedral elements. For the thermal problem the mesh is the same than in the EM problem but only a sub-set of volumes, the conductive ones, have been considered. Electrical characteristics of the tissues are in Table 3.5 whereas the thermal one are in Table 3.6. In the FEA the nanoparticles have been assumed to be uniformly distributed in the tumour volume. The intensity of the magnetic field *H* has been computed with the FEA simulator solving the magnetic problem for the geometry in Figure 8.9, assuming currents I_1= 1000Arms and I_2=500A*rms* at a frequency f=450 kHz.

Figure 8.11 shows the absolute value of the magnetic field along three orthogonal directions (Figure 8.10) inside the tumour region, in both the sources positions reported in Figure 8.7. P_n_U and P_n_NU represent the magnetic field along the path *n* for, respectively, the uniform and non uniform winding configuration. The synthesized configuration of the source inductors implies both an increase of the magnetic field value and a better uniformity inside the tumor volume.

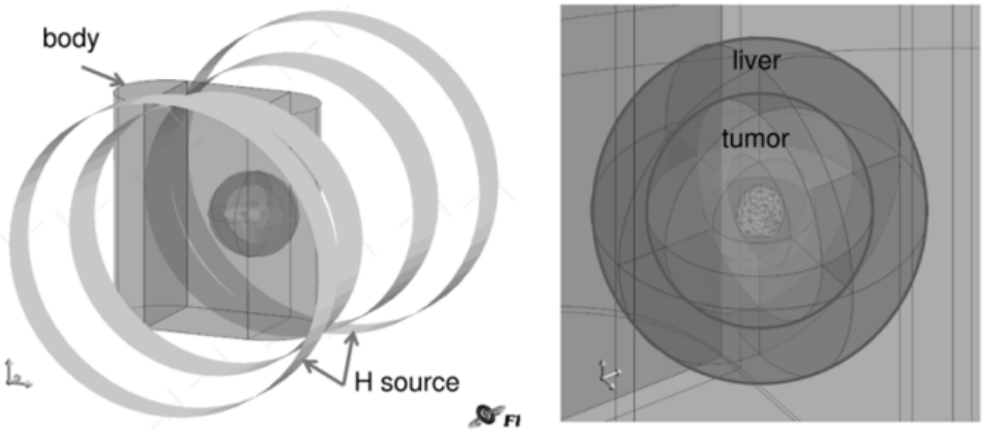

(a) (b)

Figure 8.9: Model geometry and field windings.

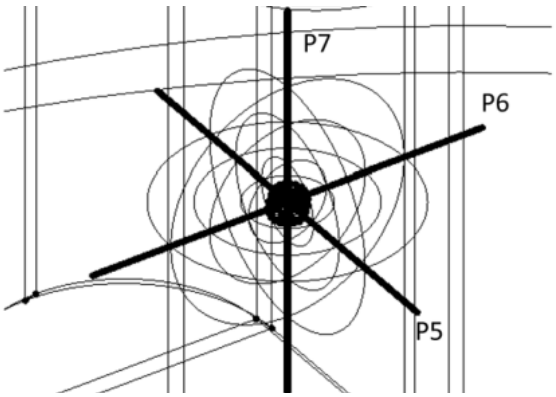

Figure 8.10: Magnetic field and temperature sampling directions.

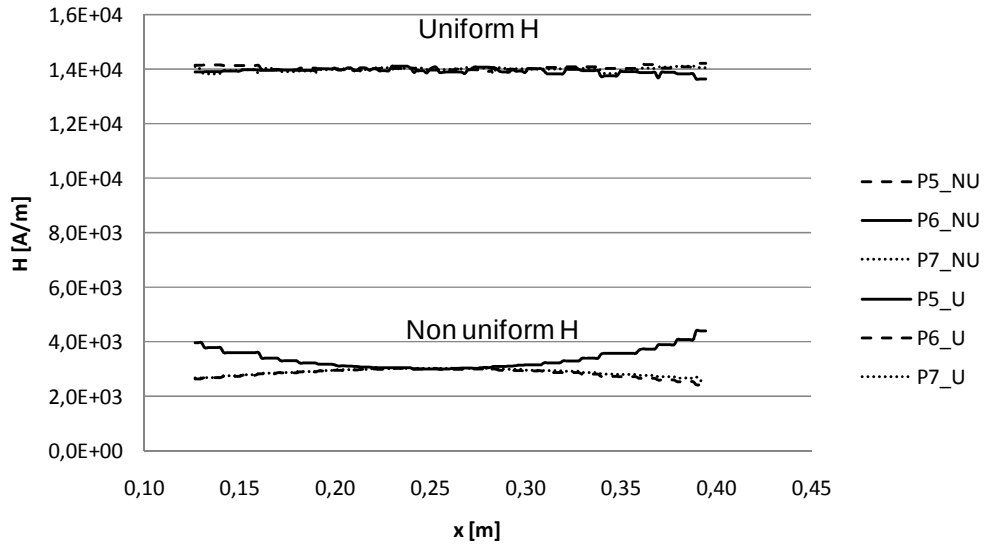

Figure 8.11: Magnetic field inside the tumor region in both synthesized and sub- optimal configuration (*rms* values).

In order to investigate the coupled-field response of the synthesized field winding, a thermal FEA has been developed. Magnetic nanoparticles produce a power density [W/ m^3] that is a function of the square of the magnetic field H and its frequency f , like that reported in [106],[199]. Then, the power density released to the tissues by means of the nanoparticles has been derived from the value of the magnetic field intensity H using the (8.16). Successively, the temperature distribution in the tumour as a function of time has been computed solving the transient thermal problem in the interval [0, 20] s. In this respect, to evaluate the tissue heating, the power density P has been set as the heat source in the Fourier equation [214] and the cooling effect of the perfusion due to the blood circulation inside tissues has been taken into account, implementing the Pennes equation by subtracting the cooling term using (4.57). In the implementation of the thermal equation, the cooling effect due to big vessels as well as the phase change of the blood has been disregarded. Moreover, in the thermal problem the nonlinear characteristics of healthy and tumor tissues [198] have been considered (Table 3.6).

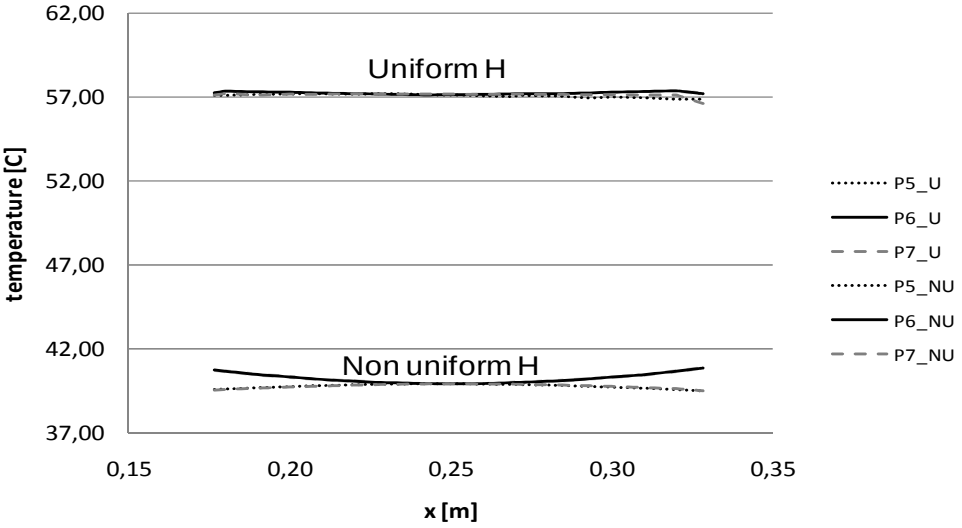

Figure 8.12: Temperature due to nanoparticles inside the tumor region in the optimal and sub-optimal configuration.

Following thermal results refer to maghemite magnetic nanoparticles with a diameter of 20nm. In the case of the uniform *H* field the concentration is 0.3% whereas in the case of a non-uniform *H* field is 2.85 % in order to have comparable temperature rate. In fact, with reference to these concentrations, the power density in the tumour region due to magnetic nanoparticles is approximately the same in both uniform and non uniform case.

The temperature inside the tumor region, sampled along the directions of the Figure 8.10, is reported in Figure 8.12 for both the cases of uniform, and non-uniform, magnetic field *H*. P_n_U and P_n_NU represent the temperature along the path *n* (*n=5, 6, 7*) for, respectively, the uniform and non uniform magnetic field. It can be noted that the behaviour of temperature follows the one of the magnetic field reported in Figure 8.11. Then, the importance to have a uniform magnetic field to obtain a uniform temperature in the region of the tumour is proved.

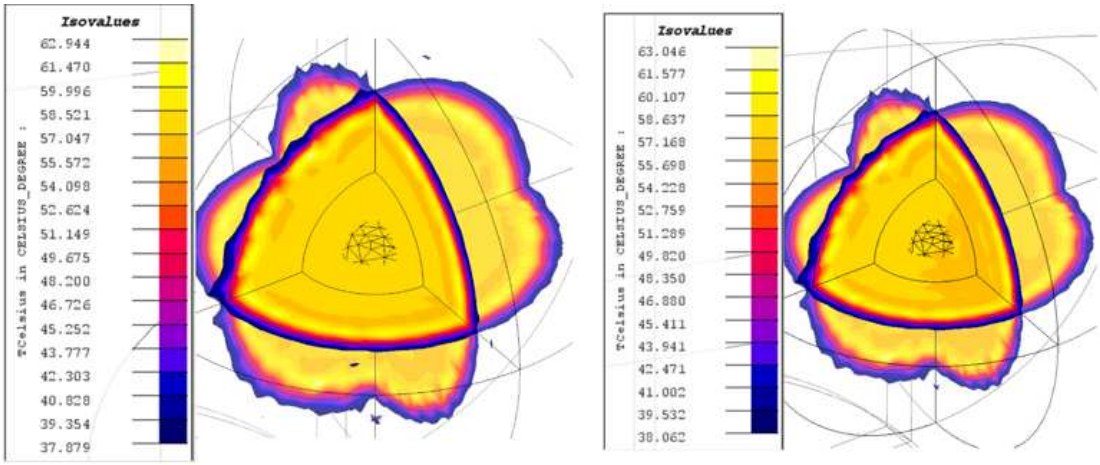

(a) (b)

Figure 8.13: Temperature distribution after 10 s in the tumor region. (a) Uniform field, (b) non uniform field.

Table 8.3: Power density and SAR due to magnetic field h and the one due to magnetic nanoparticles.

Non uniform I_1=1000Arms, I_2=500Arms				
POWER_T1	**P_H [W]**	**P_NP [W]**	**SAR H [W/kg]**	**SAR_NP[W/kg]**
POWER_LIVER	514.8	--		
POWER_T1_NP	0.25	41.9	6.1	1023.3
POWER_T2_NP	4.60	489.1	9.6	1024.7
POWER_T3_NP	88.3	3765.2	24.3	1034.3
uniform I_1=1000Arms, I_2=500Arms				
POWER_T1	**P_H [W]**	**P_NP [W]**	**SAR H[W/kg]**	**SAR_NP[W/kg]**
POWER_LIVER	12.1	--		
POWER_T1_NP	10	289.3	254.8	7065.2
POWER_T2_NP	157	3374	328.3	7068.7
POWER_T3_NP	2.327	25735.2	639.3	7069.2

Figure 8.13 shows the temperature distribution in the tumor region in the case of uniform and non uniform magnetic field. The power due to the nanoparticles only has been compared with the one due to the magnetic field *H* only. Data for uniform and non uniform coil configurations are reported in Table 8.3. The power released to tissues due both to the magnetic field *H*, *P_H*, and the nanoparticles, *P_NP*, has been expressed in terms of the

Specific Absorption Rate (SAR). In Table 8.3 *SAR_H* and *SAR_NP* are the SAR due to magnetic field *H* and that due to nanoparticles, respectively. The SAR has been computed as the power released to the tissue mass by both the energy sources, *i.e.* the *H* field and the nanoparticles. In the case of uniform field the SAR due to nanoparticles is between 11 and 27 times the one due to the magnetic field *H*. Then, synthesized field produces a higher nanoparticle SAR than the non uniform field.

8.3 Magneto-thermal coupled simulation

In the previous paragraph a first analysis of the magnetic field uniformity in the design of the time-varying magnetic field source has been presented. The uniformity of the heating depends on the magnetic nanoparticles distribution and characteristics. It is known that the power density generated by the nanoparticles depends on the magnetic field intensity in a non linear way. Then a non uniform magnetic field distribution can affect the temperature uniformity in a different way.

In order to take into account the magnetic field inhomogeneity in the optimization of the therapeutic temperature distribution, a coupled magnetic and thermal problem is proposed [249]. The design variables, shown in Figure 8.5, are the positions of winding coils, *z* and *dz*. In a real-life application, the radius of coils R_1 is constant and fixed to the value found in the previous analysis, but the coil distance can be tuned as a function of the patient size. As a consequence, the correction coils are positioned in order to improve thermal field uniformity. In this case the main coils carry 250 A_{rms} (13 turns), whereas the correcting ones carry 125 A_{rms} (10 turns).

In this paragraph a non-deterministic optimization algorithm was linked with a code for three-dimensional FEA of the coupled magnetic-thermal field. In principle, the objective function, to be maximized, is the temperature uniformity in the cancer tissue, giving a prescribed temperature value. The controlled region is constrained to be isothermal to a therapeutic temperature (*e.g.*, 42°C or >60 °C), whereas the healthy tissues is constrained to be at a safety temperature (lower than 40 °C). In practice, in view of the winding design, the magnetic inhomogeneity, U_M, and the thermal one, U_T, are both evaluated by means of the following equations:

$$U_M(z, dz) = \frac{H_{max} - H_{min}}{H_{mean}} \tag{8.35}$$

$$U_T(z, dz) = \frac{T_{max} - T_{min}}{T_{mean}} \tag{8.36}$$

where H_{max}, H_{min}, T_{max}, T_{min} are maximum and minimum values of the magnetic field and the temperature in the controlled region, respectively; in turn, H_{mean} and T_{mean} are the average values of magnetic field and temperature in the same regions. The inhomogeneity of the temperature is computed after a time transient of 300s. Therefore, the inverse problem can be formulated as follows: given nanoparticles diameter and concentration, starting from an initial solution, find *z* and *dz* such that U_M and U_T are minimized.

8.3.1. Optimization algorithm

In Figure 8.14 the flow chart of the optimization procedure is described [249]. The simulation strategy implements two steps; the first step implements the magnetic field analysis, while the second step implements the thermal field analysis in order to simulate the

temperature distribution in the target region. At first step of the analysis, a time-harmonic regime is considered for magnetic analysis. In the first algorithm run, the position of the coils is set at the initial values. The magnetic problem is solved using the total magnetic scalar potential (equations (4.33)-(4.36) in the conductive region and (4.40) and (4.41) in air region), and in the post-processing the absolute value of the magnetic field distribution is exported and saved. In this step the inhomogeneity of the magnetic field is computed using (8.35) and stored. Accordingly, the power density generated by means of the nanoparticles is obtained by means of equation (8.26) and (8.27). By this way, a non-linear thermal transient problem in the interval from 0 to 300 s is solved. Then, the inhomogeneity of the thermal field is computed using (8.36) and stored. At this point, using the Evolution Strategy algorithm, a new set of values for the optimization variables is chosen and used in order to update the position of the coils.

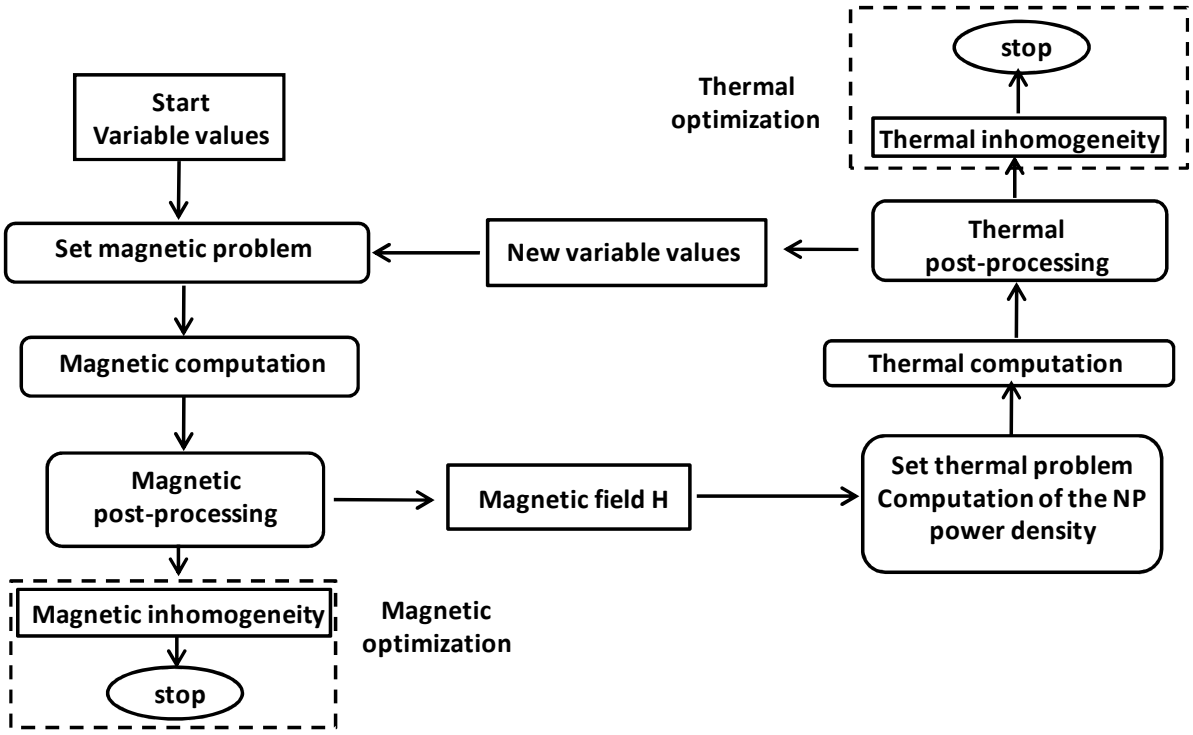

Figure 8.14: Optimization procedure flow-chart.

8.3.2. Multiobjective optimization: some results

In Table 8.4 the results of the two optimization strategies, in terms of thermal and magnetic field, are reported. It is pointed out that the inductor coils have different position if either the temperature inhomogeneity is searched for, or the magnetic field inhomogeneity is the target (Figure 8.15). The starting point is the same for both the two optimization strategies.

Table 8.4: Coils position for two optimized solutions. z and dz in [mm] U_M and U_T computed using (8.35) and (8.36).

	Start		**Stop**			
	z	***dz***	***z***	***dz***	U_M	U_T
Thermal inhomogeneity	250	150	378	0.23	$1.84 \cdot 10^{-2}$	$8.85 \cdot 10^{-3}$
Magnetic inhomogeneity	250	150	174	276	$1.09 \cdot 10^{-4}$	$5.49 \cdot 10^{-2}$

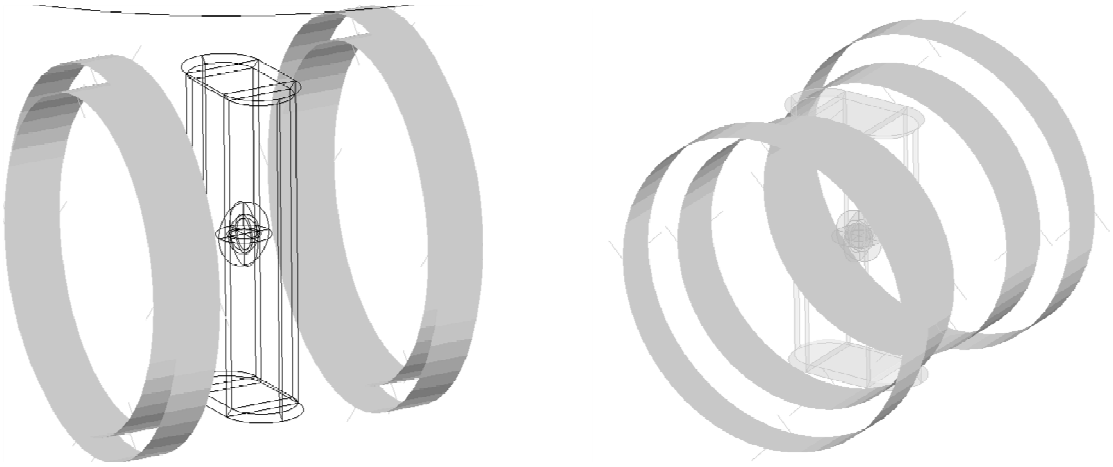

(a) (b)

Figure 8.15: Coils position for the two optimization strategies. (a) Thermal optimization and (b) magnetic optimization.

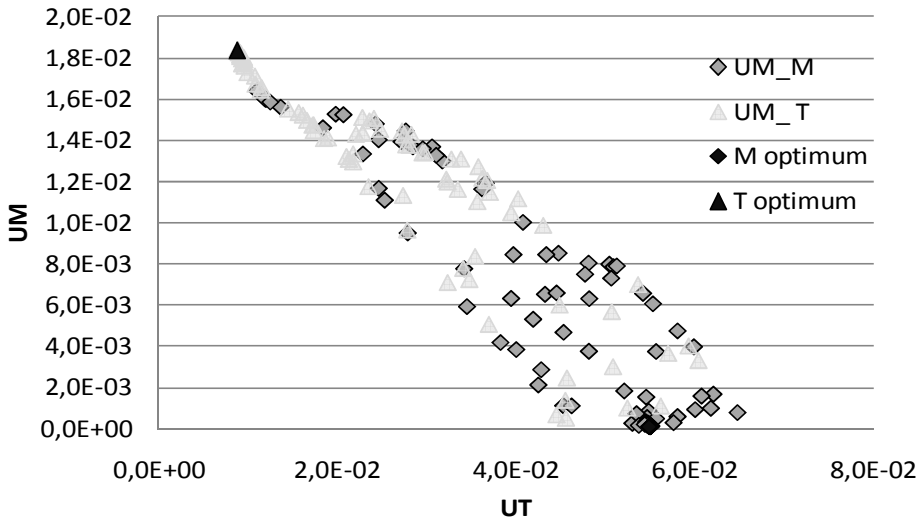

Figure 8.16: Pareto front.

In Figure 8.16 the two objective functions Pareto front is shown. The two solutions found during the optimization process for the magnetic uniformity as a function of the thermal uniformity are reported. The corresponding optimum values are black points, “H optimum” for the minimization of the magnetic uniformity, U_M-oriented strategy, and “T optimum” for the minimization of the thermal uniformity, U_T-oriented, and corresponds to two different corners of the chart. In Figure 8.17 the magnetic field and final treatment temperature is reported for both the two optimization strategies. The value of the optimized magnetic field is different for the two strategies and also its behavior in the optimization region. Also the temperature has a different target values: lower in the temperature optimization, and higher in the magnetic field optimization. This fact is correlated to the magnetic field value higher in the second case (4000 A/m versus 1400 A/m).

In Figure 8.18 three orthogonal directions along which the magnetic field and temperature are evaluated are shown. In Figure 8.19 the values of magnetic field and temperature sampled along the directions in Figure 8.18 are reported for the optimization on temperature and on magnetic field, respectively. This shows the effect of the winding shape design. It should be noted that the optimization on the temperature inhomogeneity gives a lower magnetic field value (average value close to 1395 A/m), and the average temperature in the controlled region after 300 s is close to 39,2°C. In turn, after optimizing the magnetic field inhomogeneity, the

average magnetic field is close to 3577 A/m and the average temperature in the same time interval is 60,1°C. The two optimization strategies, without constraint on field amplitude or on temperature at the end of the transient, give different therapeutic temperatures. According to the U_T-oriented strategy the temperature is near the one of mild hyperthermia, whereas according to the U_M-oriented strategy the temperature is close to the ablation threshold.

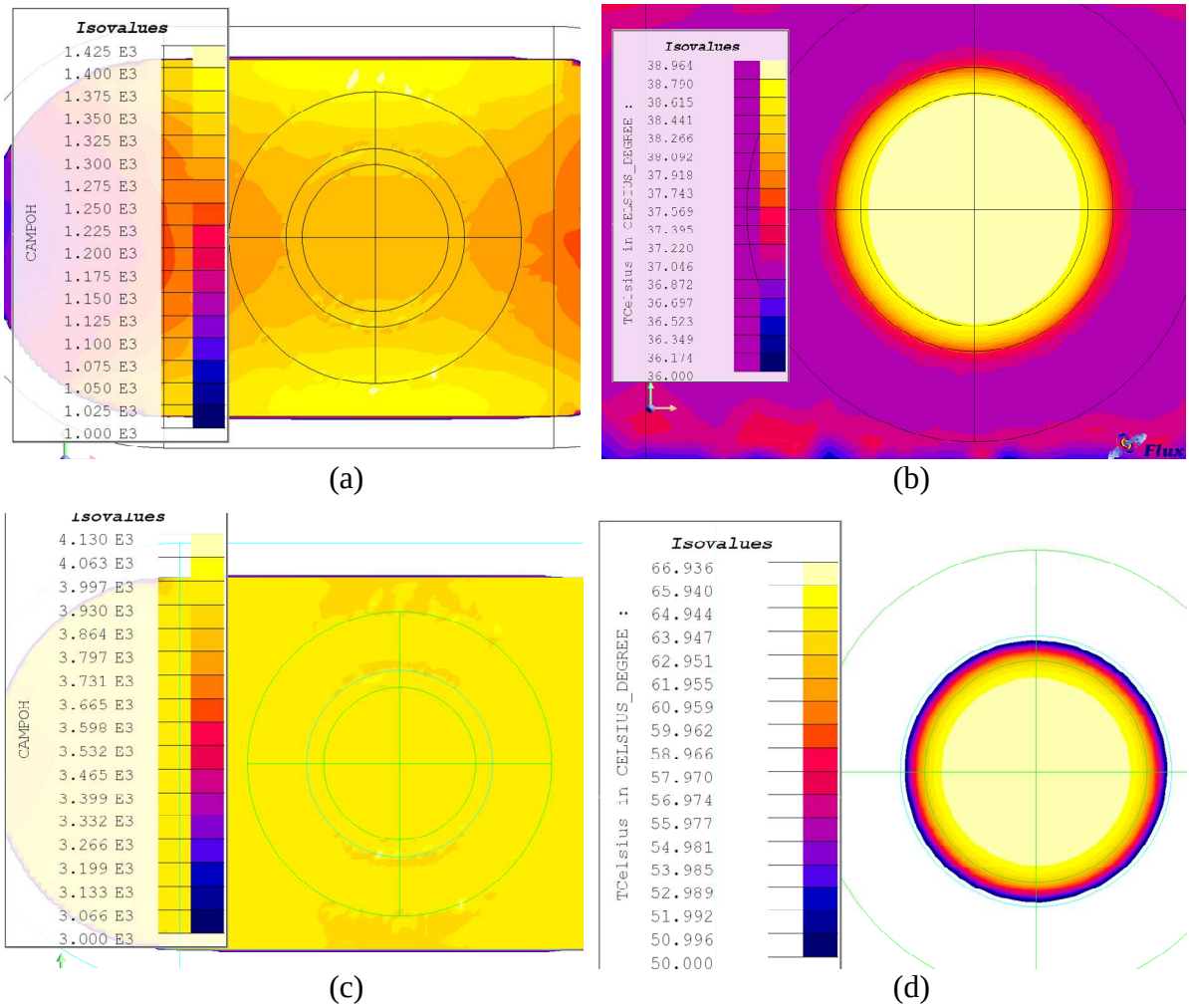

Figure 8.17: Magnetic field and temperature obtained with the two optimization strategies. (a), (b) Magnetic field and temperature for thermal optimization and (c), (d) magnetic field and temperature for magnetic optimization.

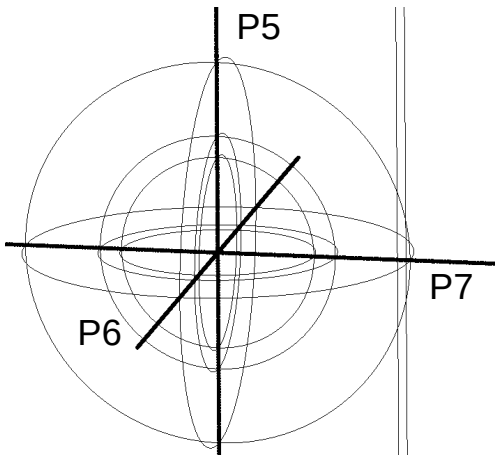

Figure 8.18: Directions along which the magnetic field and temperature are sampled.

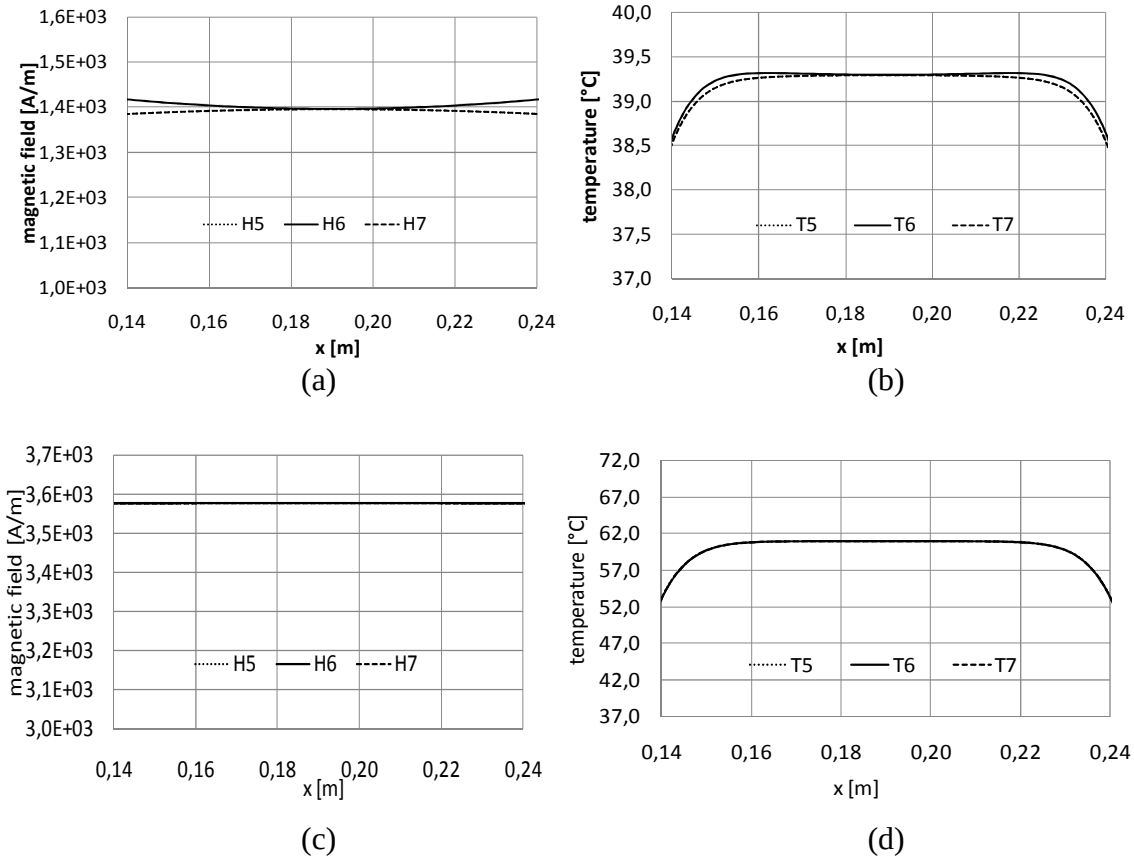

Figure 8.19: (a) Magnetic field and (b) temperature, for the optimization in the temperature inhomogeneity; (c) magnetic field and (d) temperature, for the optimization in magnetic field inhomogeneity.

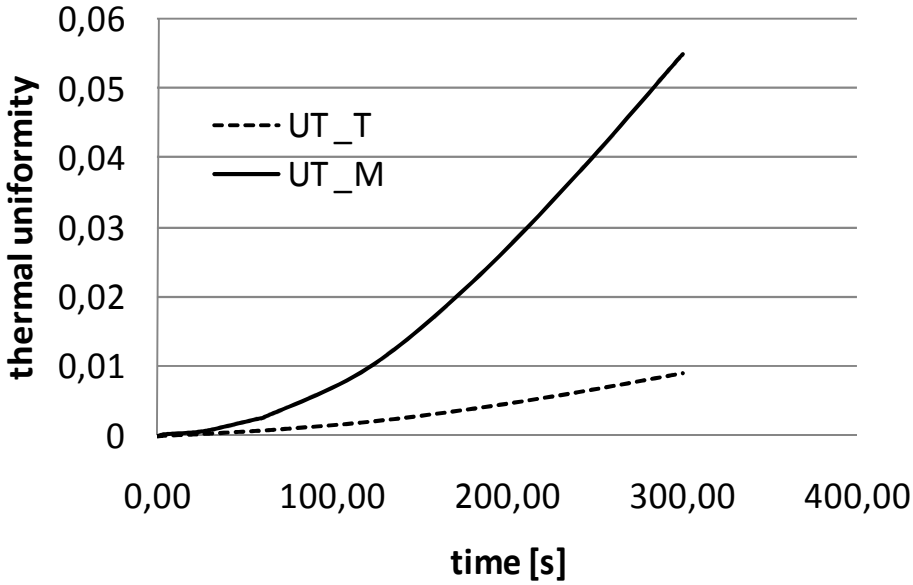

Figure 8.20: Thermal inhomogeneity as a function of time.

At the end, Figure 8.20 shows the thermal inhomogeneity as a function of the time transient interval, for both the optimization strategies, to give an idea of the time response of the synthesized device.

8.4 Thermal simulation: magnetic fluid characteristics and thermal response optimization

The power density generated by means of magnetic nanoparticles depends on nanoparticles diameter and concentration. These two variables affect the temperature rate in the tumor region and can be considered in the magnetic fluid design [250].

The magnetic field source is the one in Figure 8.21. The radius of the main coils, *i.e.* the internal ones, has been fixed to 48 cm as it has been found in [251] (*see* paragraph 8.2.2). The external coils are the secondary ones. The region Ω_T is the target region, *i.e.* the tumor, which should be appropriately heated. In this case the optimization variables are the positions of main, *z* variable, and secondary coils, *dz* as in Figure 8.18. The patient is supposed to be accommodated along the *r* axis. The height of main and correcting coils is set according to paragraph 8.2.2. The main coils carry 250 A_{rms} (13 turns), whereas the correcting ones carry 125 A_{rms} (10 turns).

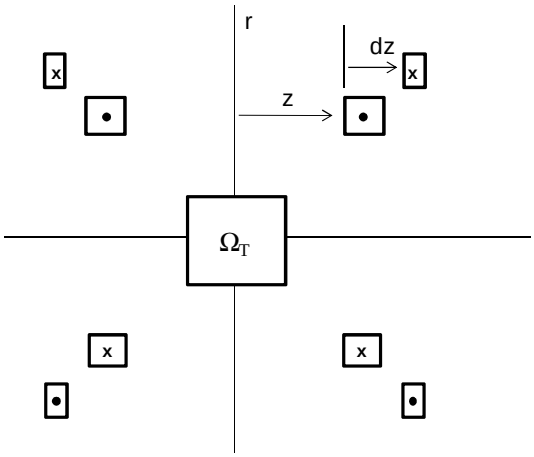

Figure 8.21: Geometry of the coils, controlled region Ω_T=tumor.

8.4.1. Optimization problem

In this model the magnetic field intensity is governed by an optimized winding configuration as it has been studied in previous paragraphs. It should be noted that the power density deposed in tissues by means of the nanoparticles (equation (8.26)), and so the temperature in the tissues, depends on the magnetic fluid characteristics as in (8.27)- (8.31). Let assume a uniform distribution of mono-dispersed nanoparticles, the target is found the characteristics of the magnetic fluid, concentration and nanoparticles diameter that allow the increasing of the tumor temperature with a suitable rate. The optimization procedure is based on a sequence of thermal analyses, with the aim of sizing the magnetic fluid concentration and nanoparticle diameter too. The objective function computation calls a FEA tool [251] solving three-dimensional transient thermal problems.

The temperature rate, which is a function of both the nanoparticle diameter and the nanoparticle concentration in the magnetic fluid, (*see* equations (8.27)- (8.31)), is a quantity of interest in the treatment planning. In fact, the temperature of the tumor region during the therapeutic treatment is supposed to reach 42°C in a few minutes, but not too quickly. Then, the magnetic fluid characteristics must be synthesized in order to have a prescribed temperature rate.

The temperature rate computation can be approximated *e.g.* by means of the average temperature of a sub-region included in the Ω_T volume, say Ω_{T1}. The average temperature, T_m, in the Ω_{T1} region is computed in two subsequent instants, t_1 and t_2; accordingly, the temperature rate is defined as:

$$\Delta T(\Omega_{T1}) = \frac{T_m(t_2) - T_m(t_1)}{t_2 - t_1} \tag{8.37}$$

In Figure 8.22 the temperature rate is reported as a function of the nanoparticle diameter for a magnetic field of 3500 A/m at 450 kHz for five nanoparticle concentrations. The perfusion term and thermal characteristic are taken into account. After Figure 8.22 it can be pointed out that at least two optimal pairs of the optimization variables might exist, that can produce the same temperature rate.

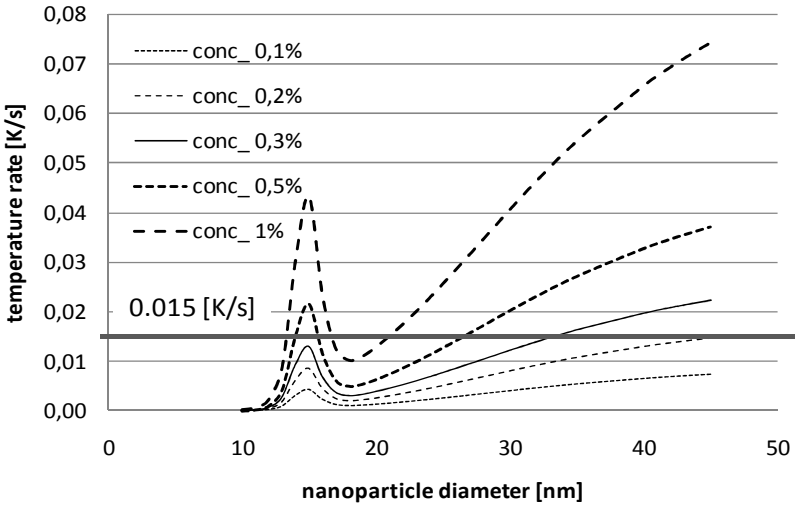

Figure 8.22: Temperature rate as a function of NP diameter for various concentrations.

In Figure 8.23 an example of the temperature rate is reported as a function of the time in a 300s treatment. The diameter of the nanoparticle is 18.7 nm and the concentration is 1.36 %. In this case the maximum temperature after 300s is 41.1 °C. The initial temperature rate is 0.004 K/s; the maximum rate occurs at 44 s and is 0.015 K/s. Initially, the temperature increases slowly, but after 40 s the temperature rate tends to a regime value. In the following, the temperature rate is evaluated at 30 s.

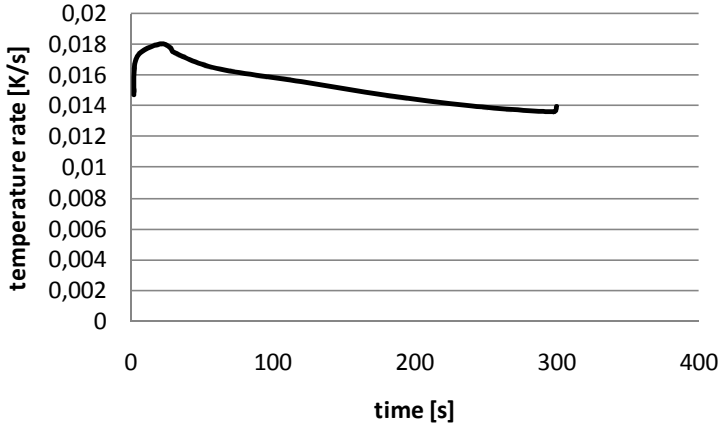

Figure 8.23: Temperature rate until 300s of treatment.

8.4.2. Optimization process

Using an Evolution Strategy algorithm [251] the optimal value of diameter and concentration giving the prescribed temperature rate is searched for. In particular the optimization algorithm searches a minimum of the discrepancy between the actual temperature rate and the prescribed one, say ΔT^*. So, the inverse problem reads:

$$find \quad \inf_{\Omega_{T1}} F(\phi, D) \quad \text{with} \quad F(\phi, D) \equiv |\Delta T(\Omega_{T1}) - \Delta T^*| \tag{8.38}$$

The design variables for the optimization procedure are the magnetic fluid nanoparticles concentration, ϕ, and the nanoparticles diameter, D. In the case considered, a uniform distribution of the nanoparticles in the treatment region is assumed.

Table 8.5: Optimization results found with the Evolution Strategy algorithm.

D [nm]	**ϕ [%]**	**ΔT(t=2s) [K/s]**	**ΔT(t=30s) [K/s]**	**ΔT(t=300s) [K/s]**	**T_{max} [°C]**	**P_c [W/m^3]**
18.7	1.36	0.00402	0.015	0.01357	41.200	595481
13.97	0.4869	0.0039	0.01499	0.01356	41.197	649001
18.88	1.339	0.00403	0.01501	0.01359	41.204	596531
39.29	0.2257	0.00623	0.01497	0.013398	41.189	275607
44.88	0.196	0.00688	0.01498	0.01336	41.19	254310
16.44	0.839	0.00397	0.01498	0.01355	41.194	628001
28.5	0.3998	0.00473	0.015	0.0135	41.201	383391

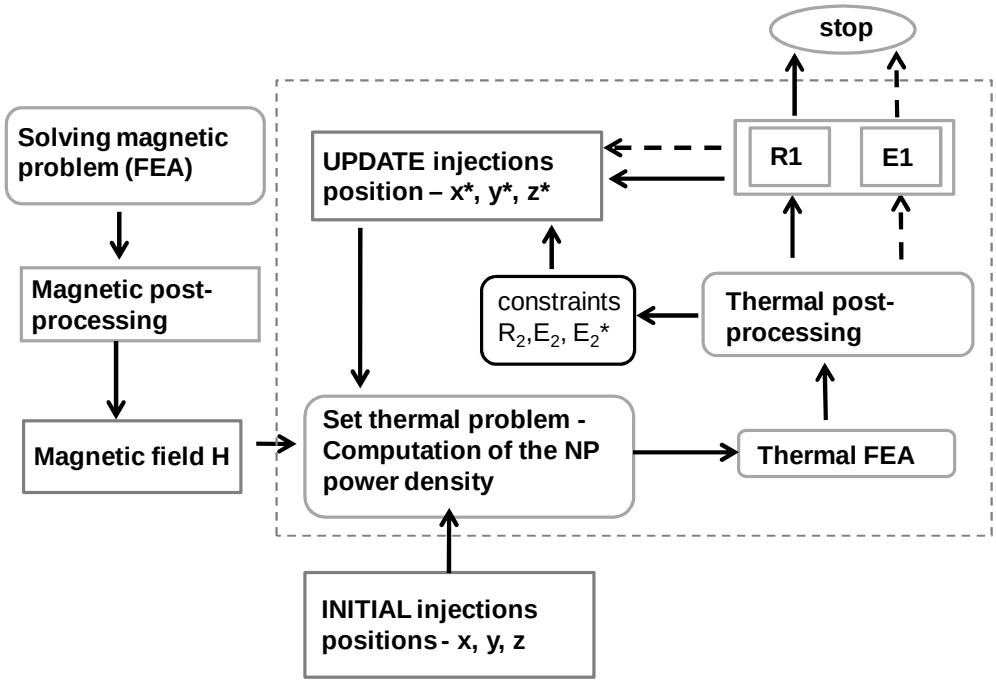

Figure 8.24: Flow chart of the optimization process.

In Table 8.5 some possible optimal solutions are reported. The value of the optimization variables, (D, ϕ), the temperature rate at 2s, 30s, and 300s, $\Delta T(t=t_i)$, the final temperature in the optimization volume, T_{max}, and the power density in the tumor centre, P_c, are reported, respectively. It can be pointed out that different pairs of radius and concentration of NP can be a possible solution of the optimization problem for the same temperature rate. Referring to Figure 8.22 optimal nanoparticles diameters, D, at the right and left of the peak are found. For lower diameters the optimal concentration is higher than the one found for nanoparticles with a bigger diameter. The power density deposed by means of nanoparticles with smaller diameter is higher than the one deposed by nanoparticles with bigger diameter. Moreover, it is interesting to note that the perfusion term, w_b in (8.37), is non linear with the temperature in the range of the treatment [198] (Table 3.6).

In Figure 8.24 the flow diagram of the optimization process is reported. The magnetic problem is solved using a previous optimized source. The spatial magnetic field distribution is used in order to compute the power density deposed by means of the nanoparticles using equation (8.27). A thermal transient problem is solved and the temperature rate has been evaluated. From the actual value of the temperature rate at the end of the transient process a new set of nanoparticles characteristics are chosen and the nanoparticles power density is recomputed. The algorithm stop when the temperature rate reaches the one desired for the therapy.

8.4.3. Optimization results

In Figure 8.25 the history of the temperature value during the optimization process is reported. In Figure 8.26 and Figure 8.27 the temperature in a layer of the tumor region and along two normal directions inside the volume are shown. The temperature is evaluated after 30 and 300 s of treatment in the case of an optimal values of nanoparticles concentration and diameter (D = 18.7 nm, $\phi(\%)$ = 1.36%), respectively.

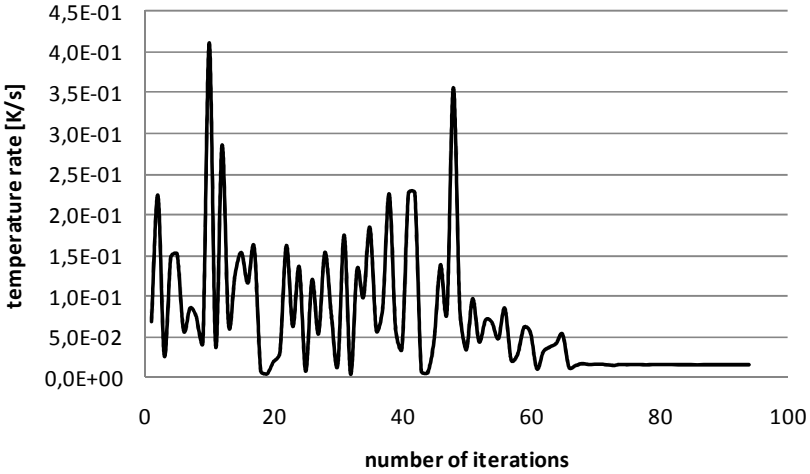

Figure 8.25: Optimization history: temperature rate as a function of iteration number.

In spite of the fact that the inverse problem depends on two variables only, it is probably an ill-posed one, because multiple optimal solutions are found. In the positive, this feature makes the thermal response control easier. In fact, magnetic fluid with different characteristics can be chosen for different type of tissues. Since the diffusion coefficients are different for different tissues [128], [252], the concentration of nanoparticles can be adjusted for different tissues.

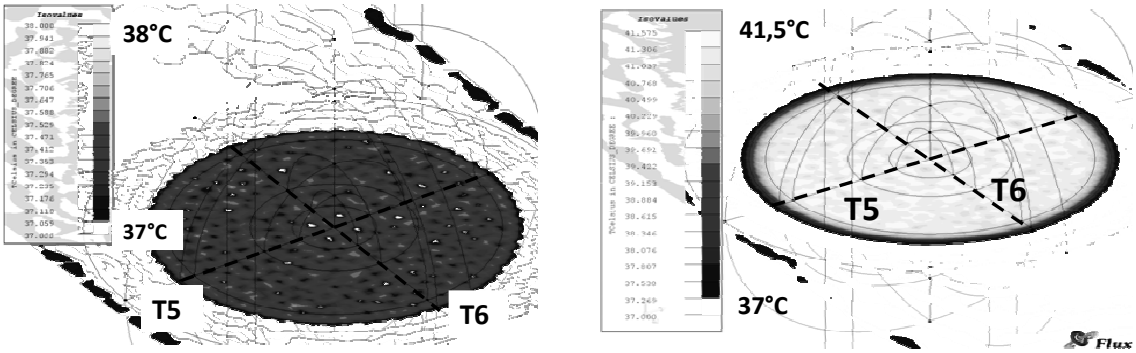

(a) (b)

Figure 8.26: Color map of temperature in a layer of the tumor region at (a) 30s and (b) 300s.

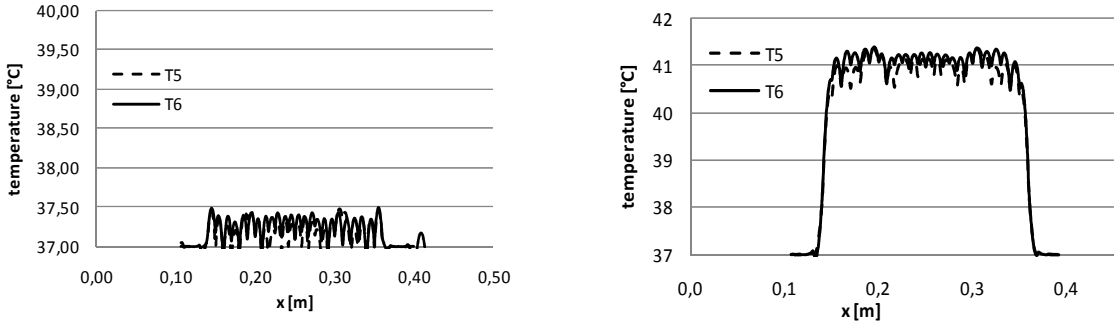

(a) (b)

Figure 8.27: Temperature along directions in Figure 8.10 at (a) 30 s and (b) 300 s. Continuous line T6 and dotted line T7.

8.5 Optimization of the spatial distribution of nanoparticles in tumor tissue

In Magnetic Fluid Hyperthermia the temperature in the tumor region depends on the nanoparticles concentration [106], [240]. Then, even if the magnetic field is more as possible uniform in the treating zone the thermal field might not have the same uniformity degree due to a non uniform distribution of nanoparticles in the tissues. Usually nanoparticles are administered by means of localized multi-site injections in the tumor mass [86]. In this case the drug diffuses from the injection point towards the tumor mass boundaries. At parity of quantity of the administered drug the local concentration is modified as a function of the time and spatial coordinates because nanoparticles diffuse on the tissues. As a first approximation a Gaussian shape function can be hypothesized for the tissues nanoparticles spatial concentration due to tissue diffusion. In [122] a thermal problem is solved considering a non uniform distribution of the nanoparticles power density evaluated experimentally [123], [124]. This power distribution is used in [122] to optimize the position of nanoparticles injections in order to satisfy some therapeutically constraints on the tumor temperature. The Evolution Strategy optimization [215] is used in order to find the position of a limited number of nanoparticles injections to have a tumor temperature near the therapeutic value. The real nanoparticles distribution is considered in the power density computed like in [106], [240].

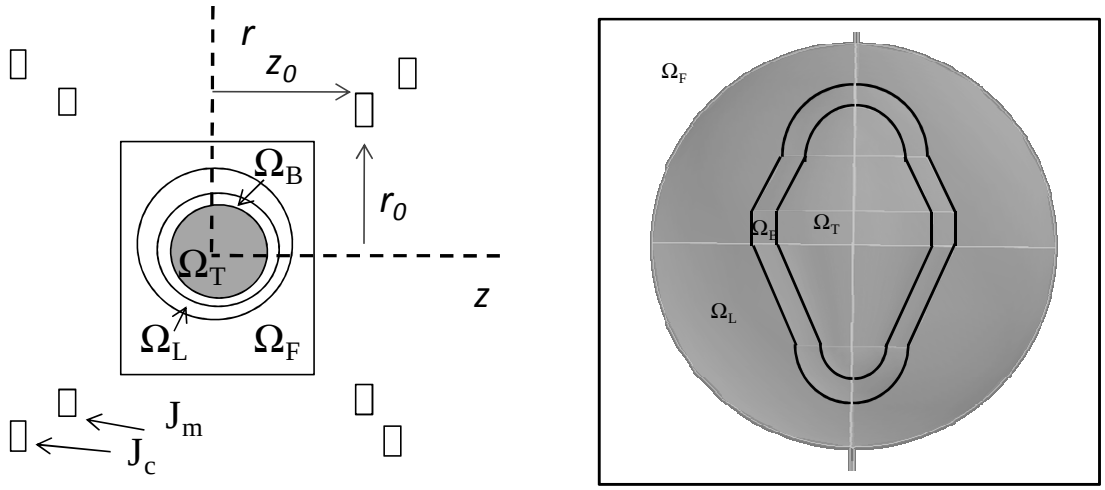

(a) (b)

Figure 8.28: Geometry of the (a) MFH devices and (b) the target volume shape.

The magnetic field source is composed of four concentric coils as represented in Figure 8.28 (a). The radius of the main coils, *i.e.* the internal ones, J_m, in Figure 8.28 (a), has been fixed to 48 cm as it has been found in a previous study [251]. The external coils are the secondary ones, J_c. The region Ω_T is the target region, *i.e.* the tumor, which should be appropriately heated. The optimization variables are firstly the positions of the nanoparticles injections (*x*, *y* and z coordinates), and the dispersion, σ, that is the Gaussian standard deviation that describe the nanoparticles dispersion on the tissues. The patient is supposed to be accommodated along the *r* axis and the height of main and correcting coils is set according to a previous investigation [251]. The main coils carry 250 A_{rms} (13 turns), whereas the correcting ones carry 125 A_{rms} (10 turns). The targeting area has an elongated form like in Figure 8.28 (b) and simulate an irregular shape tumor mass. The central volume, Ω_T, is the tumor region that must be heated by means of the nanoparticles, the surrounding volume, Ω_B, is a volume of the healthy tissues in which the temperature increasing must be limited in order to avoid damages in the healthy tissues volume, Ω_L. The Ω_F region in Figure 8.28 (a) is a region of healthy tissue around the target organ. In this case a tumor in the abdominal cavity region (in the liver) is considered and thermal properties have been suitable set.

8.5.1. The solved equations and design functions

The aim of the design is to search the optimal position of nanoparticles injections in order to have, as far as it is possible, a uniform distribution of the temperature field taking into account the real distribution of the magnetic nanoparticles in the tumor and limit the heating of the healthy tissues. The optimization procedure is based on a sequence of transient thermal analyses, with the aim of placing two nanoparticles distributions with the same initial concentration. The objective function computation calls a FEA tool [122], [249], [250] solving three-dimensional transient thermal problems for a time interval of 300 s.

The solved equation is the Fourier equation with the blood perfusion term (4.57) in which the term *P* is the nanoparticles power density evaluated considering the local nanoparticles concentration, $\phi=f(x,y,z)$:

$$P(x,y,z,H,\phi(x,y,z)) = \pi\mu_0\chi''(x,y,z,H,\phi(x,y,z))fH^2(x,y,z) \tag{8.39}$$

in which $H(x,y,z)$ is the intensity of the magnetic field that depend on the spatial coordinates (x,y,z), f the frequency of the field H and χ'' the imaginary part of the magnetic susceptivity that depends on the field H and the local concentration of nanoparticles, $\phi(x,y,z)$:

$$\begin{aligned}\chi''(\phi(x,y,z),H,\omega,\tau) &= \chi_0(\phi(x,y,z),T,H)f_1(\omega,\tau)\\ &= \chi_i\big(\phi(x,y,z)\big)f_3(T)f_2(\xi(H,T)f_1(\omega,\tau)\end{aligned} \tag{8.40}$$

where function f_2 depends on the Langevin parameter, ξ, which in turn depends on field intensity, H, and temperature, T, while function f_1 depends on field pulsation, ω, and nanoparticles relaxation time, τ, and f_1 on temperature only. Whereas the initial magnetic susceptibility written highlining the nanoparticles concentration is:

$$\chi_i\big(\phi(x,y,z,\sigma)\big) = \phi(x,y,z,\sigma)\frac{\mu_0 M_d^2 V_m}{3kT} \tag{8.41}$$

where the spatial function of the nanoparticles concentration has a Gaussian shape with σ the standard deviation that describes the nanoparticles dispersion from the injection center. For an injection point *j* the nanoparticles concentration is:

$$\phi_j(x,y,z,\sigma) = \phi_0 e^{-\frac{1}{2}\left(\frac{(x-\eta_{j,x})^2}{\sigma^2}+\frac{(y-\eta_{j,y})^2}{\sigma^2}+\frac{(z-\eta_{j,z})^2}{\sigma^2}\right)} \tag{8.42}$$

with ϕ_0 is a constant concentration and $\eta_{j,i}$, i=x,y,z, the coordinates of the injection point. The 8.42) is written under the hypothesis that the diffusion speed is equal for the three orthogonal directions. The diffusion along one of the main direction is uncorrelated with the one along the other directions. Let consider multiple injections points, N, the concentration ϕ of nanoparticles in a volume is the superposition of N Gaussian function like the (8.42):

$$\phi(x,y,z,\sigma) = \sum_{i=1}^{N} \phi_i(x,y,z,\sigma) \tag{8.43}$$

The design problem is the maximization of the sub-volume that have a temperature rise upper to a given threshold in the tumor region and a tumor surface temperature as more as possible uniform and near to the previous threshold. The first objective function evaluates the volume of the sub-region of the tumor region that has a temperature higher than 42°C. The objective is maximizing the sub-volume in which the temperature is upper to the threshold. The volumes are evaluated sampling the considered region in a uniform way and counting the sample that satisfies the prescribed constraint:

$$R_1(T) = 100 \cdot \frac{N_T(T > 42)}{N_{T,tot}} \tag{8.44}$$

where N_T is the number of the temperature samples in the tumor region Ω_T for which the temperature is higher than 42°C, whereas $N_{T,tot}$ is the number temperature samples considered in the all tumor region, Ω_T.

The second objective function is evaluated on the tumor surface. The aim of this second objective function is uniform the temperature on the tumor surface, S, at a threshold value:

$$E_1 = \frac{1}{(37-T_n)^2}\sum_{j=1}^{M}(T_j - T_n)^2 \tag{8.45}$$

where M is the number of the temperature sample, T_j, considered on the tumor surface, T_n is the temperature threshold (42°C). The objective function is minimizing the (8.45).

Moreover, in addition to the objective functions R_1 and E_1, some secondary constraints have been defined:

$$R_{2,S}(T) = 100 \cdot \frac{N_S(T > 41.5)}{N_{S,tot}} \tag{8.46}$$

The constraint $R_{2,S}$ is evaluated on the surface of the tumor, S, and considers how many point in the tumor boundary are higher than a threshold value lower than the minimum temperature considered in the tumor region, 41.5°C.

$$E_{2,B}(T) = \frac{1}{(38-T_n)^2}\sum_{j=1}^{Q}(T_j - 38)^2 \tag{8.47}$$

The second constraint $E_{2,B}$ and $E_{2,B}^*$ evaluates, respectively, the same function like the objective function E_1 and R_1 in the healthy tissue around the tumor volume region, Ω_B. In the former the difference in the sum is between the temperature in one of the Q points in the volume and the prescribed threshold for this region (38°C). In this case the temperature T_n is

42°C. The last constraint evaluates the percentage volume that has a temperature upper to the prescribed threshold for this region (38°C).

$$E^{*}_{2,B}(T) = 100\frac{N_B(T>38)}{N_{B,tot}} \tag{8.48}$$

Alternatively in the Ω_B region the sub-volume with a temperature less than 38°C can be evaluated. The constraint can be rewritten like the E_3:

$$E_{3,B}(T) = 100\frac{N_B(T<38)}{N_{B,tot}} \tag{8.49}$$

If the reference value of the desired temperature in the Ω_B region is fixed to 40.5°C the constraint is the E_4:

$$E_{4,B}(T) = 100\frac{N_B(T<40.5)}{N_{B,tot}} \tag{8.50}$$

$$E^{*}_{4,B}(T) = 100\frac{N_B(T>40.5)}{N_{B,tot}} \tag{8.51}$$

Some possible threshold values for the constraints are analyzed in the following.

8.5.2. The optimization procedure

At first the effect of the standard deviation on the (8.42) has been studied. Figure 8.29 (a) shows the position of two symmetric points, P_1 and P_2, along the *z* axis. In the Figure 8.29 (b) the temperature corresponding to a standard deviation of 0.025 m is reported in a section of the target volume.

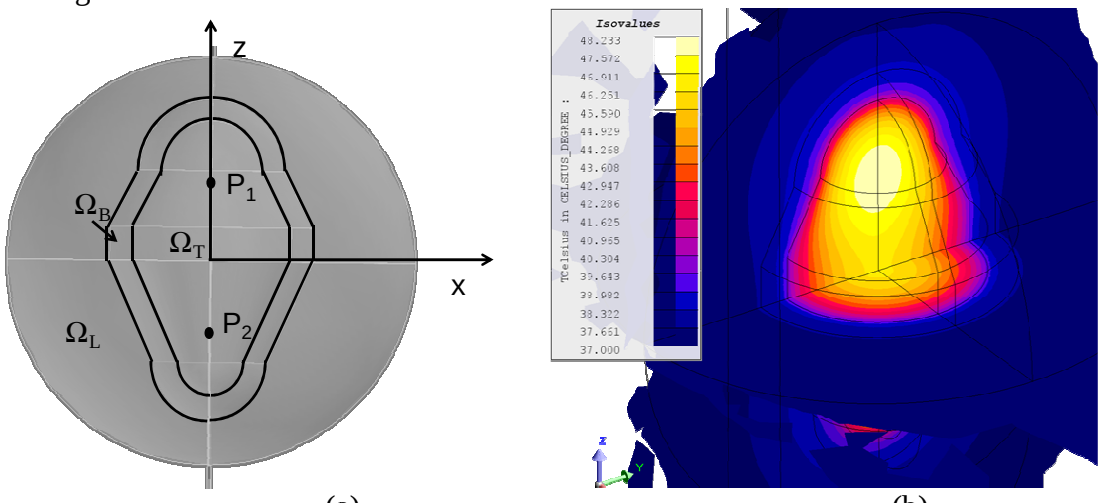

(a) (b)

Figure 8.29: (a) Geometry considered in the optimization process and (b) temperature obtained with the nanoparticle injections position in (a).

It can be pointed out that a higher concentration of the nanoparticles around the point P_1 generates a higher temperature value in the same areas. In Figure 8.31 (a) and (b) are reported, respectively, the nanoparticles concentration and temperature along the *z* axis in Figure 8.29 (a). The temperature value in treated volume is linked to the local nanoparticles concentration. Moreover, more the Gaussian function is spread in the space, higher is the effect of the superposition of more functions that describe the different injections of the nanoparticles. In

the point P_1 in Figure 8.29 (a) the total nanoparticles concentration is the sum of the one injected in the point P_1 and the one that has been diffused from the point P_2. This effect is shown in Figure 8.31 (a) where, at parity of the initial nanoparticles concentration, increasing the value of the standard deviation, σ, that describes nanoparticle diffusion, higher is the maximum of the nanoparticles local concentration. That is higher is the value of σ higher is the effect of the second injection in the local concentration. In the reported case the standard deviation, σ, of the nanoparticles injected on the point P_1 and P_2 in Figure 8.29 (a) varies between 2.5 cm and 5.5 cm. Figure 8.31 (b) shows the temperature that corresponds to a particular nanoparticles concentration: the temperature follows the nanoparticles concentration shape.

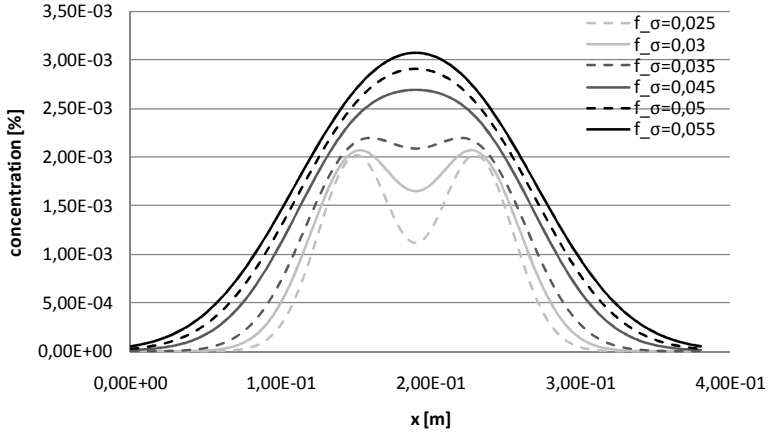

Figure 8.30: Nanoparticle concentration.

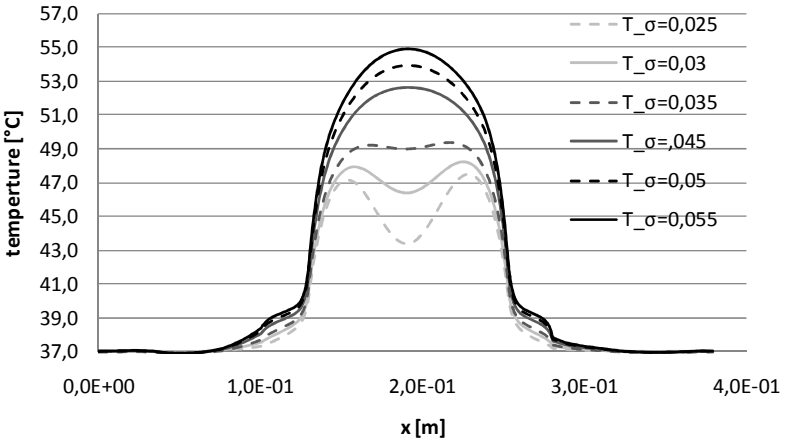

Figure 8.31: Temperature reached with concentration in Figure 8.30.

Table 8.6: Effect of standard deviation in (8.42) on objective functions and constraints.

σ[mm]	**R_1 [%]**	**R_2 [%]**	**E_2**	**E_2* [%]**	**E_2**
25	51.0	5357.27	3.0	75.0	21831
30	74.0	2110.69	22.0	92.0	37830
35	89.0	467.69	62.0	100.0	62454
45	99.0	1310.32	100.0	100.0	130444
50	100.0	2999.98	100.0	100.0	168482

In Table 8.6 the values of the objective functions (8.44)-(8.45) and constraints (8.46)-(8.48) for different values of the standard deviation σ are reported. The R_1 and E_2 values

increase with the increasing of the standard deviation, σ, whereas R_2 has a minimum for a standard deviation set to 35 mm.

A first optimization design searches the maximum of the R_1 function, whereas a second optimization strategy minimizes the E_1 function starting from the same initial point. A flow chart of the optimization procedure is reported in Figure 8.32.

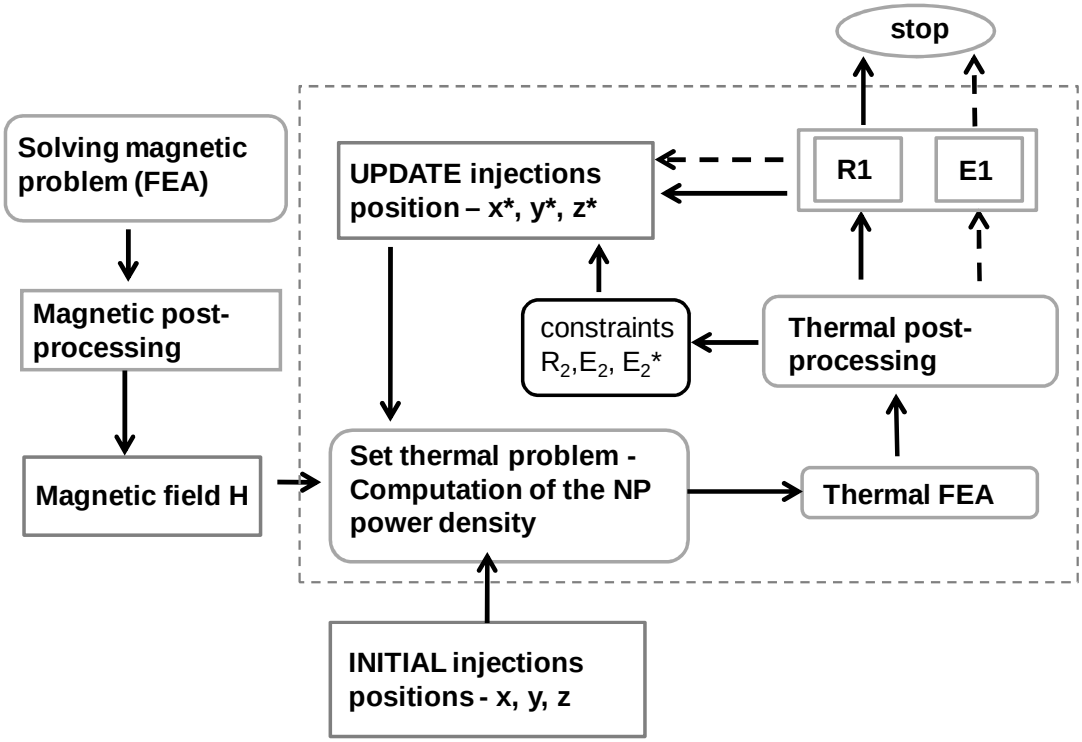

Figure 8.32: Flow chart for the optimization process.

The magnetic problem is solved using FEA algorithms in the domain of the Figure 8.28 (a) in order to compute the magnetic field intensity in the tumor and surrounding healthy tissues. From the magnetic field problem results a transient thermal problem is solved in order to study the distribution of the nanoparticles that are the power density source. Then, the input of the transient thermal problem is the power source (8.39) evaluated from the magnetic field intensity and the real distribution of nanoparticles described by means of the (8.42) and (8.43). From the thermal solution at 300 s the objective functions (8.44) and (8.45) and the constraints (8.46)-(8.51) are evaluated. In Figure 8.32 the solid and dotted lines show two different single objective optimization strategies, the one based on the function (8.42) and the other on the (8.43). Both the constraints and the objective functions act in the selections of the new points $P_i(x,y,z)$, $P_i(x,y,z) \in \Gamma$, inside the spaces of the parameters, Γ. In this case the two stopping criteria are:

$$P_i(x,y,z) = find\ max_{\ \Gamma} R_1 \tag{8.52}$$

or

$$P_i(x,y,z) = \ find\ min_{\ \Gamma} E_1 \tag{8.53}$$

The $P_i(x,y,z)$ is a valid point if the following constraints subsist:

$$P_i(x,y,z) \in \Gamma \tag{8.54}$$

In Table 8.7 the range of variability for the spatial variables are reported, whereas in Table 8.8 an example of two couples of optimized solutions, “point A” and “Point B”, found starting the optimization process from two different starting points is shown. The results of the objective functions (8.44)-(8.45) and the constraint values (8.46)- (8.51) corresponding to the optimization process starting from, respectively, the “point A” and “Point B”, are reported in Table 8.9 and Table 8.10.

Table 8.7: Range of variability of the injection point coordinates.

Variable	Min [mm]	Max [mm]
x_1	-25	25
y_1	-25	25
z_1	-50	+50
x_2	-25	25
y_2	-25	25
z_2	-50	+50

“Stop R1” and “Stop E1” in Table 8.8 are the optimized solution found searching, respectively, the maximum of the R1 and the minimum of the E1 objective functions (8.44) and (8.45).

Table 8.8: Coordinates of the starting point and corresponding result optimizing R1 or E1 objective function.

	POINT A [mm]			POINT B [mm]		
Variable	**start**	**Stop R1**	**Stop E1**	**start**	**Stop R1**	**Stop E1**
x_1	15.00	12.39	9.46	5.00	4.95	-5.06
y_1	-18.00	3.11	-1.52	7.00	6.96	11.12
z_1	-45.00	-13.86	-29.86	-15.00	-15.01	-28.61
x_2	-10.00	-6.96	-11.21	-5.00	-4.99	5.76
y_2	-9.00	0.77	3.06	-5.00	-4.99	-12.35
z_2	43.00	31.17	37.78	10.00	9.92	37.28

In Table 8.9 and Table 8.10 the values of the objective functions (8.44) and (8.45), the constraints (8.46)- (8.51) and the thermal uniformity (8.36) are reported for the optimization on the R1 (first row) and E1 (second row) functions.

Table 8.9: Objective function and constraint value for two optimal solutions starting the optimization process from the point A.

	R_1 [%]	E_1	R_2 [%]	E_2*[%]	E_2	E_3 [%]	E_4 [%]	E_4*[%]
R1	93.0	1377.5	79.0	97.0	90644.3	2.0	71.0	28.0
E1	91.0	397.83	70.0	100.0	68628.6	0.0	76.0	23.0

Table 8.10: Objective function and constraint value for two optimal solutions starting the optimization process from the point B.

	R_1 [%]	E_1	R_2 [%]	E_2*[%]	E_2	E_3 [%]	E_4 [%]	E_4*[%]
R1	93.0	2860.8	78.0	95.0	112438.1	4.0	68.0	31.0
E1	91.0	476.4	68.0	100.0	68603.4	0.0	76.0	23.0

The R_1 value is higher than 90 %. This value means that some points in the treatment region Ω_T have a temperature higher than 42°C. Let consider the constraint R_2 results that almost the 70% of the tumor surface has a temperature upper to 41.5°C. Whereas the minimum found for the E_1 function limits the distance between the threshold and actual temperature on the tumor surface, S. The $E_2 - E_4$ constraints limit the temperature in the Ω_B region, the control region around the tumor region Ω_T. The threshold value at 38 °C for this region is too much strong and a relaxed value of 40.5°C can be used. In the following suitable threshold values are analyzed for the proposed constraints.

8.5.3. Optimization results

Figure 8.34 reports the Pareto front of the R_1 objective function as a function of the E_1 starting from the "Point A" and "point B". Pareto front and the domain of the possible solutions is shown. In this case the Pareto region is on the corner on the high and at the left in Figure 8.34. "E1_minimization" and "R1_maximization" correspond, respectively, to the E_1 and R_1 value in the points used in the optimization procedure using respectively the E_1 and R_1 objective function. "Start" is the value of the E_1 and R_1 functions at the initial point, whereas "R1_maximum" and "E1_minimum" are, respectively, the value of the R_1 and E_1 functions found optimizing on the R1 and E1 objective function.

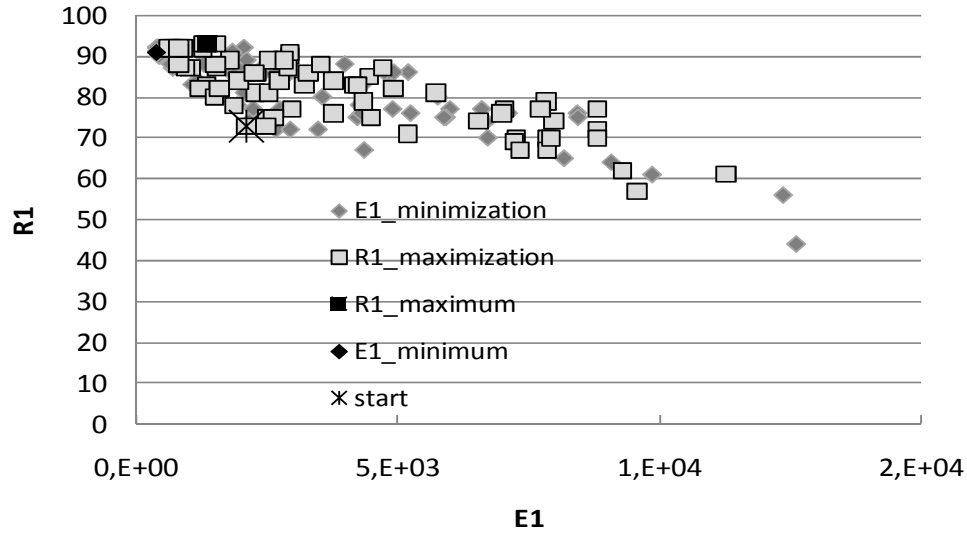

Figure 8.33: Pareto chart for starting point A.

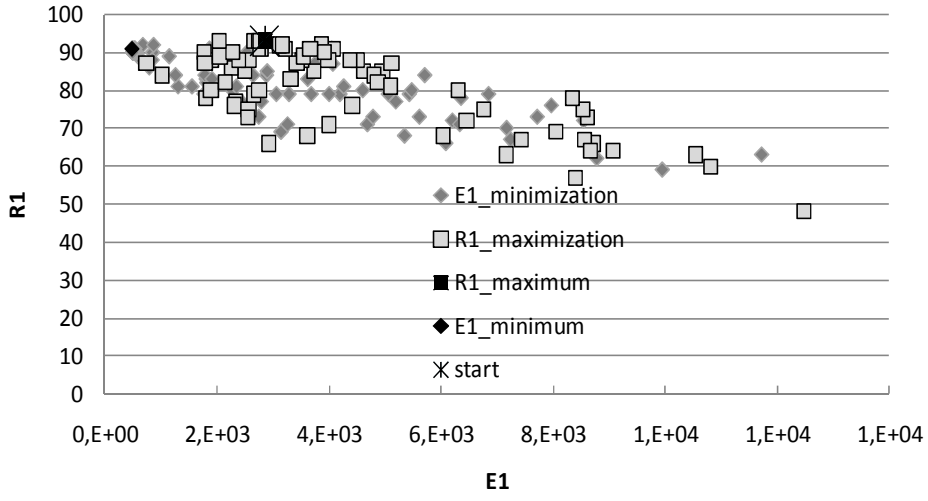

Figure 8.34: Pareto chart for starting point B.

In this case the Pareto front seems to have a corner in the left-high side of the chart in Figure 8.33 and Figure 8.34. Moreover the points with the R_1 upper to 90% are positioned in a line parallel to the abscissa axis.

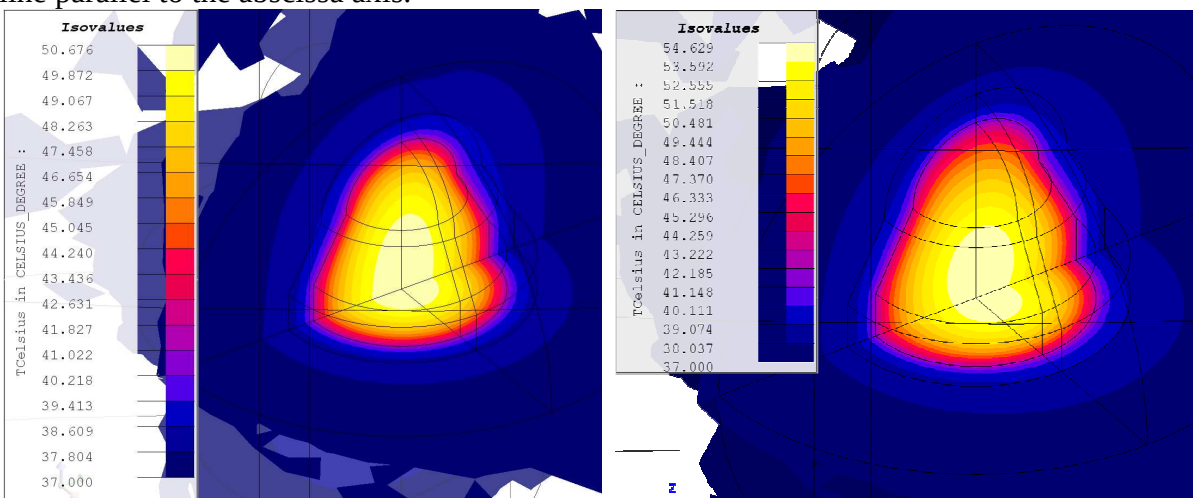

(a) (b)

Figure 8.35: Temperature using the start point A (a) E1 optimization and (b) R1 optimization.

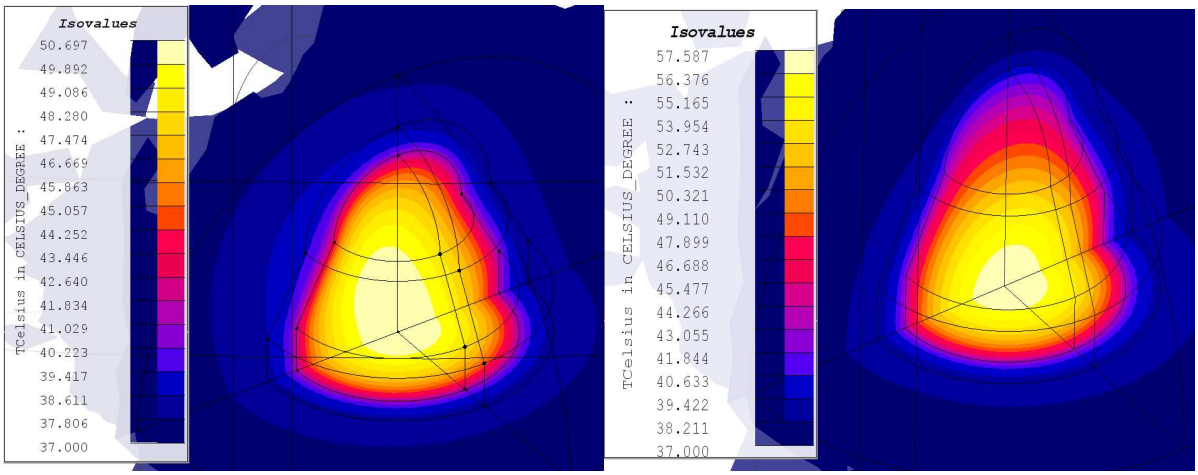

(a) (b)

Figure 8.36: Temperature using the start point B (a) E1 optimization and (b) R1 optimization.

a. Optimization on the R1 function

In Figure 8.37-Figure 8.40 the values of the function (8.46) and constraint functions (8.47)-(8.51) and the uniformity temperature (8.36) evaluated during the searching of the optimum of the R1 objective function, (8.44), are reported. The black square represents the optimum value found at the end of the optimization process. Each point of the diagram represents a different position of the nanoparticles injections.

Analyzing Figure 8.37-Figure 8.40 a suitable threshold of the constraint function (8.47) - (8.51) can be found. R_2 constraint represents the temperature at the tumor surface and evaluates the area that reaches the fixed threshold. A possible threshold for this index might be 65%, and then a solution can be considered acceptable if almost the 65% of the tumor surface is higher than 41.5°C.

The constraints E_2 and E_2* evaluate the temperature in the boundary region around the tumor. In this case the temperature of this region might be up to 38°C. The E_3 is the complementary index of E_2 and estimates the sub-volume in which the temperature is under 38°C. These constraints functions have not a high sensibility.

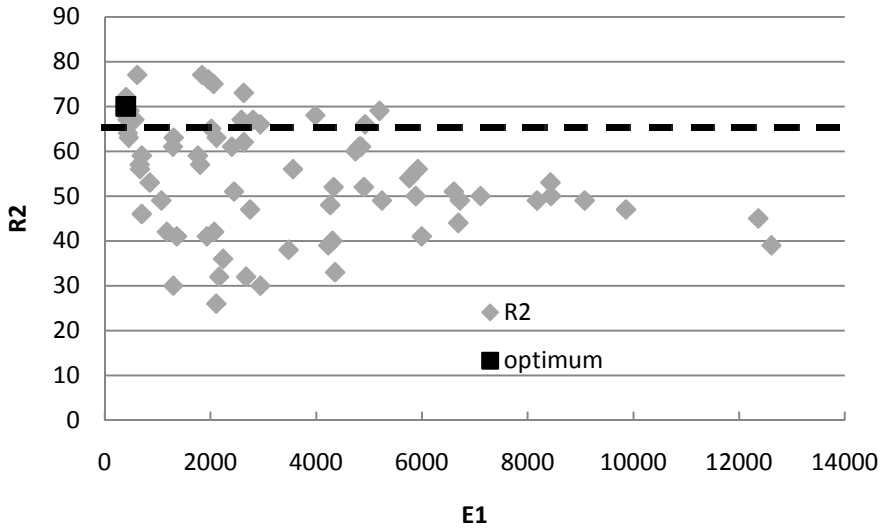

Figure 8.37: R_2 constraint as a function of the E_1 objective function.

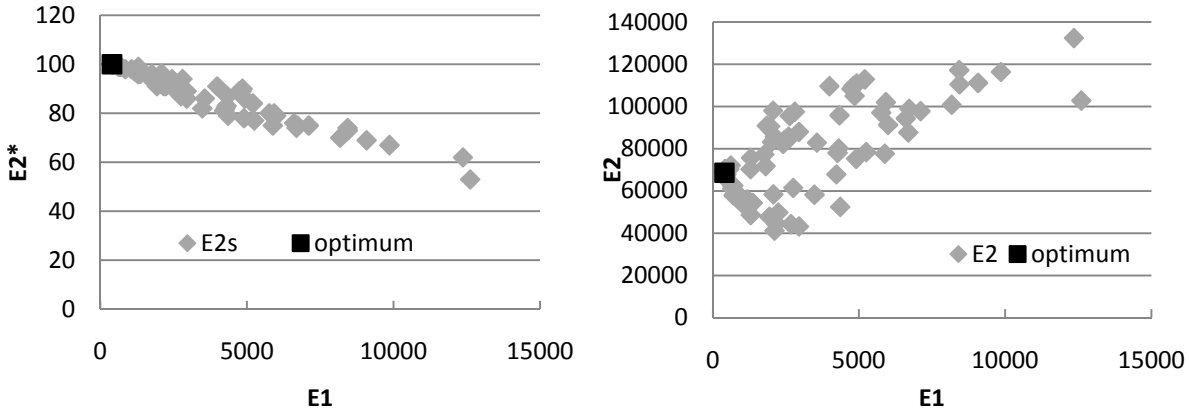

(a) (b)

Figure 8.38: (a) E_2* and (b) E_2 constraints as a function of the E_1 objective function.

The E_4 constraint considers a target temperature in the boundary region Ω_B of 40.5°C. The (8.50) and (8.51) are complementary then the possible threshold values are, respectively, above 75% and below 25 %.

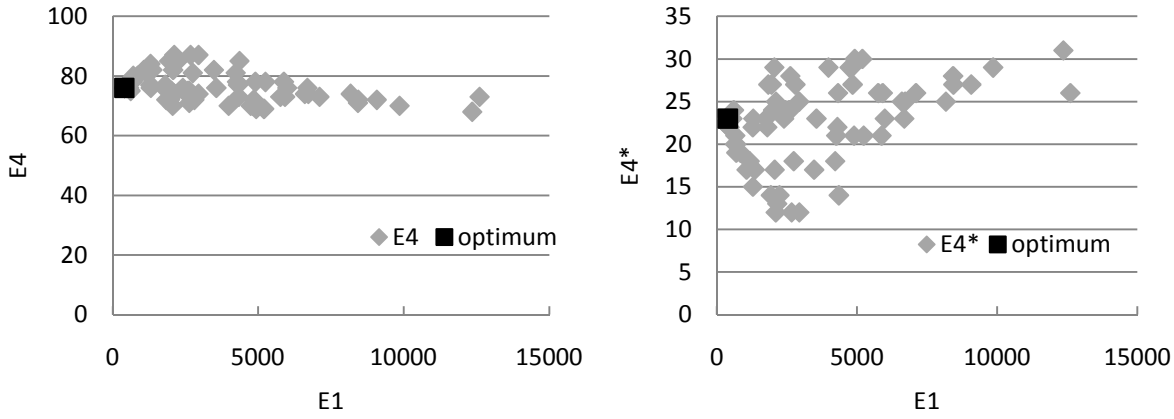

(a) (b)

Figure 8.39: (a) E_4 and (b) E_4*constraints as a function of the E_1 objective function.

b. Optimization on the E1 function

The constraint R_2 analyzes the temperature at the surface of the tumor region. The temperature in this region must be almost near to a predefined threshold. In order to avoid too high temperature in healthy tissue the threshold is fixed 0.5°C lower (*i.e.* 41.5°C) than the minimum required in the tumor region (42°C).

Figure 8.40 shows the values of the constraint R_2 as a function of the R_1 objective function. The black point shows the optimum point evaluated minimizing the R_1 objective function. The optimal point corresponds to a R1 value of 80 % which means that almost the 80% of the tumor surface has a temperature almost of 41.5°C.A possible threshold for the constraint R_2 is 70%; then, a solution for the R_1 objective function is valid if the value of the R_2 function is above 70%. This is equivalent to consider that the 70% of tumor surface has a temperature higher than the threshold considered in this analysis (41.5°C).

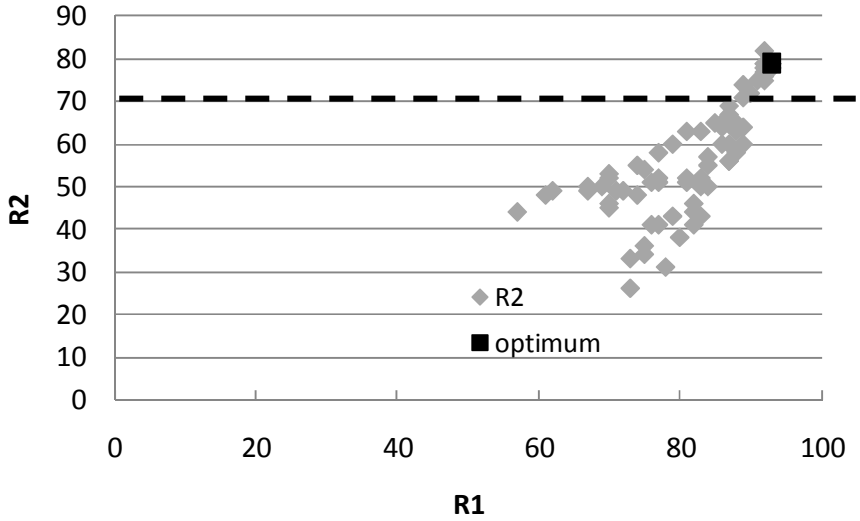

Figure 8.40: R_2 constraint as a function of the R_1 objective function.

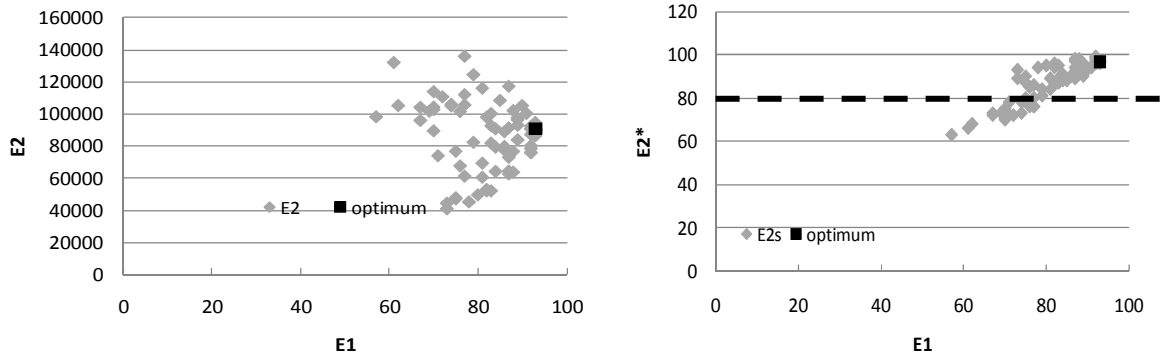

(a) (b)

Figure 8.41: (a) E2 and (b) E2* constraints as a function of the R1 objective function.

In Figure 8.41 the E_2 and $E^*_{2,B}$ constraints are shown as a function of R_1 objective function. The $E^*_{2,B}$ constraint evaluates the temperature on the healthy tissues region Ω_B. This constraint evaluates the number of points under a predefined threshold temperature (*e.g.* 40° C). Also the third constraint E_2 considers the volume of the healthy tissue Ω_B around the tumor region and impose that the temperature of each point is near to a predefined threshold value (38°C). So the sum of the square of differences between the temperature value in each point and the

threshold value might have a minimum value. In this case the E_2 function is not at its minimum value for the optimized point (black point). In this case the constraint $E^*_{2,B}$ constraint assumes a value above 80% which means that a lot of points in the considered region have a temperature above 38°C.

The E_4 constraints (Figure 8.42) evaluated the sub-volume of the boundary volume around the tumor region in which the temperature is above 40.5°C. This sub-volume might be as well as small it is possible in order to limit any heat damage of the healthy tissues. In this case the optimum value optimizing on R1 function is on the maximum of the constraint value E_4^* that is a minimum of the E_4 constraint. Using the E_4 constraint, that search all point under a threshold temperature, the number of points that satisfy the constraint is close to 70%.

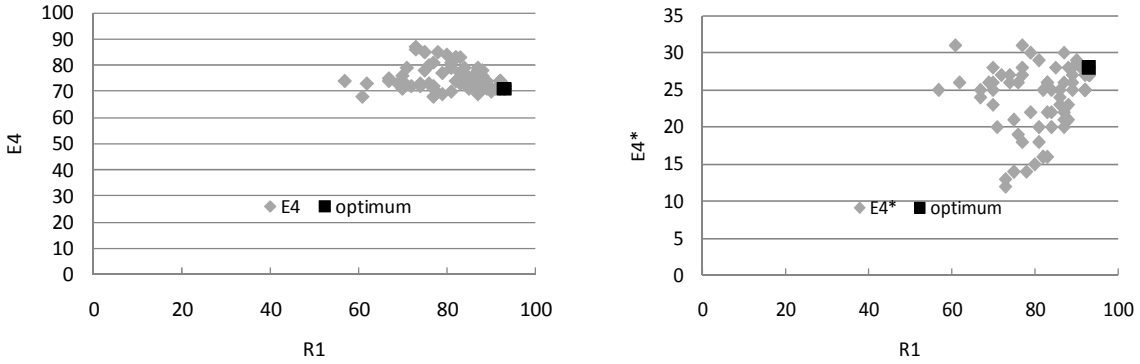

(a) (b)

Figure 8.42: (a) E_4 and (b) E_4*constraints as a function of the E_1 objective function.

The limitation of the temperature on the healthy tissue Ω_B region is not so easy to reach using only two injection points.

8.6 Conclusions

Multiobjective optimization techniques have been used in order to design Magnetic Fluid Hyperthermia devices. Both magnetic field source and power density source, that generates the therapeutic heat, have been designed. Therefore, different objective functions have been used in order to design the magnetic field source and the magnetic fluid composition. Magnetic and thermal coupled problems have been implemented in a Finite Element Analysis tool in order to solve numerically the problem. In particular, the electromagnetic and thermal problem solver was run in a multiobjective optimization core.

The magnetic problem has been solved in order to compute the magnetic field intensity that heats the magnetic nanoparticles. The thermal problem has been solved imposing the heat source. In this case the heat source is the power density generated by means of the nanoparticles. This power density has been computed by means of an analytical relation that is a function of nanoparticles characteristics, magnetic field intensity and frequency, nanoparticle concentration and temperature. In order to consider the real distribution of the nanoparticles their concentration has been described as a function of the spatial coordinates onsidering their diffusion from the injection point.

The implemented optimization procedures can be also used in order to adapt the magnetic field source to the patient size or target area that must be treated.

Chapter 9

9 Electromagnetic fields in medical applications: electric field applications

Electric field can be used to stimulate brain cells. In this example an evaluation of the possibility to reach the internal structure of the brain with an electric field enough intense to allow the cell stimulation is proposed. The electric field can be applied by means of two or more electrodes on the surface of the head.

Numerical analysis on real models of the head of living organisms (human and rat) has been conducted in order to evaluate the effect on different positions of the electrodes on the skull in order to induce an electric field in the brain structures. It is to be noted that electrical characteristics of the tissues are a function of the frequency, and then a time-varying electric field have a different behavior.

In this case an experimental evaluation on a rat has been conducted in order to validate the simulation results. The measurement of the voltage induced in the internal structure of the brain by a voltage difference applied to the skull has been evaluated by means of suitable transducers.

9.1 Anatomical models for the simulation of the electric field

In Figure 9.1 a sketch of the anatomical model used in the computations is shown. Each tissue is described by its conductivity and dielectric permittivity. Given the voltage difference between the electrodes V_0 and V_1, the equation (4.55) is solved in order to find the electric field distribution in the tissues:

$$\nabla \cdot (-([\sigma] + j\omega[\varepsilon_r]\varepsilon_0)\nabla V) = 0 \qquad (4.55)$$

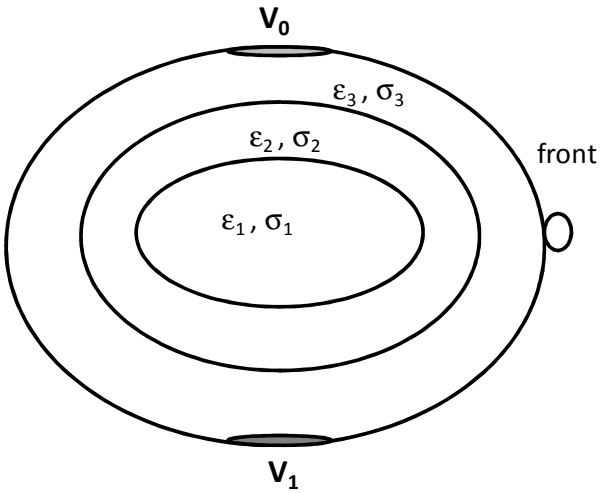

Figure 9.1: Anatomical model used in the electric field simulation.

A human and a rat head are taken into account in the computation. In this case the applied voltage is at 4 MHz. The electrical characteristics of the tissues used in the human head model are reported in Table 3.5, whereas the ones of the rat head are in Table 9.1.

The model of the rat head has been used in order to compare the voltages computed by means of the Finite Element model and the ones measured in a suitable measurement set-up.

Table 9.1: Electrical characteristics of the rat head tissues at 4MHz.

	4 MHz	
	σ [Sm^{-1}]	ε_r
BoneCortical	0.03443	68.73
BrainGreyMatter	0.2119	504.60
BrainWhiteMatter	0.1255	253.80
Cerebellum	0.2528	732.70
Dura	0.5125	231.80
Gland	0.6846	371.40
Muscle	0.5808	384.90
SkinDry	0.08823	653.80
SpinalChord	0.1842	317.40
Tongue	0.5154	529.40
Trachea	0.423	301.40
VitreousHumor	1.502	72.26

9.2 Computation results

The model of the human and rat head have been used in order to evaluate the electric field that can reach the internal area of the brain by means of numerical computation..

9.2.1. Scalar electric potential: computation of the electric field

A voltage difference applied to a conductive media generates an electric field. Let consider the model of a head in Figure 9.2. The computation region is a conductive media with the electrical characteristic of the brain tissue, the bone and head fluid (Figure 9.3). The areas indicated by arrows in Figure 9.2 and by the letter '*e*' in Figure 9.3 are the electrodes at which the voltage is applied.

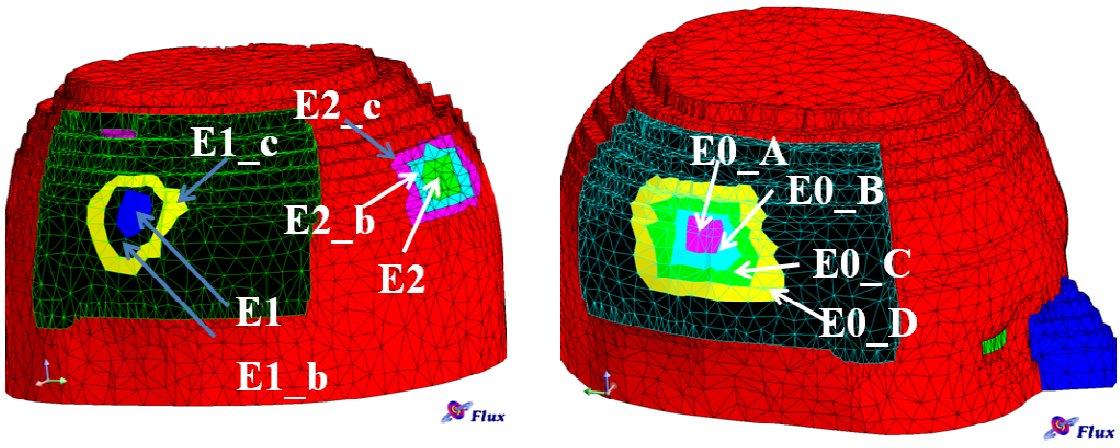

Figure 9.2: Model of an head for the computation of the electric field due to a voltage difference.

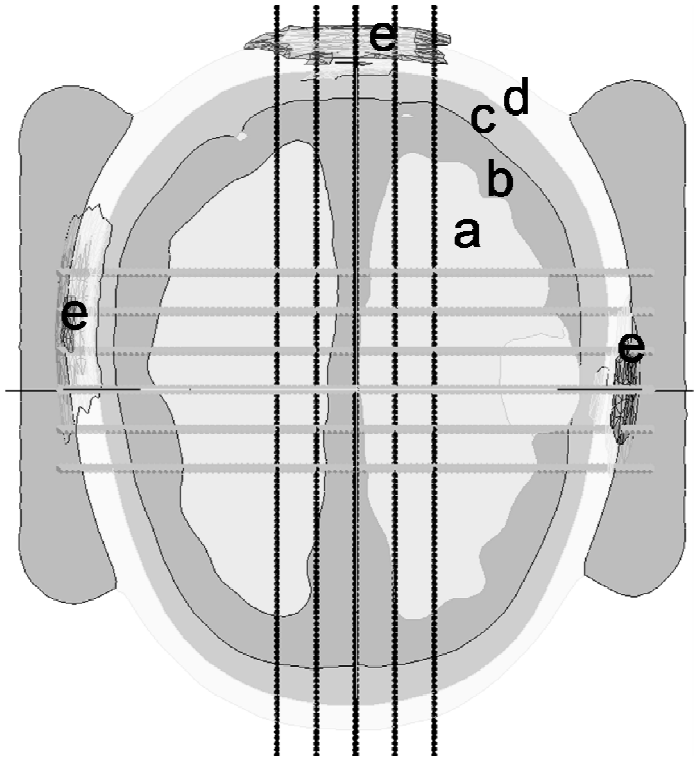

Figure 9.3: Section of the head. (a) gray matter, (b) white matter, (c) dura madre, (d) bone and (e) electrodes.

9.2.2. The distribution of the electric field in the tissues of the human head

Figure 9.4 shows the position of the electrodes on the human head. The target is to obtain a desired level of electric field on the central part of the brain in the area of the hippocampus. In this case a configuration with three electrodes has been analyzed. Two electrodes with the same polarity are on the parietal side of the head, whereas the third electrode, with inverse polarity, is in the occipital side of the head.

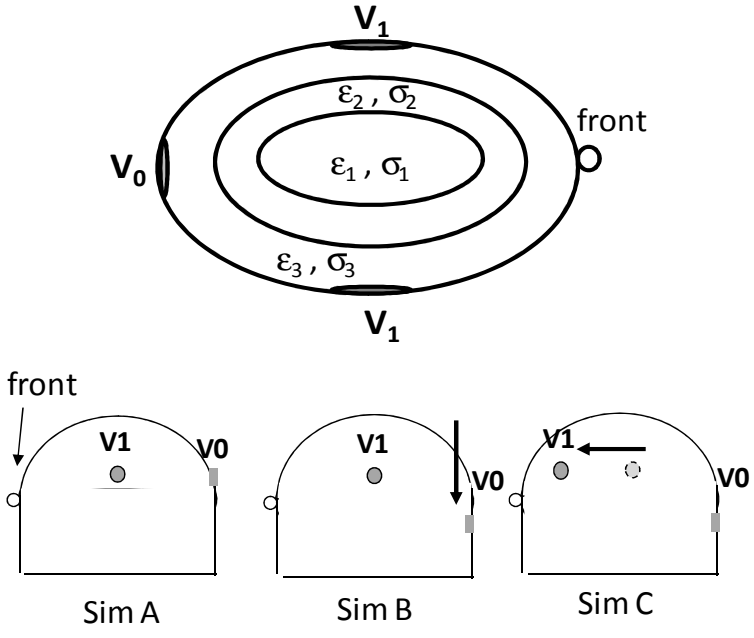

Figure 9.4: Position of the electrodes in the human head model.

In Figure 9.5 the layers and lines in which the electric field is sampled are shown.

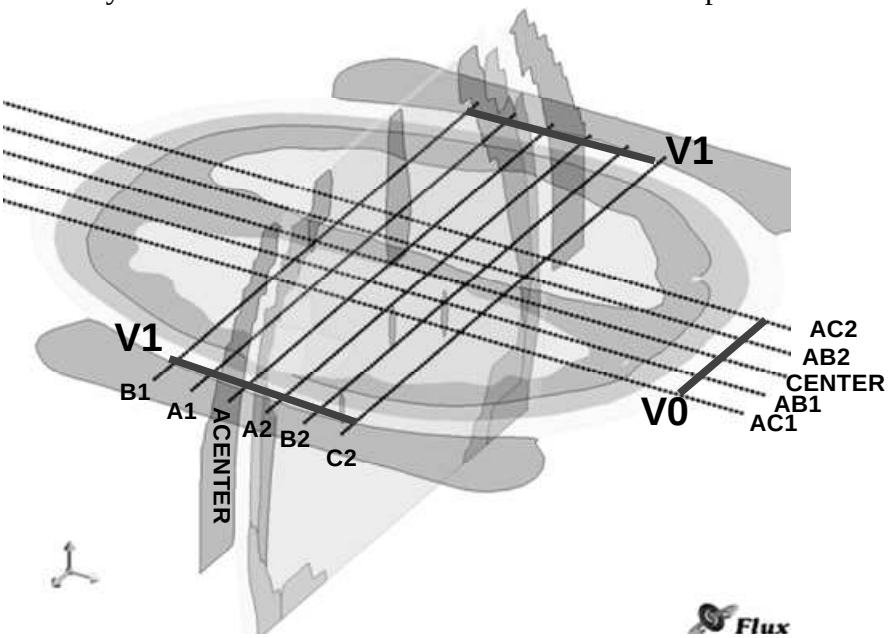

Figure 9.5: Human head section and sampling lines for electric field evaluation.

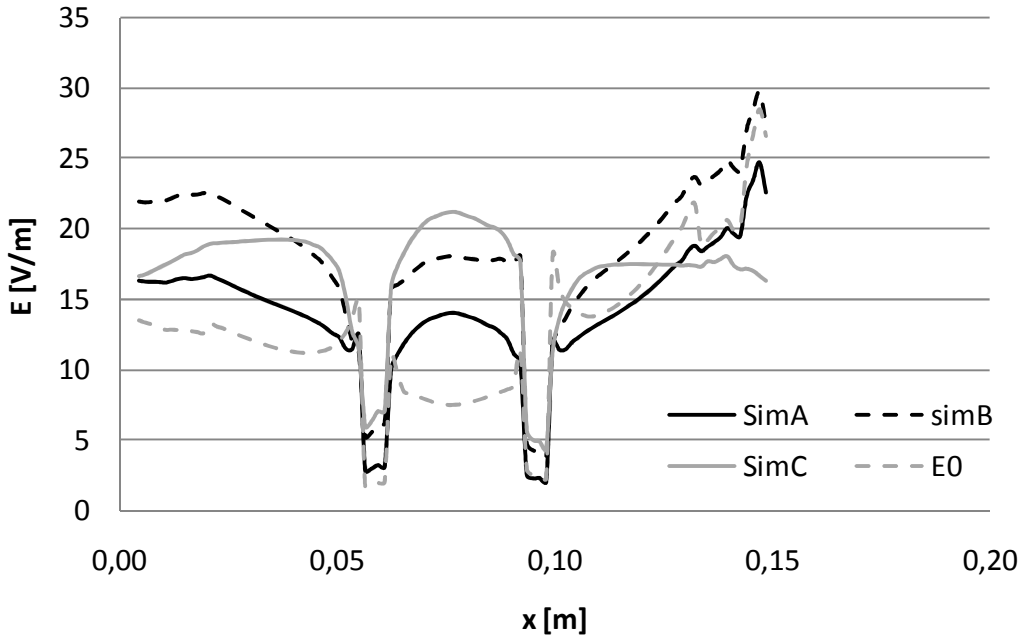

Figure 9.6: electric field along a line “Acenter” for the “simA”-“simC” and E_0 models.

In Figure 9.6 the value of the electric field along the line “Acenter” in Figure 9.5 is reported. It is to be noted that the field intensity varies with the electrodes position. The case E0 refers to only two electrodes (the V1 in Figure 9.4) on parietal position with inverse polarity. In this last case the electric field intensity is lower than the configurations with three electrodes. In Figure 9.7 - Figure 9.9 the electric field and the current density direction are shown for the three electrode positions in Figure 9.4. In this case between the electrode V1 and V0 a voltage of 10 V_{rms} is applied. With the configuration “simC” an electric field higher than the others two electrode configurations can be induced in the hippocampus region.

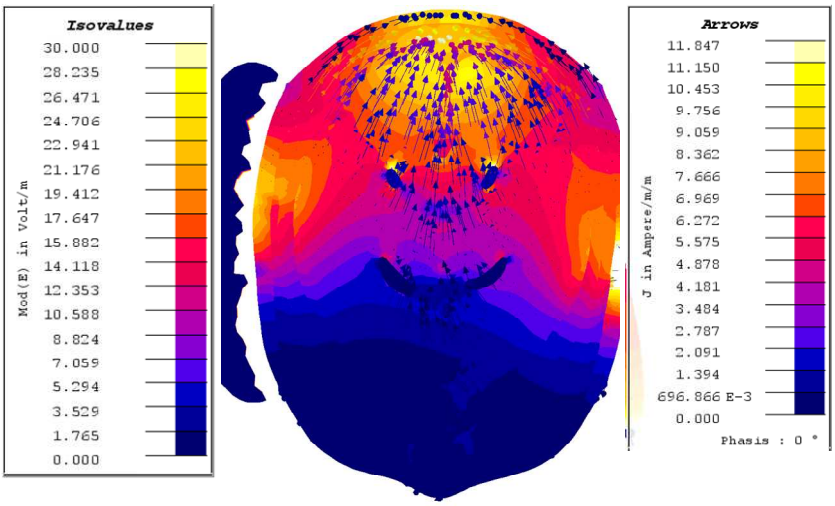

Figure 9.7: Electric field and current density direction for the geometry “Sim A” in Figure 9.4.

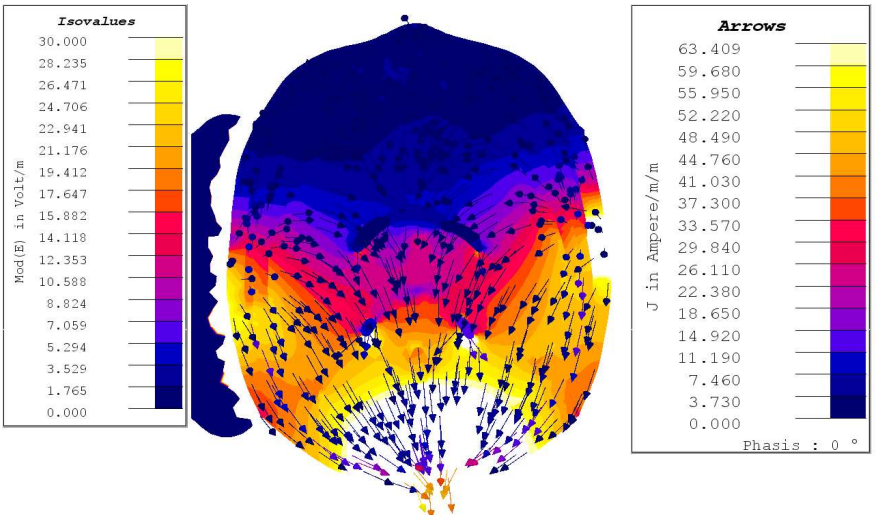

Figure 9.8: Electric field and current density direction for the geometry “Sim B” in Figure 9.4.

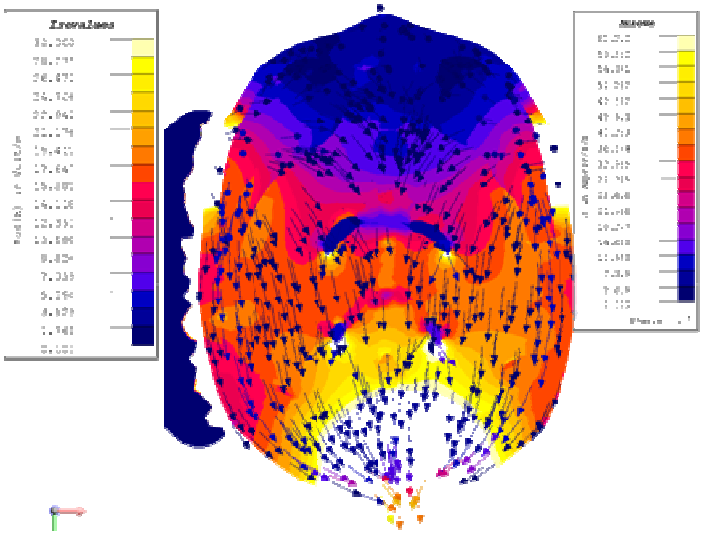

Figure 9.9: Electric field and current density direction for the geometry “Sim C” in Figure 9.4.

9.2.3. The distribution of the electric field in the tissues of the rat head

In Figure 9.10 the position of the electrodes in the rat head model is sketched. The two electrodes that generate the electric field can be attached on the external skin[29] surface (V_{1ext} and V_{0ext}) or on the internal skin surface (V_{1int} and V_{0int}). The voltage applied to the V_1 electrode is 1.3 V_{rms} at 4 MHz. The voltage has been sampled along the lines of the Figure 9.11.

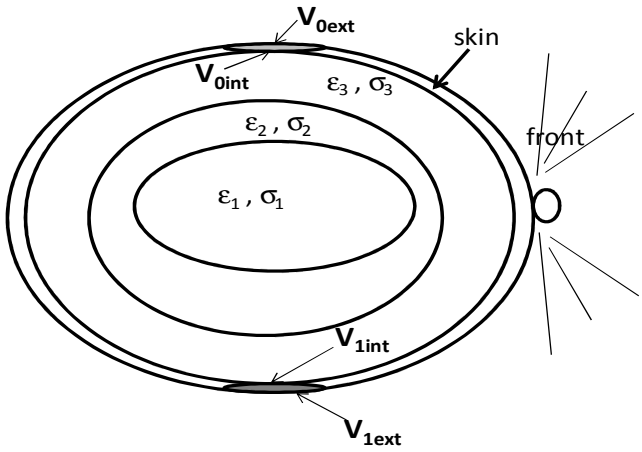

Figure 9.10: Position of the electrodes in the rat head model.

Figure 9.11 shows the lines along which the electric field has been sampled in a rat head slice. The line V5 corresponds, approximately, to a depth of 0 mm in the brain, whereas V10 to a depth of 5 mm like reported in table in Figure 9.11.

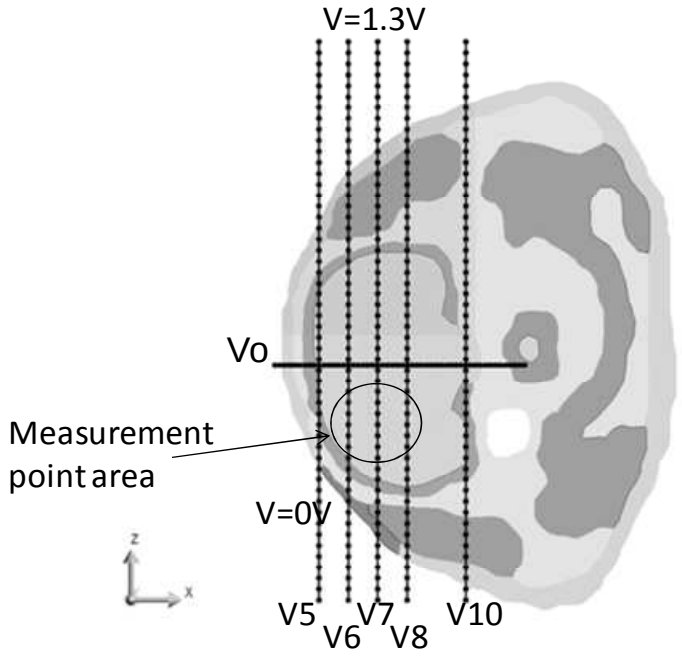

Line	Depth
V5	0 mm
V6	1 mm
V7	2 mm
V8	3 mm
V10	5 mm

Figure 9.11: Samplig lines for the evaluation of the voltage and electric field in the rat head and depth of the sampling lines in the rat brain.

Figure 9.12 and Figure 9.13 shows, respectively the voltage and the electric field in two perpendicular rat slices in the case in which the electrodes are on the external skin surface

[29] It is to be noted that the skin at 4 MHz has a lower resistivity with respect lower frequency (*e.g.* at 1 kHz ρ = 4998 Ωm and ε_r = 1136).

(V_{1ext} and V_{0ext}). It is to be noted that the electric field intensity assumes a higher value in the bone region.

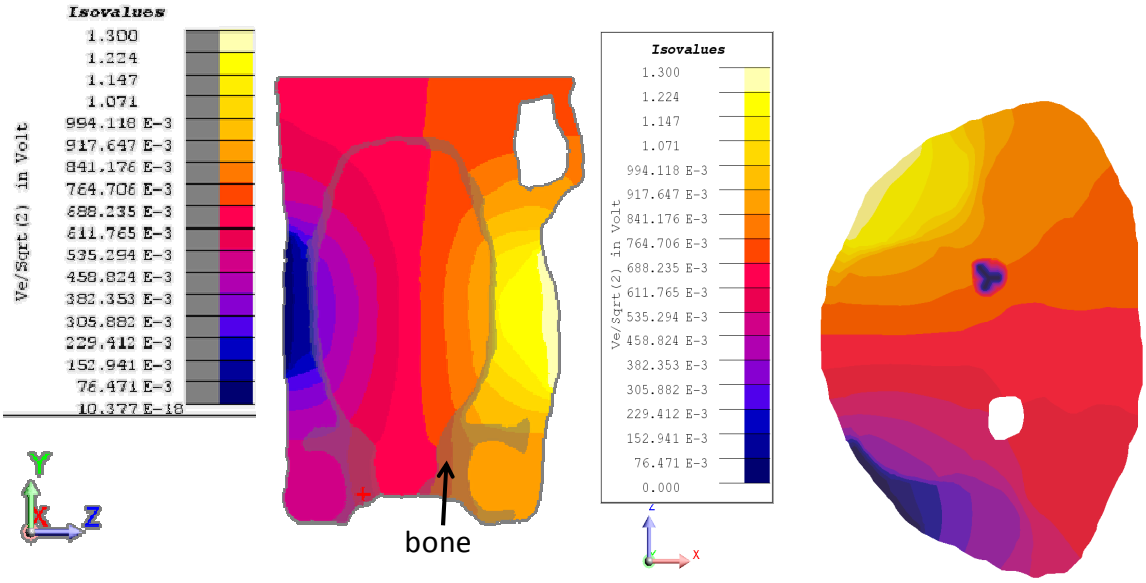

(a) (b)

Figure 9.12: Voltage in two perpendicular slices of rat head.

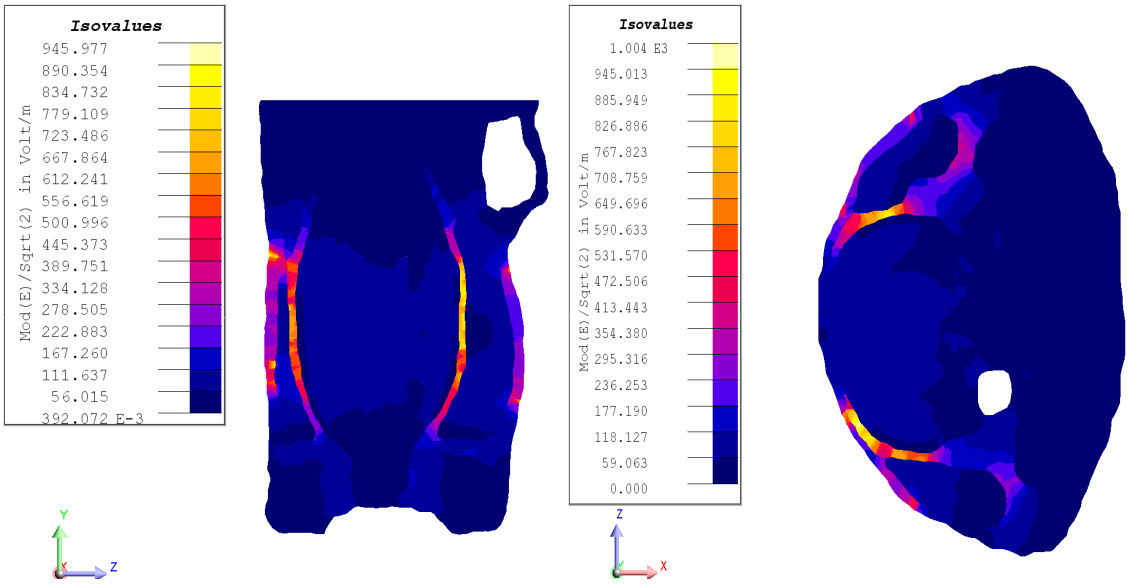

(a) (b)

Figure 9.13: Electric field in two perpendicular slices of rat head.

Figure 9.14 shows the electric field along the lines in Figure 9.11 in the case in which the voltage is applied at the external surface of the skin (V_{1ext} and V_{0ext}). It can be noted that a large drop of electric field occurs in the bone (the peak in Figure 9.14), whereas in the brain the electric field is lower. Figure 9.15 shows a zoom of the central part of the graph in Figure 9.14. In this part with a voltage difference of 1.3 V_{rms} an electric field between 40 and 80 V/m is obtained.

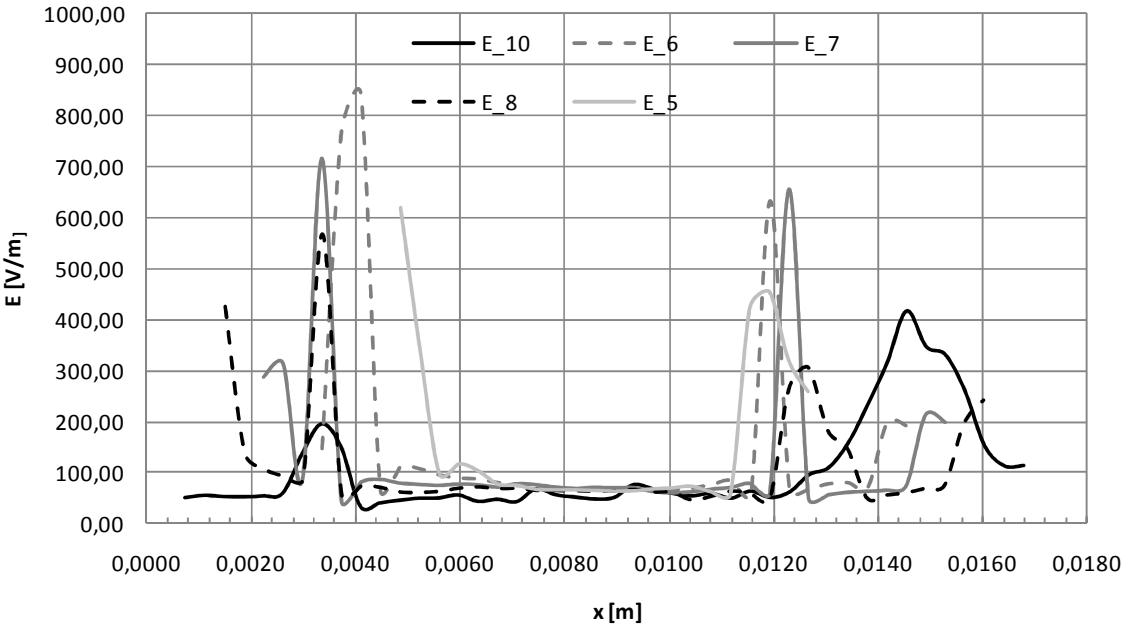

Figure 9.14: Electric field along lines in Figure 9.11 for the case of the V_{1ext} and V_{0ext} electrodes.

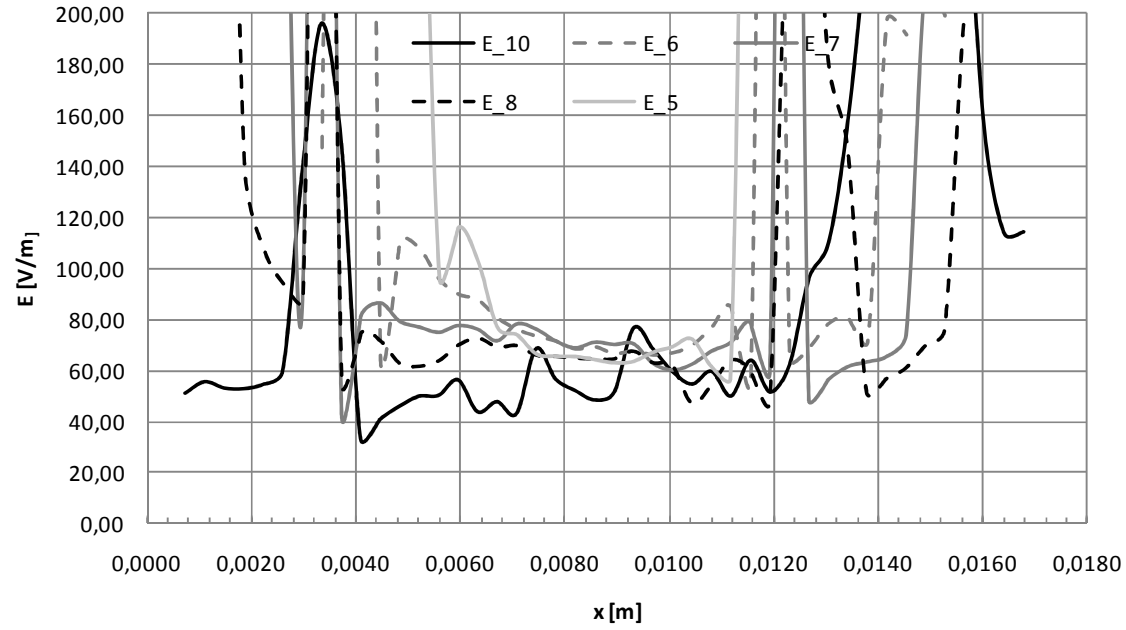

Figure 9.15: Zoom of the electric field along lines in Figure 9.11 for the case of the V_{1ext} and V_{0ext} electrodes.

Figure 9.16 and Figure 9.17 represent the electric field in the case in which the voltage difference is applied to the internal skin surface (V_{1int} and V_{0int}). In this case the electric field in the brain area is a little bit higher (between 50 an 90 V/m) than in the previous case in which the electrodes are at the external surface of the skin.

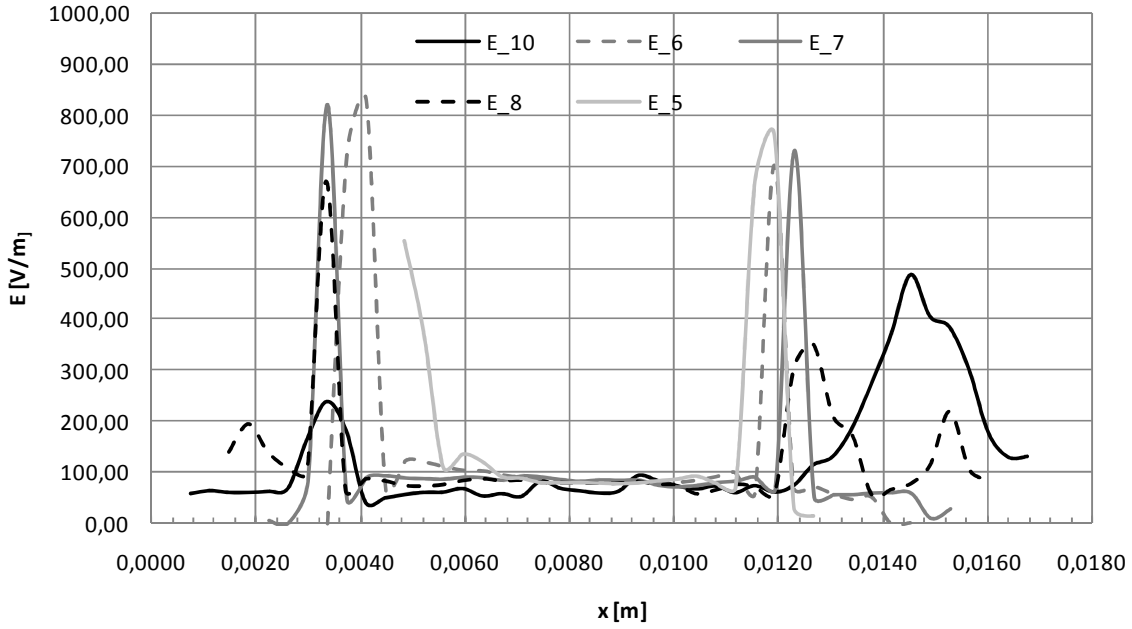

Figure 9.16: Electric field along lines in Figure 9.11 for the case of the V_{1int} and V_{0int} electrodes.

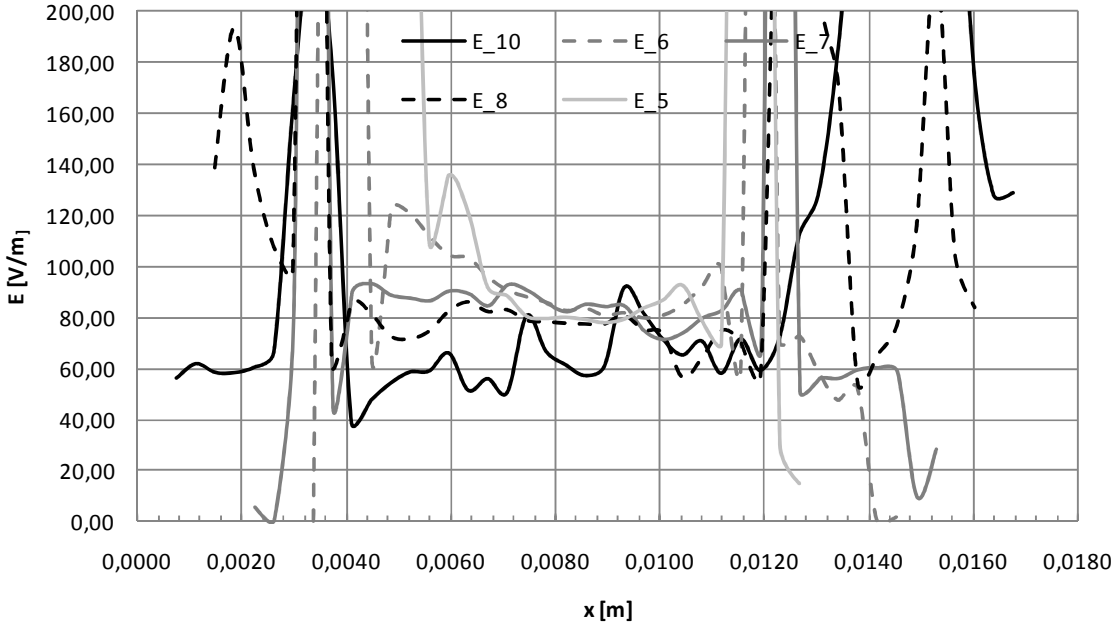

Figure 9.17: Zoom of the electric field along lines in Figure 9.11 and for the case of the V_{1int} and V_{0int} electrodes.

In Figure 9.18 the voltage evaluated along the lines in Figure 9.11 is reported. The points where a variation of the voltage slope arrives correspond to a drop down of the relative dielectric permittivity. An example of this behavior is shown in the graph of Figure 9.18 where the dielectric permittivity evaluated along the line V7 has been superimposed to the evaluated voltage in the tissues.

\

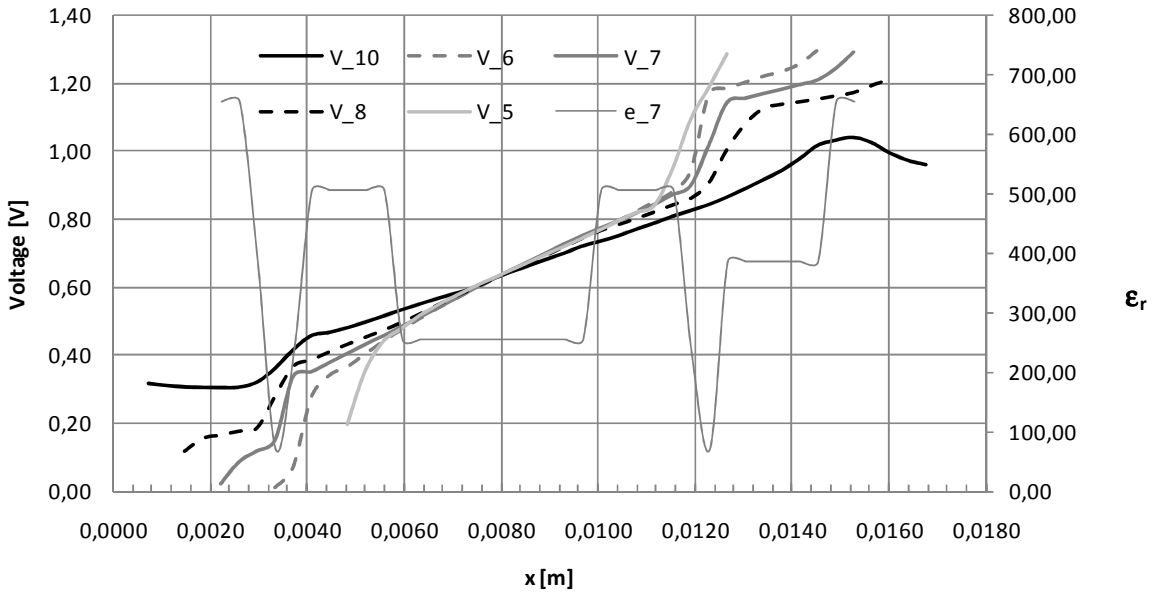

Figure 9.18: Voltage along lines in Figure 9.11 for the case of the V_{1ext} and V_{0ext} electrodes and dielectric permittivity evaluated along the line V7.

9.3 Experimental part: measurement of voltages in the rat head

In the case of the rat head the obtained results using the Finite Element computation tool are validated with a set of measurements *in vivo* in a rat brain at which a voltage difference has been applied with suitable electrodes [60], [253-255].

9.3.1. The measurement set-up

In the measurement set up is shown. A voltage is applied to the rat head and the voltage inside the brain is measured by means of a glass micropipette [60].

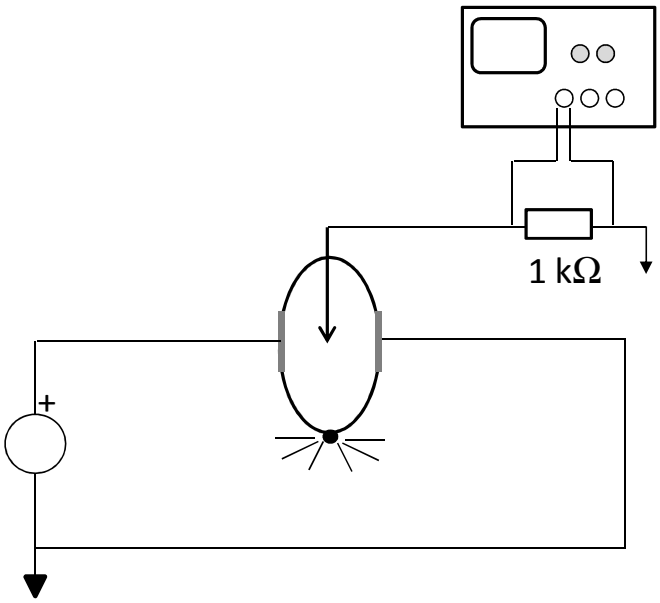

Figure 9.19: Measurement set-up for the evaluation of the induced voltage in brain tissues of a rat.

The measurement instruments used in this measurement set up are an oscilloscope Agilent 54641A[30], with suitable voltage probes, and a function generator Agilent 33220A for the generation of the voltage difference at 4 MHz. The voltage at the output of the micropipette has been measured using a resistance of 1kΩ in parallel with the oscilloscope input.

It is to be noted that the behavior of the micropipette varies the frequency as in Figure 9.20; the absolute value of the impedance and its phase decreases after 100 kHz. Then, using the micropipette in order to measure the voltage in the rat brain the measured value depends on the transducer impedance.

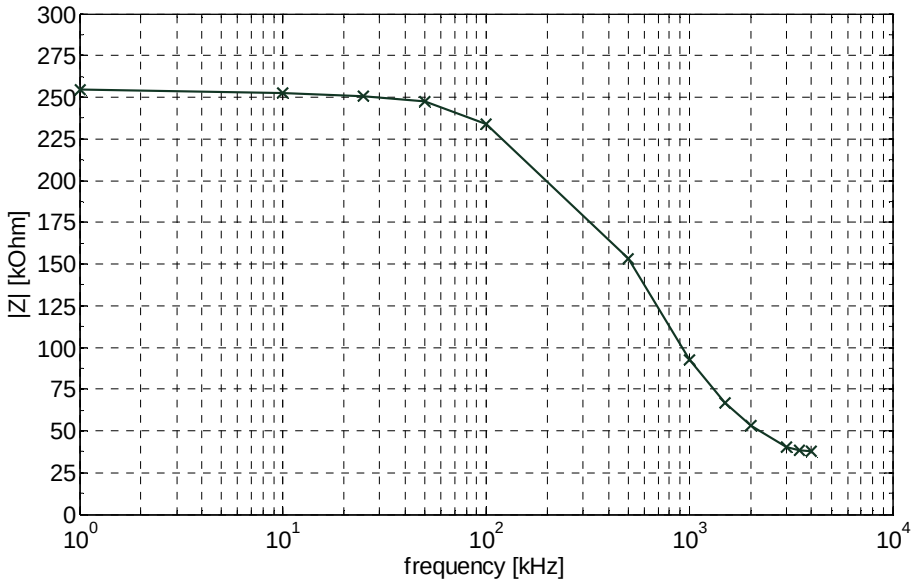

(a)

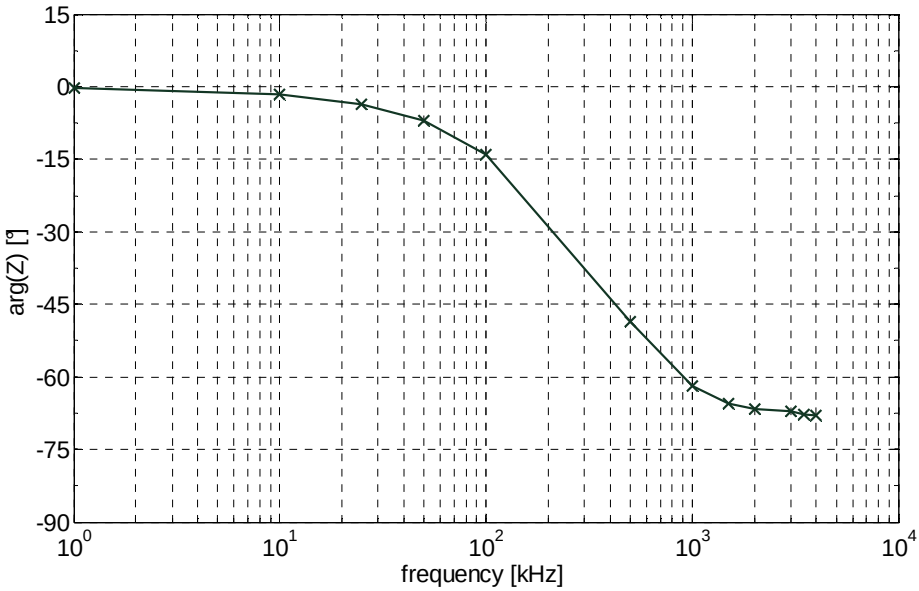

(b)

Figure 9.20: impedance, (a) absolute value and (b) phase for a micropipette.

Using a suitable set up the frequency characteristic of the impedance of the micropipette has been studied [253-258]. A known voltage has applied to a homogeneous medium (*e.g.* agar gel) in order to create a homogeneous voltage medium. The voltage of the gel has been

[30] http://www.home.agilent.com (last access January 2011)

measured by means of the micropipette at different known depths. The voltage measured is generally lower than the one applied to the gel. Varying the depth of the micropipette tip the curve in Figure 9.22 has been found. This curve has been used to rescale the voltage to the micropipette output in order to derive the one at the tip.

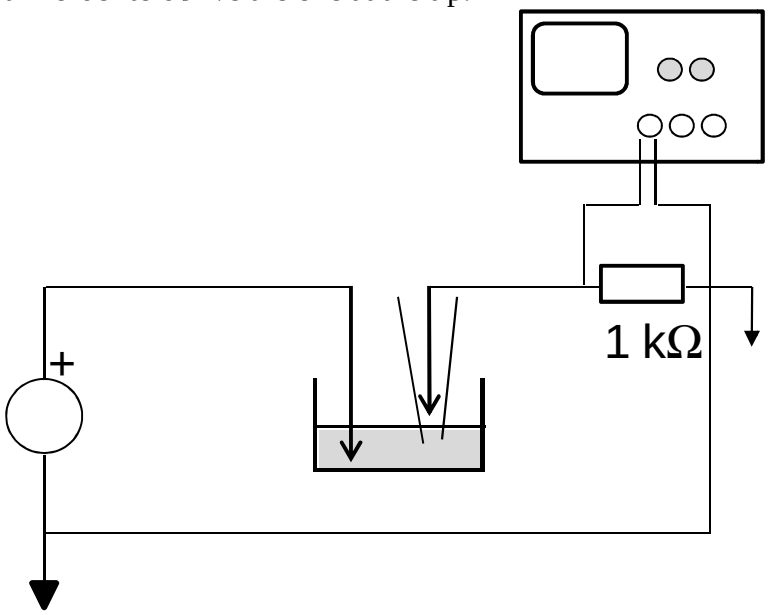

Figure 9.21: Measurement set-up for the evaluation of the input-output chracteristic of a micropipette.

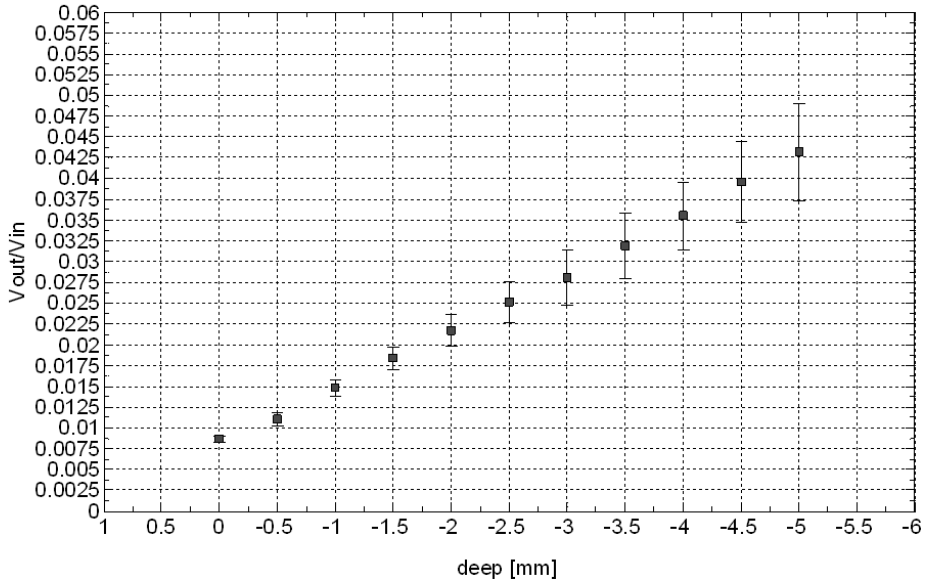

Figure 9.22: Input-output chracteristic of a micropipette as a function of the tip depth (at 4MHz).

9.3.2. Comparison between measurement and computation results

In Figure 9.23 the voltage evaluated along the lines in Figure 9.11 is reported as a function of a spatial coordinate in the case of the electrodes that generate the voltage difference are the two external (V_{1ext} and V_{0ext}). The vertical line "0m" corresponds to the line "Vo" in Figure 9.11 and represents the medial line of the brain. In this case the applied voltage difference is 1.3 V_{rms} at 4MHz. The points represent the measurements made with the micropipette *in vivo* in the brain of a rat. The points of each of the three series correspond to a different depth in the brain rat between 2.5 and 4 mm.

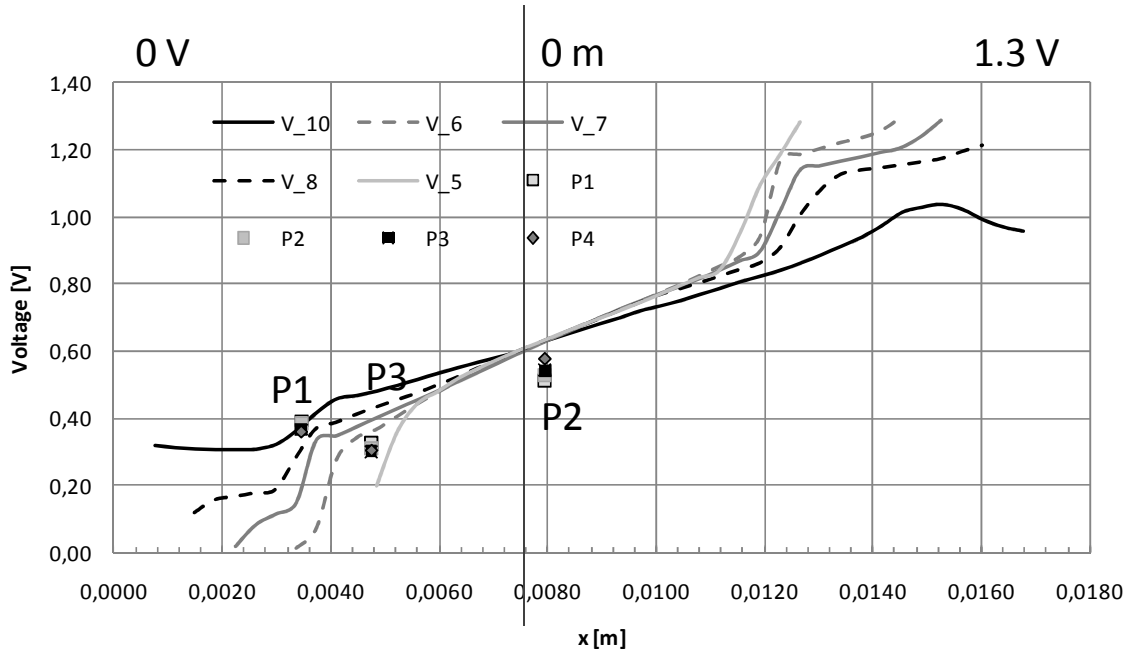

Figure 9.23: Voltage along lines in Figure 9.11 and measurement points for the case of the V_{1ext} and V_{0ext} electrodes. Applied voltage difference 1.3 $V_{rms.}$

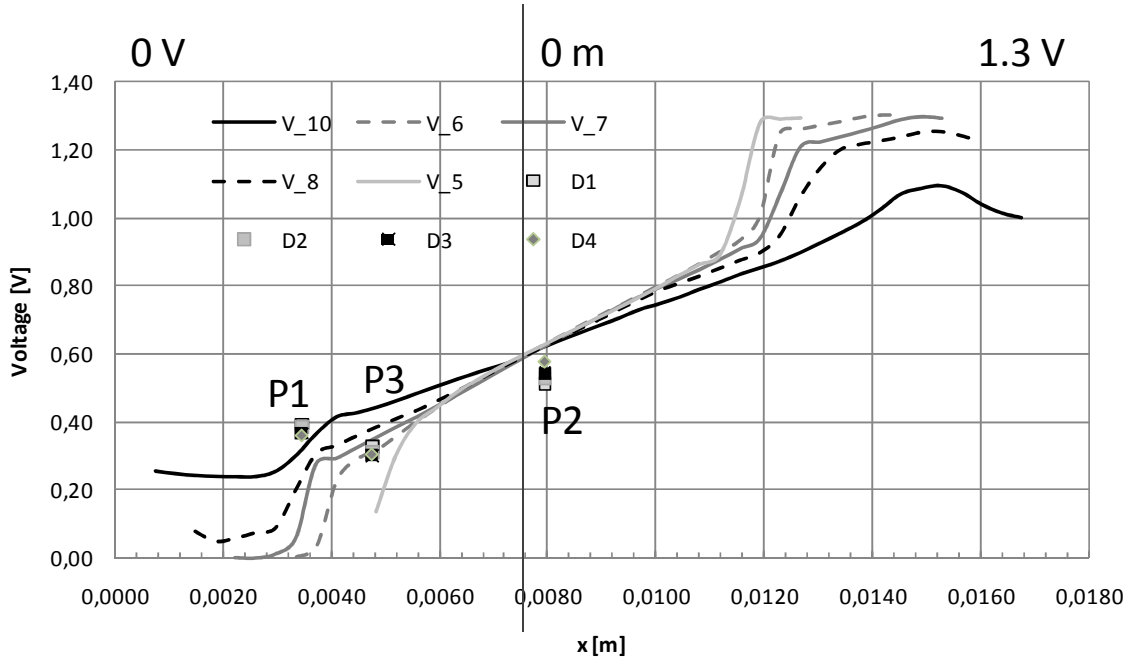

Figure 9.24: Voltage along lines in Figure 9.11 and measurement points for the case of the V_{1int} and V_{0int} electrodes. Applied voltage difference 1.3 $V_{rms.}$

Figure 9.24 is similar to Figure 9.23, but in this case the computation is made considering the electrodes under the skin, the internal ones (V_{1int} and V_{0int}). This case is more similar to the one in the measurement set up because the electrodes are under the skin layer as during measurements. The evaluated voltage is similar than in the previous case and the measured values are in agreement with the computed ones. The comparison between measurements and computation data shows a good agreement between the values.

In Figure 9.25 the measurement points and the computed voltage inside the brain has been reported for an applied voltage difference of 2.8 V_{rms} at 4MHz. Also in this case a good agreement between measurement results and computed voltage in the brain matter is shown.

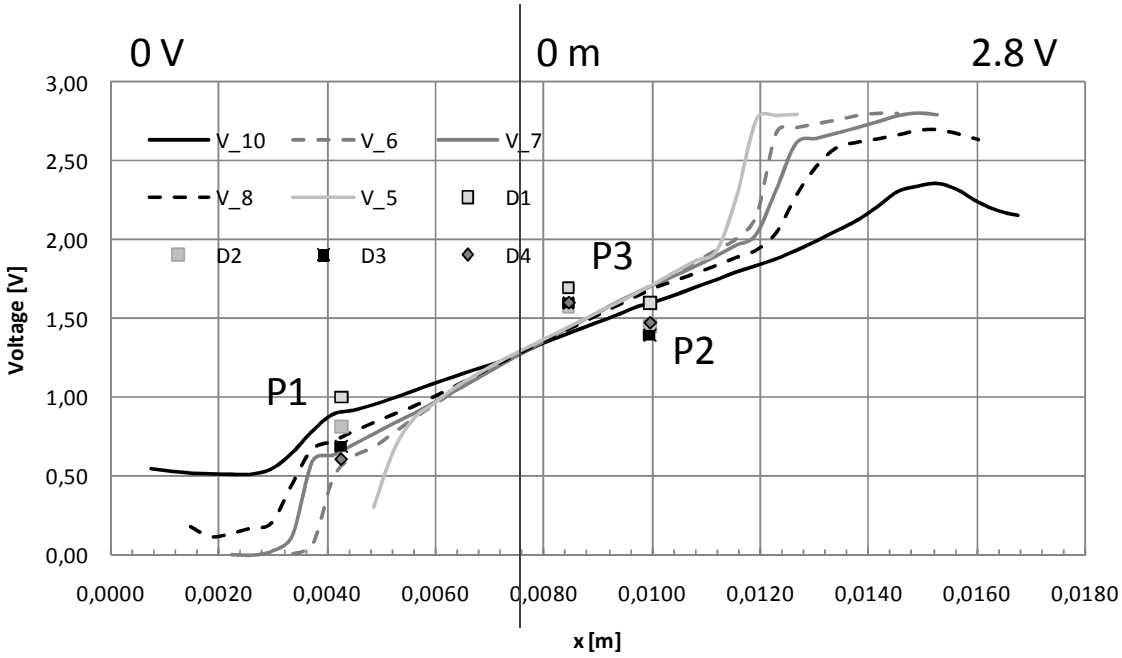

Figure 9.25: Voltage along lines in Figure 9.11 and measurement points for the case of the V_{1int} and V_{0int} electrodes. Applied voltage difference 2.8 V_{rms}.

9.4 Conclusions

Numerical analysis of the electric field induced on the brain tissues by a voltage difference has been carried out in realistic models of human and rat head.

In the case of the human body head the numerical analysis has been used in order to evaluate the effect of different positions of the electrodes on the skull surface. In this analysis the field on the hippocampus has taken into account.

The rat model has been used in order to validate the numerical results obtained using Finite Element Analysis tools. Computed voltages have been compared with measurement data. In this case experimental data had shown a good agreement with the computed one.

Conclusions

Finite Elements models for the solutions of electromagnetic and thermal problems can be used in the design of biomedical applications or as a support for the evaluations of the adverse effects deriving by electromagnetic fields exposure. Optimization techniques can be coupled with the Finite Element Analysis to obtain automated computation procedures to design electromagnetic equipments. In this work examples on welding equipments and induction cooktop magnetic field exposure, Magnetic Fluid Hyperthermia and the stimulation of the brain tissue by means of electric field using the above methodologies have been proposed.

In all the proposed problems the effects of the interaction between electromagnetic fields and biological tissues in suitable domains have been evaluated by means of Finite Element Analysis with realistic or simplified human body models. In particular realistic models have been built from medical images using suitable software tools. Realistic electrical and thermal characteristics of biological tissues have been used.

It is to be noted that in some cases electromagnetic problem in the evaluation of the human exposure and design of Magnetic Fluid Hyperthermia devices has been solved by means of the same equations. Moreover, the Magnetic Fluid Hyperthermia device has been designed using coupled magnetic and thermal problems inside a multiobjective optimization core. It is to be noted that the same optimization code has been used to design different aspects of the Magnetic Fluid Hyperthermia device: the magnetic field source as well as the power density source that generates the therapeutic heat. In particular, some methodological aspects to design devices by means of multiobjective optimization procedures have been analyzed.

At the end, in the biological model that describes the human or rat head using electrical characteristics of the brain and correlated structures the electromagnetic problem is solved in terms of electric field. This is a different problem solved with the same numerical computation tools and domain model used in the previous analysis.

The three proposed examples have shown different aspects correlated to the effects of the interaction with electromagnetic fields and biological tissues: evaluation of adverse effects as well as the possibility to use them in medical therapies.

About the electromagnetic field exposure simplified models and human models have been used in order to compute induced currents in the tissues. The effects due to the different tissue resistivity have been compared with the results obtained using a homogeneous model. The same procedures have been used to evaluate the exposure to induction cooktop electromagnetic field.

Optimization techniques have been used in the design of the magnetic field and heat source in the magnetic fluid hyperthermia treatments for the tumor therapy. A Finite Element model has been used to compute the magnetic field and the temperature in the target volume, whereas the optimization codes have been used to set the best values of the input variables. The same optimization codes implemented for the optimization of the magnetic field uniformity can be used to design the concentration and sizes of the magnetic nanoparticles in the magnetic drug utilized as an internal source of heat. Coupled magnetic and thermal problems have been solved in order to uniform both the magnetic and thermal field in the

target region. A concentration of nanoparticles similar to the real one has been taken into account and the position of nanoparticles injections has been optimized in order to obtain the best heat distribution close to the therapeutic temperature in the target region.

In the third example the electric field generated by a voltage difference has been evaluated in a model of the human and rat head in order to evaluate the electric field on the hippocampus region. In this case a measurements experiment has been designed in order to evaluate the voltage induced in a rat brain.

The methodological procedures and Finite Element models developed have been supported by practical examples and a measurements experiment.

Bibliography

[1] ICNIRP, "Guidelines for limiting exposure to time-varying electric, magnetic, and electromagnetic fields (up to 300 GHz)," *Health Physics*, vol. 74, 1998, pagg. 494-522.

[2] ICNIRP, "Guidelines on limits of exposure to static magnetic fields," *Health Physics*, vol. 66, 1994, pagg. 100-106.

[3] ICNIRP, "Guidance on Determining Compliance of Exposure to Pulsed Fields and Complex Non-Sinusoidal Waveforms below 100 kHz with ICNIRP Guidelines," *Health Physics*, vol. 84, 2003, pagg. 383-387.

[4] "Directive 2004/40/EC of the European Parliament and of the Council of 29 April 2004 on the minimum health and safety requirements regarding the exposure of workers to the risks arising from physical agents (electromagnetic fields) (18th individual Directive within the meaning of Article 16(1) of Directive 89/391/EEC)," 2004.

[5] M. Hirose, M. Hida, E. Sato, K. Kobubo, M. Nie, e H. Kobayashi, "Electromagnetic Interference of Implantable Unipolar Cardiac Pacemakers by an Induction Oven," *Pacing and Clinical Electrophysiology*, vol. 28, 2005, pagg. 540-548.

[6] W. Irnich e A.D. Bernstein, "Do induction cooktops interfere with cardiac pacemakers?," *Europace*, vol. 8, 2006, pagg. 377-384.

[7] B. Katz, *Nerve, muscle, and synapse*, New York: McGraw-Hill, 1966.

[8] D. Andreuccetti, "Normativa internazionale per la protezione dai campi elettromagnetici," *TuttoMisure*, vol. 2, 2005, pagg. 105-109.

[9] M. Battistetti, F. Dughiero, e M. Forzan, "Investigation on electromagnetic fields in the surrounding of induction heating installations," *Int. Induc. Heat. Sem.*, 1998, pagg. 473-477.

[10] P. Maruvada, "Characterization of Power Frequency Magnetic Field in Different environments," *IEEE Trans. on Power Delivery*, vol. 8, 1993, pagg. 598-605.

[11] ANPA, *Statement of the International Evaluation Comitee to Investigate the Health Risks of Exposure to Electric, Magnetic and Electromagnetic Fields (EMF)*, Maggioli Editore, 2002.

[12] NIEHS, *NIEHS report on health effects from exposure to Power-line frequency electric and magnetic fields*, 1999.

[13] J. Juutilainen, "Developmental effects of electromagnetic fields," *Bioelectromagnetics*, vol. 26, 2005, pagg. S107-S115.

[14] E.M. Goodman, B. Greenebaum, e M.T. Marron, "Effects of Electromagnetic Fields on Molecules and Cells," *A Survey of Cell Biology*, Academic Press, 1995, pagg. 279-338.

[15] WHO, "Electromagnetic fields and public health. Exposure to extremely low frequency fields," 2007.

[16] I.A.F.R.O.C. World Health Organization, "IARC Monographs on the Evaluation of Carcinogenic Risks to Humans," *Non-Ionizing Radiation, Part 1: Static and Extremely Low-Frequency (ELF) Electric and Magnetic Fields. Summary of Data Reported and Evaluation*, IARC, 2002.

[17] IARC, *Lists of IARC Evaluations*, 2004.
[18] J. Burchard, D. Nguyen, e H. Monardes, "Exposure of pregnant dairy heifer to magnetic fields at 60 Hz and 30 µT," *Bioelectromagnetics*, vol. 28, 2007, pagg. 471-476.
[19] J.H. Olsen, A. Nielsen, e G. Schulgen, "Residence near high-voltage facilities and the risk of cancer in children," *Danish Cancer Registry, AG-NIR*, 1993, pagg. 1-26.
[20] T. Cooper, *Occupational exposure to electric and magnetic fields in the context of the ICNIRP guidelines*, Chilton Didcot: National Radiological Protection Board, 2002.
[21] D.E. Foliart, G. Mezei, R. Iriye, J.M. Silva, K.L. Ebi, L. Kheifets, M.P. Link, R. Kavet, e B.H. Pollock, "Magnetic field exposure and prognostic factors in childhood leukemia," *Bioelectromagnetics*, vol. 28, 2007, pagg. 69-71.
[22] M.S. Linet, E.E. Hatch, R.A. Kleinerman, L.L. Robison, W.T. Kaune, D.R. Friedman, R.K. Severson, C.M. Haines, C.T. Hartsock, S. Niwa, S. Wacholder, e R.E. Tarone, "Residential Exposure to Magnetic Fields and Acute Lymphoblastic Leukemia in Children," *New England Journal of Medicine*, vol. 337, Lug. 1997, pagg. 1-8.
[23] S. London, D. Thomas, J. Bowman, E. Sobel, T. Cheng, e J. Peters, "Exposure to residential electric and magnetic fields and risk of childhood leukemia," *American Journal of Epidemiology*, vol. 134, 1991, pagg. 923-937.
[24] D. Savitz, H. Wachtel, F. Barnes, E. John, e J.G. Tvrdik, "Case-control study of childhood cancer and exposure to 60-Hz magnetic fields," *Epidemiology*, vol. 128, 1988.
[25] G. Theriault, "Cancer risks due to exposure to electromagnetic fields," *Recent Results in Cancer Res.*, vol. 120, 1990, pagg. 166-180.
[26] M. Feychting, N. Pedersen, P. Svedberg, B. Floderus, e M. Gatz, "Dementia and occupational exposure to magnetic fields," *Scandinavian Journal of Work, Environment and Health*, vol. 24, 1998, pagg. 46-53.
[27] M. Feychting, U. Forssén, e B. Floderus, "Occupational and Residential Magnetic Field Exposure and Leukemia and Central Nervous System Tumors," *Epidemiology*, vol. 8, Lug. 1997, pagg. 384-389.
[28] M. Feychting, F. Jonsson, N. Pedersen, e A. Ahlbom, "Occupational Magnetic Fields exposure and Neurodegenerative Diseases," *Epidemiology*, vol. 14, 2003, pagg. 420-426.
[29] T. Tenforde e W. Kaune, "Interaction of extremely low frequency electric and magnetic fields with humans," *Health Physics*, vol. 53, 1987, pagg. 585-606.
[30] M.H. Repacholi e B. Greenebaum, "Interaction of static and extremely low frequency electric and magnetic fields with living systems: Health effects and research needs," *Bioelectromagnetics*, vol. 20, 1999, pagg. 133-160.
[31] T.S. Tenforde, "Biological interactions of extremely-low-frequency electric and magnetic fields," *Bioelectrochemistry and Bioenergetics*, vol. 25, Feb. 1991, pagg. 1-17.
[32] J. Reilly, "Peripheral nerve stimulation by induced electric currents: exposure to time-varying magnetic fields," *Med. Biol. Eng. Computing*, vol. 3, 1989, pagg. 101-109.
[33] J. Reilly, "Neuroelectric mechanisms applied to low frequency electric and magnetic field exposure guidelines–part I: sinusoidal waveforms," *Health Physics*, vol. 83, 2002, pagg. 341-355.
[34] J. Reilly e A. Diamant, "Neuroelectric mechanisms applied to low frequency electric and magnetic field exposure guidelines–part II: non sinusoidal waveforms," *Health Physics*, vol. 83, 2002, pagg. 356-365.
[35] T. Shigemitsu, K. Yamazaki, S. Nakasono, e M. Kakikawa, "A review of studies of the biological effects of electromagnetic fields in the intermediate frequency range," *IEEJ*

Transactions on Electrical and Electronic Engineering, vol. 2, 2007, pagg. 405-412.
[36] B. Floderus, C. Stenlund, e F. Carlgren, "Occupational exposures to high frequency electromagnetic fields in the intermediate range (>300 Hz–10 MHz)," *Bioelectromagnetics*, vol. 23, 2002, pagg. 568-577.
[37] E. Litvak, K. Foster, e M. Repacholi, "Health and safety implications of exposure to electromagnetic fields in the frequency range 300 Hz to 10 MHz," *Bioelectromagnetics*, vol. 23, 2002, pagg. 68-82.
[38] Watanabe Kenji, H. Izuo, Tominaga Hiroshi, Fujinami Tomoya, e Isoda Keiko, "Induction heating cooker," U.S. Patent US2010176120 (A1), Luglio 15, 2010.
[39] Kim Eui Sung, Park Byeong Wook, Hee Ryu Seung, e Shin Dong Myung, "Induction heating rice cooker and its method for the same," U.S. Patent KR20050039970, Maggio 3, 2005.
[40] Sasaki Koki e Iguchi Kuniaki, "Electric cooker using induction heater," U.S. Patent CN1170847 (A), Gennaio 21, 1998.
[41] H. Lee, S. Choi, J. Jang, Y. Gimm, J. Pack, H. Choi, N. Kim, e Y. Lee, "Lack of promotion of mammary, lung and skin tumorigenesis by 20 kHz triangular magnetic fields," *Bioelectromagnetics*, vol. 28, 2007, pagg. 446-453.
[42] J. Miyakoshi, E. Horiuchi, T. Nakahara, e T. Sakurai, "Magnetic fields generated by an induction heating (IH) cook top do not cause genotoxicity in vitro," *Bioelectromagnetics*, vol. 28, 2007, pagg. 529-537.
[43] A. Fujita, I. Hirota, Y. Kawahara, e H. Omori, "Development and evaluation of intermediate frequency magnetic field exposure system for studies of in vitro biological effects," *Bioelectromagnetics*, vol. 28, 2007, pagg. 538-545.
[44] S. Kim, J. Song, S. Kim, H. Oh, Y. Gimm, D. Yoo, J. Pack, e Y. Lee, "Teratological studies of prenatal exposure of mice to a 20 kHz sawtooth magnetic field," *Bioelectromagnetics*, vol. 25, 2004, pagg. 114-117.
[45] S.M. Michaelson, "Biomedical Aspects of Microwave Exposure," *American Industrial Hygiene Association Journal*, vol. 32, 1971, pagg. 338-345.
[46] S.M. Michaelson, "Effects of Exposure to Microwaves: Problems and Perspectives," *Environmental Health Perspectives*, vol. 8, 1974, pagg. 133-155.
[47] E. Valentini, G. Curcio, F. Moroni, M. Ferrara, L. De Gennaro, e M. Bertini, "Neurophysiological effects of mobile phone electromagnetic fields on humans: A comprehensive review," *Bioelectromagnetics*, vol. 28, 2007, pagg. 415-432.
[48] S. Szmigielski, "Cancer morbidity in subjects occupationally exposed to high frequency (radiofrequency and microwave) electromagnetic radiation," *Science of The Total Environment*, vol. 180, Feb. 1996, pagg. 9-17.
[49] A. Ahlbom, A. Green, L. Kheifets, D. Savitz, A. Swerdlow, e ICNIRP (International Commission for Non-Ionizing Radiation Protection) Standing Committee on Epidemiology, "Epidemiology of Health Effects of Radiofrequency Exposure," *Environ Health Perspect*, vol. 112, 2004.
[50] F.C. Hollows e J.B. Douglas, "Microwave cataract in radiolinemen and controls," *The Lancet*, vol. 324, Ago. 1984, pagg. 406-407.
[51] P.J. Stewart-DeHaan, M.O. Creighton, L.E. Larsen, J.H. Jacobi, W.M. Ross, M. Sanwal, T.C. Guo, W.W. Guo, e J.R. Trevithick, "In vitro studies of microwave-induced cataract: Separation of field and heating effects," *Experimental Eye Research*, vol. 36, Gen. 1983, pagg. 75-90.
[52] S. Cleary, "Microwave cataractogenesis," *Proceedings of the IEEE*, vol. 68, 1980, pagg. 49-55.
[53] L.N. Heynick e J.H. Merritt, "Radiofrequency fields and teratogenesis," *Bioelectromagnetics*, vol. 24, 2003, pagg. S174-S186.

[54] EN 50366, “Household and similar electrical appliances. Electromagnetic fields. Methods for evaluation and measurement,” 2003.
[55] EN 50444, “Basic standard for the evaluation of human exposure to electromagnetic fields from equipment for arc welding and allied processes,” 2008.
[56] EN 50505, “Basic standard for the evaluation of human exposure to electromagnetic fields from equipment for resistance welding and allied processes,” 2008.
[57] CEI 211-6, “Guide for the measurement and the evaluation of electric and magnetic fields in the frequency range 0Hz-10kHz, with reference to the human exposure,” 2001.
[58] CEI 211-4, “Guide to calculation methods of electric and magnetic fields generated by power-lines,” 1997.
[59] CEI EN 60076-1, “Power transformer. Part 1: general,” 1998.
[60] J. Webster, *Medical instrumentation : application and design*, New York: Wiley, 1998.
[61] J. Rothwell, D. Burke, R. Hicks, J. Stephen, I. Woodforth, e M. Crawford, “Transcranial electrical stimulation of the motor cortex in man: further evidence for the site of activation.,” *The Journal of Physiology*, vol. 481, Nov. 1994, pagg. 243 -250.
[62] M. Tsai, W.H. Chang, K. Chang, R. Hou, e T. Wu, “Pulsed electromagnetic fields affect osteoblast proliferation and differentiation in bone tissue engineering,” *Bioelectromagnetics*, vol. 28, 2007, pagg. 519-528.
[63] A. Athanasiou, S. Karkambounas, A. Batistatou, E. Lykoudis, A. Katsaraki, T. Kartsiouni, A. Papalois, e A. Evangelou, “The effect of pulsed electromagnetic fields on secondary skin wound healing: An experimental study,” *Bioelectromagnetics*, vol. 28, 2007, pagg. 362-368.
[64] S. Delle Monache, R. Alessandro, R. Iorio, G. Gualtieri, e R. Colonna, “Extremely low frequency electromagnetic fields (ELF-EMFs) induce in vitro angiogenesis process in human endothelial cells,” *Bioelectromagnetics*, vol. 29, 2008, pagg. 640-648.
[65] L.E. Gerweck, “Hyperthermia in Cancer Therapy: The Biological Basis and Unresolved Questions,” *Cancer Research*, vol. 45, 1985, pagg. 3408 -3414.
[66] K.M. Krishnan, “Biomedical Nanomagnetics: A Spin Through Possibilities in Imaging, Diagnostics, and Therapy,” *Magnetics, IEEE Transactions on*, vol. 46, 2010, pagg. 2523-2558.
[67] Phillips J.L., “A Topical Review of Magnetic Fluid Hyperthermia,” *JOSHUA*, vol. 3, 2005, pagg. 14-18.
[68] S.A. Sapareto, L.E. Hopwood, W.C. Dewey, M.R. Raju, e J.W. Gray, “Effects of Hyperthermia on Survival and Progression of Chinese Hamster Ovary Cells,” *Cancer Research*, vol. 38, Feb. 1978, pagg. 393 -400.
[69] A. Jordan, R. Scholz, P. Wust, H. Fahling, e Roland Felix, “Magnetic fluid hyperthermia (MFH): Cancer treatment with AC magnetic field induced excitation of biocompatible superparamagnetic nanoparticles,” *Journal of Magnetism and Magnetic Materials*, vol. 201, Lug. 1999, pagg. 413-419.
[70] A. Jordan, P. Wust, H. Fähling, W. John, A. Hinz, e R. Felix, “Inductive heating of ferrimagnetic particles and magnetic fluids: Physical evaluation of their potential for hyperthermia,” *International Journal of Hyperthermia*, vol. 25, 2009, pagg. 499-511.
[71] J.G. Short e P.F. Turner, “Physical hyperthermia and cancer therapy,” *Proceedings of the IEEE*, vol. 68, 1980, pagg. 133-142.
[72] J.M. Larkin, “A Clinical Investigation of Total-Body Hyperthermia as Cancer Therapy,” *Cancer Research*, vol. 39, Giu. 1979, pagg. 2252 -2254.
[73] P. Vaupel, F. Kallinowski, e P. Okunieff, “Blood Flow, Oxygen and Nutrient Supply, and Metabolic Microenvironment of Human Tumors: A Review,” *Cancer research*, vol. 49, Dic. 1989, pagg. 6449-6465.

[74] C.W. Song, A. Lokshina, J.G. Rhee, M. Patten, e S.H. Levitt, "Implication of Blood Flow in Hyperthermic Treatment of Tumors," *Biomedical Engineering, IEEE Transactions on*, vol. BME-31, 1984, pagg. 9-16.
[75] A. Guyton, *Textbook of medical physiology*, Philadelphia: W.B. Saunders, 1996.
[76] C. Marino e A. Cividalli, "Combined radiation and hyperthermia: Effects of the number of heat fractions and their interval on normal and tumour tissues," *International Journal of Hyperthermia*, vol. 8, 1992, pagg. 771-781.
[77] Hergt R., Dutz S., Müller R., e Zeisberger M., "Magnetic particle hyperthermia: nanoparticle magnetism and materials development for cancer therapy," *Journal of Physics: Condensed Matter*, vol. 18, 2006, pag. S2919.
[78] I. Herr e K. Debatin, "Cellular stress response and apoptosis in cancer therapy," *Blood*, vol. 98, Nov. 2001, pagg. 2603-2614.
[79] J.F.R.-. Kerr, C.M.-. Winterford, e B.V.-. Harmon, - *Apoptosis. Its significance in cancer and cancer Therapy*, 1994.
[80] B. Hildebrandt, P. Wust, O. Ahlers, A. Dieing, G. Sreenivasa, T. Kerner, R. Felix, e H. Riess, "The cellular and molecular basis of hyperthermia," *Critical reviews in oncology/hematology*, vol. 43, 2002, pagg. 33-56.
[81] A.W. Hergt R, "Magnetic hyperthermia and thermoablation," *Magnetism in Medicine*, 2006, pag. 550.
[82] I. Hilger, R. Hergt, e W.A. Kaiser, "Use of magnetic nanoparticle heating in the treatment of breast cancer," *IEE proceedings.Nanobiotechnology*, vol. 152, Feb. 2005, pagg. 33-39.
[83] J.W. Strohbehn e E.B. Douple, "Hyperthermia and Cancer Therapy: A Review of Biomedical Engineering Contributions and Challenges," *Biomedical Engineering, IEEE Transactions on*, vol. BME-31, 1984, pagg. 779-787.
[84] P. Wust, B. Hildebrandt, G. Sreenivasa, B. Rau, J. Gellermann, H. Riess, R. Felix, e P.M. Schlag, "Hyperthermia in combined treatment of cancer," *The Lancet Oncology,*, vol. 3, 2002, pagg. 487-497.
[85] I.A. Brezovich, W.J. Atkinson, e M.B. Lilly, "Local Hyperthermia with Interstitial Techniques," *Cancer Research*, vol. 44, Ott. 1984, pagg. 4752s -4756s.
[86] P. Moroz, S.K. Jones, e B.N. Gray, "Magnetically mediated hyperthermia: current status and future directions," *International Journal of Hyperthermia*, vol. 18, 2002, pagg. 267-284.
[87] F. Dughiero e S. Corazza, "Numerical simulation of thermal disposition with induction heating used for oncological hyperthermic treatment," *Medical and Biological Engineering and Computing*, vol. 43, Feb. 2005, pagg. 40-46.
[88] M.R. Gilchrist R K, "Selective inductive heating of lymph nodes," *Ann. Surg.*, vol. 146, 1957, pag. 596???606.
[89] S. Mornet, S. Vasseur, F. Grasset, e E. Duguet, "Magnetic nanoparticle design for medical diagnosis and therapy," *J. Mater. Chem.*, vol. 14, 2004, pagg. 2161-2175.
[90] V. Labhasetwar, *Biomedical applications of nanotechnology*, Hoboken N.J.: Wiley-Interscience, 2007.
[91] Goya G.F., Grazu V., e Ibarra M.R., "Magnetic Nanoparticles for Cancer Therapy," *Current Nanoscience*, Feb. 2008, pagg. 1-16.
[92] G. Bertotti, *Hysteresis in magnetism : for physicists, materials scientists, and engineers*, San Diego: Academic press, 1998.
[93] D.L. Leslie-Pelecky e R.D. Rieke, "Magnetic Properties of Nanostructured Materials," *Chemistry of Materials*, vol. 8, 1996, pagg. 1770-1783.
[94] P.C. Fannin, "Characterisation of magnetic fluids," *Journal of Alloys and Compounds*, vol. 369, 2004, pagg. 43-51.

[95] P.C. Fannin e W.T. Coffey, “Contribution of particle inertial effects to resonance in ferrofluids,” *Phys. Rev. E*, vol. 52, Dic. 1995, pagg. 6129–6140.
[96] C. Kumar, *Nanomaterials for cancer therapy*, Weinheim: Wiley-VCH, 2006.
[97] Y. Liu, H. Miyoshi, e M. Nakamura, “Nanomedicine for drug delivery and imaging: A promising avenue for cancer therapy and diagnosis using targeted functional nanoparticles,” *International Journal of Cancer*, vol. 120, 2007, pagg. 2527-2537.
[98] A. Ito, M. Shinkai, H. Honda, e T. Kobayashi, “Medical application of functionalized magnetic nanoparticles,” *Journal of bioscience and bioengineering*, vol. 100, Lug. 2005, pagg. 1-11.
[99] H.R. Hergt R, “Enhancement of AC-losses of magnetic nanoparticles for heating applications,” *J. Magn. Magn. Mater.*, vol. 280, 2004, pag. 358.
[100] C. Kumar, *Nanomaterials for medical diagnosis and therapy*, Weinheim: Wiley-VCH, 2007.
[101] T.K. Jain, M.K. Reddy, M.A. Morales, D.L. Leslie-Pelecky, e V. Labhasetwar, “Biodistribution, Clearance, and Biocompatibility of Iron Oxide Magnetic Nanoparticles in Rats,” *Molecular Pharmaceutics*, vol. 5, Apr. 2008, pagg. 316-327.
[102] S.J. DeNardo, G.L. DeNardo, L.A. Miers, A. Natarajan, A.R. Foreman, C. Gruettner, G.N. Adamson, e R. Ivkov, “Development of Tumor Targeting Bioprobes (111In-Chimeric L6 Monoclonal Antibody Nanoparticles) for Alternating Magnetic Field Cancer Therapy,” *Clinical Cancer Research*, vol. 11, Ott. 2005, pagg. 7087s -7092s.
[103] S.J. DeNardo, G.L. DeNardo, A. Natarajan, L.A. Miers, A.R. Foreman, C. Gruettner, G.N. Adamson, e R. Ivkov, “Thermal Dosimetry Predictive of Efficacy of 111In-ChL6 Nanoparticle AMF-Induced Thermoablative Therapy for Human Breast Cancer in Mice,” *J Nucl Med*, vol. 48, Mar. 2007, pagg. 437-444.
[104] P.C. Fannin, A. Slawska-Waniewska, P. Didukh, A.T. Giannitsis, e S.W. Charles, “Dynamic properties of a system of cobalt nanoparticles,” *Eur. Phys. J. AP*, vol. 17, Gen. 2002, pagg. 3-9.
[105] G. Baldi, D. Bonacchi, C. Innocenti, G. Lorenzi, e C. Sangregorio, “Cobalt ferrite nanoparticles: The control of the particle size and surface state and their effects on magnetic properties,” *Journal of Magnetism and Magnetic Materials*, vol. 311, 2007, pagg. 10-16.
[106] Rosensweig R E, “Heating magnetic fluid with alternating magnetic field,” *J. Magn. Magn. Mater.*, vol. 252, 2002, pag. 370.
[107] J.P. Fortin, F. Gazeau, e C. Wilhelm, “Intracellular heating of living cells through Neel relaxation of magnetic nanoparticles,” *European biophysics journal : EBJ*, vol. 37, Feb. 2008, pagg. 223-228.
[108] P.F.D. Châtel, I. Nándori, J. Hakl, S. Mészáros, e K. Vad, “Magnetic particle hyperthermia: Néel relaxation in magnetic nanoparticles under circularly polarized field,” *Journal of Physics: Condensed Matter*, vol. 21, 2009, pag. 124202.
[109] T. Torigoe, Y. Tamura, e N. Sato, “Heat shock proteins and immunity: Application of hyperthermia for immunomodulation,” *International Journal of Hyperthermia*, vol. 25, 2009, pagg. 610-616.
[110] K. Tanaka, A. Ito, T. Kobayashi, T. Kawamura, S. Shimada, K. Matsumoto, T. Saida, e H. Honda, “Heat immunotherapy using magnetic nanoparticles and dendritic cells for T-lymphoma,” *Journal of bioscience and bioengineering*, vol. 100, Lug. 2005, pagg. 112-115.
[111] R. Ivkov, S.J. DeNardo, W. Daum, A.R. Foreman, R.C. Goldstein, V.S. Nemkov, e G.L. DeNardo, “Application of High Amplitude Alternating Magnetic Fields for Heat Induction of Nanoparticles Localized in Cancer,” *Clinical Cancer Research*, vol. 11, Ott. 2005, pagg. 7093s -7103s.

[112] M.A. Dobrovolskaia, P. Aggarwal, J.B. Hall, e S.E. McNeil, "Preclinical Studies To Understand Nanoparticle Interaction with the Immune System and Its Potential Effects on Nanoparticle Biodistribution," *Molecular Pharmaceutics*, vol. 5, 2008, pagg. 487-495.
[113] S.R. Jordan A, "Endocytosis of dextran and silan-coated magnetite nanoparticles and the effect of intracellular hyperthermia on human mammary carcinoma cells in vitro," *J. Magn. Magn. Mater.*, vol. 194, 1999, pag. 185.
[114] A. Ito e T. Kobayashi, "Intracellular Hyperthermia Using Magnetic Nanoparticles: A Novel Method for Hyperthermia Clinical Applications," *Thermal Medicine*, vol. 24, 2008, pag. 113.
[115] A. Pasqualino, *Anatomia umana : citologia, istologia, embriologia, anatomia sistematica*, Torino: UTET, 2002.
[116] G. Kong, R.D. Braun, e M.W. Dewhirst, "Characterization of the Effect of Hyperthermia on Nanoparticle Extravasation from Tumor Vasculature," *Cancer Research*, vol. 61, Apr. 2001, pagg. 3027 -3032.
[117] S.K. Jones e J.G. Winter, "Experimental examination of a targeted hyperthermia system using inductively heated ferromagnetic microspheres in rabbit kidney," *Physics in Medicine and Biology*, vol. 46, 2001, pag. 385.
[118] K. Stribley, B. Gray, R. Chmiel, J. Heggie, e R. Bennett, "Internal radiotherapy for hepatic metastases II: The blood supply to hepatic metastases," *Journal of Surgical Research*, vol. 34, Gen. 1983, pagg. 25-32.
[119] N. Tsafnat, G. Tsafnat, T.D. Lambert, e S.K. Jones, "Modelling heating of liver tumours with heterogeneous magnetic microsphere deposition," *Physics in Medicine and Biology*, vol. 50, 2005, pag. 2937.
[120] J.S. Kim, T. Yoon, K.N. Yu, B.G. Kim, S.J. Park, H.W. Kim, K.H. Lee, S.B. Park, J. Lee, e M.H. Cho, "Toxicity and Tissue Distribution of Magnetic Nanoparticles in Mice," *Toxicological Sciences*, vol. 89, Gen. 2006, pagg. 338-347.
[121] J.W. Baish e R.K. Jain, "Fractals and Cancer," *Cancer Research*, vol. 60, Lug. 2000, pagg. 3683 -3688.
[122] M. Salloum, R. Ma, e L. Zhu, "Enhancement in treatment planning for magnetic nanoparticle hyperthermia: Optimization of the heat absorption pattern," *International Journal of Hyperthermia*, vol. 25, 2009, pagg. 309-321.
[123] M. Salloum, R. Ma, e L. Zhu, "An in-vivo experimental study of temperature elevations in animal tissue during magnetic nanoparticle hyperthermia," *International Journal of Hyperthermia*, vol. 24, 2008, pagg. 589-601.
[124] M. Salloum, R.H. Ma, D. Weeks, e L. Zhu, "Controlling nanoparticle delivery in magnetic nanoparticle hyperthermia for cancer treatment: Experimental study in agarose gel," *International Journal of Hyperthermia*, vol. 24, 2008, pagg. 337-345.
[125] M. Pavel, G. Gradinariu, e A. Stancu, "Study of the Optimum Dose of Ferromagnetic Nanoparticles Suitable for Cancer Therapy Using MFH," *Magnetics, IEEE Transactions on*, vol. 44, 2008, pagg. 3205-3208.
[126] M. Pavel e A. Stancu, "Study of the Optimum Injection Sites for a Multiple Metastases Region in Cancer Therapy by Using MFH," *Magnetics, IEEE Transactions on*, vol. 45, 2009, pagg. 4825-4828.
[127] M. Pavel e A. Stancu, "Ferromagnetic Nanoparticles Dose Based on Tumor Size in Magnetic Fluid Hyperthermia Cancer Therapy," *Magnetics, IEEE Transactions on*, vol. 45, 2009, pagg. 5251-5254.
[128] C. Nicholson, "Diffusion and related transport mechanisms in brain tissue," *Reports on Progress in Physics*, vol. 64, 2001, pag. 815.
[129] V.S. Kalambur, E.K. Longmire, e J.C. Bischof, "Cellular Level Loading and Heating of

Superparamagnetic Iron Oxide Nanoparticles," *Langmuir*, vol. 23, Nov. 2007, pagg. 12329-12336.
[130] J. Zhou, C. Leuschner, C. Kumar, J.F. Hormes, e W.O. Soboyejo, "Sub-cellular accumulation of magnetic nanoparticles in breast tumors and metastases," *Biomaterials*, vol. 27, Mar. 2006, pagg. 2001-2008.
[131] J.P. Fortin, C. Wilhelm, J. Servais, C. Menager, J.C. Bacri, e F. Gazeau, "Size-sorted anionic iron oxide nanomagnets as colloidal mediators for magnetic hyperthermia," *Journal of the American Chemical Society*, vol. 129, Mar. 2007, pagg. 2628-2635.
[132] Hao-Yu Tseng, Chen-Yi Lee, Ying-Hsia Shih, Xi-Zhang Lin, e Gwo-Bin Lee, "Hyperthermia Cancer Therapy Utilizing Superparamagnetic Nanoparticles," *Nano/Micro Engineered and Molecular Systems, 2007. NEMS '07. 2nd IEEE International Conference on*, 2007, pagg. 163-166.
[133] N.A. Brusentsov, L.V. Nikitin, T.N. Brusentsova, A.A. Kuznetsov, F.S. Bayburtskiy, L.I. Shumakov, e N.Y. Jurchenko, "Magnetic fluid hyperthermia of the mouse experimental tumor," *Journal of Magnetism and Magnetic Materials*, vol. 252, Nov. 2002, pagg. 378-380.
[134] T. Atsumi, B. Jeyadevan, Y. Sato, e K. Tohji, "Heating efficiency of magnetite particles exposed to AC magnetic field," *Journal of Magnetism and Magnetic Materials*, vol. 310, Mar. 2007, pagg. 2841-2843.
[135] R. Hergt, R. Hiergeist, I. Hilger, W.A. Kaiser, Y. Lapatnikov, S. Margel, e U. Richter, "Maghemite nanoparticles with very high AC-losses for application in RF-magnetic hyperthermia," *Journal of Magnetism and Magnetic Materials*, vol. 270, Apr. 2004, pagg. 345-357.
[136] L. Zhang, H. Gu, e X. Wang, "Magnetite ferrofluid with high specific absorption rate for application in hyperthermia," *Journal of Magnetism and Magnetic Materials*, vol. 311, Apr. 2007, pagg. 228-233.
[137] A. Jordan, R. Scholz, K. Maier-Hauff, M. Johannsen, P. Wust, J. Nadobny, H. Schirra, H. Schmidt, S. Deger, S. Loening, W. Lanksch, e R. Felix, "Presentation of a new magnetic field therapy system for the treatment of human solid tumors with magnetic fluid hyperthermia," *Journal of Magnetism and Magnetic Materials*, vol. 225, 2001, pagg. 118-126.
[138] Gneveckow U et al, "Description and characterization of the novel hyperthermia- and thermoablation system," *Med. Phys.*, vol. 31, 2004, pag. 1444.
[139] B. Alberts, *Molecular biology of the cell*, New York: Garland Science, 2002.
[140] A. Pasqualino e G. Panattoni, *Anatomia umana : citologia, istologia, embriologia, anatomia sistematica*, Torino: UTET, 2002.
[141] D. Reato, A. Rahman, M. Bikson, e L.C. Parra, "Low-Intensity Electrical Stimulation Affects Network Dynamics by Modulating Population Rate and Spike Timing," *J. Neurosci.*, vol. 30, Nov. 2010, pagg. 15067-15079.
[142] C. Ariza, A. Fleury, C. Tormos, V. Petruk, S. Chawla, J. Oh, D. Sakaguchi, e S. Mallapragada, "The Influence of Electric Fields on Hippocampal Neural Progenitor Cells," *Stem Cell Reviews and Reports*, vol. 6, Dic. 2010, pagg. 585-600.
[143] J. Lefaucheur, "Methods of therapeutic cortical stimulation," *Neurophysiologie Clinique/Clinical Neurophysiology*, vol. 39, Feb. 2009, pagg. 1-14.
[144] J.K. Deans, A.D. Powell, e J.G.R. Jefferys, "Sensitivity of coherent oscillations in rat hippocampus to AC electric fields," *The Journal of Physiology*, vol. 583, 2007, pagg. 555 -565.
[145] J.G. Jefferys, "Influence of electric fields on the excitability of granule cells in guinea-pig hippocampal slices.," *The Journal of Physiology*, vol. 319, Gen. 1981, pagg. 143 - 152.

[146] W.E. Brownell, F. Qian, e B. Anvari, “Cell Membrane Tethers Generate Mechanical Force in Response to Electrical Stimulation,” *Biophysical Journal*, vol. 99, Ago. 2010, pagg. 845-852.
[147] J. Behari, K.K. Kunjilwar, e S. Pyne, “Interaction of low level modulated RF radiation with Na+-K+-ATPase,” *Bioelectrochemistry and Bioenergetics*, vol. 47, Dic. 1998, pagg. 247-252.
[148] M. Sadiku, *Numerical techniques in electromagnetics*, Boca Raton: CRC Press, 2000.
[149] D. Andreuccetti, M. Bini, A. Checcucci, A. Ignesti, L. Millanta, R. Olmi, e N. Rubino, *Protezione dai campi elettromagnetici non ionizzanti*, IROE, 2001.
[150] M. Stuchly e T. Dawson, “Interaction of low-frequency electric and magnetic fields with the human body,” *Proc. of the IEEE*, vol. 88, 2000, pagg. 643 - 664.
[151] O.P. Gandhi, “Some numerical methods for dosimetry: extremely low frequencies to microwave frequencies,” *Radio science*, vol. 30, 1995, pagg. 161-177.
[152] R. Scorretti, N. Burais, O. Fabregue, A. Nicolas, e L. Nicolas, “Computation of the Induced Current Density Into the Human Body Due to Relative LF Magnetic Field Generated by Realistic Devices,” *IEEE Trans. on Magnetics*, vol. 40, 2004, pagg. 643-646.
[153] K. Yee, “Numerical solution of initial boundary value problems involving Maxwell's equations in isotropic media,” *IEEE Trans. Antennas Propag.*, vol. 14, 1966, pagg. 585-589.
[154] D. Sullivan, D. Borup, e O. Gandhi, “Use of the Finite-Difference Time-Domain methid for calculating absorption in human tissues,” *IEEE Trans. Biomed. Eng.*, vol. 34, 1987, pagg. 148-1575.
[155] D. Sullivan, O. Gandhi, e A. Taflove, “Use of the finite-difference time-domain method for calculating EM absorption in man models,” *Biomedical Engineering, IEEE Transactions on*, vol. 35, 1988, pagg. 179-186.
[156] J.D. Moerloose, T. Dawson, e M. Stuchly, “Application of the finite difference time domain algorithm to quasi-static field analysis,” *Radio Sci.*, vol. 32, 1997, pagg. 329-341.
[157] F. Gustrau, A. Bahr, M. Rittweger, S. Goltz, e S. Eggert, “Simulation of induced current densities in the human body at industrial induction heating frequencies,” *IEEE Trans. on Electromagn. Compat.*, vol. 41, 1999, pagg. 480 - 486.
[158] O. Gandhi, J. DeFord, e H. Kanai, “Impedance method for calculation of power deposition patterns in magnetically induced hypertemias,” *IEEE Trans. Biomed. Eng.*, vol. 31, 1984, pagg. 644-651.
[159] N. Orcutt e O. Gandhi, “A 3-D impedance method to calculate power deposition in biological bodies subjected to time varying magnetic fields,” *IEEE Trans. Biomed. Eng.*, vol. 35, 1988, pagg. 577-583.
[160] M. Nadeem, T. Thorlin, O. Ghandi, e M. Persson, “Computation of electric and magnetic simulation in human head using 3-D impedance method,” *IEEE Trans. Biomed. Eng.*, vol. 50, 2003, pagg. 900-907.
[161] J. Deford e O. Gandhi, “An impedance method to calculate currents induced in biological bodies exposed to quasi-static electromagnetic fields,” *IEEE Trans. on Electromagn. Compat.*, vol. 27, 1985, pagg. 168-173.
[162] W. Xi, M. Stuchly, e O. Gandhi, “Induced electric currents in models of man and rodents from 60 Hz magnetic fields,” *IEEE Trans. Biomed. Eng.*, vol. 41, 1994, pagg. 1018-1023.
[163] J. Cheng, M.A. Stuchly, C. DeWagtert, e L. Martenss, “Magnetic field induced currents in a human head from use of portable appliances,” *Phys. Med. Biol*, vol. 40, 1995, pagg. 495-510.

[164] M. Eberdt, P.K.Brown, e G. Lazzi, “Two-dimensional SPICE-linked multiresolution impedance method for low-frequency electromagnetic interactions,” *IEEE Trans. Biomed. Eng.*, vol. 50, 2003, pagg. 881-889.
[165] O. Gandhi e J. DeFord, “Calculation of EM power deposition for operator exposure to RF induction heaters,” *IEEE Trans. on Electromagn. Compat.*, vol. 30, 1984, pagg. 63-68.
[166] E. Gjonaj, M. Bartsch, M. Clemens, S. Schupp, e T. Weiland, “High-resolution human anatomy models for advanced electromagnetic field computations,” *IEEE Trans. on Magnetics*, vol. 38, 2002, pagg. 357 - 360.
[167] R. Spiegel, “High-voltage electric field coupling to humans using moment method techniques,” *IEEE Trans. Biomed. Eng.*, vol. 24, 1977, pagg. 466-472.
[168] T.W.Dawson, K. Caputa, e M.A.Stuchly, “Organ dosimetry for human exposure to non-uniform 60-Hz magnetic fields,” *IEEE Trans. Power Delivery*, vol. 14, 1999, pagg. 1234-1239.
[169] K. Chen, H. Chuang, e C. Lin, “Quantification of interaction between ELF-LF electric fields and human bodies,” *IEEE Trans. Biomed. Eng.*, vol. 33, 1986, pagg. 746-755.
[170] J. Shen, *Computational electromagnetics using boundary elements*, Computational Mechanics Publications, 1995.
[171] C. Arturi, L.D. Renzo, S. Garoni, e A. Gattinoni, “Dosimetria su un modello di testa umana,” *AEI*, vol. 91, 2004, pagg. 42-45.
[172] O. Bottauscio, M. Chiampi, e L. Zilberti, “Boundary Element Approaches for the Evaluation of Human Exposure to Low Frequency Electromagnetic Fields,” *Magnetics, IEEE Transactions on*, vol. 45, 2009, pagg. 1674-1677.
[173] E. Tonti, “Finite formulation of electromagnetic field,” *Magnetics, IEEE Transactions on*, vol. 38, 2002, pagg. 333-336.
[174] M. Bullo, F. Dughiero, M. Guarnieri, e E. Tittonel, “Nonlinear coupled thermo-electromagnetic problems with the cell method,” *Magnetics, IEEE Transactions on*, vol. 42, 2006, pagg. 991-994.
[175] M. Bullo, V. D'Ambrosio, F. Dughiero, e M. Guarnieri, “A 3-D Cell Method Formulation for Coupled Electric and Thermal Problems,” *Magnetics, IEEE Transactions on*, vol. 43, 2007, pagg. 1197-1200.
[176] F. Gustrau, A. Bahr, M. Rittweger, S. Goltz, e S. Eggert, “Simulation of induced current densities in the human body at industrial induction heating frequencies,” *IEEE Trans. on Electromagn. Compat.*, vol. 41, 1999, pagg. 480 - 486.
[177] I. Zubal, C. Harrell, E. Smith, Z. Rattner, G. Gindi, e P. Hoffer, “Computerized three-dimensional segmented human anatomy.,” *Med Phys*, vol. 21, Feb. 1994, pagg. 299-302.
[178] T. Dawson e M. Stuchly, “High-resolution organ dosimetry for human exposure to low-frequency magnetic fields,” *Magnetics, IEEE Transactions on*, vol. 34, 1998, pagg. 708-718.
[179] R. Scorretti, N. Burais, L. Nicolas, e A. Nicolas, “Modeling of induced current into the human body by low-frequency magnetic field from experimental data,” *IEEE Trans. on Magnetics*, vol. 41, 2005, pagg. 1992-1995.
[180] T. Matsumoto, N. Hayashi, e K. Isaka, “Analysis of induced current density in ellipsoidal human model exposed to concurrent ELF electric and magnetic fields with phase differences,” *Proc. IEEE EMC Conference*, 2003, pagg. 2343-2346.
[181] S. Nishizawa, H. Ruoss, F. Landstorfer, e O. Hashimoto, “Numerical study on an equivalent source model for inhomogeneous magnetic field dosimetry in the low-frequency range,” *Biomedical Engineering, IEEE Transactions on*, vol. 51, 2004, pagg. 612-616.

[182] P. Dimbylow, “Current densities in a 2 mm resolution anatomically realistic model of the body induced by low frequency electric fields,” *Phys. Med. Biol*, vol. 45, 2000, pagg. 1013-1022.
[183] P. Dimbylow, “Development of the female voxel phantom, NAOMI, and its application to calculations of induced current densities and electric fields from applied low frequency magnetic and electric fields,” *Phys. Med. Biol*, vol. 50, 2005, pagg. 1047-1070.
[184] P. Dimbylow, “Induced current densities from low-frequency magnetic fields in a 2 mm resolution, anatomically realistic model of the body,” *Phys. Med. Biol*, vol. 48, 1998, pagg. 221-230.
[185] G. Mouchawar, J. Nyenhuist, J. Bourlandt, L. Geddest, D. Schaefer, e M. Riehl, “Magnetic Stimulation of Excitable Tissue: Calculation of Induced Eddy-Currents With a Three-Dimensional Finite-Element Model,” *IEEE Trans. on Magnetics*, 1993, pagg. 3355-3357.
[186] W. Wang e S. Eisemberg, “A three-dimensionale finite element method for computing magnetically induced currents in tissues,” *IEEE Trans. on Magnetics*, vol. 30, 1994, pagg. 5015-5023.
[187] O. Gandhi, G. Kang, D. Wu, e G. Lazzi, “Currents induced in anatomic models of the human for uniform and nonuniform power frequency magnetic fields,” *Bioelectromagnetics*, vol. 22, 2001, pagg. 112-121.
[188] A. Barchanski, M.Clemens, E. Gjonaj, H.D. Gersem, e T. Weiland, “Large-Scale Calculation of Low-Frequency-Induced Currents in High-Resolution Human Body Models,” *IEEE Trans. on Magnetics*, vol. 43, 2007, pagg. 1693-1696.
[189] V. D'Ambrosio, F. Dughiero, e M. Forzan, “Numerical models of RF-thermal ablation treatments,” *International Journal of Applied Electromagnetics and Mechanics*, vol. 25, Gen. 2007, pagg. 429-433.
[190] C.M. Furse e O.P. Gandhi, “Calculation of electric fields and currents induced in a millimeter-resolution human model at 60 Hz using the FDTD method,” *Bioelectromagnetics*, vol. 19, 1998, pagg. 293-299.
[191] V. D’Ambrosio e F. Dughiero, “Numerical model for RF capacitive regional deep hyperthermia in pelvic tumors,” *Medical and Biological Engineering and Computing*, vol. 45, Mag. 2007, pagg. 459-466.
[192] F. Dughiero e V. D'Ambrosio, “FEM models of radiofrequency thermal treatments in cancer cure,” Padova: SGE Editoriali, 2004, pagg. 709-716.
[193] V. D'Ambrosio, F. Dughiero, M. Giri, e S. Maluta, “Numerical model for RF capacitive hyperthermia for brain tumours,” *ESHO Proceeding*, 2006, pagg. 47-49.
[194] S.Gabriel, R. Laul, e C.Gabriel, “The dielectric properties of biological tissues: II. Measurements in the frequency range 10 Hz to 20 GHz,” *Phys. Med. Biol*, vol. 41, 1996, pagg. 2251-2269.
[195] S.Gabriel, R. Laul, e C.Gabriel, “The dielectric properties of biological tissues: III. Parametric models for the dielectric spectrum of tissues,” *Phys. Med. Biol*, vol. 41, 1996, pagg. 2271-2293.
[196] D.Andreuccetti e R.Fossi,, “Proprietà dielettriche dei tessuti umani: definizioni, modello parametrico, codici di calcolo,” 2000.
[197] M. Stuchly e S. Stuchly, “Dielectric properties of biological substances-Tabulated,” *J. Microwave Power*, vol. 15, 1980, pagg. 19-26.
[198] J. Lang, “Impact of nonlinear heat transfer on temperature control in regional hyperthermia,” *IEEE Trans Biomed Eng.*, vol. 46, 1999, pagg. 1129-38.
[199] A. Candeo e F. Dughiero, “Numerical FEM Models for the Planning of Magnetic Induction Hyperthermia Treatments With Nanoparticles,” *Magnetics, IEEE*

Transactions on, vol. 45, 2009, pagg. 1658-1661.
[200] K.J. Binns, P.J. Lawrenson, e C.W. Trowbridge, *The analytical and numerical solution of electric and magnetic fields*, Chichester: Wiley, 1992.
[201] H. Carslaw, *Conduction of heat in solids*, Oxford [Oxfordshire] New York: Clarendon Press; Oxford University Press, 1986.
[202] J. Stratton, *Electromagnetic theory*, New York ;St. Louis ;Paris [etc.]: McGraw-Hill, 1941.
[203] T. Morisue, "A comparison of the Coulomb gauge and Lorentz gauge magnetic vector potential formulations for 3D eddy current calculations," *Magnetics, IEEE Transactions on*, vol. 29, 1993, pagg. 1372-1375.
[204] O. Biro, "Edge element formulations of eddy current problems," *Computer Methods in Applied Mechanics and Engineering*, vol. 169, Feb. 1999, pagg. 391-405.
[205] C.J. Carpenter, "Comparison of alternative formulations of 3-dimensional magnetic-field and eddy-current problems at power frequencies," *Electrical Engineers, Proceedings of the Institution of*, vol. 124, 1977, pagg. 1026-1034.
[206] T. Nakata, N. Takahashi, K. Fujiwara, e Y. Okada, "Improvements of the T-Ω method for 3-D eddy current analysis," *Magnetics, IEEE Transactions on*, vol. 24, 1988, pagg. 94-97.
[207] T. Preston e A. Reece, "Solution of 3-dimensional eddy current problems: The T-Ω method," *Magnetics, IEEE Transactions on*, vol. 18, 1982, pagg. 486-491.
[208] O. Biro, K. Preis, G. Vrisk, K. Richter, e I. Ticar, "Computation of 3-D magnetostatic fields using a reduced scalar potential," *Magnetics, IEEE Transactions on*, vol. 29, 1993, pagg. 1329-1332.
[209] Y. Marechal, G. Meunier, e H. Ben Harara, "A new 3D AV-Φ-Φr formulation," *Magnetics, IEEE Transactions on*, vol. 28, 1992, pagg. 1204-1207.
[210] T. Morisue, "Infinitely many formulations using the magnetic vector potential with the Coulomb gauge for 3D field calculations," *Magnetics, IEEE Transactions on*, vol. 26, 1990, pagg. 715-718.
[211] T. Morisue e T. Yajima, "The Lorentz gauge vector potential formulation for the boundary integral equation method," *Magnetics, IEEE Transactions on*, vol. 30, 1994, pagg. 3032-3035.
[212] T. Morisue, "Magnetic vector potential and electric scalar potential in three-dimensional eddy current problem," *Magnetics, IEEE Transactions on*, vol. 18, 1982, pagg. 531-535.
[213] O. Biro e K. Preis, "On the use of the magnetic vector potential in the finite-element analysis of three-dimensional eddy currents," *Magnetics, IEEE Transactions on*, vol. 25, 1989, pagg. 3145-3159.
[214] H.H. Pennes, "Analysis of Tissue and Arterial Blood Temperatures in the Resting Human Forearm," *Journal of applied physiology*, vol. 85, Lug. 1998, pagg. 5-34.
[215] P. Di Barba, *Multiobjective Shape Design in Electricity and Magnetism*, Springer, 2010.
[216] V. D'Ambrosio, P.D. Barba, F. Dughiero, M. Mognaschi, e A. Savini, "Non-invasive thermometry for the thermal ablation of liver tumor: A computational methodology," *International Journal of Applied Electromagnetics and Mechanics*, vol. 25, 2007, pagg. 407-412.
[217] L.M. Schmitt, "Theory of genetic algorithms," *Theoretical Computer Science*, vol. 259, Mag. 2001, pagg. 1-61.
[218] S. Forrest, "Genetic Algorithms: Principles of Natural Selection Applied to Computation," *Science*, vol. 261, 1993, pagg. 872-878.
[219] C.M. Fonseca e P.J. Fleming, "An overview of evolutionary algorithms in

multiobjective optimization," *Evol. Comput.*, vol. 3, 1995, pagg. 1-16.
[220] T. Hanne, "Global Multiobjective Optimization Using Evolutionary Algorithms," *Journal of Heuristics*, vol. 6, Ago. 2000, pagg. 347-360.
[221] E. Zitzler e L. Thiele, "Multiobjective evolutionary algorithms: a comparative case study and the strength Pareto approach," *Evolutionary Computation, IEEE Transactions on*, vol. 3, 1999, pagg. 257-271.
[222] F. Glover, "Tabu Search — Part I," *ORSA Journal on Computing*, vol. 1, 1989, pagg. 190-206.
[223] S. Kirkpatrick, C.D. Gelatt, e M.P. Vecchi, "Optimization by Simulated Annealing," *Science*, vol. 220, Mag. 1983, pagg. 671-680.
[224] I. Zelinka, "Real-time deterministic chaos control by means of selected evolutionary techniques," *Engineering Applications of Artificial Intelligence,*, vol. In Press, Corrected Proof.
[225] K. Deep e Dipti, *A new hybrid Self Organizing Migrating Genetic Algorithm for function optimization*, 2007.
[226] K. Yamazaki, T. Kawamoto, H. Fujinami, e T. Shigemitsu, "Investigation of ELF Magnetically induced current inside the human body: development of estimation tools and effect of organ conductivity," *Electrical Engineering in Japan*, vol. 134, 2001.
[227] Dughiero F., M. Forzan, e Sieni E., "Simple 3D fem models for evaluation of EM exposure produced by welding equipments," *Studies in Applied Electromagnetics and Mechanics*, Ios Pr Inc, 2010, pagg. 911-919.
[228] Dughiero F., Forzan M., e Sieni E., "A numerical evaluation of electromagnetic fields exposure on real human body models until 100 kHz," *COMPEL: Int J for Computation and Maths. in Electrical and Electronic Eng.*, vol. 29, 2010, pagg. 1552-1561.
[229] B. Bullo M., Chiampi M., Dughiero F., Sieni E., e Zilberti L., "Numerical prediction of currents produced in human models by induction cooking appliances , Proc. International Symposium on Heating by Electromagnetic Sources," Padova: SGE Editoriali, 2010, pagg. 67-74.
[230] IEC 62226-3-1, "Exposure to electric and magnetic fields in the low and intermediate frequency range – Methods for calculating the current density and internal electric field induced in the human body," 2008.
[231] T. Fawzi, M. Ahmed, e P. Burke, "On the use of the impedance boundary conditions in eddy current problems," *Magnetics, IEEE Transactions on*, vol. 21, 1985, pagg. 1835-1840.
[232] E.Sieni e M.Bertocco, "Nonuniform low frequency magnetic field measurement," *Proc. IMTC*, 2006, pagg. 2194-2199.
[233] M.Bertocco, C. Greggio, E. Sieni, e A. Sona, "Magnetic Field Measurement in Industrial Environment," *Proc. IMTC*, 2007.
[234] O. Bottauscio, M. Chiampi, G. Crotti, e M. Zucca, "Probe influence on the measurement accuracy of non uniform LF magnetic fields," *IEEE Trans. on Instrument. and Meas.*, vol. 54, 2005, pagg. 722-726.
[235] K. Jokela, "Restricting exposure to pulsed and broadband magnetic fields," *Health Physics*, vol. 79, 2000, pagg. 373-388.
[236] Dughiero F., M. Forzan, e Sieni E., "Numerical FEM models for the evaluation of EM fields exposure near welding machines," *Proceeding of COMPUMAG*, 2009.
[237] F. Menestrina, "Metodologie per la valutazione dell'esposizione ai campi elettromagnetici in macchine per saldatura elettrica," Padova, 2008.
[238] Dughiero F., M. Forzan, e Sieni E., "Simple 3D fem models for evaluation of EM exposure produced by welding equipments," *Proceeding of ISEF*, 2009.
[239] S. Odenbach, "Recent progress in magnetic fluid research," *Journal of Physics:*

Condensed Matter, vol. 16, 2004, pag. R1135.
[240] R.E. Rosensweig, R. Kaiser, e G. Miskolczy, "Viscosity of magnetic fluid in a magnetic field," *Journal of Colloid and Interface Science*, vol. 29, Apr. 1969, pagg. 680-686.
[241] P.C. Fannin, C.M. Oireachtaigh, S. Odenbach, e N. Mattoussevitch, "Investigation of the isotropic properties of an aggregated cobalt based magnetic fluid," *Journal of Physics D: Applied Physics*, vol. 40, 2007, pag. 6484.
[242] P.C. Fannin, B.K.P. Scaife, e S.W. Charles, "Relaxation and resonance in ferrofluids," *Journal of Magnetism and Magnetic Materials*, vol. 122, 1993, pagg. 159-163.
[243] I. Hilger, R. Hergt, e W.A. Kaiser, "Use of magnetic nanoparticle heating in the treatment of breast cancer," *IEE proceedings.Nanobiotechnology*, vol. 152, Feb. 2005, pagg. 33-39.
[244] W. Andra, C.G. d'Ambly, R. Hergt, I. Hilger, e W.A. Kaiser, "Temperature distribution as function of time around a small spherical heat source of local magnetic hyperthermia," *Journal of Magnetism and Magnetic Materials*, vol. 194, Apr. 1999, pagg. 197-203.
[245] P. Di Barba, F. Dughiero, e F. Trevisan, "Optimization of the Loney's solenoid through quasi-analytical strategies: a benchmark problem reconsidered," *Magnetics, IEEE Transactions on*, vol. 33, 1997, pagg. 1864-1867.
[246] P. Di Barba, M. Mognaschi, R. Palka, e A. Savini, "Optimization of the MIT Field Exciter by a Multiobjective Design," *Magnetics, IEEE Transactions on*, vol. 45, 2009, pagg. 1530-1533.
[247] P. Di Barba, "Evolutionary Multiobjective Optimization Methods for the Shape Design of Industrial Electromagnetic Devices," *Magnetics, IEEE Transactions on*, vol. 45, 2009, pagg. 1436-1441.
[248] E. Durand, *Magnétostatique*, Masson et C. Ed., 1968.
[249] P. Di Barba, F. Dughiero, E. Sieni, e A. Candeo, "Coupled field synthesis in Magnetic Fluid Hyperthermia," *in press on IEEE Tansaction on magnetics*.
[250] P. Di Barba, F. Dughiero, e E. Sieni, "Synthesizing a nanoparticle distribution in magnetic fluid hyperthermia," Padova: SGE Editoriali, 2010, pagg. 483-490.
[251] P.D. Barba, F. Dughiero, e E. Sieni, "Magnetic Field Synthesis in the Design of Inductors for Magnetic Fluid Hyperthermia," *Magnetics, IEEE Transactions on*, vol. 46, 2010, pagg. 2931-2934.
[252] P.N. Sen, "Diffusion and tissue microstructure," *Journal of Physics: Condensed Matter*, vol. 16, 2004, pag. S5213.
[253] L. Geddes, *Electrodes and the measurement of bioelectric events*, New York: Wiley-Interscience, 1972.
[254] L. Geddes, *Principles of applied biomedical instrumentation*, New York: Wiley, 1989.
[255] A. Carlon, "Esperimenti per la misura di campi elettrici in cervello di ratto," 2010.
[256] A. Rustgi, "Modelling of the glass microelectrode tip," *Science, Measurement and Technology, IEE Proceedings* -, vol. 141, 1994, pagg. 391-394.
[257] D.R. Klingler, "Capacitive Modulation of Micropipet Impedance," *Biomedical Engineering, IEEE Transactions on*, vol. BME-24, 1977, pagg. 129-134.
[258] O. Schanne, M. Lavallee, R. Laprade, e S. Gagne, "Electrical properties of glass microelectrodes," *Proceedings of the IEEE*, vol. 56, 1968, pagg. 1072-1082.